Inhibitory Circuits of the CA3-Dentate Gyrus System

Dissertation

zur

Erlangung des Doktorgrades (Dr. rer. nat.)

der

Mathematisch-Naturwissenschaftlichen Fakultät

der

Rheinischen Friedrich-Wilhelms-Universität Bonn

vorgelegt von

Daniel Müller-Komorowska

aus

Mechernich

Bonn 2021

Angefertigt mit Genehmigung der Mathematisch-Naturwissenschaftlichen Fakultät
der Rheinischen Friedrich-Wilhelms-Universität Bonn

1. Gutachter: Prof. Dr. Heinz Beck
2. Gutachter: Prof. Dr. Michael Pankratz

Tag der Promotion: September 30. 2021
Erscheinungsjahr: 2021

Disclosure statement

I hereby certify that the work presented here was accomplished by myself and without the use of illegitimate means or support, and that no sources and tools were used other than those cited.

Parts of this thesis were previously published.

Chapter 5:
Müller-Komorowska, D., Opitz, T., Elzoheiry, S., Schweizer, M., Ambrad Giovannetti, E., & Beck, H. (2020). Nonspecific Expression in Limited Excitatory Cell Populations in Interneuron-Targeting Cre-driver Lines Can Have Large Functional Effects. Frontiers in Neural Circuits, 14(April), 1–13. https://doi.org/10.3389/fncir.2020.00016

Chapter 6:
Braganza, O., Müller-Komorowska, D., Kelly, T., & Beck, H. (2020). Quantitative properties of a feedback circuit predict frequency-dependent pattern separation. ELife, 813188. https://doi.org/10.7554/eLife.53148

Bonn, May 26., 2021

Abstract

Neuronal inhibition is an essential feature of all brain areas. Besides controlling the average rate of neuronal firing, it also controls the precise timing of action potentials and mediates several types of network oscillations that are related to cognition. Inhibition is provided primarily by interneurons that release gamma-Aminobutyric acid (GABA). Many interneuron subtypes have been identified based on their morphology, electrophysiology, and molecular markers. Here we characterize a novel interneuron subtype of the hippocampus that is primarily found in the CA3 area. It colocalizes the molecular interneuron markers somatostatin (Sst) and glutamate decarboxylase (Gad) but also solute carrier family 17 member 8 (Slc17a8). Slc17a8 is a gene encoding the vesicular glutamate transporter 3 and is therefore a marker of glutamatergic neurons. We used patch seq to transcriptomically and electrophysiologically characterize this $Sst^+/Slc17a8^+$ interneuron subtype, finding that it is electrophysiologically not clearly distinguishable from other interneuron subtypes. To investigate its functional role, future studies should establish methods to specifically target them with optogenetic constructs. We tested a transgenic mouse line that was developed to guide expression to Sst interneurons.

Transgenic mouse lines are widely used to express constructs that allow targeted manipulation of neuronal activity. We used the SST-Cre mouse line to express channelrhodopsin attached to yellow fluorescent protein by intracranial viral injection in somatostatin positive interneurons of CA3. Viral transduction resulted in widespread axon signal in contralateral hippocampus and optogenetic activation caused strong excitatory postsynaptic currents in contralateral CA1 pyramidal cells. At the injection site, somatostatin negative cells in the pyramidal cell layer were expressing the viral construct. In other CA3 layers almost all expressing cells were also somatostatin positive. These data show that the mouse line is unsuitable to optogenetically study somatostatin interneurons in CA3 because it also targets pyramidal cells. Pyramidal cells however, do not express Slc17a8 and an intersectional strategy with a mouse line expressing another recombinase in $Slc17a8^+$ interneurons could in the future specifically target $Sst^+/Slc17a8^+$ interneurons.

While circuit level experiments are key to understanding behavior, only small parts of the network are accessible for manipulation and measurement at the same time. Computational modeling can be a powerful tool and provide a more complete picture of the entire simulated network. Experimentally well constrained models can provide testable hypotheses. Many of the inputs into CA3 come from the dentate gyrus. The dentate gyrus has the special property that

its outputs are pattern separated. We implemented a circuit model of the dentate gyrus to study the role feedback inhibition plays during pattern separation.

Feedback inhibition is a specific type of inhibition that is activated by the same principal cells that receive the inhibition. For the model implementation we used data from optogenetic experiments to constrain properties of feedback inhibition. Pattern separation is a neuronal computation that decreases the similarity of the network output as compared to the networks input pattern. It is known to occur in the dentate gyrus and inhibition has been shown to support pattern separation. Accordingly, we found that removing feedback inhibition from the model impaired pattern separation. The size of this effect, however, depended on the frequency of oscillatory activity we imposed on the input pattern. At higher frequencies, feedback inhibition had a stronger effect. This was not the case for feedforward inhibition, which had similar effects regardless of frequency. These findings highlight the role of input frequency for pattern separation and suggest that different circuit motifs engage differently depending on the oscillatory state of the upstream area. Behaviorally our model predicts that interfering with oscillatory activity could affect hippocampal pattern separation

Abbreviations

Abbreviation	Description
AB	Antibody
BC	Basket Cell
CA1	Cornu Ammonis 1
CA3	Cornu Ammonis 3
CCK	Cholecystokinin
CPM	Counts Per Million
DG	Dentate Gyrus
DIO	Double-Floxed Inverted Open reading frame
EYFP	Enhanced Yellow Fluorescent Protein
GABA	Gamma-Aminobutyric Acid
Gad1-2	Glutamate decarboxylase 1-2
GC	Granule Cell
GLM	Generalized Linear Model
IN	Interneuron
LC	Locus Coeruleus
LHb	Lateral Habenula
MC	Mossy Cell
O-LM	Oriens-Lacunosum Moleculare
PCL	Pyramidal Cell Layer
PCR	Polymerase Chain Reaction
PFA	Paraformaldehyde
PV	Parvalbumin
ROI	Region of Interest
Slc17a6-8	Solute Carrier family 17 member 6-8
SO	Stratum Oriens
SR	Stratum Radiatum
Sst	Somatostatin
Th	Tyrosine Hydroxylase
TSNE	t-Distributed Stochastic Neighbor Embedding
VGluT1-3	Vesicular Glutamate Transporter 1-3
VTA	Ventral Tegmental Area

Contents

1 Introduction

The brain is a complex organ made of many different cell types. Neurons are a cell type that has a clear role in information processing. Neurons themselves can be divided into two major groups: principal cells and interneurons. Principal cells relay signals between different brain areas. Interneurons on the other hand control the excitability of principal cells and other interneurons. They do so mainly by directly inhibiting them. While it is important to keep principal cell excitability under control, interneurons fulfil a variety of other functions. They tune the precise spike timing at a millisecond range (Pouille & Scanziani, 2001) and control important network oscillations (Allen & Monyer, 2015). They have also been implicated in specific cognitive functions like memory formation and pattern discrimination (Sun et al., 2020).

Interneurons themselves are not one homogeneous cell type. In the visual cortex alone, 28 different interneuron subtypes were identified based on their morphology, electrical properties and mRNA expression (Gouwens et al., 2020). Depending on their subtype, they engage differently with their microcircuit. Some interneuron subtypes participate primarily in feed-forward inhibition, feedback inhibition, lateral inhibition, or disinhibition. Furthermore, different cell types preferentially inhibit different cortical layers. These different types of connectivity together with the large number of interneuron subtypes paint a complex picture of interneuron diversity.

Interneuron diversity has been approached with a variety of techniques, including intracellular electrophysiology, histochemistry and single cell transcriptomics. We used a technique called patch seq, a combination of intracellular electrophysiology and transcriptomic profiling (Cadwell, Scala, et al., 2017). Patch seq allows for the identification of subtypes with a combination of electrophysiological properties and molecular markers. However, identification of single cell subtypes alone is not sufficient to study the connectivity and larger network properties of interneuron populations. Ideally, patch seq could identify novel subtype markers to genetically target optogenetic actuators specifically to interneurons populations. This would allow for the manipulation of activity in specific population and the downstream effects.

Another important technique is computational modeling. While it does not prove biological mechanisms, it is widely used to discover possible mechanisms and guide experimental designs. Taken together, patch seq, transgenic expression and computational modeling provide a powerful toolbox to investigate interneuron diversity at multiple levels. The

single cell, network and computational level will become more relevant as increasingly rare interneuron subtypes are identified. Experiments regarding the functional relevance of small interneuron populations should be guided by solid characterization of their properties but also strong computational theory of the circuit they engage in.

This thesis focuses on the interneurons of the dentate gyrus – CA3 network of the mouse hippocampus. Therefore, the next chapter 1.1 will introduce some of the interneuron subtypes that are crucial in these regions. This network is interesting for several reasons. Unlike other hippocampal regions, the dentate gyrus and CA3 are recurrently connected (Scharfman, 2007). Chapter 1.2 will introduce the connectivity of the two regions. Furthermore, both regions are involved with two complementary functions of pattern separation and pattern completion. Both are introduced in Chapter 1.3.

1.1 Interneurons of the DG-CA3 system

In the hippocampus, any non-principal neuron capable of releasing gamma-aminobutyric acid (GABA) is considered an interneuron (Freund & Buzsáki, 1996). GABA is the main inhibitory neurotransmitter of the central nervous system. In the rat hippocampus, these inhibitory interneurons constitute 10%-15% of the entire neuronal population. They can be subdivided into subcategories according to four key features: molecular markers, electrophysiology, morphology, and connectivity (Maccaferri & Lacaille, 2003; The Petilla Interneuron Nomenclature Group (PING), 2008). All four are highly relevant for the hippocampus (Pelkey et al., 2017) and the CA3-DG system (Hosp et al., 2014). Here, we will focus on a few interneuron subtypes that are particularly important for hippocampal function.

1.1.1 Interneuron connectivity

Connectivity is a key characteristic of many interneuron subtypes (Espinoza et al., 2018). The input connectivity determines from which cell an interneuron receives its inputs. As we will discuss later, this is crucial for the function of interneurons, because the inputs determine whether they can participate in feedback, feed-forward or other inhibitory circuit motifs (Braganza & Beck, 2018). The output connectivity determines which cells an interneuron inhibits. For example, some interneuron subtypes more strongly target deep as opposed to superficial pyramidal cells in hippocampal CA1 (Soltesz & Losonczy, 2018). Moreover, the location of inhibition is crucial, as one of the most prominent interneuron distinctions is between dendritic (Klausberger, 2009) and perisomatic (Freund & Katona, 2007) targeting interneurons.

Two of the most extensively studied interneuron subtypes of the hippocampus are Parvalbumin (PV) positive basket cells (PVBCs) and oriens-lacunosum moleculare (O-LM) interneurons. Both interneuron subtypes feature distinct connectivity that is closely intertwined with their morphology. PVBCs are called basket cells because most of their axon is in the pyramidal cell layer, where they appear as thick, basket-like structures around principal cell somata during fluorescent imaging. O-LM cells on the other hand have most of their axon in the stratum lacunosum moleculare, where the distal dendrites of pyramidal cells are located.

Axon location does not necessarily prove functional neurotransmitter release. However, for PVBC and O-LM cells the functional consequences of somatic versus dendritic innervation have been studied extensively. Dendritic patch clamp recordings have shown that silencing PV cells has little effect on dendritic potentials evoked by schaffer-collateral stimulation, whereas silencing O-LM cells increases the depolarization from excitatory synaptic inputs (Lovett-Barron et al., 2012). This means that O-LM cells could exhibit control over post synaptic plasticity directly at the dendrite, whereas PVBCs have tighter control over somatic spiking. By controlling somatic spiking, they could indirectly influence plasticity because many plasticity mechanism depend on postsynaptic spiking.

The two cell types also receive inputs from different principal cell populations. O-LM interneurons participate primarily in feedback inhibition because they are mainly driven by local principal cells. PVBCs on the other hand provide feedforward inhibition because they are driven by the upstream principal cells. However, PVBCs also receive feedback drive from their local principal cells. This means that they are driven by a mixture of feedback and feed-forward excitation (Freund & Katona, 2007).

The inputs and outputs of a cell are crucial for the circuit motifs they participate in and thereby for their function. Feedforward inhibition for example has been shown to influence spike timing precision (Pouille & Scanziani, 2001) and normalizes the input-output relation of the network (Ferrante et al., 2009; Olsen et al., 2010). Feedback inhibition implements sparse computations such as Winner-Take-All mechanisms (de Almeida et al., 2009).

Another interneuron feature are molecular markers. While these molecular markers are somewhat correlated with connectivity and function, many of the known interneuron markers are not specific for a single connectivity type. Nevertheless, molecular markers have been crucial for the study of interneurons for a long time.

1.1.2 Molecular markers of interneurons

Molecular markers are an important pillar of interneuron classification (Cauli et al., 1997; Monyer & Markram, 2004). The Petilla nomenclature mentions ten types of molecular markers with the concession that there are probably more (The Petilla Interneuron Nomenclature Group (PING), 2008). Here we will focus on the three molecular markers that are important for hippocampal interneurons: parvalbumin (PV), somatostatin (Sst) and cholecystokinin (CCK; Kawaguchi, 2002).

We already mentioned parvalbumin in the context of connectivity, because the parvalbumin positive basket cell is an important interneuron type that engages in perisomatic connectivity. However, they are not the only type of basket cell found in the hippocampus. Cholecystokinin basket cells (CCKBCs) are another prominent basket cell type. However, several CCK positive interneurons are not basket cells but are dendrite targeting (Pawelzik et al., 2002). An interesting feature of CCKBCs is that they are the only established hippocampal interneuron type that colocalizes solute carrier family 17 (Sodium-Dependent Inorganic Phosphate Cotransporter), Member 8 (Slc17a8), the gene protein coding for the vesicular glutamate transporter 3 (VGluT3). They were recently shown to release glutamate with excitatory postsynaptic effects onto hippocampal principal cells (Pelkey et al., 2020).

Sst is another important interneuron marker. Most O-LM cells are Sst positive and some of them also contain PV (Katona et al., 1999). However, many Sst cells are bistratified interneurons (Buhl et al., 1996; Halasy et al., 1996). Bistratified interneurons express PV like O-LM cells, but additionally express neuropeptide Y (Müller & Remy, 2014). This complexity of molecular marker expression illustrates that molecular markers alone are not sufficient to identify well-defined interneuron sub types. Nevertheless, focusing on interneurons that have a molecular marker in common can reduce the scope of interneuron diversity. In particular, mouse lines that target molecular interneuron markers have been instrumental for the study of interneurons (He et al., 2016). The third feature that helps to distinguish interneuron subtypes is their electrophysiology.

1.1.3 Electrophysiology of interneurons

Electrophysiology describes the electrical features of cells. Probably the most prominent electrical feature of neurons is the action potential, which is also thought to be the main unit of information transfer in the nervous system. Many important electrophysiological features are therefore concerned with the number, timing, and shape of action potentials. Because action potentials are also called spikes, we use both interchangeably.

Interneurons vary widely regarding their electrophysiological features. They can generally sustain much higher firing rates than principal cells but some interneurons spike much faster than others. Therefore, the most prominent distinction between electrophysiological interneuron subtypes is between fast spiking (Espinoza et al., 2018; Hu et al., 2014) and non-fast spiking (Urban-Ciecko & Barth, 2016). While fast firing rate is a salient feature, this dichotomy is likely an oversimplification, given the complexity of neuronal spiking and the many types of action potential discharge behavior. For example, interneurons can also be late-spiking, such that there is a delay between the onset of current injection and spiking. They can also be bursting, with few spikes occurring together at extremely high frequency. Finally, stuttering describes spiking interrupted by periods without firing (Pelkey et al., 2017).

On the one hand these spiking types are cell type markers. For example, basket cells can on average sustain higher maximum frequencies than dendrite targeting cells. However, electrophysiology alone is rarely used in this regard, because of the large variability in spiking behavior within subtypes. On the other hand, spiking types are also important for the function of interneurons. The type of action potential patterns they can sustain determines the role it can play in the network.

To conclude, there are three established pillars of interneuron diversity: connectivity, molecular markers, and electrophysiology. Because the work described in this thesis was done in either the CA3 area or the dentate gyrus of the hippocampus, the next chapter gives a brief description of the connectivity within and between those two areas.

1.2 Dentate gyrus and CA3 connectivity

The dentate gyrus (DG) receives its excitatory input primarily from the entorhinal cortex. The predominant principal cell is the DG granule cell (GC). The DG features another excitatory principal cell called mossy cell (MC; Scharfman, 2016). They are crucial for regulating DG network activity by providing feedback excitation to GCs. They also project to the contralateral dentate gyrus, while GCs remain unilateral. Finally, MCs also excite other hilar interneurons, thereby providing polysynaptic feedback inhibition (Amaral et al., 2007).

Like most cortical areas the microcircuit of the DG features an intricate combination of feedback and feed-forward inhibition. Basket cells are primarily driven by feed-forward inputs while the dendrite targeting interneurons are driven by a combination of feed-forward and feedback. The DG connectivity is complicated by the fact that MCs drive interneurons and many interneuron types inhibit each other.

The primary output of the DG is CA3, where each GC makes contact with 15-20 CA3 pyramidal cells (Amaral et al., 2007). This connectivity is very sparse compared to other brain areas and it is thought to convert sparse firing of granule cells into sparse CA3 ensemble activity. Inhibition works somewhat similar in CA3 as it does in the DG regarding the different drives of basket and dendrite targeting cells. However, the pyramidal cell is the only principal cell type in CA3. The pyramidal cells in CA3 also receive direct excitatory input from the entorhinal cortex. Furthermore, CA3 pyramidal cells recurrently excite other pyramidal cells.

Another interesting feature of CA3-DG connectivity is the CA3 backprojection (Scharfman, 2007). This is an excitatory projection from CA3 pyramidal cells to DG mossy cells and interneurons. This again highlights the prominent role of mossy cells but also the importance of feedback inhibition, as mossy cells primarily drive inhibition.

The dentate gyrus is known to perform a computation called pattern separation, which will be introduced in the next chapter.

1.3 Pattern separation

Pattern separation decreases the similarity of synaptic input patterns at the spiking output of a network (Cayco-Gajic & Silver, 2019; Chavlis & Poirazi, 2017). It occurs in several brain areas such as the hippocampus (Leutgeb et al., 2007; Yassa & Stark, 2011), the cerebellum (Cayco-Gajic et al., 2017) and olfactory bulb (Friedrich & Laurent, 2001). In the hippocampus, pattern separation has memory related functions. It is thought to support encoding of episodic memories by disambiguating them. The inverse of pattern separation is pattern completion, and it is thought to primarily aid memory recall by activating full ensembles from incomplete patterns. The network mechanisms that support pattern separation have been studied extensively in computer models.

The first computational description of pattern separation came from Marr (1969) and it was about motor learning in the cerebellum. Marr suggested that the activity patterns of mossy fibers are being separated by the cerebellar granule cells they innervate. He further introduced the codon representation, a mathematical formalism where a codon represents a set of active mossy fiber inputs which can activate codon cells (granule cells in case of the cerebellum). Pattern separation occurs when codons with many mossy fibers have few codon cells in common. This is easier to achieve when a small absolute number of codon cells is active and thus presents the first description of network sparsity as a pattern separation mechanism. D. Marr (1971) later applied the codon representation to the hippocampus.

One way to achieve sparse network activity is sparse synaptic input connectivity. A competition matrix model has shown that sparse connectivity as it is found between the DG and CA3 supports pattern separation (Rolls, 1989). Inhibition is another mechanisms besides sparse connectivity that also supports pattern separation by keeping principal cell activity sparse (Gibson et al., 1991). Dendrite morphology in the dentate gyrus was also shown to support sparsity (Chavlis et al., 2017). Finally, the addition of a leak conductance can recover pattern separation during pathological hyperexcitability (Yim et al., 2015). In summary, anything that decreases principal cell activity is predicted to support pattern separation.

Pattern separation has not only been studied with computational models but has also been demonstrated behaviorally in animal models. When gradually changing the environment of a rat, the population activity changes to a larger extent in DG than compared to CA3 (Leutgeb et al., 2007). This suggests that the DG amplifies small differences of the environment at the network level. Pattern separation was also shown to be relevant for olfactory behavior. Mice that were trained to distinguish similar odors in a lick/no-lick task were able to perform better when their network outputs were more different. Importantly, optogenetic activation of inhibitory neurons in the olfactory bulb improved network pattern separation as well as behavioral performance (Gschwend et al., 2015).

Several features of the dentate gyrus and its connectivity to CA3 make it particularly well suited for pattern separation in the hippocampus. The next chapter highlights these cellular and network features as well as others that might hinder pattern separation.

1.4 Aim and outline of this thesis

This thesis begins with our work on interneuron diversity in hippocampal CA3. We used patch seq to characterize a novel interneuron subtype that co-expresses Sst and Slc17a8. We found that these cells are not electrophysiologically distinct from Sst or Slc17a8 interneurons but could express tyrosine hydroxylase as a marker. Somatic tyrosine hydroxylase expression has not been described previously in the hippocampus and remains to be validated.

In the second part of this thesis we present published work about the validation about a transgenic mouse line that was used to genetically target Sst positive interneurons. We found that it specifically targets Sst positive interneuron specifically in stratum oriens and stratum radiatum of CA3 but also targets a large number of pyramidal like cells in the pyramidal cell layer. Some transduced cells make contralateral projections which produce strong functional excitation in CA1, as would be expected from CA3 projections.

Finally, we present work on the quantitative properties of feedback inhibition in the DG. We found that very few granule cells are sufficient to recruit the maximal amount of feedback inhibition. Furthermore, feedback inhibition is recruited more strongly onto nearby granule cells and facilitates at 50Hz. We incorporated these circuit features into a computational model of the dentate gyrus and quantified the ability of this model to separate input patterns. We found that the temporal structure of the input patterns in only relevant for pattern separation when the model includes feedback inhibition. We therefore predict that interfering with temporal oscillations in the dentate gyrus would interfere with pattern separation.

2 Materials and Methods

2.1 RNAScope in situ hybridization

The RNAScope experiments were performed by Dr. Erick Martinez Chavez at the Neurodevelopmental Genetics laboratory headed by Prof. Dr. Sandra Blaess.

Animals were deeply anesthetized with ketamine-xylazine (100 mg/kg – 16 mg/kg body weight) and were transcardially perfused with 4% paraformaldehyde (PFA; Sigma-Aldrich). Brains were removed and post-fixed in 4% PFA overnight at 4 °C. Brains were then rinsed in PBS and cryoprotected in ascending sucrose series (10%, 20% and 30% in PBS), and 14-µm thick sections were cut on a cryostat. *In situ* hybridization on frozen sections was performed using RNAScope Fluorescent Multiplex Detection Reagents (323110, ACDBio) according to the manufacturer's instruction for fixed frozen tissue (User Manual: 323100-USM). Probes (Mm-Gad1-O1-C3: 511931-C3; Mm-Gad2-C3: 439371-C3; Mm-Slc17a6: 319171; Mm-Scl17a7: 416631; Mm-Scl17a8: 431261; Mm-Scl17a8-C3: 431261-C3; Mm-Sst-C2: 404631-C2) were designed by ACDBio. Following *in situ* hybridization, sections were rinsed twice in TBST (0.005% Tween20 in TBS, 5 min), and incubated with blocking buffer (1% BSA in TBS) for 30 min. Sections were incubated in primary antibody (rabbit anti-Somatostatin-14 IgG, T-4102, Peninsula Laboratories International; 1:500) in blocking buffer overnight at 4 °C. Sections were rinsed in TBST three times (5 min) and incubated with secondary antibody in blocking buffer (Alexa 488-conjugated donkey anti-rabbit, A-31573, Thermo Fischer Scientific; 1:100) at room temperature for 2 hrs. Sections were counterstained with Hoechst (Sigma-Aldrich), then rinsed twice in TBST (5 min) and twice in TBS. Sections were mounted with Aqua-PolyMount (18606, Polysciences Inc.).

2.2 Imaging and colocalization analysis

Images were taken on a Visitron VisiScope spinning disk microscope (images in **Figure 2** were taken on a confocal microscope. Details below). To image the Hoechst staining, a 405nm laser was used with a 460/50 emission filter at 200ms exposure time. Sst-AB was imaged with a 488nm laser laser and a 525/50 emission filter set. Sst-mRNA (Mm-Sst-C2: 404631-C2 ACDBio probe) was imaged using a 561nm laser with a 609/54 bandpass emission filter. Slc17a8 (Mm-Scl17a8-C3: 431261-C3 ACDBio probe) was imaged using a 640nm laser with a 700/75 bandpass emission filter. For the experiments including Gad RNAScope (**Figure 4**) the RNAScope channel of Slc17a8 was changed to channel 2. Gad 1 and 2 were stained in channel 3. Therefore, Slc17a8 was visualized with the 561nm laser with the 609/54 bandpass

emission filter and Gad1/2 was visualized with the 640nm laser with a 700/75 bandpass emission filter. A 40x water immersion objective was used (C-Apochromat, 1.2 NA, 0.28 WD).

Individual channels were segmented for somata using ilastik. It is freely available open source software which uses a random forest classifier to label pixels as foreground or background (Berg et al., 2019). Since this is a supervised learning algorithm, it requires some amount of labeled training data. Therefore, three images were randomly chosen and three somata in each region (CA1, CA3, Hilus) were manually labeled. Furthermore, some background was labeled in each region.

After segmentation, regions of interest (ROIs) were extracted with the Fiji (Schindelin et al., 2012) particle analyzer. It groups connected pixels into ROIs. ROIs were only recorded if they were 500 to 6000 pixels in size and had a circularity index between 0.3 and 1.0. Next, images were thresholded to calculate the area fraction of each ROI in the other channels. Area fraction is a measure for the number of pixels inside a ROI that were above threshold. Thresholding was performed in Fiji with the "Yen White" method, which finds the optimal threshold by optimizing the difference between the original and the thresholded image as well as the bits required to encode the thresholded image.

Colocalization was determined based on the area fraction. For example, a ROI extracted from the Sst channel might have an area fraction of 0.8 in the thresholded Slc17a8 channel. This means that 80% of pixels in the ROI were above threshold in the Slc17a8 channel. How large would the area fraction need to be, to classify a cell as colocalizing? To determine this colocalization threshold we calculated the area fraction for each ROI in its own channel and calculated the distribution, for example, the area fraction of Sst ROIs in the Sst channel. This yielded the area fraction of ROIs that were highly likely to be Sst positive. To ensure cells were colocalizing, we took the lower 5% percentile of the distribution as the colocalization threshold. For the experiment in **Figure 3** the following thresholds were calculated: Sst-AB, 0.44; Sst-mRNA, 0.44; Slc17a8, 0.06. To further illustrate this threshold: a ROI from a SST antibody soma with an area covered larger than 0.06 in the Slc17a8 channel would be classified as Slc17a8 colocalizing. The thresholds of the experiment in **Figure 4** were: Sst-AB, 0.47; Gad1/2, 0.25; Slc17a8, 0.26.

Images in **Figure 2** were taken with a SP8 confocal microscope (Leica). Overview images were taken with a 25x water immersion objective (HC PL; FLUOTAR; 0.95 NA, 2.5 WD (mm) #(11)506374). Scan speed was 600Hz. Inset images were taken with a 40x water immersion objective (HC PL, APO; 1.1 NA Corr, 0.65 WD (mm) #(15)506357).

2.3 Stereotaxic injections of viral particles

All animal experiments were carried out according to the guidelines stated in Directive 2010/63/EU of the European Parliament on the protection of animals used for scientific purposes and were approved by authorities in Nordrhein-Westfalen (Landesamt für Natur, Umwelt und Verbraucherschutz Nordrhein Westfalen (LANUV), 81-02.04.2019.A192). To genetically label Sst or Slc17a8 positive cells we used viral gene transfer in SST-Cre (CA3 characterized in Müller-Komorowska et al., 2020; Originally described by Savanthrapadian et al., 2014) or Tg(Slc17a8-icre)1Edw/SealJ mouse lines (Jackson Laboratory; Grimes et al., 2011). 12 SST-Cre and 13 Tg(Slc17a8-icre)1Edw/SealJ mice were injected. They were anesthetized with a Fentanyl/Midazolam/Medetomidin mixture (0.05/5.0/0.5 mg/kg body weight, volume 10ml/g body weight) intraperitoneally (Microlance 3^{TM} injection needles from BD Medical). 20 minutes ahead of first surgical cut, they also received Ketoprofen (5 mg/kg body weight, volume 10ml/g body weight) as an analgesic subcutaneously. To prevent the eyes from drying out, eye-nose cream (Bepanthen; Bayer) was applied to the eyes. Hair on the head was removed and Xylocain was applied to the skin on the head. Animals were woken up with a Naloxon/Flumazenil/Atipamezole mixture. During sugery, mice were placed on a heating blanket controlled with a temperature controller TC01 (multichannel systems) set to 37˚C. Injections were placed at the following stereotaxic coordinates: 2.3 mm posterior; 1.7 mm lateral; 2.4 mm ventral. All injections were made into the right hemisphere. A 1mm diameter burr hole was drilled above the coordinates using a K.1070 high speed rotary micromotor (Foredom). The injected recombinant adeno-associated virus led to gene transfer of a sequence expressing enhanced yellow fluorescent protein with a nuclear localization sequence (NLS-EYFP, rAAV1/2-Ef1a-DIO-NLS-EYFP) in a Cre-Recombinase dependent manner. It was created and produced in the laboratory of Prof. Susanne Schoch. To achieve Cre-dependence, a LoxP site based genetic switch (DIO: Double-Floxed Inverted Open reading frame) was used (Schnütgen et al., 2003). Injection volume was 500nl at a speed of 100 nl/minute. After the five minutes of injection, the syringe was left in place for 2.5 minutes. It was then moved dorsally by less than a millimeter and left there for another 2.5 minutes to let the tissue relax. A NanoFil sub-microliter injection syringe (World Precision Instruments) was used with a UltraMicroPump3 with SMARTouch controller. After surgery, the skin above the skull was closed with coated Vicryl plus antibacterial (polyglactin 910) sutures (Ethicon). To prevent bacterial infection, Refobacin Crème (1 mg/g Gentamicin; Almirall) was applied to the head. Mice were used for electrophysiology 3 to 10 days after viral injections.

2.4 In vitro electrophysiology with patch seq sample acquisition

To anesthetize mice, they were transferred to a bell-shaped glass vessel, where 2-4 drops of Isoflurane (Abbott Laboratories) were previously placed to evaporate. When animals were deeply anesthetized after approximately 30 seconds, they were rapidly decapitated. Their brain was removed from the skull by a series of incisions. One incision went through the skin from the neck to the nose. Then, sharp forceps were placed in the eye cavities for stability. To remove the skull, another incision was made through the skull on the left side of the brain from the spine to the eye, followed by an incision from the left to the right eye. The skull was then lifted, the brain was removed with a spatula and was placed in ice-cold, carbogenated artificial cerebrospinal fluid (ACSF) with sucrose (in mM: NaCl, 60; sucrose, 100; KCL, 2.5; NaH_2PO_4, 1.25; $NaHCO_3$, 26; $CaCl_2$, 1; $MgCl_2$, 5; glucose, 20; all from Sigma-Aldrich). 300 µm slices were cut on a vibratome (Leica VT 1200S) and stored in the same ACSF with sucrose at 37 ˚C for 30 min. Afterwards, they were transferred to ACSF without sucrose (in mM: NaCl, 125; KCL, 3.5; NaH2PO4, 1.25, NaHCO3, 26; CaCl2, 2; MgCl2, 2; glucose, 20; from Sigma-Aldrich) for at least 1 hour at room temperature before experiments began.

The intracellular solution in the patch pipettes consisted of (in mM) K-gluconate, 123; KCL 12; 4-(2-hydroxyethyl)-1-piperazineethanesulfonic acid (HEPES) 10; ethylene glycol-bis(β-aminoethyl ether)-N,N,N′,N′-tetraacetic acid (EGTA) 0.2; Mg-ATP 4; Na-GTP 0.3; Na_2-phosphocreatine 10 and finally glycogen 20 µg/ml. The solution was entirely prepared under an RNAse free laminar flow cabinet. The pH was adjusted to 7.25 with KOH and the pH meter was cleaned with ElectroZap (AM9785; Ambion/ThermoFisher Scientific). The water used for the intracellular solution was nuclease-free water (AM9930; Ambion/ThermoFisher Scientific). Spoons and other equipment that came in contact with any of the compounds were backed at 220˚C for at least 2 hours. The intracellular solution was stored in aliquots at -20 ˚C and was thawed on days of experiments. After thawing, 2.3 µl of murine RNAse inhibitor (M0314S; BioLabs) was added. Glass pipettes were filled with 300 µl of intracellular solution. Access resistance in bath with positive pressure applied was between 4 MOhm and 9 MOhm.

To ensure mRNA stability during patch seq experiments, all equipment that would come into contact with the intracellular solution had to undergo special treatment to eliminate RNAses. Thin pipette tips (Microloader; Eppendorf) used to backfill glass electrodes were autoclaved. The borosilicate glass with filament (Science Products) used to pull patch clamp glass electrodes was backed at 220˚C. The silver chloride wire used to record electrical signals was cleaned each day before experiments with ElectroZap (AM9785; Ambion/ThermoFisher Scientific) and rinsed with nuclease-free water (AM9930; Ambion/ThermoFisher Scientific).

The syringe and its tip that were used to eject the intracellular solution after recording and cytosol extraction were cleaned with RNaseZAP (Sigma-Aldrich Merck) and rinsed with 70% ethanol. Other patch clamp equipment that did not come in direct contact with intracellular solution was cleaned weekly with RNaseZAP and 70% ethanol.

Patch clamp experiments were performed with an Axopatch 200B and digitized on a Digidata 1322A or Digidata 1550B plus HumSilencer (Molecular Devices). All signals were lowpass filtered at 10kHz.

We first recorded a protocol of depolarizing 1 s long current steps starting at 0 pA up in steps of 20 pA. The protocol was stopped when the number of elicited spikes visibly decreased or at a maximum of 600 pA. Afterwards we used 1 s long hyperpolarizing current steps starting from 0 pA in steps of minus 20 pA. This protocol was stopped after the recording where the voltage reached minus 100 mV or after minus 400 pA injected current.

After the recording protocols, suction was applied to the pipette for up to 10 minutes to collect the cell contents. The glass pipette tip was then broken into the lysis buffer (details in 2.6) and the pipette contents were ejected by applying positive pressure with a syringe. The lysis buffer was shock frozen in liquid nitrogen and stored at -80˚C before cDNA synthesis.

2.5 Analysis of electrophysiological properties

We quantified three passive properties, seven active properties and six single spike properties. The single spike properties were quantified for three different spikes: the first spike at rheobase, the first spike during the action potential series with the highest frequency and the last spike of that same action potential series. The rheobase is the minimum amplitude of step current injection required to elicit at least one action potential. Because we were injecting current in increasing steps of 20 pA, the estimation of the rheobase is limited to that resolution. The maximum frequency action potential series is the one that contains the maximum number of spikes during the step current injection (see **Figure 4A** for representative examples of action potential series at rheobase and maximum frequency). In total 28 electrophysiological features were extracted.

The three passive properties were:

- **Input resistance (MOhm)** - During small hyperpolarizing current steps, the voltage response increases linear with the input resistance. To make measurement more precise, the input resistance was calculated from at least three hyperpolarizing current steps. A line was fit through the current-voltage relationship. The slope of that line is the input resistance.

- **Membrane capacitance (pF)** – The voltage response to a step current injection rises faster when the membrane capacitance is smaller. Because the early voltage response is described by an exponential function, we fit an exponential decay function to these data. The membrane capacitance is then given by the time constant of the exponential function divided by the input resistance.
- **Resting membrane potential (mV) –** The resting membrane potential is the voltage while no current is injected, and it was read from the amplifier shortly after opening the cell for patch clamp recordings. The liquid junction potential of 16mV was subtracted from the amplifier reading.

Detecting action potentials is a critical step to calculating most active neuronal properties. Action potentials were detected by finding points in the recording where the voltage became larger than 0mV. The seven active properties were:

- **Maximum average frequency (Hz) –** Largest number of action potentials during any of the one-second-long depolarizing current steps.
- **Current at maximum frequency (pA) –** The amplitude of the current step necessary to elicit the maximum frequency.
- **Slow afterhyperpolarization (AHP; mV) –** Most negative voltage after the current step that elicited the maximum frequency minus the voltage before the current injection.
- **Rheobase (pA) –** The smallest amplitude of the current step necessary to evoke at least one action potential.
- **Adaptation ratio –** The ratio between the time interval of the last two spikes divided by the time interval of the first two action potentials during the maximum frequency response.
- **Average spike time (s) –** The mean spike time of all action potential during the maximum frequency response.

To analyze the properties of single action potentials, their waveform must be extracted from the signal. To achieve this, we took the point where the signal crosses the 0mV threshold and extracted the signal 2ms to the left and 2.5ms to the right of the threshold point. This was done for the first action potential during the rheobase and the last action potential during the maximum frequency response. The six single spike properties were:

- **Action potential threshold (mV) –** This is the voltage that is depolarized enough to enter a positive feedback loop that causes the action potential. We quantify the threshold by

finding the voltage at the first point during the action potential waveform where the voltage increases by more than 10 mV/ms. The liquid junction potential of 16 mV is subtracted.

- **Fast afterhyperpolarization amplitude (mV) –** The minimum voltage during the action potential waveform minus the action potential threshold.
- **Maximum slope (mV/ms) –** The largest voltage change during the waveform. Calculated by taking the maximum of the first order derivative of the voltage with respect to time.
- **Minimum slope (mV/ms) –** The most negative voltage change during the waveform. Calculated by taking the minimum of the first order derivative of the voltage with respect to time.
- **Peak (mV) –** The maximum voltage reached during the action potential waveform. The liquid junction potential of 16 mV is subtracted.
- **Half width (ms) –** The half width is commonly used to express how wide an action potential is. It is calculated by first finding the voltage that is half-way between the threshold and the peak of the action potential, called the half-height. Then two time points need to be identified. The first time point is when the voltage crosses the half-high during the rising phase (before the peak) of the action potential and the second time point is when the voltage crosses the half-height during the decaying phase (after the peak). The half width is the time between these two time points.

Raw recording files were loaded into Python with neo (Garcia et al., 2014). Analysis was performed with NumPy (van der Walt et al., 2011). Fitting of the exponential decay function for capacitance analysis and fitting of the linear function for membrane resistance measurement were both done with SciPy (Virtanen et al., 2020)

2.6 Single cell sequencing

Single cell sequencing was performed at the PRECISE core facility at the German Center for Neurodegenerative Diseases in Bonn, Germany. Cytosol and nucleus of patched cells was collected in lysis buffer (40mM Guanidine Hydrochloride, dNTPs 5mM each, 2uM SMART polyT RT primer) and processed to NGS sequencing libraries according to the SMART-Seq2 protocol (Picelli et al. 2014).

In short, mRNA was reverse transcribed using Superscript II (Invitrogen) and a template switch oligo (TSO) to produce full-length cDNA copies of the mRNA containing PCR handles on both ends prior to PCR amplification. Amplified and cleaned cDNA was quantified via High Sensitivity DNA5000 assay on a Tapestation 4200 System (Agilent), 200pg each were

tagmented using a Nextera XT kit (Illumina) and amplified and indexed in a subsequent PCR reaction to create the final NGS library. Library fragment size distribution was analyzed via High Sensitivity DNA5000 assay on a Tapestation 4200 System (Agilent) and quantified using the Qubit HS dsDNA assay (Thermofisher). Cell libraries were equimolarly pooled, clustered at 1.4pM concentration using High Output v2.1 chemistry and sequenced SR 75 cycles and 8 cycles each for i7 and i5 indexes on a NextSeq500 system (Illumina). Single-cell data was demultiplexed using bcl2fastq2 v2.20 and STAR aligned using the mouse GENCODE reference genome and transcriptome mm10.

2.7 Transcriptomics analysis

To convert ensemble identifiers to human readable gene names we used MyGene.py (Xin et al., 2016). Read count tables were analyzed using scanpy (Wolf et al., 2018). The first step was quality control to exclude low quality cells (**Figure 1**). This is necessary to avoid technical artifacts during further analysis. Low sample quality can occur when not enough mRNA has been collected from a cell or the mRNA has degraded during processing.

First, we examined the total read counts of each cell summed (**Figure 1A**). It is likely that cells with extremely low total counts had a low amount of mRNA collected from them, giving an incomplete measurement of mRNA expression. We thus excluded cells with log10 transformed total read counts below the median minus 3 times the median absolute deviation. The median absolute deviation is calculated from each samples deviation from the mean and taking the median of that distribution. This kind of measure that takes the sample deviation into account is useful when there are no previously established quality criteria (Lun et al., 2016). This is the case for patch seq from interneurons in CA3, which has not been performed thus far. 11 of 136 cells were excluded based on the total reads counts.

The second quality measure for cells was the total number of genes with read counts larger than one (**Figure 1B**). Cells that express very few genes likely suffer from similar quality issues as those with low total counts. We excluded cells based on the same criterion of median minus 3 times the median absolute deviation. 9 of 136 cells were excluded based on the number of expressed genes.

The third and fourth quality measures were the percentage of reads aligned to exons or introns, respectively (**Figure 1D,E**). These statistics are calculated during alignment. Of all sequence reads from a cell, some are aligned to intronic or exonic parts of a gene and other reads do not align to any part. Low alignment rates indicate sample contamination with non-murine RNA. We applied the same criterion of median minus 3 times the median absolute

deviation to both alignment rates. 4 of 136 cells were excluded because of exon alignment and 0 of 136 were excluded because of intron alignment.

The final quality control step of samples was performed based on mitochondrial genes. Large percentages of mitochondrial reads indicate an apoptotic cell state which will result in non-physiological expression profiles (**Figure 1C**; Ilicic et al., 2016). We excluded cells if more than 10% of their reads were from mitochondrial genes (Lun et al., 2016). 4 of 136 cells were excluded because of mitochondrial gene expression. Based on all quality criteria, 17 out of 136 cells were excluded from further analysis.

The next quality control step was performed to exclude genes containing little information about cells. Besides technical reasons like those at the sample level, some of these genes have low information content for biologically reasons. For example, a gene can be completely absent from neurons or it can be expressed at similar levels in all cells. Of 53465 genes, 17024 had zero read counts across all samples and were removed. Next, we removed genes with low average counts. Those genes are prone to noise. Genes were excluded if their log10 transformed read counts were smaller than 0 (**Figure 1F**). 14246 of 36441 genes were excluded based on low read counts.

2.8 Statistics and software

Dimensionality reduction of electrophysiological parameters was done with scikit-learn (Pedregosa et al., 2011) on the top principal components that explain 99% of variance. Plotting was done with Matplotlib (Hunter, 2007) and Seaborn. The generalized linear model (GLM) was used from statsmodels (Seabold & Perktold, 2010). Hierarchical linkage clustering was used from SciPy (Virtanen et al., 2020). Pandas was used for saving and loading data frames (McKinney, 2010). The Wilcoxon rank sum tests were done in R (R Core Team, 2020).

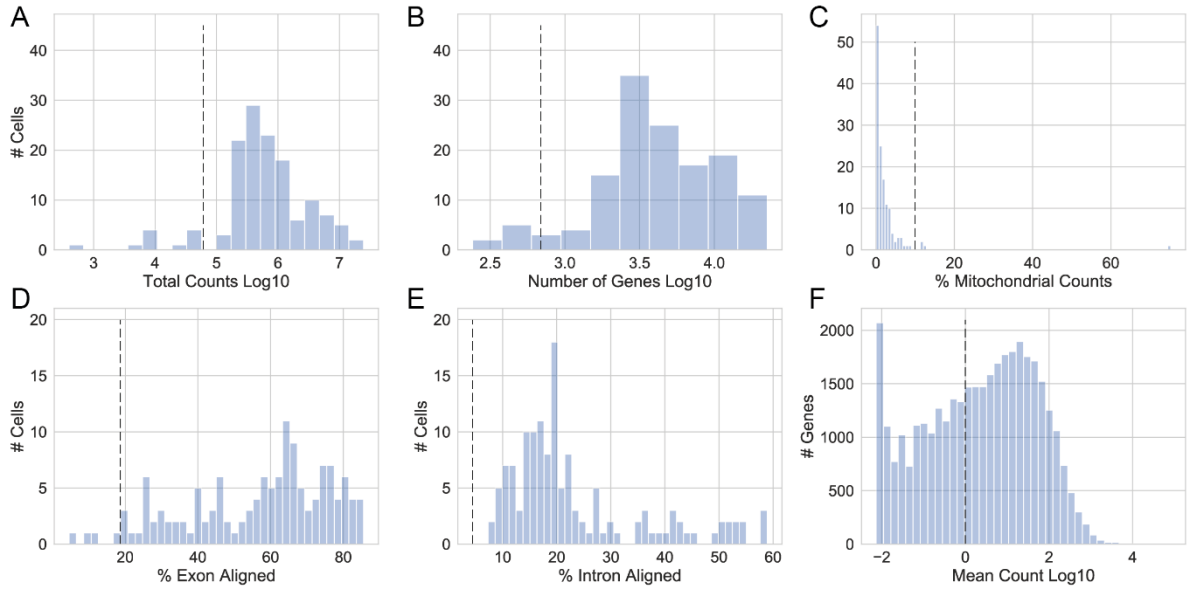

Figure 1: Quality control of single cell sequencing samples. Samples below the threshold (dashed line) were excluded from further analysis. The threshold is the median minus three times the median absolute deviation. Except for C, where the threshold is 10% and cells above the threshold are excluded. In F the threshold is 0 and genes below are excluded. A) Log10 transformed total counts per cell. B) Log10 transformed number of genes per cell. C) Percentage of read counts from mitochondrial genes. D) Percentage of counts aligned to exonic parts of a gene. E) Percentage of counts aligned to intronic parts of a gene. F) Log10 transformed mean counts per gene. Only includes genes that have more than zero counts.

3 Results

3.1 RNAScope reveals Sst/Slc17a8 colocalizing interneurons

We performed RNAScope to identify cells that colocalize somatostatin (Sst) mRNA and mRNA from either solute carrier family 17 (sodium-dependent inorganic phosphate cotransporter) member 6 (Slc17a6), solute carrier family 17 (sodium-dependent inorganic phosphate cotransporter), member 7 (Slc17a7) or solute carrier family 17 (sodium-dependent inorganic phosphate cotransporter), member 8 (Slc17a8). We found that Slc17a7 was strongly expressed in all principal cell layers of the hippocampus (**Figure 2A**). We found this qualitative pattern in 12 coronal sections from dorsal hippocampi of 4 wild type mice (3 sections per animal). This is expected, as Slc17a7 is protein-coding for the vesicular glutamate transporter 1 (VGluT1), the main glutamate transporter of cortical principal cells. Slc17a6 expression on the other hand was found to be extremely low in all areas and layers of the dorsal hippocampus (**Figure 2B**). We observed nearly no Slc17a6 in 6 coronal slices from dorsal hippocampi of 2 wild type mice (3 slices per animal). Slc17a8 showed a sparse expression pattern mostly outside of the principal layer (**Figure 2C**).

We moved on to investigate whether Slc17a7 or Slc17a8 positive somata colocalize Sst. We did not investigate Slc17a6 further due to the low expression level. We also included an immunostaining for the peptide product of Sst. We denote the antibody labeling for that peptide product as Sst-Ab and the RNAScope labeling as Sst-mRNA. We found no evidence that Slc17a7 positive cells colocalize Sst-Ab or Sst-mRNA even when they are immediately adjacent to the pyramidal cell layer (**Figure 3A**). We manually scanned 12 coronal sections from the dorsal hippocampus of 4 wild type mice (3 slices per animal). Slc17a8 positive cells on the other hand were found to colocalize both Sst-Ab and Sst-mRNA (**Figure 3B)**.

To quantify somatic colocalization, we used an analysis pipeline (Methods 2.2) on 9 sections from three wild type animals. We detected a total of 630 Slc17a8 positive cells and of those 101 (16.0%) colocalized Sst-mRNA and 20 were Sst-Ab positive (3.2%). The lower percentage for Sst-Ab colocalization is most likely due to a lower signal to noise ratio of immunolabeling compared to RNAScope. We furthermore quantified colocalization by hippocampal area, finding that Sst-Ab-mRNA/Slc17a8 colocalization is more frequent in CA3 compared to CA1 and DG (**Figure 3C**). Out of 350 Slc17a8 positive cells detected in CA3, 79 (22.6%) colocalized Sst-mRNA. In CA1 on the other hand, out of 215 detected cells, only 19 (8.8%) were Sst-mRNA positive. The difference between CA3 and CA1 was even more pronounced for Sst-mRNA positive cells colocalizing Slc17a8. Of 320 Sst-mRNA positive cells

93 (29.1%) colocalized Slc17a8 in CA3. This contrasts with CA1, where out of 591 Sst-mRNA positive cells only 22 (3.8%) colocalized Slc17a8 (**Figure 3C**).

Having identified this novel subtype containing Sst-mRNA, Sst-Ab and Slc17a8, we decided to ascertain, whether these cells are also gamma-aminobutyric acid (GABA) positive. This would be expected, because Sst is an interneuron marker and most hippocampal interneurons are GABAergic. Glutamic acid decarboxylase 1 (Gad1) and glutamic acid decarboxylase 2 (Gad2) are both markers for GABAergic cells, since they are protein coding for enzymes that catalyze L-glutamic acid to GABA. We combined Gad1 and Gad2 RNAScope probes into a single channel to detect GABAergic interneurons. Consistent with Sst being a marker for GABAergic interneurons we found that the vast majority of Sst-Ab or Slc17a8 positive cells also colocalize Gad1-Gad2 in CA1, CA3 and DG (**Figure 4A,B,C**). For the following quantification (**Figure 4C**), 7 sections from 3 wild type mice were used. From a total of 470 Sst-Ab positive cells, 397 (84.5%) colocalized Gad1-Gad2. From 432 Slc17a8 positive cells, 363 (83.8%) colocalized Gad1-Gad2. This still leaves a small population of both Gad1-Gad2 negative cells in both populations. To test whether the Sst/Slc17a8 colocalizing cells specifically are Gad1-Gad2 positive, we analyzed especially those colocalizing cells. In total we detected 44 Sst-Ab/Slc17a8 colocalizing cells (this includes both Sst positive cells colocalizing Slc17a8 and Slc17a8 positive cells colocalizing Sst-Ab). Of those 44 cells, 43 (97.7%) colocalized Gad1-Gad2. These data suggest that the novel Sst/Slc17a8 colocalizing population is almost entirely GABAergic.

We moved on to characterize the electrophysiological and transcriptomic properties of this novel interneuron subtype.

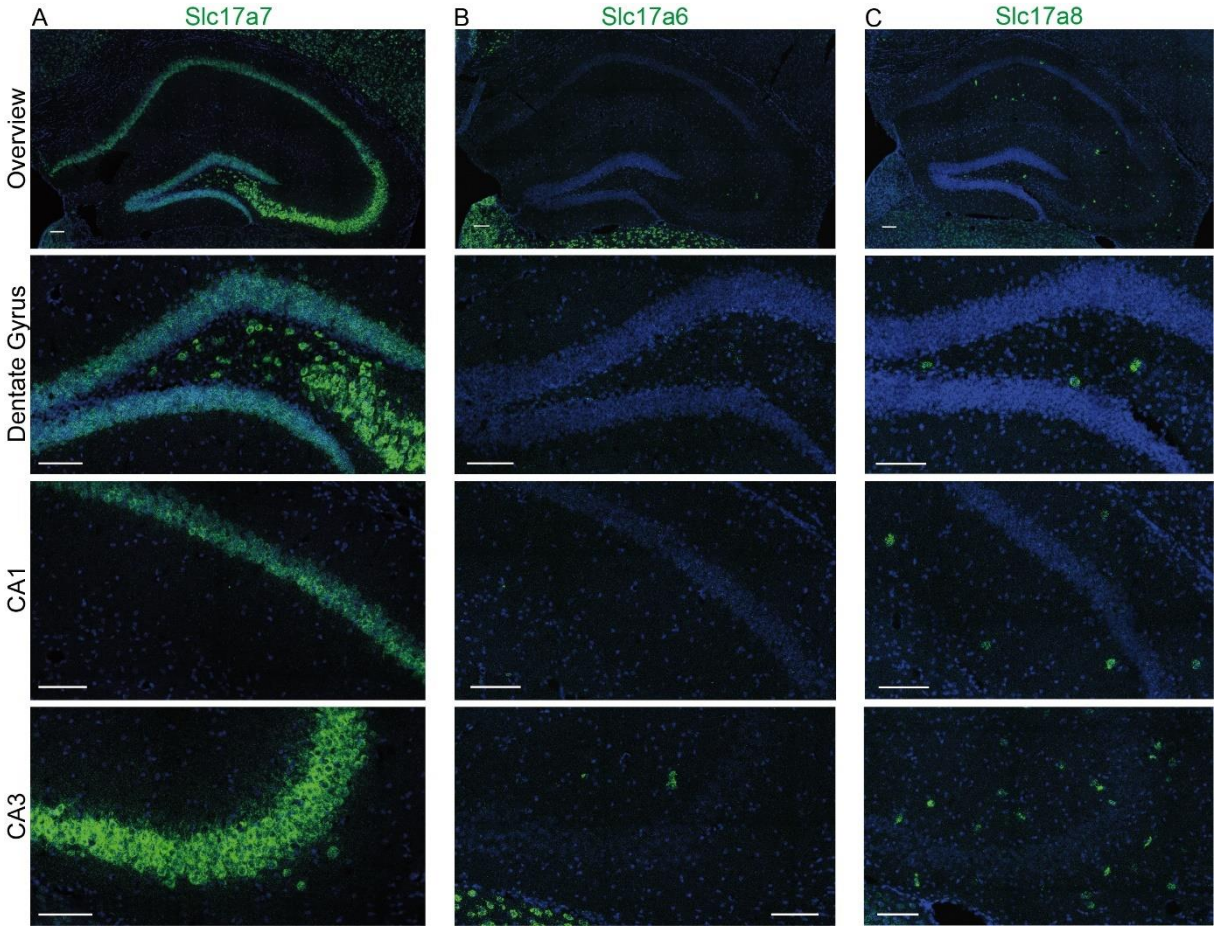

Figure 2: Distribution of RNAScope labeling from Slc17a7, Slc17a6 and Slc17a8. A) Overview of Slc17a7 distribution. Slc17a7 was strongly expressed in all hippocampal principal cell layers. B). Overview of Slc17a6 distribution. Slc17a6 was not detected in the hippocampus. C) Overview of Slc17a8 distribution. Slc17a8 was sparsely expressed, mostly outside the principal cell layers. All scalebars are 100 µm. The blue channel shows a Hoechst staining that is used to visualize DNA for anatomical orientation. CA1, cornu ammonis 1; CA3, cornu ammonis 3; Slc17a7, solute carrier family 17 member 7; Slc17a6, solute carrier family 17 member 6; Slc17a8, solute carrier family 17 member 8.

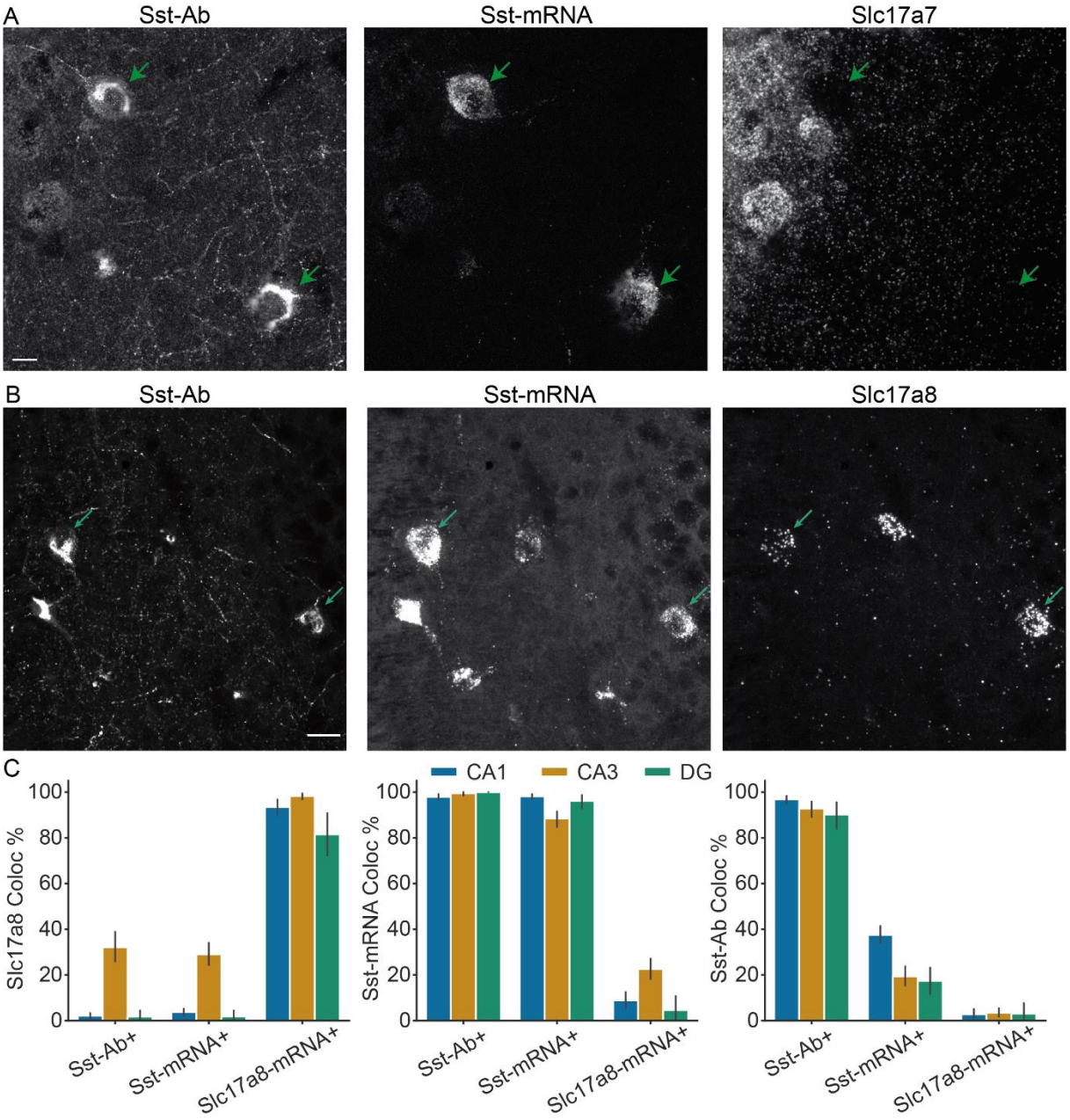

Figure 3: Sst-mRNA+ and Sst-Ab+ cells in CA3 colocalize Slc17a8. A) Sst-mRNA/Sst-Ab+ cells do not colocalize Slc17a7, even when they are adjacent to the pyramidal cell layer. Green arrows mark two Sst-mRNA/Sst-Ab+ cells. Example image from CA3. Scalebar 10 µm. B) Sst-mRNA/Sst-Ab+ cells colocalize Slc17a8 in CA3. Geen arrows mark two Sst-mRNA/Sst-Ab+ cells that are also Slc17a8+. Scalebar 10 µm. C) Quantification of colocalization. In total 2479 cells were segmented from 9 slices of 3 animals. 783 were Sst-Ab+, 1066 were Sst-mRNA+, 630 were Slc17a8+. Out of the Sst-Ab+ cells, 478 were in CA1, 193 in CA3, 112 in DG. Out of the Sst-mRNA+ cells, 591 were in CA1, 320 in CA3, 155 in DG. Out of the Slc17a8+ cells, 215 were in CA1, 350 in CA3, 65 in DG. Around 30% of both Sst-Ab+ and Sst-mRNA+ cells in CA3 colocalize Slc17a8. Very few cells colocalize VGlut3 in CA1 or DG. Percentage of cells that colocalize Sst-mRNA. Around 20% of VGlut3 positive cells colocalize Sst-mRNA+ in CA3. Very few cells colocalize Sst-mRNA in CA1 and DG. Virtually all cells that are Sst-mRNA+ colocalize Sst-AB as expected. A minority of Sst-mRNA+ cells colocalizes Sst-Ab. Sst, somatostatin; Slc17a7, solute carrier family 17 member 7; Slc17a8, solute carrier family 17 member 8, DG, dentate gyrus; CA1, cornu ammonis 1; CA3, cornum ammonis 3.

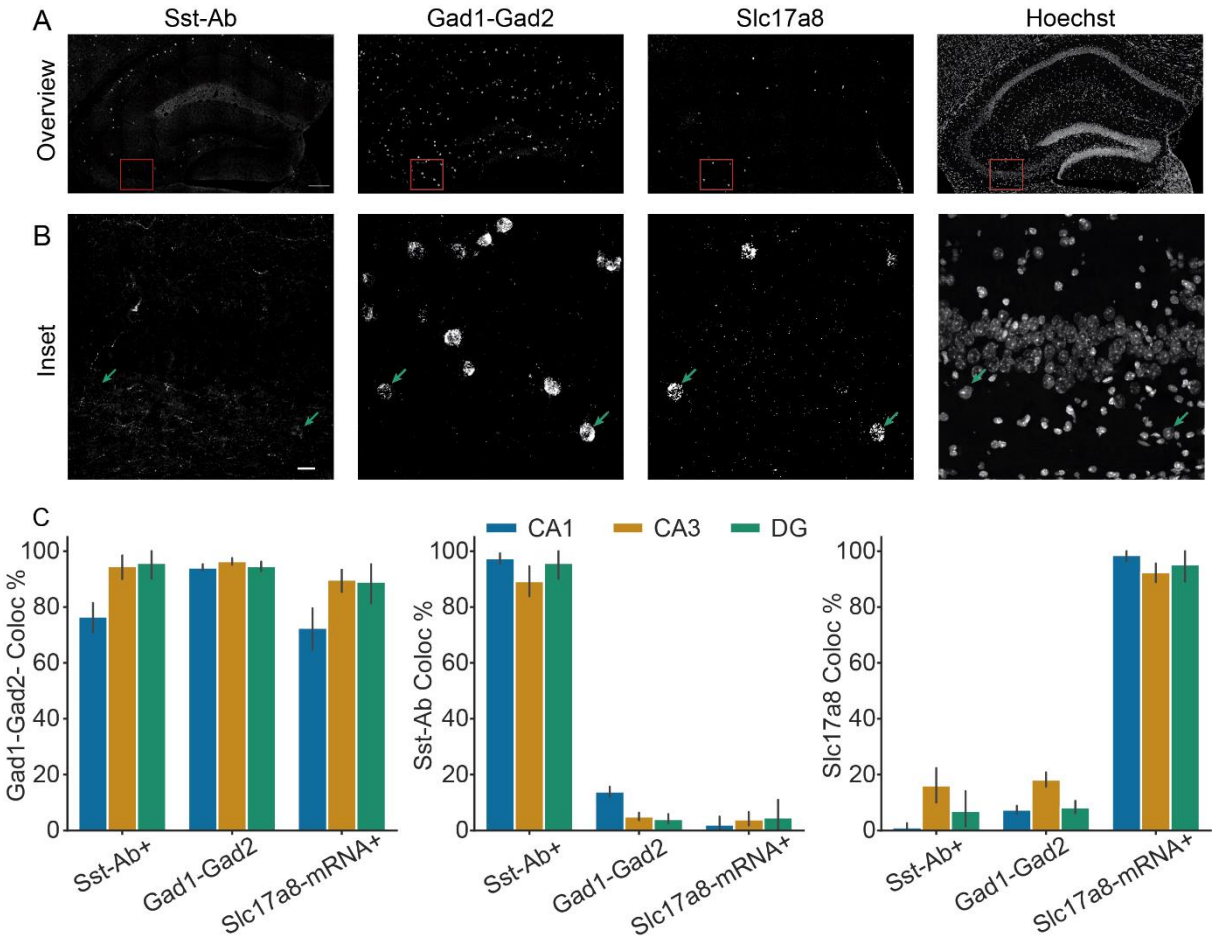

Figure 4: The majority of Sst and Slc17a8 positive cells colocalize Gad1-Gad2. A) Overviews of Sst-Ab, Gad1-Gad2, Slc17a8 and Hoechst in the same section. Scalebar 100 µm. B). Inset into red square from A in CA3. Green arrows mark two Slc17a8 positive cells, both of which colocalize Gad1-Gad2. One of them (right) also colocalizes Sst-Ab. Scalebar: 10 µm. C) The vast majority of Sst-Ab+ and Slc17a8+ cells colocalizes Gad1-Gad2 in all major areas. Quantification on 7 sections from 3 wild type mice. From a total of 470 Sst-Ab+ cells, 397 (84.5%) colocalized Gad1-Gad2. From 432 Slc17a8+ cells, 363 (83.8%) colocalized Gad1-Gad2. Sst, somatostatin; Gad1 & 2, glutamate decarboxylase 1 & 2; Slc17a8, solute carrier family 17 member 8; DG, dentate gyrus; CA1, cornu ammonis 1; CA3, cornu ammonis 3.

3.2 Electrophysiology alone does not identify interneuron cell types

To characterize Sst+/Slc17a8+, we performed patch seq (Cadwell, Scala, et al., 2017) to acquire electrophysiological recordings and transcriptomic profiles from the same single cells. We recorded cells only in CA3 because our RNAScope data showed that Sst+/Slc17a8+ colocalizing cells were more frequent there. Moreover, we recorded most cells in SO, since Sst-Ab positive cells are predominantly located there. To increase the number of recorded Sst and Slc17a8 positive cells we used the SST-Cre and Tg(Slc17a8-icre)1Edw/SealJ mouse lines which target Cre-recombinase to Sst and Slc17a8 positive cells respectively. Viral transduction with a Cre-dependent viral construct (Methods 2.3) led to yellow fluorescence in some cells and fluorescent cells were recorded whenever possible. In the absence of fluorescent cells other neurons in CA3 were also recorded.

In total, 155 cells were recorded in CA3. These cells were recorded from 45 animals of which 12 were wild type, 19 were SST-Cre and 14 were Tg(Slc17a8-icre)1Edw/SealJ. Some of the cells recorded in the transgenic mouse lines were fluorescently labeled. **Table 1** gives an overview of all cells, which mouse line and which layer of CA3 they were recorded in. Numbers of cells that were not fluorescently labeled are in parentheses. We also recorded cells in the pyramidal cell layer to have a cluster of cells that is expected to be exlectrophysiologically distinct from interneurons.

Table 1: Numbers of recorded cells by mouse line and CA3 layer. First number are the cells that were fluorescently labeled and in parentheses are the recorded cells that were unlabeled. WT, wild type; SO, stratum oriens, PCL, pyramidal cell layer; SR, stratum radiatum.

	SST-Cre	Tg(Slc17a8-icre)1Edw/SealJ	WT
SO	23 (27)	12 (6)	0 (40)
PCL	0 (7)	0 (0)	0 (10)
SR	0 (0)	15 (15)	0 (0)

We first asked whether transgenic interneuron subtypes can be identified by their electrophysiological properties. To this end, we calculated 22 electrophysiological features for each cell based on hyper- and depolarizing current steps (representative examples in **Figure 5A,B,C**). The passive features were input resistance, membrane capacitance, sag amplitude and resting potential. The active features were maximum frequency, current at maximum frequency, slow afterhyperpolarization, rheobase, adaptation ratio and average spike time. The single spike properties were the fast afterhyperpolarization amplitude, maximum slope, minimum slope, peak, half-width, and threshold. Those single spike properties were quantified for the first action

potential at rheobase and the last action potential at maximum frequency. All properties are detailed in the methods **chapter 2.5**.

For each feature we performed a Wilcoxon rank sum test to determine whether Sst-EYFP and Slc17a8-EYFP positive cells were significantly different. After correction for multiple comparisons with the Benjamini-Hochberg method, only the sag amplitude was found to be significantly larger in Sst-EYFP cells. This is also seen in the hyperpolarizing example trace in **Figure 5A,B.** Descriptive statistics and statistical test for all features are in **Table 2**. We went on to use a non-linear clustering technique that could discover differences in high-dimensional feature space although individual features are not significantly different.

We used the non-linear dimensionality reduction technique TSNE (van der Maaten & Hinton, 2008) on the principal components that explain 99% of the sample variance of the 22 parameters. This reliably identified two clusters (**Figure 5D**). One of those clusters consisted of 27 cells, 19 of which were recorded in the PCL. We concluded that this cluster contains putative principal cells and performed TSNE again with that cluster excluded. This did not result in well-defined clusters (**Figure 5E**). While the sag amplitude was significantly different, the distributions are not sufficiently separated to reliably distinguish cells (**Figure 5F**). This confirms electrophysiology alone does not identify these transgenic cell types. We therefore went on to analyze the single cell transcriptomic profiles.

Table 2: Descriptive statistics and results of the Wilcoxon rank sum test to compare Sst-EYFP and Slc17a8-EYFP positive cells. Only Sag Amplitude (mV) was significant after Benjamini-Hochberg correction for multiple comparisons at 0.05 false detection rate. Mad, median absolute deviation; W, test statistic of the Wilcoxon rank sum test; p, p-value of the Wilcoxon rank sum test; Sig., asterisk indicated significance after Benjamini-Hochberg correction for multiple comparison.

	Sst-EYFP		Slc17a8-EYFP		Wilcoxon rank sum test		
Feature	**Median**	**Mad**	**Median**	**Mad**	**W**	**p**	**Sig.**
Adaptation Ratio	1.36	0.4	1.42	1	269	0.5804	
Avg Spike Time (s)	0.48	0.01	0.46	0.06	349	0.3006	
Capacitance (pF)	82.36	30.98	72.56	21.01	355	0.2478	
I at Max. Freq. (pA)	390	163.09	360	148.26	344	0.349	
Input R (MOhm)	219.69	95.07	174.82	50.73	382	0.08941	
LS AHP Amp. (mV)	-10.07	3.85	-8.85	6.33	231	0.1879	
LS Half Width (ms)	0.84	0.34	0.64	0.36	392	0.05746	
LS Max. Slope (mV/ms)	1140.59	653.23	1602.17	950.15	191.5	0.0348	
LS Min. Slope (mV/ms)	-587.46	237.54	-747.68	610.81	380	0.09725	
LS Peak (mV)	7.65	12.44	7.8	13.57	276.5	0.6876	
LS Threshold (mV)	-42.86	6.56	-50.48	7.69	421	0.01301	
Max. Freq. (Hz)	67	24.46	73	37.06	262.5	0.4942	
Resting (mV)	-64	4.45	-65	5.93	345	0.3382	
Rheobase (pA)	60	29.65	80	29.65	213	0.08845	
RS AHP Amp. (mV)	-19.53	5.66	-13.12	9.05	166	0.008705	
RS Half Width (ms)	0.57	0.12	0.42	0.15	459.5	0.001126	
RS Max. Slope (mV/ms)	2510.07	475.08	2983.09	373.27	201	0.05491	
RS Min. Slope (mV/ms)	-1377.11	316.72	-1670.84	678.68	417.5	0.01586	
RS Peak (mV)	18.33	7.69	22.76	9.05	317.5	0.6876	
RS Threshold (mV)	-56.44	4.52	-55.67	3.17	290	0.896	
Sag Amplitude (mV)	-13.41	4.53	-8.22	2.81	76	9.33E-06	*
Slow AHP (mV)	-2.07	3.55	0.09	1.59	205	0.06588	

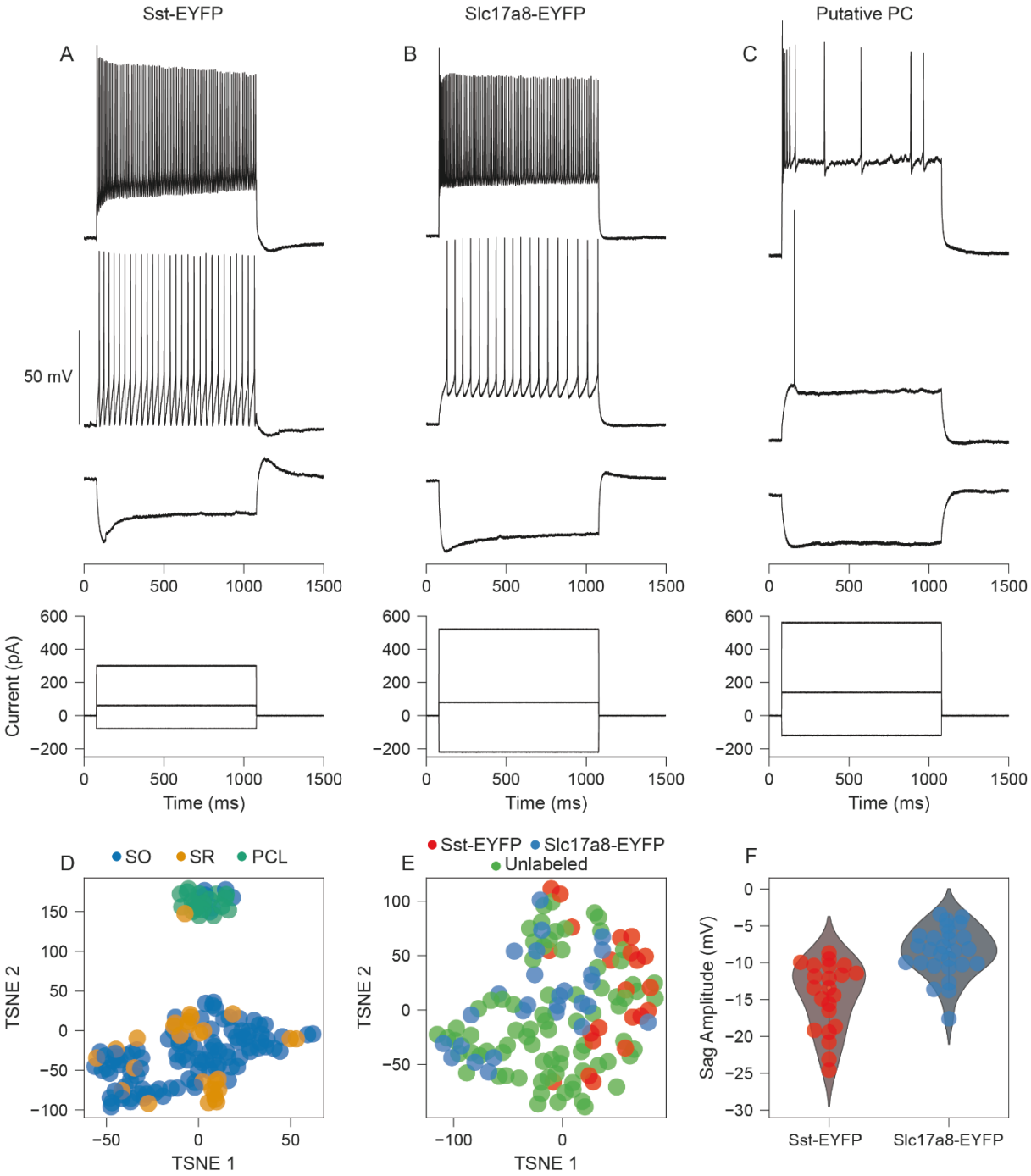

Figure 5: Electrophysiological parameters alone do not divide CA3 interneurons into clusters. A,B,C) Representative example traces for the two transgenic cell types and PCs. Sst-EYFP cells were EYFP positive cells in the SST-Cre mouse line. Slc17a8-EYFP cells were EYFP positive cells in the Tg(Slc17a8-icre)1Edw/SealJ mouse line. Putative pyramidal cells were patched in the pyramidal cell layer. D) TSNE dimensionality reduction of 28 electrophysiological parameters from 155 cells. Colors indicate where the cell was recorded. 27 cells in the cluster containing all PCL cells were classified as putative PCs. E) TSNE dimensionality reduction of 128 remaining interneurons. Colors indicate the transgenic type. Unlabeled cells were cells without fluorophore. Sst, somatostatin; Slc17a8, solute carrier family 17 member 8; PC, pyramidal cell; SO, stratum oriens; SR, stratum radiatum, PCL, pyramidal cell layer. TSNE, t-distributed stochastic neighbor embedding.

3.3 Electrophysiology of Sst-mRNA$^+$/Slc17a8-mRNA$^+$ cells

In total 136 samples were sequenced. Quality control excluded 17 of those cells based on total read count, number of genes, percentage of exonic and intronic alignment and mitochondrial genes (**Figure1**, Methods 2.7). Another 7 cells were excluded because no electrophysiological recordings were available for them. Out of 53465 genes, 31270 were excluded because they were not expressed at all or their log10 transformed read count was too low (**Figure 1F**). The remaining read counts were converted to counts per million (CPM) by normalizing to the sample's total counts.

First, we identified Sst-mRNA$^+$/Slc17a8-mRNA$^-$, Sst-mRNA$^-$/Slc17a8-mRNA$^+$ and Sst-mRNA$^+$/Slc17a8-mRNA$^+$ based on CPM larger than 0 for the respective gene. We identified 11 Sst-mRNA$^+$/Slc17a8-mRNA$^+$ putative interneurons, confirming the existence of colocalizing neurons (**Figure 6A**).

We then checked how these transcriptomic types relate to the transgenic types (**Table 3**). With respect to EYFP expression, 23.52% of samples are false negative for Sst-mRNA and 50.00% of samples are false negative for Slc17a8-mRNA. To estimate the false positive rate we investigated cells that were recorded in the PCL. Because cells form the PCL were all putative pyramidal cells regarding their electrophysiology (**Figure 5D**), we would expect them to express neither Sst-mRNA nor Slc17a8-mRNA. However, 3 of 12 samples were Sst-mRNA positive, hinting at a relatively high false positive rate. Slc17a8 on the other hand was not false positively expressed, which suggests that the false positive rate for colocalization should be low.

Table 3: Correspondence between transgenic type (EYFP) and transcriptomic type (mRNA). Percentages are calculated column-wise.

mRNA		**EYFP**			
Sst	Slc17a8	Sst	Slc17a8	Unlabeled	PCL
+	-	10 (58.82%)	11 (42.31%)	23 (45.10%)	3 (25.00%)
-	+	0	11 (42.31%)	2 (3.92%)	0 (0%)
+	+	3 (17.65%)	2 (7.69%)	6 (11.76%)	0 (0%)
-	-	4 (23.52%)	2 (7.69%)	20 (39.22%)	9 (75.00%)

We first used the low-dimensional embedding of electrophysiological feature space we generated in chapter 3.2 and annotated the Sst-mRNA$^+$/Slc17a8-mRNA$^+$ colocalizing cells as identified by their CPM (**Figure 6A**). We found that colocalizing cells did not form a distinct cluster in the low dimensional embedding (**Figure 6B**). This suggests that Sst-mRNA$^+$/Slc17a8-

mRNA$^+$ colocalizing cells are not electrophysiologically distinct from canonical Sst-mRNA$^+$/Slc17a8-mRNA$^-$ or Sst-mRNA$^-$/Slc17a8-mRNA$^+$ interneurons.

To investigate whether any single electrophysiological parameter is different between Sst-mRNA$^+$/Slc17a8-mRNA$^+$ colocalizing and other cell types, we used the Wilcoxon rank sum test to find significant differences (**Table 4**). We found that none of the electrophysiological properties was significant for classifying colocalizing cells. These data suggest that colocalizing cells are not electrophysiologically distinct from other interneurons types in our dataset. We next moved on to identify gene expression patterns that might distinguish colocalizing cells from others.

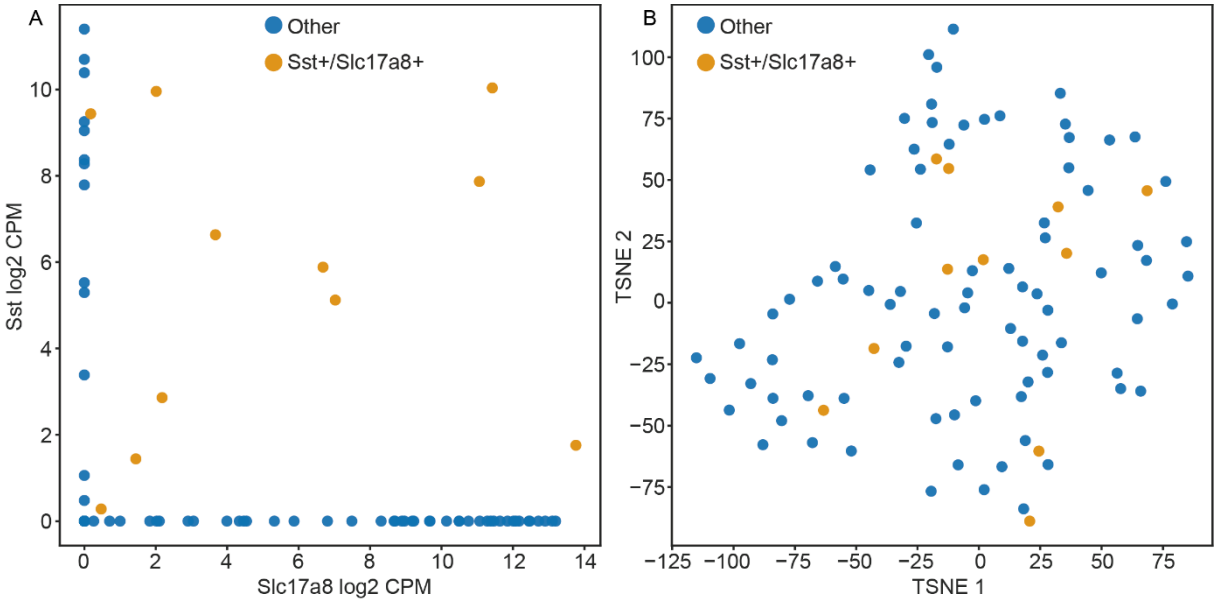

Figure 6: Sst-mRNA$^+$/Slc17a8-mRNA$^+$ colocalizing cells do not form a distinct cluster in low-dimensional electrophysiological space. A) 11 Sst-mRNA$^+$/Slc17a8-mRNA$^+$ cells were identified based on CPM larger than 0. B) The low-dimensional embedding of interneurons as calculated in chapter 3.2. The Sst colocalizing cells do not form a distinct cluster. TSNE, t-distributed stochastic neighbor embedding; CPM, counts per million.

The transcriptomic profile of these cells allowed us to identify Sst-mRNA$^+$/Slc17a8-mRNA$^+$ colocalizing cells based on their CPM. However, the CPM suffer from high false negative rates. Therefore, we performed another analysis where we take the transgenic EYFP expression into account. This means that we included the 11 samples that were Sst-mRNA$^-$/Slc17a8-mRNA$^+$ but Sst-EYFP positive were included in the colocalizing group (**Figure 7A**). As before, those colocalizing cells did not form a distinct electrophysiological cluster (**Figure 7A**).

Table 4: Descriptive statistics and results of the Wilcoxon rank sum test to compare Sst-mRNA$^+$/Slc17a8-mRNA$^+$ positive cells to all others. None of the electrophysiological features was found to be significant. Mad, median absolute deviation; W, test statistic of the Wilcoxon rank sum test; p, p-value of the Wilcoxon rank sum test; Sig., asterisk indicated significance after Benjamini-Hochberg correction for multiple comparison.

	Sst & Slc17a8 +		Other		Test		
Feature	**Median**	**Mad**	**Median**	**Mad**	**W**	**p**	**Sig.**
Adaptation ratio	1.43	0.64	1.77	1.14	670	0.3969	
Avg Spike Time (s	0.48	0.03	0.47	0.04	501	0.4358	
Capacitance (pF)	66.6	23.8	86.26	37.28	713	0.2065	
I at Max. Freq. (pA)	460	118.61	440	177.91	579	0.9806	
Input R (MOhm)	185.88	94.67	193.24	78.03	608	0.8050	
LS AHP Amp. (mV)	-7.78	4.3	-10.07	5.43	432.5	0.1491	
LS Half Width (ms)	0.77	0.27	0.76	0.39	568	0.8960	
LS Max. Slope (mV/ms)	1731.87	1023.68	1533.51	893.6	518	0.5387	
LS Min. Slope (mV/ms)	-644.68	254.51	-747.68	429.83	517	0.5324	
LS Peak (mV)	12.69	8.6	9.94	12.22	563.5	0.8616	
LS Threshold (mV)	-50.48	7.24	-47.13	8.6	640.5	0.7863	
Max. Freq. (Hz)	80	34.1	72	51.89	506	0.4648	
Resting (mV)	-64.5	4.45	-66	5.93	566.5	0.8844	
Rheobase (pA)	80	29.65	80	59.3	609	0.7958	
RS AHP Amp. (mV)	-15.26	5.66	-13.43	8.14	640	0.5777	
RS Half Width (ms)	0.46	0.06	0.48	0.15	588.5	0.9537	
RS Max. Slope (mV/ms)	2967.83	571.22	3028.87	531.63	581	0.9961	
RS Min. Slope (mV/ms)	-1510.62	622.12	-1640.32	622.12	527	0.5978	
RS Peak (mV)	20.32	10.86	24.28	9.5	664	0.4300	
RS Threshold (mV)	-56.74	4.75	-56.59	4.52	514.5	0.5164	
Sag Amplitude (mV)	-10.15	4.9	-9.65	6.89	637	0.5978	
Slow AHP (mV)	-1.57	4.08	-0.08	3.71	760	0.0857	

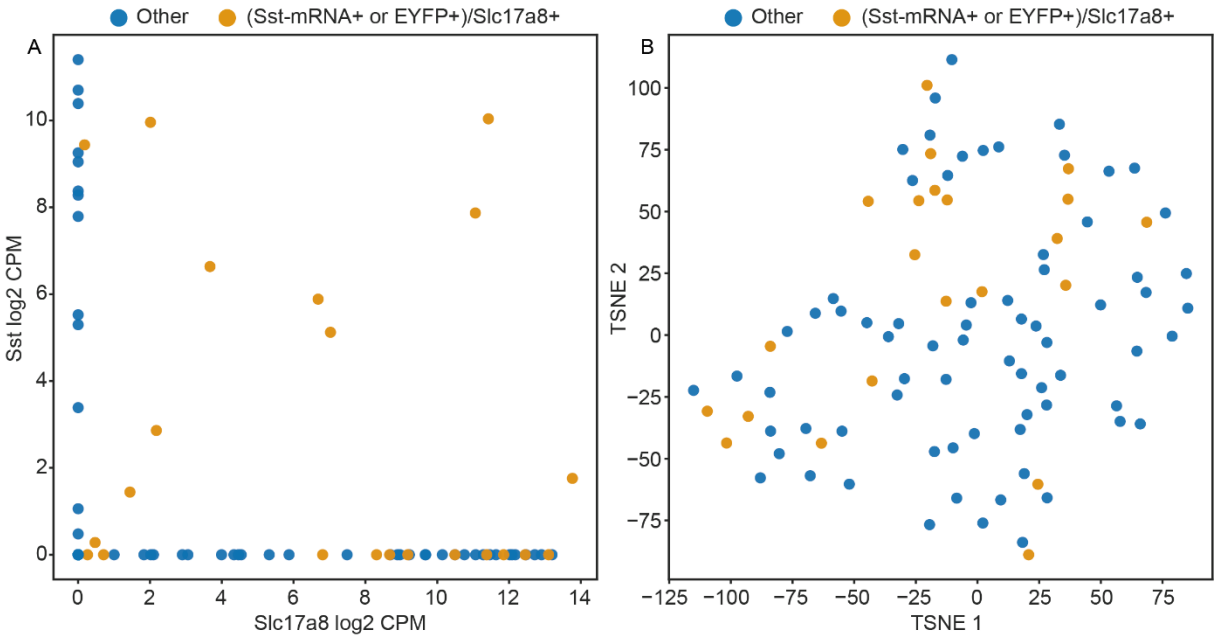

Figure 7: Like Figure 6 but with an extended definition of colocalization. A) 22 (Sst-mRNA$^+$ or EYFP$^+$)/Slc17a8-mRNA$^+$ cells were identified. B) The low-dimensional embedding of interneurons as calculated in chapter 3.2. Colocalizing cells do not form a distinct cluster. TSNE, t-distributed stochastic neighbor embedding; CPM, counts per million.

3.4 Tyrosine hydroxylase is a possible marker for Sst-mRNA$^+$/Slc17a8-mRNA$^+$ cells

To identify marker genes that are enriched in Sst-mRNA$^+$/Slc17a8-mRNA$^+$ cells, we used differential expression analysis with the scanpy package (Wolf et al., 2018). We used it to identify the 50 top genes that are most enriched in the colocalizing group as opposed to all other cells. Because of the small sample size, we used a non-parametric Wilcoxon rank-sum test to statistically test enrichment. Since we tested 50 genes, we needed to correct for 50 statistical comparisons, and we used the Benjamini-Hochberg method for this correction. **Figure 6C** shows the log2 transformed CPM profiles of the top 50 genes. However, none of those was significantly enriched after correction for multiple comparison.

Next, we analyzed whether colocalizing cells have different expression levels regarding known neuronal subtype markers (Muñoz-Manchado et al., 2018). Out of 26 marker genes, 12 were excluded in our dataset due to zero counts or low variance (Gpr88, G-protein coupled receptor 88; D830015G02Rik, myosin heavy chain associated RNA transcript; Adora2a, adenosine A2a receptor; Drd1a, dopamine receptor D1; Pthlh, parathyroid hormone-like peptide; Chodl, chondrolectin; Hhip, Hedgehog-interacting protein; Mia, melanoma inhibitory activity; Slc5a7, solute carrier family 5 (choline transporter), member 7; Trh, thyrotropin releasing hormone; Igfbp4, insulin like growth factor binding protein 4; Igfbpl1, insulin-like growth factor binding protein-like 1). We used a binomial generalized linear model (GLM) to classify samples into colocalizing or non-colocalizing (non-colocalizing cells are all cells of the dataset that are not part of the 11 Sst-mRNA$^+$/Slc17a8-mRNA$^+$ cells), based on log2 CPM of the remaining 14 genes. A generalized linear model allows for statistical inference because it does not only calculate the optimal parameter but also calculates the variance for each parameter through maximum likelihood estimation. The z-statistic can be calculated with this variance, which in turn allows for p-value calculation. Only the tyrosine hydroxylase (Th) expression was significantly enriched in colocalizing cells (**Table 5**). **Figure 8B** shows log2 transformed CPM in violin plots. Th is a gene that is involved in the physiology of adrenergic neurons. Cell types expressing it in the hippocampus have not been described previously. Altogether, our exploratory analysis suggests that Th could be a specific marker of Sst/Slc17a8 colocalizing cells.

We repeated the above analysis with cell type classifications that consider the transgenic expression. Sst-EYFP and Slc17a8-EYFP cells were included in the Sst or Slc17a8 positive groups and cells were included in the colocalizing group if they had either mRNA or EYFP expression (**Figure 9**). In this analysis Th was not significant (**Table 6)** because cells with low

Th CPM were included in the Sst-mRNA$^+$/Slc17a8-mRNA$^+$ group (**Figure 9A**). The Sst and Slc17a8 genes on the other hand were significantly enriched in colocalizing cells. The differential expression analysis did not reveal significantly enriched genes (heatmap in **Figure 9B**). These data suggest that although Th is a putative Sst-mRNA$^+$/Slc17a8-mRNA$^+$ specific marker, few cells express it at high CPM.

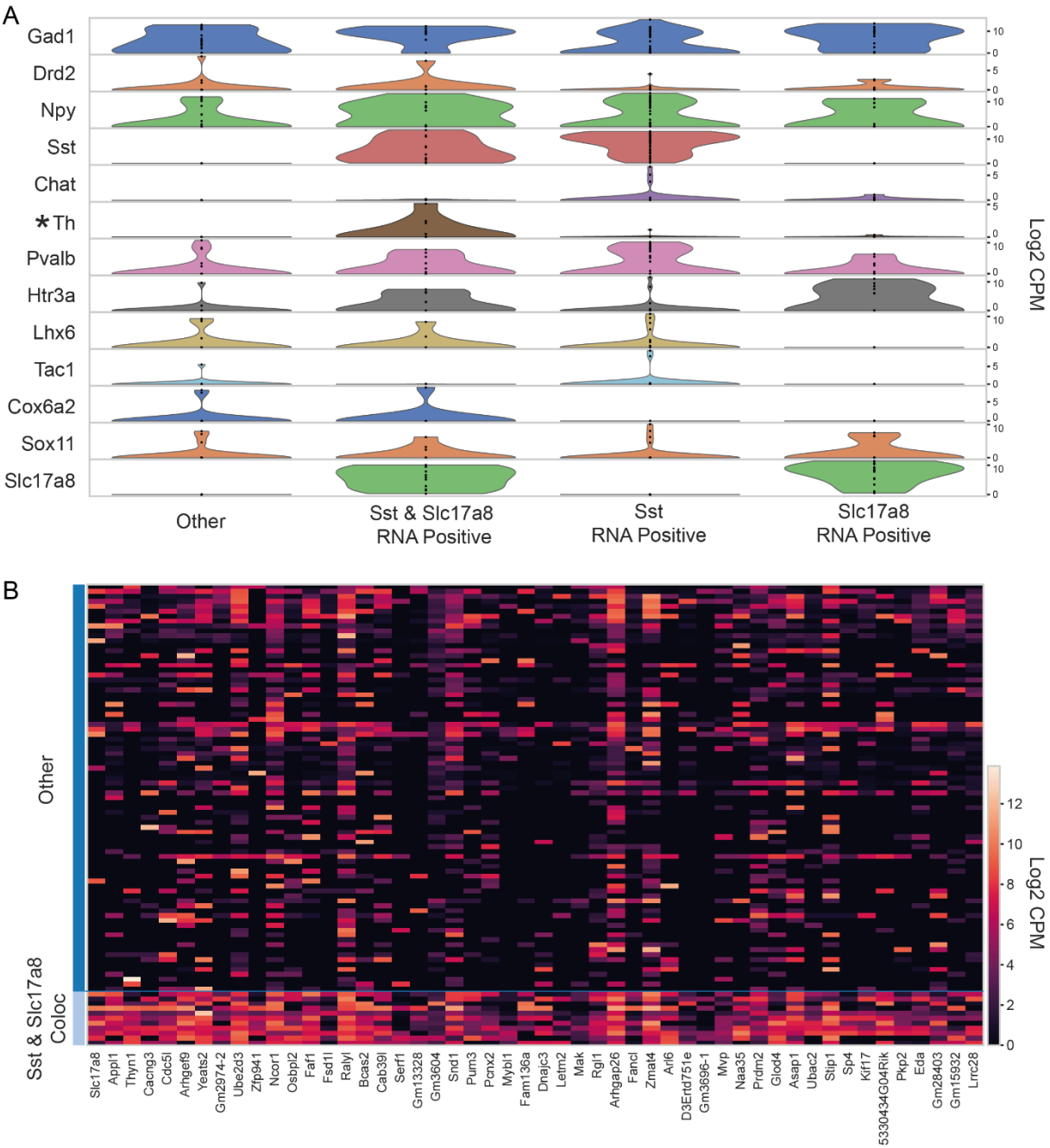

Figure 8: Tyrosine Hydroxylase is a putative marker for Sst-mRNA$^+$/Slc17a8-mRNA$^+$ interneurons. A) Comparison of known interneuron markers between transcriptomic cell types. Compared are cells that are positive for both Sst & Slc17a8, cells expressing Sst or Slc17a8 but not both and finally all other cells of the dataset. The generalized linear model that detected Th as significant was trained to distinguish only two groups. For this, cells expressing either Sst or Slc17a8 but not both were grouped with other cells. B) Top 50 genes enriched in colocalizing cells a determined by scanpy differential expression analysis. None were found to be significantly enriched. Genes in A: Gad1, glutamate decarboxylase 1; Drd2, dopamine receptor D2; Npy, neuropeptide Y; Sst, somatostatin; Chat, choline acetyltransferase; Th, tyrosine hydroxylase; Pvalb, parvalbumin; Htr3a 5-hydroxytryptamine (serotonin) receptor 3A; Asap1, ArfGAP with SH3 domain, ankyrin repeat and PH domain1; Rgl1, ral guanine nucleotide dissociation stimulator,-like 1; Lhx6, LIM homeobox protein 6; Tac1, tachykinin 1; Cox6a2, cytochrome c oxidase subunit 6A2; Slc17a8, solute carrier family 17 member 8. Genes in B: Slc17a8, solute carrier family 17 member 8.; Appl1, adaptor protein, phosphotyrosine interaction, PH domain and leucine zipper containing 1; Thyn1, thymocyte nuclear protein 1;

Continuation Figure 8: Cacng3, calcium channel, voltage-dependent, gamma subunit 3; Cdc5l, cell division cycle 5-like (S. pombe); Stip1, stress-induced phosphoprotein 1, Mvp, major vault protein; Faf1, Fas-associated factor 1; Osbpl2, oxysterol binding protein-like 2; Ralyl, RALY RNA binding protein-like; Zfp941, zinc finger protein 941; Gm2974, predicted gene 2974; Pcnx2, pecanex homolog 2; Arhgef9, CDC42 guanine nucleotide exchange factor (GEF) 9; Ube2d3, ubiquitin-conjugating enzyme E2D 3; Prdm2, PR domain containing 2, with ZNF domain; Letm2, leucine zipper-EF-hand containing transmembrane protein; 2Bcas2, breast carcinoma amplified sequence 2; Rgl1, ral guanine nucleotide dissociation stimulator,-like 1; Serf1, small EDRK-rich factor 1; Mybl1, myeloblastosis oncogene-like 1; Dnajc3, DnaJ heat shock protein family (Hsp40) member C3; Fancl, Fanconi anemia, complementation group L; Glod4, glyoxalase domain containing 4; Pkp2, plakophilin 2; Gm3604, predicted gene 3604; Gm3696, predicted gene 3696;Cab39l, calcium binding protein 39-like; Gm13328, predicted gene 13328; Fsd1l, fibronectin type III and SPRY domain containing 1-like; Yeats2, YEATS domain containing 2; Fam136a, family with sequence similarity 136, member A; Pum3, pumilio RNA-binding family member 3; Sp4, trans-acting transcription factor 4; Stip1, stress-induced phosphoprotein 1; Ubac2, ubiquitin associated domain containing 2; Gm16332, predicted gene 16332; Zmat4, zinc finger, matrin type 4; Naa35, N(alpha)-acetyltransferase 35, NatC auxiliary subunit; Arl6, ADP-ribosylation factor-like 6; D3Ertd751e, DNA segment, Chr 3, ERATO Doi 751, expressed; Arhgap26, Rho GTPase activating protein 26; Snd1, staphylococcal nuclease and tudor domain containing 1; Glb1l2, galactosidase, beta 1-like 2; 5330434G04Rik, RIKEN cDNA 5330434G04 gene; Mak, male germ cell-associated kinase; Ncor1, nuclear receptor co-repressor 1; Atad3a, ATPase family, AAA domain containing 3A; Letm2, leucine zipper-EF-hand containing transmembrane protein 2; Mia3, melanoma inhibitory activity 3; Eda, ectodysplasin-A; Lrrc28, leucine rich repeat containing 28; Maf, avian musculoaponeurotic fibrosarcoma oncogene homolog; Mrnip, MRN complex interacting protein; Med30, mediator complex subunit 30; Kif17, kinesin family member 17; Ccdc149, coiled-coil domain containing 149; Tbx19, T-box 19; Gm28403, predicted gene 28403.

Table 5: Output of binomial GLM for classifying cells as colocalizing or non-colocalizing based on 14 interneuron marker genes. Tyrosine hydroxylase (Th) was the only gene found to be significantly enriched in colocalizing cells. Coef, the mean coefficient or weight found by the model for a given feature. Std Err, standard error of the coefficient estimate. z, the z score of the coefficient. P>|z|, the absolute p value of the z score of the coefficient. [0.025, 0.975], the 2.5% and 97.5% percentile of the coefficient estimate, respectively. const, a constant term added to the linear model. Gad1, glutamate decarboxylase 1; Drd2, dopamine receptor D2; Npy, neuropeptide Y; Sst, somatostatin; Chat, choline acetyltransferase; Th, tyrosine hydroxylase; Pvalb, parvalbumin; Htr3a 5-hydroxytryptamine (serotonin) receptor 3A; Lhx6, LIM homeobox protein 6; Tac1, tachykinin 1; Cox6a2, cytochrome c oxidase subunit 6A2; Sox11, SRY (sex determining region Y)-box 11; Slc17a8, solute carrier family 17 member 8.

	Coef	Std Err	z	P>|z|	[0.025	0.975]
const	-21.5532	10.016	-2.152	0.031	-41.184	-1.923
Gad1	-0.0038	0.408	-0.009	0.992	-0.803	0.795
Drd2	1.4454	1.177	1.228	0.219	-0.861	3.752
Npy	0.3776	0.375	1.008	0.313	-0.357	1.112
Sst	1.2193	0.763	1.598	0.110	-0.276	2.715
Chat	-6.9372	7.162	-0.969	0.333	-20.974	7.099
Th	32.0976	13.227	2.427	*0.015	6.173	58.022
Pvalb	-0.4939	0.609	-0.811	0.417	-1.688	0.700
Htr3a	-0.5315	0.432	-1.231	0.218	-1.378	0.315
Lhx6	-0.2952	0.580	-0.509	0.611	-1.431	0.841
Tac1	-14.2569	4.94e+06	-2.89e-06	1.000	-9.68e+06	9.68e+06
Cox6a2	1.8618	1.296	1.437	0.151	-0.677	4.401
Sox11	-0.0513	0.632	-0.081	0.935	-1.290	1.188
Slc17a8	1.8356	0.970	1.893	0.058	-0.065	3.736

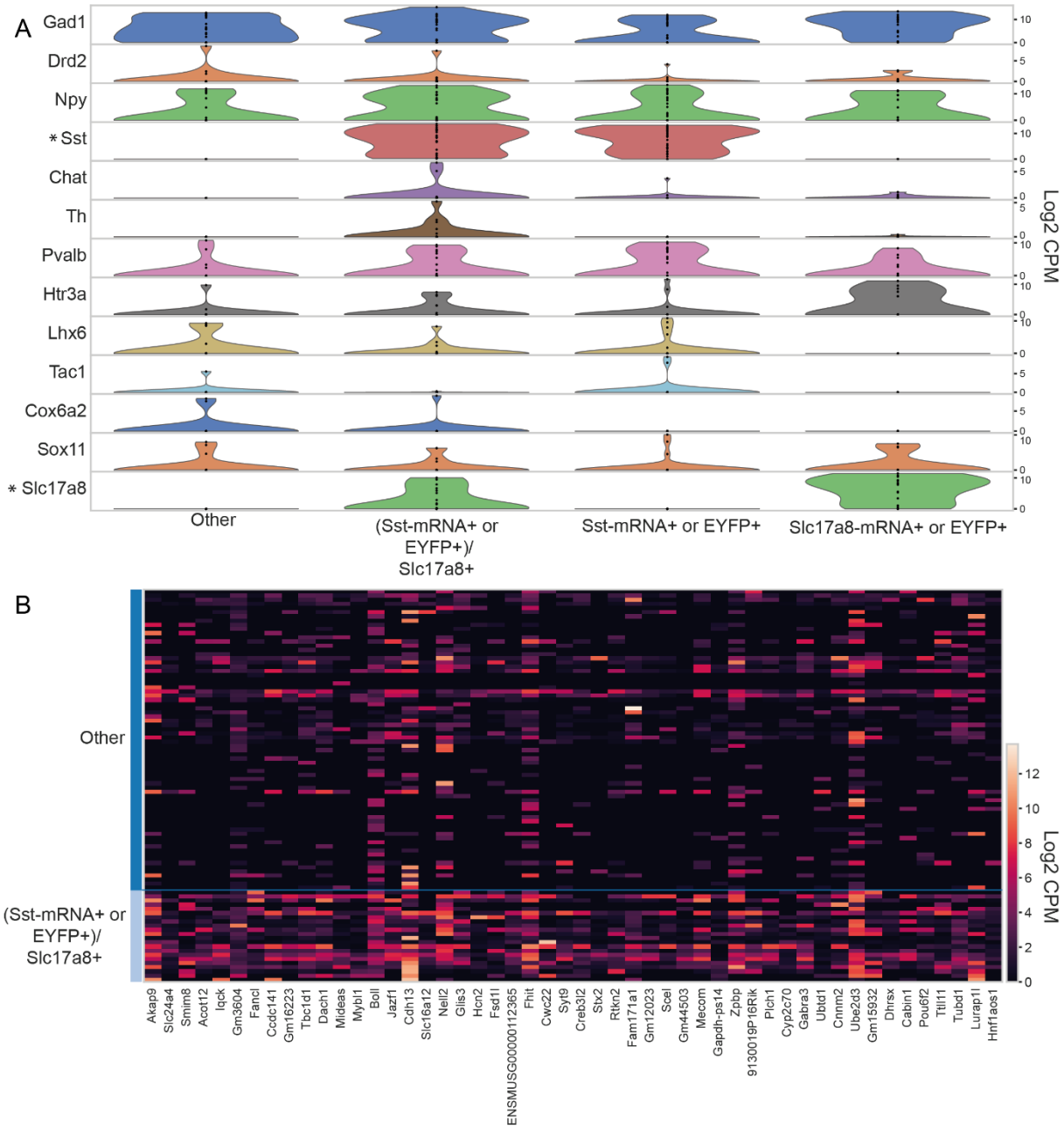

Figure 9: Analysis as in Figure 8 but with transgenic EYFP included in cell type classification. 22 cells were identified as Sst-mRNA$^+$/Slc17a8-mRNA$^+$ or Sst-EYFP$^+$/Slc17a8-mRNA$^+$. A) Comparison of known interneuron markers between transcriptomic/transgenic cell types. The GLM identified Sst and Slc17a8 as significantly enriched in colocalizing cells. Th was not positive in this analysis, most likely because the transgenic classification included several Th negative samples in the colocalizing group. B) Top 50 genes enriched in colocalizing cells a determined by scanpy differential expression analysis. None were found to be significantly enriched. Genes in A: Gad1, glutamate decarboxylase 1; Drd2, dopamine receptor D2; Npy, neuropeptide Y; Sst, somatostatin; Chat, choline acetyltransferase; Th, tyrosine hydroxylase; Pvalb, parvalbumin; Htr3a 5-hydroxytryptamine (serotonin) receptor 3A; Asap1, ArfGAP with SH3 domain, ankyrin repeat and PH domain1; Rgl1, ral guanine nucleotide dissociation stimulator,-like 1; Lhx6, LIM homeobox protein 6; Tac1, tachykinin 1; Cox6a2, cytochrome c oxidase subunit 6A2; Slc17a8, solute carrier family 17 member 8. **Genes in B**: Akap9, A-kinase anchoring protein; Slc24a4, solute carrier family 24 (sodium/potassium/calcium exchanger), member 4; Smim8, small integral membrane protein 8; Acot12, acyl-CoA thioesterase 12; Iqck, IQ motif containing K; Gm3604, predicted gene 3604;

Continuation Figure 9: Fancl, Fanconi anemia, complementation group L; Ccdc141, coiled-coil domain containing 141; Gm16223, Predicted gene 16223; Tbc1d1, TBC1 domain family, member 1; Dach1, dachshund family transcription factor 1; Mideas, mitotic deacetylase associated SANT domain protein; Mybl1, myeloblastosis oncogene-like 1; Boll, boule homolog, RNA binding protein; Jazf1, JAZF zinc finger 1; Cdh13, cadherin 13; Slc16a12, solute carrier family 16 (monocarboxylic acid transporters), member 12; Nell2, NEL-like 2; Glis3, GLIS family zinc finger 3; Hcn2, hyperpolarization activated cyclic nucleotide gated potassium and sodium channel 2; Fsd1l, fibronectin type III and SPRY domain containing 1-like; Fhit, fragile histidine triad gene; Cwc22, CWC22 spliceosome-associated protein; Syt9, synaptotagmin; Creb3l2, cAMP responsive element binding protein 3-like 2; Stx2, syntaxin 2; Rtkn2, rhotekin 2; Fam171a1, family with sequence similarity 171, member A1; Scel, sciellin; Mecom, MDS1 and EVI1 complex locus; Gapdh-ps14, glyceraldehyde-3-phosphate dehydrogenase, pseudogene 14; Zpbp, zona pellucida binding protein; Plch1, phospholipase C, eta 1; Cyp2c70, cytochrome P450, family 2, subfamily c, polypeptide 70; Gabra3, gamma-aminobutyric acid type A receptor subunit alpha 3; Ubtd1, ubiquitin domain containing 1; Dhrsx, dehydrogenase/reductase (SDR family) X chromosome; Cabin1, calcineurin binding protein 1; Pou6f2, POU domain, class 6, transcription factor 2; Ttll11, tubulin tyrosine ligase-like family, member 11; Tubd1, tubulin, delta 1; Lurap1l, leucin rich adaptor protein 1-like; Hnf1aos1, HNF1 homeobox A, opposite strand 1.

Table 6: Output of binomial GLM for classifying cells as colocalizing or non-colocalizing based on 14 interneuron marker genes. Like **Table 4** but including the transgenic type into the cell type classification. Tyrosine hydroxylase (Th) was not found to be significantly enriched in colocalizing cells. Instead, Sst and Slc17a8 were significant. Coef, the mean coefficient or weight found by the model for a given feature. Std Err, standard error of the coefficient estimate. z, the z score of the coefficient. P>|z|, the absolute p value of the z score of the coefficient. [0.025, 0.975], the 2.5% and 97.5% percentile of the coefficient estimate, respectively. const, a constant term added to the linear model. Gad1, glutamate decarboxylase 1; Drd2, dopamine receptor D2; Npy, neuropeptide Y; Sst, somatostatin; Chat, choline acetyltransferase; Th, tyrosine hydroxylase; Pvalb, parvalbumin; Htr3a 5-hydroxytryptamine (serotonin) receptor 3A; Lhx6, LIM homeobox protein 6; Tac1, tachykinin 1; Cox6a2, cytochrome c oxidase subunit 6A2; Sox11, SRY (sex determining region Y)-box 11; Slc17a8, solute carrier family 17 member 8.

	Coef	Std Err	z	P>|z|	[0.025	0.975]
const	-3.7592	0.997	-3.770	0.000	-5.714	-1.805
Gad1	-0.0213	0.083	-0.258	0.796	-0.183	0.140
Drd2	-0.5252	0.721	-0.728	0.466	-1.938	0.888
Npy	0.0834	0.080	1.038	0.299	-0.074	0.241
Sst	0.2991	0.099	3.028	*0.002	0.106	0.493
Chat	0.1319	0.355	0.371	0.710	-0.565	0.828
Th	8.1279	4.348	1.869	0.062	-0.395	16.651
Pvalb	-0.1025	0.115	-0.895	0.371	-0.327	0.122
Htr3a	-0.1619	0.192	-0.842	0.400	-0.539	0.215
Lhx6	-0.1142	0.157	-0.727	0.467	-0.422	0.194
Tac1	-1.0499	13.463	-0.078	0.938	-27.437	25.337
Cox6a2	0.4060	0.263	1.547	0.122	-0.109	0.921
Sox11	-0.0821	0.166	-0.496	0.620	-0.407	0.243
Slc17a8	0.3125	0.115	2.712	*0.007	0.087	0.538

4 Discussion

Using patch seq we were able to characterize a novel interneuron subtype that colocalizes Sst and Slc17a8. These colocalizing cells are not electrophysiologically distinct but they could be enriched in tyrosine hydroxylase (Th). Patch seq is a novel technique that combines advantages and limitations of intracellular patch clamp recordings and single cell sequencing. The next chapter will discuss these in the context of characterizing rare neuronal subtypes.

4.1 Using patch seq to characterize rare neuronal subtypes

Patch seq is an extension of patch clamp, where intracellular electrical access allows for the recording of the electrical potential across parts of the cell membrane. After the electrical recordings are finished, the cytosol of the cell is extracted, the cDNA is amplified and then sequenced. The most obvious advantage is that electrophysiology and transcriptomic profile can be assessed in the same single cell. Even morphological reconstruction of the same cell is possible but has low success rates (around 20%), even in laboratories that pioneered the technique (Cadwell et al., 2016; Cadwell, Sandberg, et al., 2017). Recently this has been pushed to roughly 45% success rate (Lee et al., 2020)

The advantage of highly multimodal single cell data comes with some disadvantages regarding each data modality and a large workflow. From a patch clamp perspective, patch seq requires RNAse minimized working conditions. This means regular cleaning efforts at much higher rate than in normal patch clamp. It also changes the recording conditions, because RNAse inhibitors need to be introduced into the intracellular solution. The intracellular solutions is in direct contact with the cytosol and the RNA it contains, making RNAse inhibitors a necessity for sufficient RNA quality. Adding the RNAse inhibitors drastically increases the osmolarity of the solution, which makes it harder to get stable intracellular access to a cell and hold the recording stable. This limits the effective recording time to around 5 minutes.

From the single-cell sequencing perspective, the RNA quality of patch seq is on average worse than that of microfluidics techniques used to isolate single cells (Kalisky et al., 2018). This is the case because despite the precautions described above, it is nearly impossible to completely avoid RNAse contamination of the cytosolic samples during patch seq, as the patch pipette must move through neuronal tissue. Another downside of patch seq has the lower throughput. With a highly optimized workflow, datasets of more than 3700 interneurons are possible (Gouwens et al., 2020). While this is large dataset for the field of intracellular

electrophysiology, it pales in comparison to sequencing datasets with more than a million cells (Yao et al., 2021).

An advantage of patch seq that is particularly relevant for the characterization of rare neuronal subtypes is the high spatial precision of cell selection. During in-vitro patch clamp experimenters visualize the cell before and during patching. They therefore know exactly where the cell was recorded and to some extent even what type of cell. With microfluidics approaches it is possible to dissect specific areas such as CA1, CA3 or DG. However, dissecting layers such as SR, PCL or SO is not well established. This means that such datasets represent the most abundant cell types of an area. Cell type specificity can also be achieved through fluorescence-activated cell sorting (FACS). However, this requires a specific and efficient fluorescent marker for the cell type population, which does not exist for most rare subtypes. In that case, patch seq can target specific areas, if the subtype is known to be more abundant there.

Patch seq allowed us to perform electrophysiological and transcriptomic characterization in the same dataset. This has revealed the similarity of Sst/Slc17a8 colocalizing to known interneuron subtypes. Furthermore, we were able to identify tyrosine hydroxylase (Th) as a putative marker for these cells. Th is involved in the catecholaminergic system and is strongly expressed in the locus coeruleus (Benarroch, 2018) among other areas. In the following chapter we will discuss the possible role Th could play in this rare interneuron subtype.

4.2 Functional roles for tyrosine hydroxylase expression

The tyrosine hydroxylase gene (Th) is protein coding for the tyrosine hydroxylase enzyme (ThE). It catalyzes the amino acid L-tyrosine to L-3,4-dihydroxyphenylalanine (L-DOPA), a precursor to dopamine. Dopamine can in turn be converted to Norepinephrine and Norepinephrine into Epinephrine (Kaufman, 1995). Dopamine (McNamara & Dupret, 2017) and Norepinephrine (Bacon et al., 2020) have both been shown to be released into the hippocampus with functional effects. However, in both cases the release source are fibers that project into the hippocampus from other brain regions. Namely, the ventral tegmental area (VTA) and the locus coeruleus (LC). Release from hippocampal neurons has not been reported. The only report of somatic ThE expression comes from Kosaka et al. (1987) who did antibody labeling in rat tissue. They found extremely rare ThE positive somata in the hippocampus. What might be the functional role of a rare, dopamine synthesizing interneuron population in the hippocampus?

Dopamine released into the hippocampus has effects on memory in mice. Optogenetic activation of Th positive LC fibers in the hippocampus enhances memory in a similar way as

novel environments. At the network level optogenetic activation increases synaptic efficacy and this effect is blocked by the Dopamine1/Dopamine5 receptor antagonist SCH23390 (Takeuchi et al., 2016). Similarly, optogenetic burst activation of Th positive fibers from VTA facilitates the reactivation of pyramidal cell ensembles after mice explored a novel environment (McNamara et al., 2014). Importantly, both of these examples propose that the main effect of dopamine is on the schaffer-collateral synapses located in dorsal CA1. The cell type we identify here is primarily located in CA3 and could therefore influence synapses located in CA3 with behavioral effects distinct from those in CA1.

In any case, the expression of Th in hippocampal neurons remains to be validated and there are several strategies for this. RNAScope for Th is especially promising since it has an exceptionally good signal-to-noise ratio (Anderson et al., 2016). It therefore has the potential to discover expression where previous techniques had negative results. An antibody strategy could also be feasible, since many anti-Th antibodies have been developed since Kosaka et al. (1987) performed their stainings. Some of these newer antibodies might show more labeling in the hippocampus. The third possibility is to use transgenic mouse lines that express Cre-recombinase in Th expressing cells (for example Savitt, 2005). Such mouse lines would also offer a way to target optogenetic actuators to these cells for further functional experiments. However, putative Th expression is not the only interesting feature of this cell type. The colocalization of Sst and Slc17a8 - a GABAergic and a Glutamatergic marker respectively – opens the possibility of excitatory/inhibitory corelease. A rare type of synaptic connectivity but with interesting functions as discussed in the next chapter.

4.3 GABA/Glutamate corelease in the hippocampus

GABA and Glutamate are important neurotransmitters of the mammalian central nervous system. GABA has inhibitory and Glutamate has excitatory effects in adult animals. The corelease of these two opposing neurotransmitters is rare in the mammalian central nervous system but has been reporter for example in the rat VTA (Root et al., 2014). There, the neurons that project to the lateral habenula (LHb) express Slc17a6 (which is protein coding for VGluT2) and either Gad1 or Gad2 (both GABAergic interneuron markers). Furthermore, the same axon terminal has both $GABA_A$ and GluR1 located post-synaptically. Optogenetic stimulation elicits currents which are sensitive to pharmacological blockers of both Glutamatergic and GABAergic transmission. Together, these data make it likely that the same axon can release both GABA and Glutamate. In vivo stimulation of these axons has mixed effects, with some neurons showing increased spiking and other decreased.

In the hippocampus the cholecystokinin (CCK) positive basket cells have been known for a long time to colocalize GABA and Slc17a8 (Herzog et al., 2004; Somogyi et al., 2004) but their postsynaptic effects and their ability to corelease has been inconclusive for a long time. Knocking out Slc17a8 in interneurons had effects on the hippocampal network (Fasano et al., 2017). For example, the frequency of mini-inhibitory postsynaptic currents was increased in the knockouts. This is thought to occur, because the glutamate released from hippocampal interneurons acts on presynaptic group-III metabotropic glutamate receptors (mGluRs). Those receptors have an inhibitory effect on the presynapse and when glutamate is not released in the Slc17a8 knockouts, event frequency is increased because a source of inhibition was knocked out. mGluR4 which is part of the group-III receptors colocalizes synaptically with VGluT3. Importantly, Fasano et al. (2017) never constrain their knockout or their analysis to CCK interneurons. Therefore, some of the effects they observe could come from Sst/Slc17a8 colocalizing cells rather than the CCK/Slc17a8 interneurons. This highlights the demand for Slc17a8 knockouts in interneuron subtypes.

Recently, Pelkey et al. (2020) provided evidence for glutamate release from hippocampal CCK basket cells with excitatory postsynaptic effects onto CA1 pyramidal cells. They performed paired patch clamp of CCK interneurons and pyramidal cells in CA1 and showed that spikes in CCKs cause currents with components that are sensitive to glutamate receptor blockers. They also find colocalization of genetic fluorophore expression in the VGluT3.Cre-Ai14 mouse line with Sst Ab in both SO and SR for a subset of Sst cells. This contrasts with our data, where we found fewer colocalizing Sst cells in CA1. This could be due to the use of the VGluT3.Cre-Ai14 mouse line, which might nonspecifically target some VGluT3 negative cells. Despite glutamate release, the net-effect of VGluT3 positive cells is inhibition. Inhibitory conductances are larger than excitatory conductances by a factor of 10.

Paired patch clamp recordings are the ideal technique to disentangle connectivity between single cells because they provide intercellular access to multiple single cells at the same time. They therefore convincingly show corelease. However, even high-throughput paired patch clamp experiments only target a relatively small part of the whole population and do not work during animal behavior. Tools to specifically express transgenic constructs in large parts of a neuronal population are important to understand the role of a neuronal population inside the larger network and during animal behavior. The next chapter discusses strategies to achieve this in rare neuronal populations with a focus on investigating the novel Sst/Slc17a8 colocalizing neurons.

4.4 Genetic targeting of rare Sst/Slc17a8 population

Strategies to genetically express fluorophores, sensors or optogenetic actuators have been used with great success in many neuronal populations. One such strategy uses mice that express a transgene only in the presence of a recombinase protein. Madisen et al. (2016) alone present 17 such mouse lines. The two most widespread recombinases are Cre and Flp (Kim et al., 2018). To target specific neuronal populations, one of these recombinases must be expressed exclusively in the neuronal population. This can be achieved by virally transducing a vector expressing the recombinase or alternatively using a transgenic mouse line that expresses it. Mouse lines expressing Cre recombinase were found to be more specific for neuronal populations under most circumstances. In this case, the construct that should be expressed is virally transduced into the Cre expressing mice.

What kind of strategy could target the novel Sst/Slc17a8 population? Here we already targeted a fluorophore to Sst cells in the SST-Cre mouse line and Slc17a8 cells in the Tg(Slc17a8-icre)1Edw/SealJ mouse line. An intersectional genetic approach (Madisen et al., 2015) could allow expression only in those cells that express both Sst & Slc17a8. For this we have acquired $Sst^{tm3.1(flpo)Zjh}$/J mice (Sst-ires-Flp; He et al., 2016), which expresses Flp-recombinase under the Slc17a8 promoter. By crossing this line with the Tg(Slc17a8-icre)1Edw/SealJ, we can generate mice that should express both Cre- and Flp-recombinase only in the Sst/Slc17a8 cells. We will then transduce the viral vector AAV phSyn1-FSF-FLEX-ChR2(H134R)-EYFP-WPRE-bGHpA (#65454 addgene plasmid), which expresses the ChR2(H134R) optogenetic construct with the EYFP fluorophore. If successful, this approach can lead to several insights.

For one, the fluorophore expression would allow for reconstruction of dendritic and axonal morphology. Such reconstructions could hint to functional insights, since the dendritic morphology is somewhat correlated with the types of inputs a neuron receives and the axon morphology is correlated with the output targets. For example, axon morphology like that of basket cells could hint at perisomatic targeting by these cells. Such findings could then be corroborated by function experiments with ChR2(H134R). This includes experiments regarding the possibility of GABA/Glutamate corelease. Although such experiments would themselves need to be confirmed with paired patch recordings. This is because a single CA3 pyramidal cell that nonspecifically expresses ChR2(H134R), could cause excitatory postsynaptic currents on other CA3 pyramidal cells. For such paired patch clamp experiments the genetic EYFP expression would be necessary to have a reasonable chance to record from the rare Sst/Slc17a8 cell type.

Another line of experiments could give insights into the behavioral role of Sst/Slc17a8 neurons. For behavioral experiments, optogenetic inhibition would be the preferred approach to show the effect of turning the population off during relevant behaviors. However, viral plasmids for intersectional expression under Cre-Flp-Recombinase do not exist yet for optogenetic inhibitors. Experiments limited to excitatory optogenetics would need to focus on over-excitation the Sst/Slc17a8 population. Excitation would be relevant since many interneuron populations have rhythmic activity or contribute to such activity in downstream populations. Continuously exciting them or driving them at different frequencies could disrupt these natural rhythms and could have interesting behavioral effects.

Nonspecific expression is a major problem for genetic expression strategies, especially when targeting interneuron populations that are small in absolute terms. Therefore, transgenic animals require careful validation of their expression profiles. We performed such a validation for the SST-Cre mouse we used to increase the number of Sst positive cells in our patch seq data. We found that this mouse line is highly specific in stratum oriens and stratum radiatum of CA3. That means recording from cells in those areas indeed results in recordings from mostly Sst positive cells. However, in the pyramidal cell layer many Sst negative pyramidal like cells expresses nonspecifically. The next chapter details the transgenic characterization.

5 Nonspecific Expression in Limited Excitatory Cell Populations in Interneuron-Targeting Cre-driver Lines

5.1 Introduction

The ability to express transgenic constructs specifically in neuronal subtypes has been crucial to many advances in neuroscience. Especially the study of interneurons and their many subtypes has benefitted from the transgenic mouse lines that allow for cell type specific expression (He et al., 2016). These mouse lines can be used to record from specific cell types during patch clamp or express optogenetic actuators. However, optogenetic experiments are difficult to interpret when nonspecific expression occurs in other cell types. Therefore, it is important to carefully verify the identity of cells that are genetically targeted in a mouse line. This publication describes the results of verifying transgene expression in the SST-Cre mouse line, the same line we used to target Sst cells in CA3. While this line is highly specific to Sst cells in SO, we found that it is not suited for optogenetic experiments on interneurons because it also targets pyramidal cells in CA3.

frontiers in Neural Circuits

ORIGINAL RESEARCH
published: 27 April 2020
doi: 10.3389/fncir.2020.00016

Nonspecific Expression in Limited Excitatory Cell Populations in Interneuron-Targeting Cre-driver Lines Can Have Large Functional Effects

*Daniel Müller-Komorowska[1,2], Thoralf Opitz[1], Shehabeldin Elzoheiry[3], Michaela Schweizer[4], Eleonora Ambrad Giovannetti[5] and Heinz Beck[1]**

[1]*Institute for Experimental Epileptology and Cognition Research, University of Bonn, Bonn, Germany,* [2]*International Max Planck Research School for Brain and Behavior, University of Bonn, Bonn, Germany,* [3]*Institute of Physiology and Pathophysiology, University Heidelberg, Bonn, Germany,* [4]*Department of Electron Microscopy, Center of Molecular Neurobiology, University Medical Center Hamburg-Eppendorf, Hamburg, Germany,* [5]*German Center for Neurodegenerative Diseases (DZNE) within the Helmholtz Association, Bonn, Germany*

OPEN ACCESS

Edited by:
Jérôme Epsztein, Institut National de la Santé et de la Recherche Médicale (INSERM), France

Reviewed by:
Maxime Assous, Rutgers, The State University of New Jersey, United States
Agnès Baude, Institut National de la Santé et de la Recherche Médicale (INSERM), France

***Correspondence:**
Heinz Beck
heinz.beck@ukbonn.de

Received: *27 November 2019*
Accepted: *30 March 2020*
Published: *27 April 2020*

Citation:
Müller-Komorowska D, Opitz T, Elzoheiry S, Schweizer M, Ambrad Giovannetti E and Beck H (2020) Nonspecific Expression in Limited Excitatory Cell Populations in Interneuron-Targeting Cre-driver Lines Can Have Large Functional Effects. Front. Neural Circuits 14:16. doi: 10.3389/fncir.2020.00016

Transgenic Cre-recombinase expressing mouse lines are widely used to express fluorescent proteins and opto-/chemogenetic actuators, making them a cornerstone of modern neuroscience. The investigation of interneurons in particular has benefitted from the ability to genetically target specific cell types. However, the specificity of some Cre driver lines has been called into question. Here, we show that nonspecific expression in a subset of hippocampal neurons can have substantial nonspecific functional effects in a somatostatin-Cre (SST-Cre) mouse line. Nonspecific targeting of CA3 pyramidal cells caused large optogenetically evoked excitatory currents in remote brain regions. Similar, but less severe patterns of nonspecific expression were observed in a widely used SST-IRES-Cre line, when crossed with a reporter mouse line. Viral transduction on the other hand yielded more specific expression but still resulted in nonspecific expression in a minority of pyramidal layer cells. These results suggest that a careful analysis of specificity is mandatory before the use of Cre driver lines for opto- or chemogenetic manipulation approaches.

Keywords: Cre mouse line, cell-type specificity, optogenetics, interneuron, somatostatin, hippocampus, CA3

INTRODUCTION

Transgenic Cre-recombinase expressing mouse lines are widely used in modern neuroscience to specifically direct the expression of fluorescent proteins or opto- and chemogenetic actuators to neuronal subtypes. Accordingly, they are a key element of most neuronal perturbation studies. Cre driver mouse lines have been extensively used to examine the function of interneuron subtypes *in vitro* and *in vivo*, with increasing numbers of Cre mouse lines for specific molecular markers of different interneuron subtypes (Taniguchi et al., 2011). Very commonly used are mice expressing Cre in subsets of GABAergic interneurons under the parvalbumin (PV) or somatostatin (SST) promoters. Those lines have allowed us to target two main categories of interneurons. In the

hippocampus, PV^+ cells include fast-spiking basket cells, axo-axonic cells, and interneuron types targeting proximal dendrites of pyramidal cells. SST^+ cells, on the other hand, are regularly spiking and inhibit pyramidal cells at their distal dendrites (Lovett-Barron et al., 2012; Pelkey et al., 2017).

Commonly used Cre-lines have been widely assumed to be specific, with Cre-expression confined to the cells of interest. However, this assumption has been called into question in some cases. For example, in the widely used somatostatin–IRES-Cre line (SST-IRES-Cre, Taniguchi et al., 2011), a population of 5% of Cre-reporter positive cells were found to be fast-spiking PV^+ cells (Hu et al., 2013). In the hippocampal CA1 subfield, this mouse line also targets a small (6%) population of fast-spiking interneurons as well as several putative pyramidal cells (Mikulovic et al., 2015). Opto- and chemogenetic studies in particular often depend on highly specific expression patterns to disseminate the function of neuronal subtypes. Even though these findings are worrisome, one defense of such mouse lines is that the absolute number of nonspecifically targeted cells is small. One could therefore assume that the observed *in vitro* and *in vivo* effects are dominated by the interneuron type in question.

Here we show that in SST-Cre mice (Savanthrapadian et al., 2014), recombination is not only induced in GABAergic interneuron types. Also, recombination occurs in a small subset of excitatory neurons largely confined to the CA3 pyramidal cell layer. Moreover, we find powerful functional effects of optogenetic activation that are not only contaminated by nonspecifically expressing glutamatergic cells but are completely lacking any interneuron contribution. Finally, we were also unable to find anatomical or functional differences between nonspecifically targeted cells and canonical CA3 pyramidal cells. This suggests that these cells are not a specific subtype of CA3 pyramidal cells. Further control experiments should be carried out in a region-specific manner, before using Cre-lines for the investigation of circuit function in behavior.

MATERIALS AND METHODS

Transgenic Animals

All animal experiments were carried out according to the guidelines stated in Directive 2010/63/EU of the European Parliament on the protection of animals used for scientific purposes and were approved by authorities in Nordrhein-Westfalen (Landesamt für Natur, Umwelt und Verbraucherschutz Nordrhein Westfalen (LANUV), AZ 84-02.04.2014.A254).

The SST-Cre mouse line (C-SST^{tm1Npa}) was kindly provided to us by Marlene Bartos and was described previously (Savanthrapadian et al., 2014). We hereafter refer to this line as the SST-Cre mouse line. In brief, the SST-Cre mice were generated by knocking NLS-Cre into the endogenous SST gene (Dinkel et al., 1999). The line was maintained by backcrossing with C57B6/N mice. Animals were bred heterozygously and were genotyped for Cre recombinase using the forward primer CCATCTGCCACCAGCCAG and the reverse primer TCGCCATCTTCCAGCAGG. Animals with an amplified fragment at 281 bp were classified as transgenic. For the cross-breeding experiments (**Figure 6F**), we used the Ai14 reporter line (Jackson Laboratories Stock No. 007914).

B6N.Cg-*Sst*$^{tm2.1(cre)Zjh}$/J mice (SST-IRES-Cre, stock number 018973, The Jackson Laboratory) express Cre recombinase (IRES-Cre-pA cassette) in the 3′UTR of the Somatostatin locus (Taniguchi et al., 2011). We consistently refer to this line as the SST-IRES-Cre mouse line. These mice were crossbred to B6.Cg-Tg(APPswe, PSEN1dE9) 85Dbo/Mmjax (Jankowsky et al., 2004) mice and only Cre heterozygous offspring were used for experiments. Mice used in this study were negative for the APP/PS1 transgene. The wild type C57BL/6J animals were negative for both the APP/PS1 gene and SST-Cre. Mice were genotyped for SST-IRES-Cre with the following primers: GGGCCAGGAGTTAAGGAAGA; TC TGAAAGACTTGCGTTTGG and TGGTTTGTCCAAAC-TC ATCAA. We genotyped for the APP/PS1 gene using AA TAGAGAACGGCAGGAGCA; GCCATG-AGGGCACTAATC AT; CTAGGCCACAGAATTGAAAGATCT; GTAGGTGGAA-ATTCTAGCATCATCCW.

Stereotaxic Intracranial Viral Injections

Animals were anesthetized with a ketamine/rompun or a fentanyl/midazolam/medetomidine mixture i.p. Animals also received ketoprofen analgesia (5 mg/kg, 0.1 ml/10 g body weight) before the surgery and daily 2 days after the surgery. Viral particles (250 nl at a rate of 100 nl/min) were injected into CA3/hilus of the right hemisphere at the following coordinates relative to Bregma: 2.3 mm posterior; 1.6 mm lateral (1.75 for SST-IRES-Cre animals); 2.5 mm ventral. We used rAAV1/2-Ef1a-DIO-hChR2(H134R)-EYFP-WPRE-pA (received as a gift from Karl Deisseroth, Addgene plasmid # 20298; http://n2t.net/addgene:20298; RRID:Addgene_20298) for Cre-mediated opsin expression, AAV1/2-Ef1a-DIO-Syp-miniSOG-t2A-mCherry-WPRE-hPa (received as a gift from Roger Tsien; Shu et al., 2011) for electron microscopy experiments and AAV1/2.Syn-hChR2(H134R)-EYFP (received as a gift from Karl Deisseroth, Addgene plasmid # 26973; http://n2t.net/addgene:26973; RRID:Addgene_26973) for general expression. Cholera Toxin subunit B (CT-B, 50 nl), Alexa Fluor 555 conjugate (C-34775, Thermo Fischer) was injected into CA1 at Bregma coordinates: 1.9 mm posterior; 1.5 mm lateral; 1.7 ventral. Mice were used for electrophysiological experiments 4–5 weeks after viral injection.

Somatostatin Immunostaining and Colocalization Analysis

Animals were transcardially perfused with 4% PFA and the brains were post-fixed with 4% PFA overnight at 4°C. The brains were washed in PBS the next day and slices of the dorsal hippocampus were cut on a vibratome (HM 650V; Thermo Scientific) at 50 μm. Acute 300 μm slices were postfixed for 1 h in 4% PFA. After washing, slices were left in a blocking solution, consisting of 3% BSA in 0.25% PBS-T, for 2 h at room temperature (RT). Then the primary antibody, rabbit anti-SST (T-4102, Peninsula Laboratories International), was applied 1:500 in blocking solution overnight shaking at 4°C.

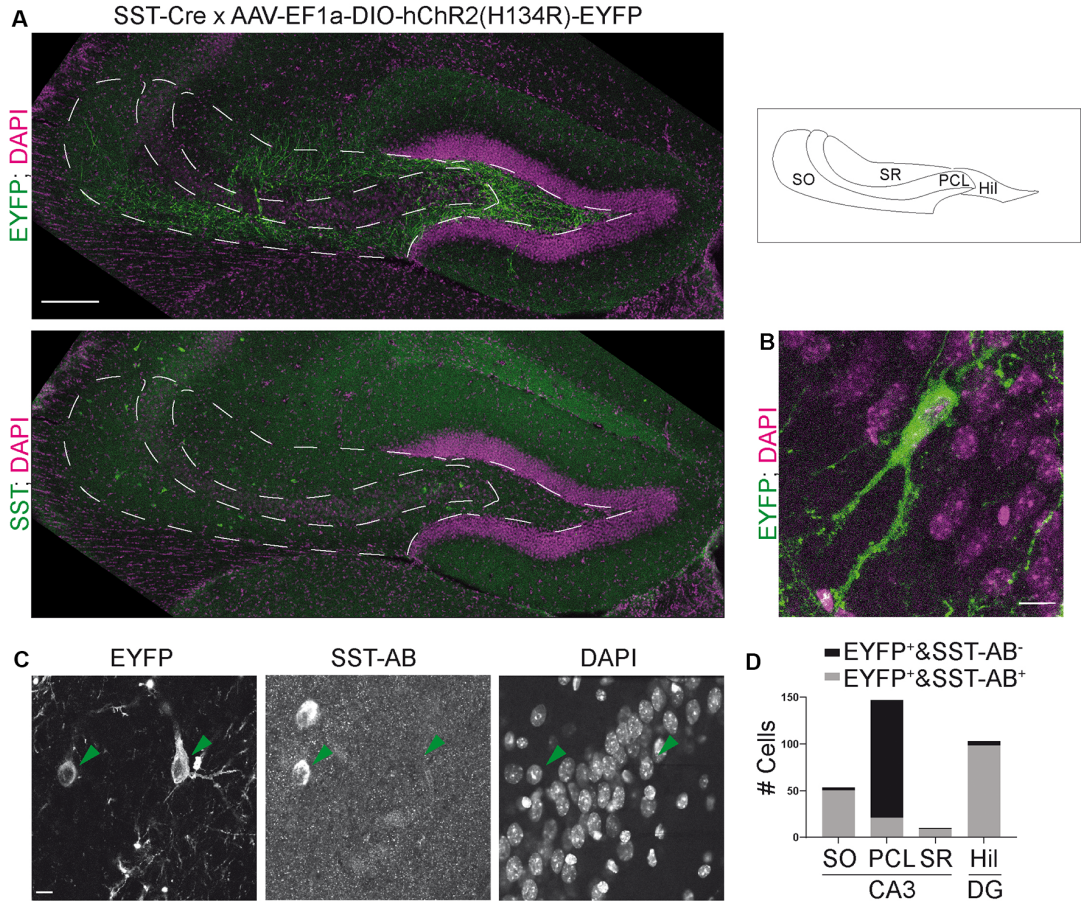

FIGURE 1 | The somatostatin-Cre (SST)-Cre line is not specific for SST$^+$ interneurons in CA3. **(A)** CA3 and the hilus of the dentate gyrus were virally transduced by intracranial stereotactic injection with a Cre dependent, enhanced yellow fluorescent protein (EYFP) expressing construct. Lower image shows SST staining in the same slice. 10× objective. Scale bar: 200 μm. Contrast adjusted for visualization. **(B)** EYFP$^+$ cell in CA3 pyramidal cell layer (PCL) and two apical dendrites in stratum lucidum. Scale bar: 10 μm. **(C)** Example images showing two EYFP$^+$ cells, one in stratum oriens (SO) and one in the PCL. The cell in SO is also SST positive, the cell in the PCL is SST negative. 40× magnification. Scale bar: 10 μm. **(D)** Quantification of SST colocalization from 40× images in six slices of five animals. Two of those were 300 μm thick acute slices.

The following day slices were left at RT for 30 min and washed in a blocking solution. The secondary antibody, donkey anti-rabbit IgG, Alexa fluor 647 (ab150075, Abcam), was applied 1:500 overnight shaking at 4°C. Finally, slices were washed, stained with 1:1,000 DAPI for 30 min at RT shaking and mounted with aqua-poly mount. The SST staining for the cholera toxin-B (CT-B) injected animals followed a slightly different protocol where slices were blocked with 5% donkey serum instead of BSA and the secondary antibody was donkey anti-rabbit IgG FITC 1:500 (ab6798, Abcam).

For colocalization, 40× confocal images were taken with a Leica SP8 confocal microscope. Enhanced yellow fluorescent protein (EYFP) positive cells were sought out in dentate gyrus and CA3. Colocalization was quantified manually by inspecting signals in the SST channel at the somatic localization of the EYFP signal. **Figure 1C** shows representative examples for both SST colocalizing and non-colocalizing cells. Automatic quantification was not feasible because the eYFP neuropil signal did not allow automatic soma segmentation. Overview image (**Figures 5A,B**) was taken on a spinning-disk microscope.

In vitro Electrophysiology

Adult mice were anesthetized with isofluorane, rapidly decapitated and the dissected brains were transferred to ice-cold, carbogenated artificial cerebrospinal fluid with sucrose (ACSF; in mM: NaCl, 60; sucrose, 100; KCL, 2.5; NaH_2PO_4, 1.25; $NaHCO_3$, 26; $CaCl_2$, 1; $MgCl_2$, 5; glucose, 20; from Sigma-Aldrich) and sliced to 300 μm. Slices were then transferred to ACSF at 37°C and left for 20 min. They were then transferred to carbogenated ACSF without sucrose (NaCl, 125; KCL, 3.5; NaH_2PO_4, 1.25, $NaHCO_3$, 26; $CaCl_2$, 2; $MgCl_2$, 2; glucose, 20; from Sigma-Aldrich) and were used for experiments after at least 1 h at RT. All experiments were performed in the same ACSF without sucrose at RT. The intracellular solution for voltage-clamp experiments contained in mM: Cs methanesulfonate, 120; $MgCl_2$, 0.5; 2-(4-(2-Hydroxyethyl)-

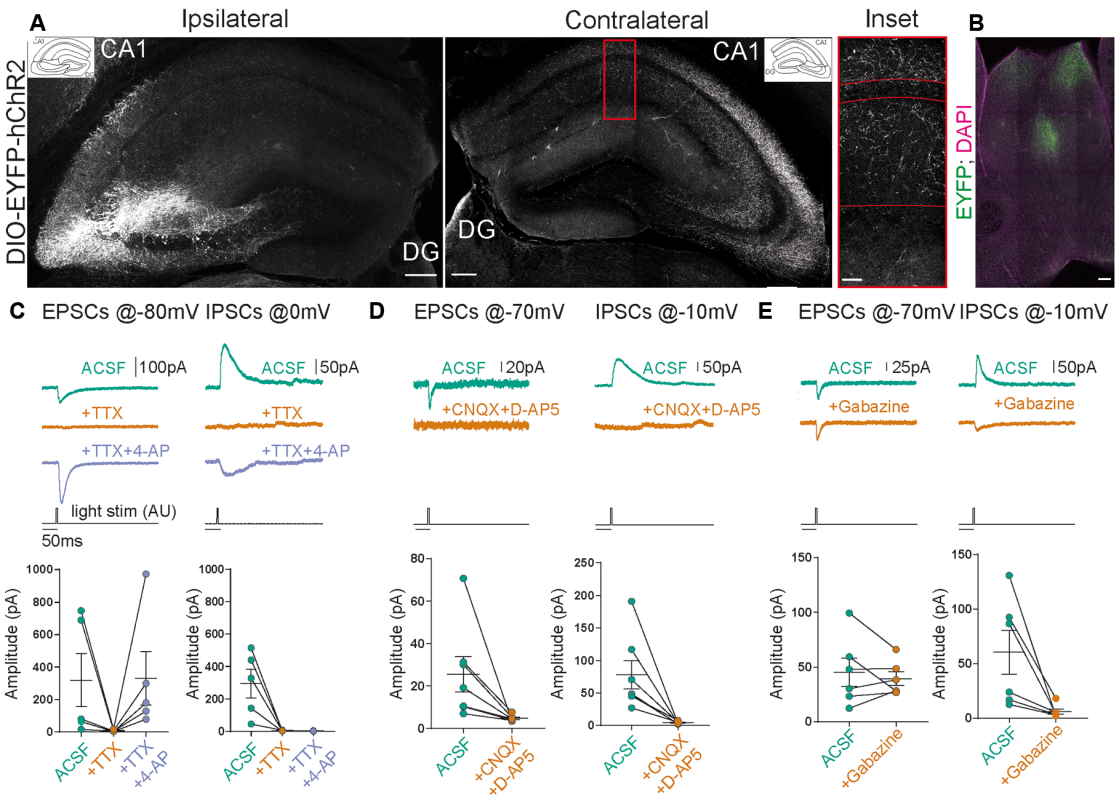

FIGURE 2 | Stimulation of contralateral projections of CA3 neurons in the SST-Cre mouse line. **(A)** Confocal images from post-fixed acute slices of the ipsilateral injection site (left) and the contralateral hippocampus (right). The inset shows the fluorescent fiber signal in the contralateral hemisphere. Scale bars: 200 μm; inset: 20 μm. **(B)** Slice showing the projection from CA3 to the septum in the SST-Cre line. Scale bar: 100 μm. **(C–E)** Excitatory postsynaptic currents (EPSCs) and inhibitory postsynaptic currents (IPSCs) measured in contralateral CA1 pyramidal cells. Light stimulus is 5 ms long with 26 mW total light-fiber output. **(C)** The application of tetrodotoxin (TTX) alone abolished both excitatory and inhibitory currents. However, the co-application of TTX+4-AP recovered EPSCs but not IPSCs in all except one cell. Ratio *t*-test of dependent samples between artificial cerebrospinal fluid with sucrose (ACSF) and +TTX+4-AP one-tailed: EPSCs, $p = 0.1412$, $t = 1.241$; IPSCs, $p < 0.0001$, $t = 13.18$; $n = 5$ cells from three animals. **(D)** The application of CNQX+D-AP5 abolishes both EPSCs and IPSCs. Ratio *t*-test of dependent samples one-tailed: EPSCs, $p = 0.0017$, $t = 4.681$; IPSCs, $p < 0.0001$, $t = 8.082$; $n = 7$ cells from four animals. **(E)** The application of Gabazine does not affect EPSCs but inhibits IPSCs. Ratio *t*-test of dependent samples one-tailed: EPSCs, $p = 0.4818$, $t = 0.04799$; IPSCs, $p = 0.0021$, $t = 4.947$; $n = 6$ cells from three animals. All responses were recorded at 26 mW fiber output.

1-piperazinyl)-ethansulfonsäure (HEPES), 5; Ethylenglycol-bis(aminoethyl ether)-N, N,N′,N′-tetraessigsäure (EGTA), 5; Adenosine 5′-triphosphate disodium salt (Na_2-ATP), 5; N-(2,6-Dimethylphenylcarbamoylmethyl)triethylammonium chloride (QX 314 Cl^-), 5; from Sigma Aldrich. For pharmacology, we furthermore used 10 μM gabazine (SR 95531 hydrobromide; Tocris), 1 μM tetrodotoxin (TTX, Tocris), 200 μM 4-aminopyridine (4-AP, Sigma Aldrich), 50 μM 6-Cyano-7-nitroquinoxaline-2,3-dione disodium salt (CNQX, Tocris), 200 μM D-(-)-2-Amino-5-phosphonopentanoic acid (D-AP5, Tocris). All these compounds were applied in the recording chamber for at least 10 min before continuing measurements. Most were applied for 20 min.

Patch-clamp experiments were performed with an Axopatch 200B and digitized on a Digidata 1322A or Digidata 1550B plus HumSilencer (Molecular Devices). Light stimulation was performed with an Omicron Luxx 473 nm laser attached to a light fiber submerged in the ACSF. Light stimuli were 5 ms long unless otherwise stated.

For the conductance analysis, we assumed a chloride reversal potential of −80 mV (−78.9 mV calculated with Nernst equation) and a cation reversal potential of 0 mV. The excitatory conductance was calculated from a current trace measured at a holding voltage near the chloride reversal with gabazine washed-in, to ensure pure excitatory response. To isolate the inhibitory conductance, we subtracted the pure excitatory response at a depolarized holding voltage from the mixed response in normal ACSF.

In **Figure 2C** we only included cells that showed complete block by TTX wash-in. We excluded one cell that did not show a complete block, which is likely due to a wash-in failure.

Electron Microscopy With miniSOG Photooxidation

SST-Cre animals were virally transduced with AAV1/2-Ef1a-DIO-Syp-miniSOG-t2A-mCherry-WPRE-hpA. Three weeks later, mice were transcardially perfused with Ringer solution followed by 4% formaldehyde in 0.15 M cacodylate-buffer. Brains

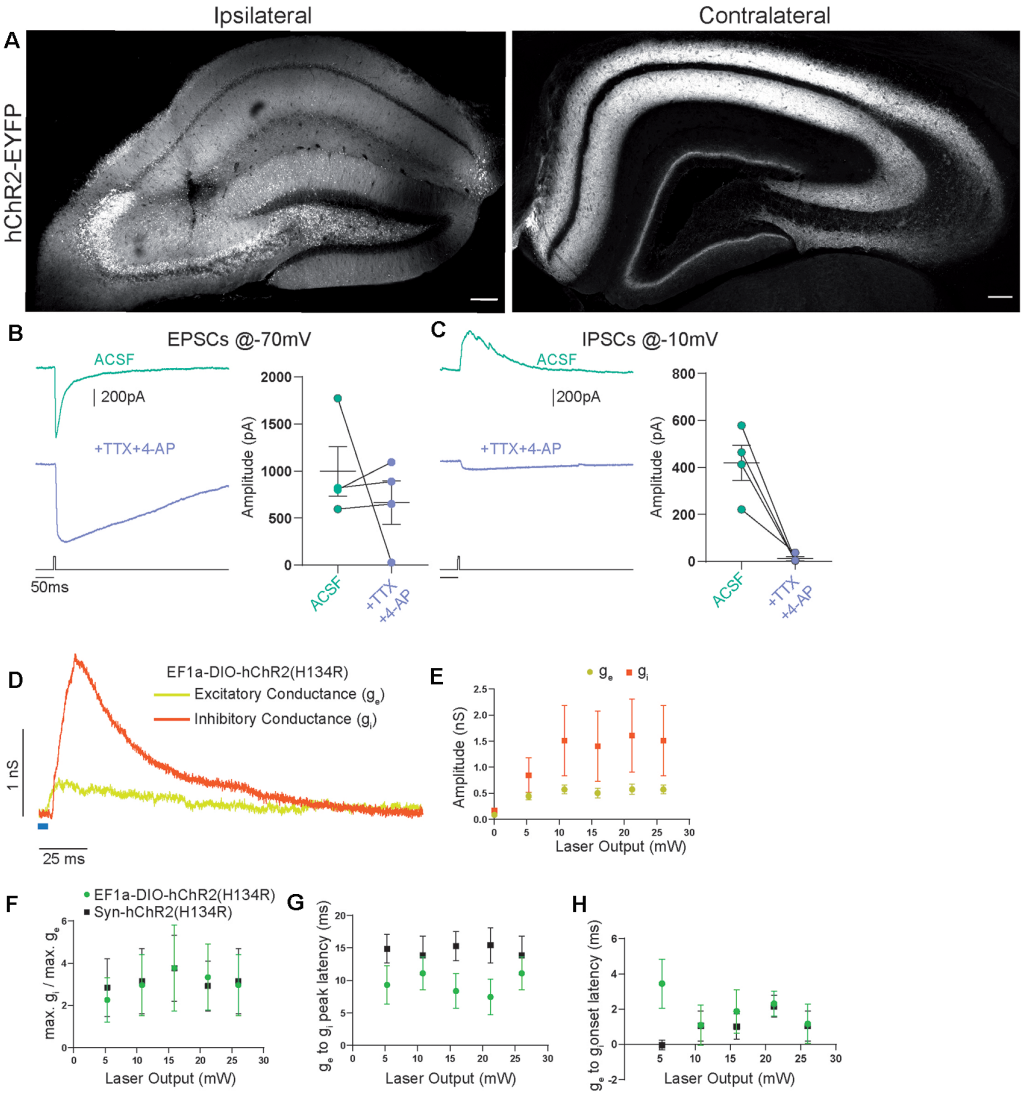

FIGURE 3 | Contralateral projections originating from Cre-expressing cells in CA3 vs. the general CA3 neuron population are functionally indistinguishable. **(A)** Confocal images from post-fixed acute slices of the ipsilateral injection site (left) and the contralateral hippocampus (right). Unconditional viral expression. **(B)** EPSCs and **(C)** IPSCs (right) before and after bath application of TTX and 4-AP measured in contralateral CA1 pyramidal cells. 5 ms light stimulation at 26 mW fiber output. Ratio *t*-test of dependent samples one-tailed: EPSCs, $p = 0.2284$, $t = 0.8519$; IPSCs, $p = 0.0069$, $t = 5.200$, $n = 4$ cells from two animals. **(D)** Example from conductance analysis of fibers in the SST-Cre mouse line, conditionally expressing. Twenty-six microwatt light fiber output and 5 ms light stimulation. Excitatory conductance was calculated from gabazine traces. Inhibitory conductance was calculated from gabazine subtracted traces. **(E)** Quantification of excitatory and inhibitory peak conductance at different laser powers. 2-way ANOVA Greenhouse-Geisser corrected: main effects, Laser Output: $p = 0.0422$, $DF = 5$, $F_{(1.182,7.091)} = 5.849$, Conductance Type: $p = 0.2189$, $DF = 1$, $F_{(1.000,6.000)} = 1.885$. Interaction: $p = 0.2527$, $DF = 5$, $F_{(1.115,6.693)} = 1.600$. $n = 6$ cells from three animals, same as EF1a-DIO-hChR2(H134R) in **(F–H)**. **(F)** Quantification of conductance ratios (inhibitory peak conductance divided by excitatory peak conductance) for conditional viral expression (EF1a-DIO-hChR2(H134R)) and unconditional expression (Syn-hChR2(H134R)). 2-way ANOVA Greenhouse-Geisser corrected: main effects, Laser Output: $p = 0.1406$, $DF = 4$, $F_{(1.393,15.33)} = 2.341$, Expression Type: $p = 0.9614$, $DF = 1$, $F_{(1,11)} = 0.002455$. Interaction: $p = 0.7974$, $DF = 4$, $F_{(4,44)} = 0.4143$. **(G)** Quantification of latency between excitatory peak conductance and inhibitory peak conductance. 2-way ANOVA Greenhouse-Geisser corrected: main effects: Laser Output: $p = 0.6446$, $DF = 4$, $F_{(1.720,18.92)} = 0.4014$, Expression Type: $p = 0.1766$, $DF = 1$, $F_{(1,11)} = 2.085$. Interaction: $p = 0.0320$, $DF = 4$, $F_{(4,44)} = 2.912$. **(H)** Quantification of latency between excitatory conductance onset and inhibitory conductance onset. 2-way ANOVA Greenhouse-Geisser corrected: main effects, Laser Output: $p = 0.6474$, $DF = 4$, $F_{(2.306,25.37)} = 0.4853$, Expression Type: $p = 0.1759$, $DF = 1$, $F_{(1,11)} = 2.092$. Interaction: $p = 0.3588$, $DF = 4$, $F_{(4,44)} = 1.121$. EF1a-DIO-hChR2(H134R) $n = 6$ cells from three animals; Syn-hChR2(H134R) $n = 7$ cells from three animals.

were removed and post-fixed overnight at 4°C. Coronal slices (100 μm) were taken on a vibratome and slices with distinct mCherry fluorescence were chosen. Slices were fixed with 2% glutaraldehyde for 30 min, washed with ice-cold cacodylate-buffer, and blocked for 20 min in a solution containing 20 mM glycine, 10 mM KCN, and 20 mM aminotriazoline in cacodylate-buffer. For photooxidation, slices were immersed in freshly prepared and filtered (0.22 μm) 3,3'-diaminobenzidine (DAB)

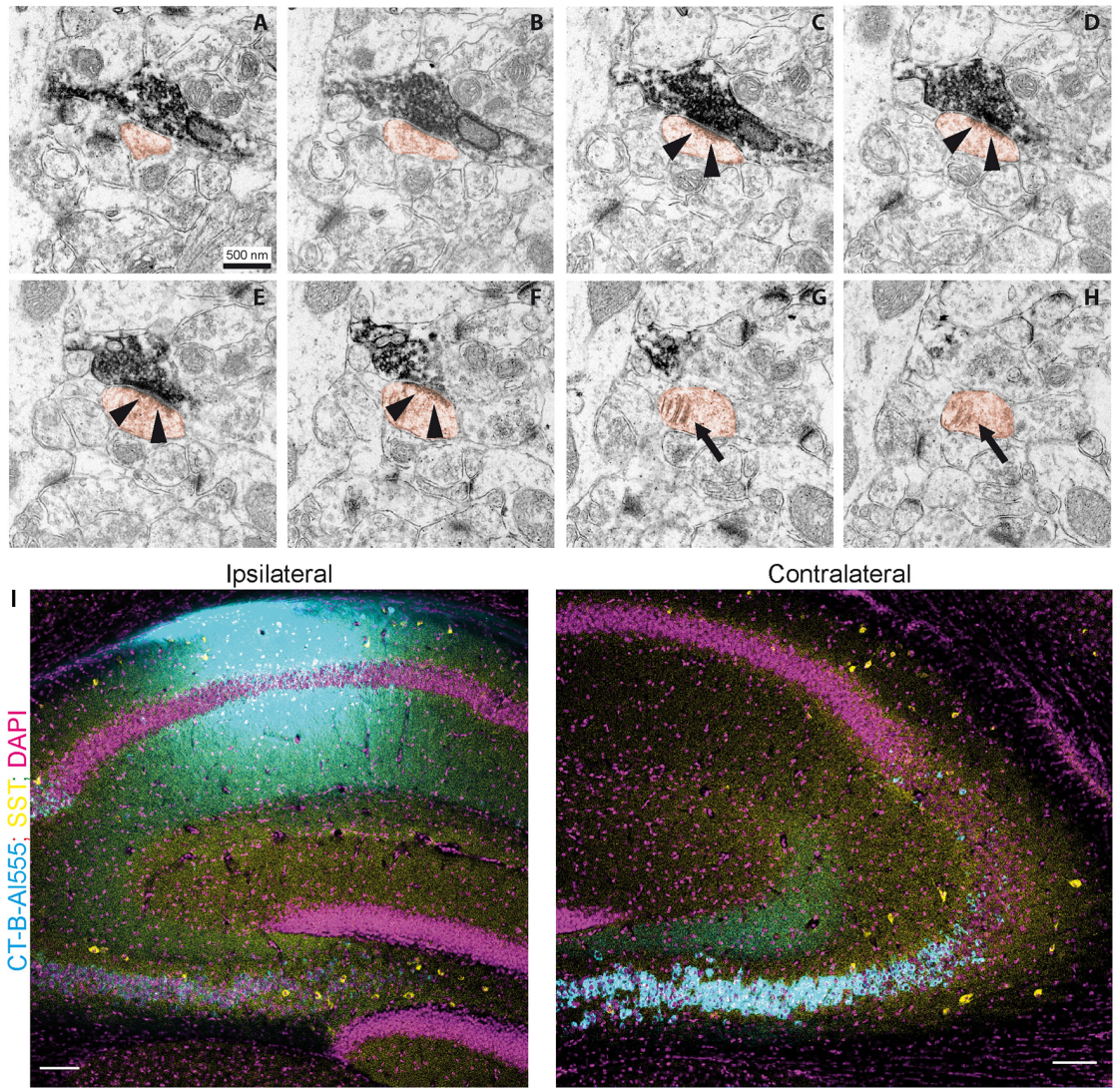

FIGURE 4 | Contralaterally projecting axons originating from Cre-expressing neurons in CA3 are excitatory. **(A–H)** miniSOG positive electron-dense structure making presynaptic contact on a spine (orange) in CA1 SO. Arrows in **(C–F)** show postsynaptic density. Arrows in **(G–H)** show the spine apparatus. Scale bar: 500 nm. **(I)** Cholera toxin-B tracing in CA1. Ipsilateral injection of CT-B subunit in CA1. Contralateral, retrogradely traced cells (cyan) and SST immunoreactive cells (yellow). Scale bar: 200 μm.

solution (1 mg/ml DAB in 0.1 M cacodylate-Buffer, pH 7.4) that was aerated with oxygen. The miniSOG was activated with a blue light (FITC filter set: EX470/40, DM510, BA520) applied through a LUMPlanFl 60 × NA 0.90 W at an inverted Olympus microscope equipped with a 100 W HBO-Lamp. Light was applied for 20 min and fresh DAB solution was exchanged after 10 min. After illumination, slices were stored in cacodylate-buffer for further processing.

After photoconversion, the converted region containing DAB reaction product in the hippocampus was documented and images were taken at a Zeiss Axiophot light microscope. Thereafter the sections were rinsed three times in 0.1 M sodium cacodylate buffer (pH 7.2–7.4; Sigma-Aldrich, Germany) and incubated with 1% osmium tetroxide (Science Services, Germany) in cacodylate buffer for 20 min on ice. The osmication of sections was followed by dehydration through ascending ethyl alcohol concentration steps and rinsing twice in propylene oxide (Carl Roth, Germany). Infiltration of the embedding medium was performed by immersing the sections first in a mixture of 2:1 of propylene oxide and Epon (Carl Roth, Germany) then in a 1:1 mixture and finally in neat Epon and polymerized at 60°C for 48 h. The region of interest was dissected and ultrathin sections (60 nm) were prepared with a Leica Ultracut UC7. Images were taken using an EM902 transmission electron microscope (Zeiss, Germany) equipped with a CCD in lens 2K digital camera and running the ImageSP software (Tröndle, Moorenweis, Germany).

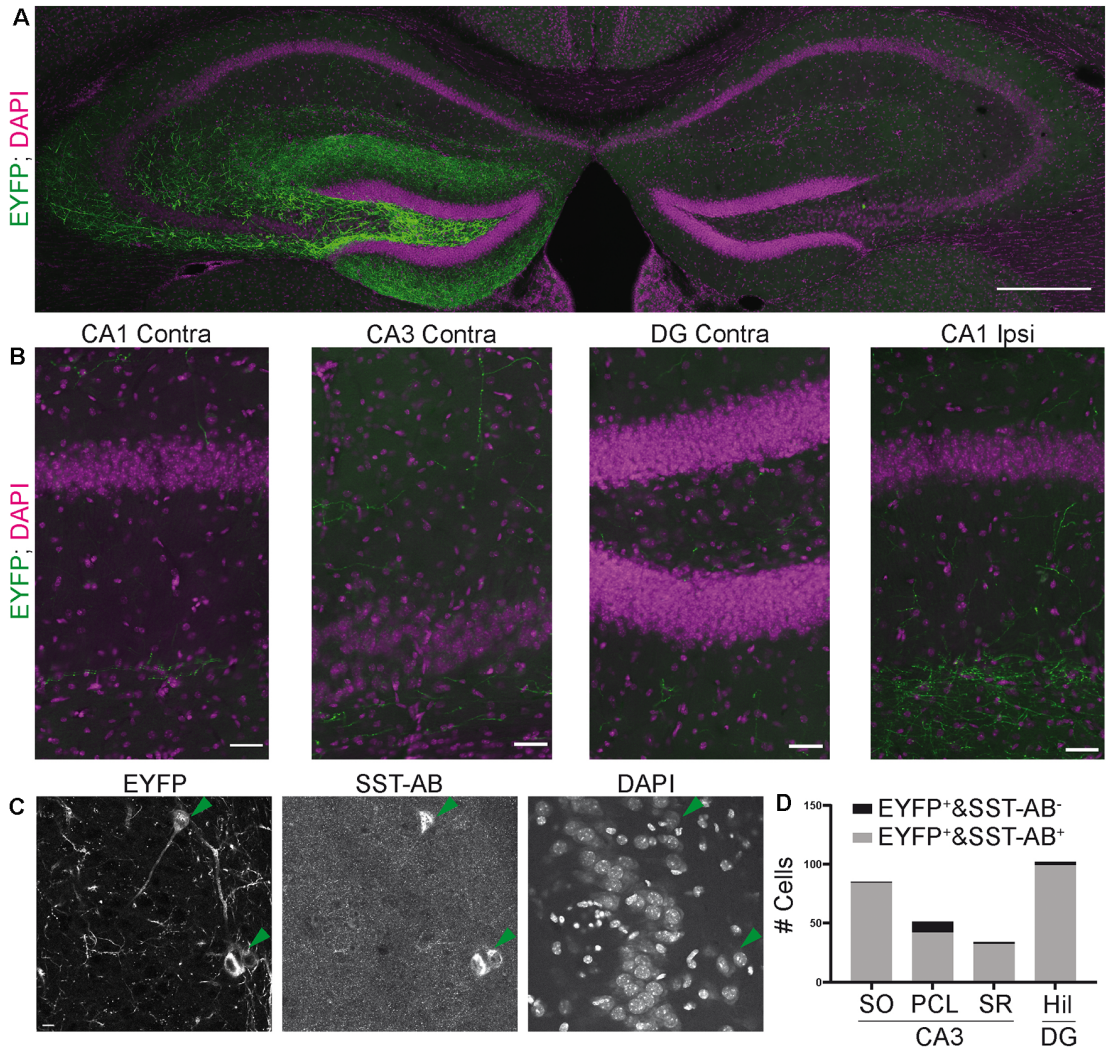

FIGURE 5 | Viral transduction in the SST-IRES-Cre line results in a more specific expression. **(A)** Overview image of the ipsilateral injection site (left) and contralateral hemisphere. Virtually no contralateral fibers were observed (compare with **Figure 2A**). Mosaic merge, 20× magnification. Scale bar: 200 μm. **(B)** Enlarged views from **(A)** showing the lack of contralateral fiber signal. Even in ipsilateral CA1, fiber signal is constrained to stratum lacunosum moleculare, as would be expected from OLM-interneuron specific labeling. Scale bar: 20 μm. **(C)** Image of EYFP positive cells in CA3 SO. 40× magnification confocal microscope. Scale bar: 10 μm. **(D)** Quantification of EYFP and SST positive cells, 15 slices from six SST-IRES-Cre animals.

Quantification and Statistical Analysis

We used Python with Matplotlib (Hunter, 2007) and GraphPad Prism for plotting. Electrophysiological data were analyzed manually in Clampfit (Molecular Devices) or with python and NumPy (van der Walt et al., 2011). To load .abf files into python we used the python-neo package (Garcia et al., 2014). GraphPad Prism was used for statistical analysis. We used the *t*-test to compare 2 groups and two-way ANOVA to compare two groups across multiple conditions.

For the quantification of the Allen Brain Institute data (Oh et al., 2014), we used the Allen Software Development Kit to download .jpg images. tdTomato positive cells were segmented by maximum entropy thresholding, erosion, dilation and the particle counter in ImageJ (Schindelin et al., 2012). Colocalization with fluorescent *in situ* hybridization probe was assessed manually. In total, we quantified 23 images of the dorsal hippocampus from four experiments (**Table 1**). A detailed technical description can be found in the Transgenic Characterization whitepaper: http://help.brain-map.org/display/mouseconnectivity/Documentation.

RESULTS

The SST-Cre Line Is Not Specific for SST⁺ Interneurons in CA3

Somatostatin (SST) positive interneurons in CA3 are located predominantly in stratum oriens (SO) and stratum radiatum (SR). SST positive cells have a characteristic dendrite morphology, with most of the dendritic arbor confined to

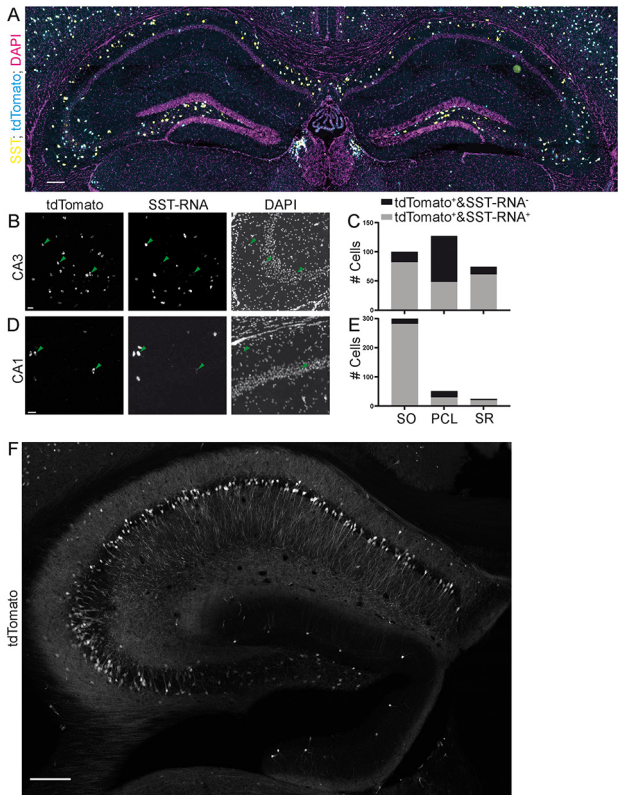

FIGURE 6 | Specificity of expression in SST-IRES-Cre mice achieved by crossing with a reporter mouse line. Images **(A,B,D)** from the Allen Brain Institute. The SST-IRES-Cre mouse line was crossed with the tdTomato reporter line Ai14. **(A)** Experiment 167643437, image ID 167643516. Contrast auto-adjusted and lookup tables changed. Scale bar: 100 μm. **(B–E)** Example images cropped from **(A)**, contrast unadjusted. Quantification on the right. Scale bar: 20 μm. **(F)** The SST-Cre mouse line crossed with the Ai14 reporter line. Scale bar: 200 μm.

the same sublayer as the soma (Freund and Buzsáki, 1996). We expressed a construct that leads to Cre-dependent expression of EYFP in the CA3 region of heterozygous SST-Cre mice using rAAV-dependent gene transfer. We found EYFP expression in cells of the pyramidal cell layer (PCL; **Figure 1A**). In SO and SR, cells also expressed EYFP but the signal there was almost dominated by the neuropil. EYFP$^+$ cells in the PCL showed features typical for CA3 pyramidal cells (**Figure 1B**) such as thorny excrescences on apical dendrites.

To determine if these EYFP$^+$ cells are also SST$^+$, we immunostained for SST. This revealed that EYFP expression was highly specific for SST$^+$ interneurons in SO, where 50/53 EYFP$^+$ cells expressed SST. Similarly, in SR 9/10 EYFP$^+$ cells expressed SST. In marked contrast, we found that a minority of EYFP$^+$ cells in the pyramidal cell layer of CA3 coexpressed SST (21/147 cells; **Figures 1C,D** data from six slices of five animals). Injection of the Cre-dependent virus into control animals lacking Cre-recombinase activity did not lead to EYFP expression (nine slices, three animals).

These results show that Cre recombinase is not only targeted to SST$^+$ interneurons in the adult hippocampus. It is also expressed in pyramidal-like neurons within the PCL that is devoid of detectable somatostatin levels, leading to the targeting of these cells even with viral gene transfer in adult animals. In contrast, the SST-Cre mouse line showed local specificity in CA3 SO, SR and the hilus of the dentate gyrus.

Commissural Projections Make Direct Excitatory Connections in Contralateral CA1

Does a relatively small number of CA3 neurons targeted in SST-Cre mice have a measurable functional impact on neuronal networks? CA3 pyramidal neurons are known to make extensive long-range connections to the contralateral hippocampus (Buzsáki and Czéh, 1981; Buzsáki and Eidelberg, 1982; Finnerty and Jefferys, 1993) and the septum (Risold and Swanson, 1997). We therefore examined if the small number of CA3 neurons targeted in SST-Cre mice is sufficient to generate detectable contralateral projections. Unilateral rAAV injection in the CA3 region of SST-Cre mice led to a strong axonal EYFP signal in the contralateral hippocampus (**Figure 2A**) and the septum (**Figure 2B**). The axon distribution was as described for CA3 pyramidal cells, with EYFP-expressing axons mainly in SO and SR of both the CA1 and CA3 regions.

Contralateral projections have been described not only for CA3 pyramidal neurons but also for inhibitory hippocampal interneurons including SST-expressing subtypes (Zappone and Sloviter, 2001; Eyre and Bartos, 2019). We, therefore, went on to further characterize the functional properties of contralaterally projecting axons, to assess: (i) if they correspond to excitatory projections arising from CA3 pyramidal neurons; and (ii) if they are sufficiently numerous to cause significant physiological effects. To this end, we obtained patch-clamp recordings from CA1 pyramidal neurons in mice expressing hChR2 in the contralateral CA3 region in SST-Cre mice. This allowed us to perform light-based stimulation of contralaterally projecting axons while recording from CA1 pyramidal neurons. To separate excitatory from inhibitory neurotransmission, we voltage-clamped CA1 neurons to different holding voltages. Currents

TABLE 1 | Experiments and images from the Allen Brain Institute used for the quantification in **Figures 6**, **7**.

Line	Experiment			Img ID			
SST-IRES-Cre	182530118	182530130	182530134	182530136	182530140	182530142	182530156
	167643437	167643500	167643502	167643504	167643514	167643516	
Pvalb-IRES-Cre	81657984	81636703	81636705	81636709	81636711	81636713	81636715
	111192541	111192610	111192612	111192625	111192627	111192629	

All images can be found here: http://connectivity.brain-map.org/transgenic.

at −80 or −70 mV were evoked close to the chloride reversal potential and are therefore dominated by excitatory postsynaptic currents (EPSCs), whereas currents evoked at 0 or −10 mV are dominated by inhibitory postsynaptic currents (IPSCs). In all CA1 pyramidal neurons, blue light illumination reliably evoked both excitatory and inhibitory currents (**Figures 2C–E**). To ascertain which of these components are monosynaptic, we applied the Na^+ channel blocker tetrodotoxin (TTX, 1 μM), which invariably blocked synaptic transmission completely. Coapplying TTX with 4-aminopyridine (4-AP, 200 μM) enables direct light-based transmitter release from terminals expressing ChR2, and thus indicates monosynaptic connections. Coapplication of 4-AP recovered EPSCs, but not IPSCs (**Figure 2C**; EPSCs 217%, IPSCs 1% of baseline). The recovery of EPSCs but not IPSCs indicates that contralateral projections in SST-Cre mice are excitatory. Additionally, these results indicate that the light-evoked IPSCs are due to polysynaptic recruitment of interneurons. This idea is supported by the temporal delay between excitatory and inhibitory conductances (**Figures 3G,H**). Consistent with polysynaptic recruitment of inhibitory interneurons, light-evoked IPSCs were abrogated by blocking glutamatergic transmission with CNQX (50 μM) and D-AP5 (200 μM; **Figure 2D**; EPSCs 29%, IPSCs 8% of baseline). Finally, we show that—as expected—light-evoked IPSCs were sensitive to the GABA-A blocker gabazine (10 μM; **Figure 2E**; EPSCs 114%, IPSCs 14% of baseline).

Taken together, we found no evidence for direct commissural inhibition from SST^+ interneurons from CA3 to CA1. Instead, direct excitatory transmission recruited strong polysynaptic inhibition.

Properties of Commissural Axons Targeted Unconditionally or in an SST-Cre Mouse Line Are Functionally Indistinguishable

To investigate if this is consistent with the canonical CA3 to CA1 commissural projection, we induced broad expression of ChR2 in all CA3 cell types using viral gene transfer of an unconditional construct leading to expression of EYFP-hChR2. Light-based manipulations should be dominated by the activity of pyramidal cells, since they vastly outnumber other neuronal subtypes. Virus injection resulted in a strong fluorescence signal in CA1, CA3, and DG that was dominated by fiber signal at the injection site (**Figure 3A**). Contralateral to the injection site, we found prominent labeling of axons in CA1 and CA3 in both SR and SO as well as the inner molecular layer of the DG. The DG fiber pattern was consistent with the commissural mossy cell projection and the fiber patterns in CA1 and CA3 with the commissural CA3 projection. We again assessed the monosynaptic transmission onto contralateral CA1 pyramidal cells using the combined application of TTX and 4-AP (1 μM, 200 μM) and found that it completely inhibited IPSCs (**Figures 3B,C**; EPSCs 88%, IPSCs 4% of baseline). Next, we asked if there are quantitative differences between the SST-Cre fibers and the unconditionally transduced fibers. We converted the pharmacologically isolated currents (**Figure 2E**) to conductances (**Figure 3D**) according to holding and reversal potentials (see "Materials and Methods" section). Because the density of EYFP-hChR2 positive fibers is much larger in the unconditional case, the absolute conductances cannot be compared meaningfully. However, because the inhibition is polysynaptic, it is expected to scale to some extent with the excitation. Therefore, the ratio between excitation and inhibition can give insights into differential recruitment in the micro-network.

We found that in the SST-Cre line, the inhibitory conductance was stronger than the excitatory one (**Figures 3D,E**). Comparing the SST-Cre line with the unconditional case, we did not detect a difference between the ratios of maximum inhibition and excitation (**Figure 3F**). In both cases, the amplitude of inhibition was larger than that of inhibition for different strengths of light-based stimulation. Furthermore, the latencies between the onset of excitation and inhibition showed no significant difference (**Figure 3H**) and were consistent with values found in CA3 to CA1 Schaffer collateral projections (Pouille and Scanziani, 2001). However, the latencies between the peak of the excitatory conductance and the inhibitory conductance showed a significant interaction between laser output and the type of expression. The main effects were not significant (**Figure 3G**, Greenhouse-Geisser corrected 2-way ANOVA).

Commissural CA3 Fibers Make Synaptic Contacts on Spines and Originate Primarily From PCL Cells

To further confirm that contralateral projections are excitatory, we used miniSOG photooxidation to generate electron-dense labeling in contralateral CA1 SO localized to fibers with Cre recombinase activity in the SST-Cre line (**Figure 4**). Of 70 miniSOG positive structures, 40 were presynaptic boutons making postsynaptic contacts. All 40 structures made contact on a spine, four of them made contact on two spines. Serial imaging sections of 25 boutons showed that 22 of them unambiguously made contact on spines (**Figures 4A–H**, quantification from two slices). The other three boutons were not entirely sectioned. The types of most synaptic contacts could not be defined clearly because of the electron-dense labeling in the pre-synapse. However, the postsynaptic densities that are clearly in the imaging plane appear asymmetric. Together with the fact that they all contact spines, this data suggests that the direct contacts are predominantly excitatory, and we found no evidence for direct inhibitory contacts in CA1 SO.

Next, we used retrograde tracing in CA1 with CT-B to determine which cell types project to contralateral CA1 (**Figure 4I**). We found that virtually all projecting cells were in the CA3 pyramidal cell layer. With the SST staining we identified 81 cells (12 slices from four animals), none of which was CT-B positive. This data suggests that somatostatin interneurons are not part of the commissural projection.

Finally, we related our findings to the more commonly used SST-IRES-Cre mouse line (Taniguchi et al., 2011). For this purpose, we used data from the Allen Brain Institute. We also virally injected SST-IRES-Cre animals for direct comparison of genetic and viral expression.

Viral Gene Transfer Leads to More Specific Expression Compared to the Use of Reporter Mouse Lines

Do these findings generalize to other, commonly used SST-Cre mouse lines? The SST-IRES-Cre line (Taniguchi et al., 2011) has been widely used, with 203 publications relating to it according to Jackson Laboratories (as of 11.10.2019). We therefore examined if viral transduction in adult SST-IRES-Cre animals also leads to nonspecific expression in non-SST expressing neurons. We found that viral gene transfer in SST-IRES-Cre mice led to a much more specific expression pattern in CA3 compared to the SST-Cre line. Labeling of contralaterally projecting axons was almost completely absent in the contralateral CA1 region. Few axons were present in the contralateral CA3 region and DG, potentially corresponding to DG interneuronal axons (**Figures 5A,B**). The fiber signal in the ipsilateral CA1 region was strongest in stratum lacunosum moleculare, as would be expected for SST positive oriens lacunosum moleculare cells. Somatostatin staining confirmed that viral expression is highly specific for somatostatin positive cells (**Figure 5C**). Quantification in 15 slices from 6 animals showed that 257/272 (94.5%) $EYFP^+$ cells were also SST positive. In the CA3 SO 84/85 (98.8%), in SR 32/34 (94.1%) and DG 99/102 (97.1%) of $EYFP^+$ cells were SST positive. In the CA3 PCL, the specificity was somewhat lower (42/51 cells, 82.4%), Thus, also in the SST-IRES-Cre mouse, specificity was least in the PCL of CA3, with almost 20% of neurons lacking SST expression. However, SST-IRES-Cre mice are more selective than SST-Cre mice following viral transduction.

Since many experimenters also breed Cre driver mouse lines with conditional mouse lines expressing fluorescent proteins or opto- or chemogenetic actuators, we also evaluated the specificity of both the SST-Cre or the SST-IRES-Cre line when they were crossed with the Ai14 tdTomato reporter mouse line. For the SST-IRES-Cre line, we used the Allen Brain Institute transgenic characterization data of the mouse connectome project (Oh et al., 2014). We used two experiments in which the SST-IRES-Cre mouse line was crossed with the Ai14 tdTomato reporter mouse line and fluorescent *in situ* hybridization (FISH) was performed for SST. We found that in these experiments, the SST-IRES-Cre mouse line is nonspecific in CA3, with only 48/127 (37.8%) $tdTomato^+$ cells being $SST\text{-}mRNA^+$ in the PCL, 82/100 (82%) in SO and 61/74 (82.4%) in SR (**Figures 6A–C**). The CA1 area also contained some SST- cells in the PCL but appeared overall more specific with 29/51 (56.9%) $tdTomato^+$ cells being SST-mRNA positive, 281/299 (94%) in SO and 20/24 (83.3%) in SR (**Figures 6A,D,E**). Thus, using breeding with reporter mouse lines, even the more specific SST-IRES-Cre mouse line lacks sufficient specificity, in particular in the subfield most affected in the SST-Cre mouse line.

We also crossed SST-Cre mice with Ai14 tdTomato reporter mice. This approach led to an even more unselective pattern of expression, with pyramidal-like tdTomato expressing cells in the PCL of CA3, but also the CA2 and CA1 subregions. We also found a very small number of granule cell-like neurons in the granule cell layer of the dentate gyrus (**Figure 6F**) that were not observed in virally transduced animals. Since this pattern was unselective, it was not further quantified.

Finally, we also assessed the quality of a third commonly used mouse line targeting PV containing interneurons. We quantified the colocalization of Cre-induced recombination with PV expression in the Pvalb-IRES-Cre mouse line (Hippenmeyer et al., 2005). We found that this mouse line was much more specific than both SST-Cre mouse lines in both the CA3 and CA1 regions (**Figures 7A–E**; CA3: 45/46, 97.8% SO; 112/112, 100% PCL; 26/26, 100% SR. CA1: 170/191, 89% SO; 284/294, 96.6% PCL; 29/34, 85.3% SR).

DISCUSSION

We show that CA3 PCs that are nonspecifically targeted in an SST-Cre mouse line (Savanthrapadian et al., 2014) make functional connections indistinguishable from those of canonical CA3 PCs. While the specificity of SST-Cre lines has been questioned before, the functional relevance of the nonspecific expression of Cre-recombinase was unknown. Estimating the potential effects of nonspecific expression is essential for neuronal perturbation studies that seek to isolate the function of specific cell-types. Our data suggest that studies that perturb SST cells in CA3 with the SST-Cre line would be massively confounded by Cre-recombinase expression in CA3 pyramidal cells. We also demonstrate that a commonly used SST-IRES-Cre line is more specific, but still exhibits low levels of nonspecific Cre expression in particular in specific subfields, in this case, the Ca3 pyramidal cell layer. We also show that crossing SST-Cre and SST-IRES-Cre mouse lines with a reporter mouse line leads to more extensive nonspecific expression compared to viral gene transfer. This may be due to the widespread activity of the SST promoter in non-SST interneurons during early development (Zingg et al., 1984; Lowe et al., 1987; Xiang et al., 2001). Additionally, the activity of the SST promoter may be regulated by neuronal activity (Gonzalez and Montminy, 1989).

An additional comparison is of interest: nonspecific Cre expression was more widespread in the SST-Cre compared to the SST-IRES-Cre mouse line. This was surprising as both Cre mouse lines were generated using a knockin strategy into the endogenous SST gene. However, the targeting strategy was different. While the SST-IRES-Cre mouse was generated by inserting an IRES-Cre cassette immediately after the STOP codon (Taniguchi et al., 2011), the SST-Cre mouse was generated by knocking NLS-Cre into the endogenous SST gene (Savanthrapadian et al., 2014). It is thus possible that these different targeting strategies, with a different relationship of the inserted gene sequence to the endogenous SST promoter, affect the expression pattern of Cre recombinase.

How Relevant Are These Findings for Other Cre Mouse Lines?

We demonstrate wide-spread physiological effects of nonspecific Cre-expression in the SST-Cre mouse line but have found anatomical evidence for a less pronounced nonspecific genetic expression in the SST-IRES-Cre mouse line. Indeed, specificity issues with an SST-IRES-Cre mouse line were raised previously

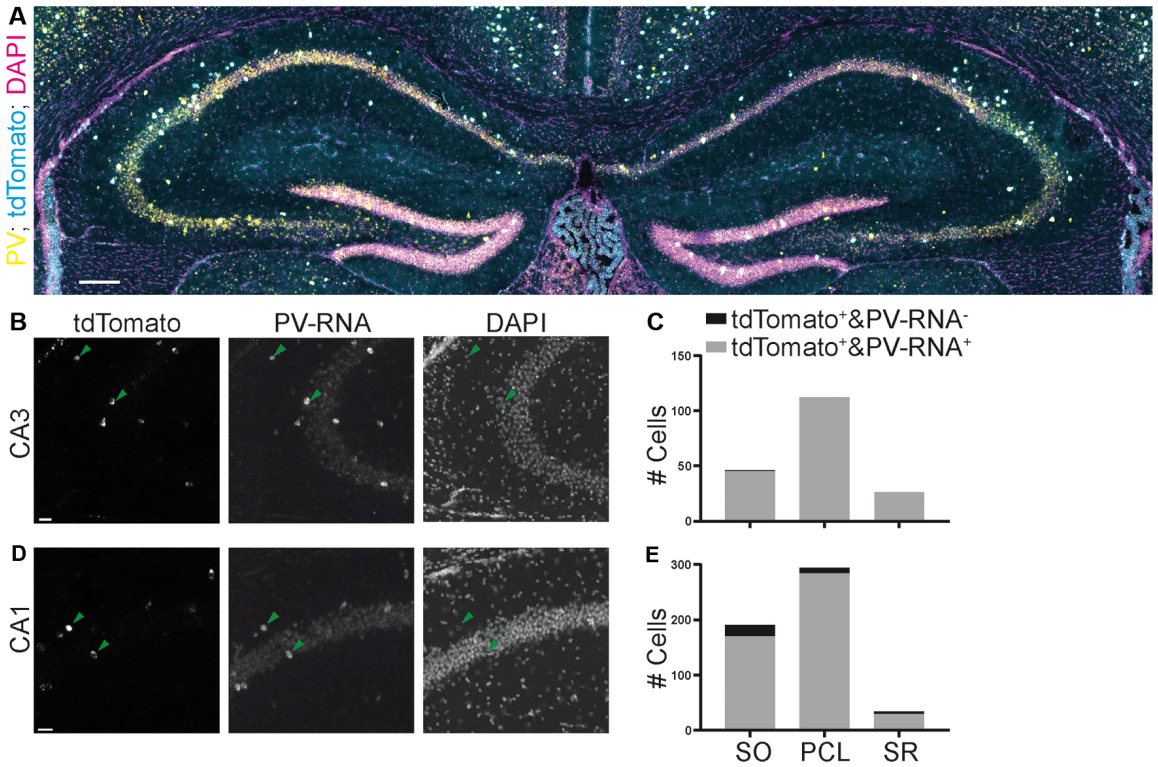

FIGURE 7 | Specificity of expression in a parvalbumin (PV)-Cre mouse line achieved by crossing with a reporter mouse line images **(A,B,D)** from the Allen Brain Institute. **(A)** Experiment 111192541, image ID 111192610. Contrast auto-adjusted and lookup tables changed. **(B–E)** Example images cropped from **(A)** contrast unadjusted. Quantification on the right. Scale bars: 100 and 20 μm.

(Taniguchi et al., 2011). Moreover, a further study has found targeting of a large number (31%) of slow-spiking cells in the CA1 PCL, also consistent with nonspecific genetic expression (Mikulovic et al., 2015). Specificity can vary widely between Cre lines and brain areas, as our comparison of the SST-IRES-Cre and the Pvalb-IRES-Cre lines shows. Therefore, specificity should not be generalized lightly to other Cre mouse lines or even to other brain areas in the same mouse line. We suggest that pending careful quantitative analysis in all the subregions under investigation in the specific study, caution is warranted in assuming specificity.

Do SST-Expressing Interneurons Make Contralateral Connections?

In addition to CA3 pyramidal cells, the SST-Cre mouse line targets SST^+ INs in CA3. We found that the projection of the contralateral CA1 region arises mainly from nonspecifically targeted pyramidal cells. We found no evidence for direct inhibition from SST^+ interneurons onto contralateral CA1 PCs in our patch-clamp experiments. Even slices with nonconditional ChR2 expression did not exhibit monosynaptic inhibition, despite all inhibitory cell types being targeted. Furthermore, our anatomical EM data showed no evidence for inhibitory synapses in contralateral CA1 SO. Finally, the CT-B data did not reveal cells outside CA3 PCL projecting to contralateral CA1. This leads us to the conclusion that an inhibitory CA3 to contralateral CA1 connection is extremely weak or nonexistent and SST^+ interneurons do not contribute to it.

Although we focused on the CA3 and CA1 subfields, we noted a very sparse fiber signal in the outer molecular layer of DG in the SST-Cre line. This is in line with previous anatomical evidence showing a commissural projection with a GABAergic component (Deller et al., 1995; Zappone and Sloviter, 2001). However, using *in vivo* patch-clamp and optogenetics we did not find evidence for a functional connection onto granule cells (data not shown).

Eyre and Bartos (2019) have also assessed interhemispheric connections of inhibitory interneurons using unilateral viral gene transfer in either GAD2-Cre and the SST-IRES-Cre mouse lines. In the SST-IRES-Cre mouse line, virus injection into the CA3 regions revealed a large number of cells in the CA3 PCL far exceeding cell numbers in CA3 stratum radiatum or oriens (see Eyre and Bartos, 2019; **Figure 2B**). This distribution of targeted cells in CA3 is reminiscent of the SST-Cre mouse line described in this article (**Figures 1A–D**, **2A**) and is not in line with our experiments in the SST-IRES-Cre line (**Figures 5A–D**). As the high number of CA3 PCL neurons in the SST-Cre mouse line was due mainly to neurons nonspecifically expressing Cre, this raises the disturbing possibility that with some viral injection protocols, even the SST-IRES-Cre mouse may display substantial

nonspecific expression patterns. In line with our findings, Eyre and Bartos (2019) did not find evidence for functional direct interhemispheric inhibitory connections in the hippocampal dentate gyrus.

The Utility of Mouse Lines With Nonspecific Principal Cell Expression for *in vivo* Experiments

A common use of Cre lines is circuit perturbation during behavioral tasks. Principal cell connections can span wide areas of the brain and must be accounted for when studying interneurons. When light is delivered to the brain through light fibers, it can travel considerable distances. Therefore, light delivered to areas where transgene expression is specific, could affect nonspecifically expressing cells and fibers in faraway areas. Notably, such effects cannot be excluded with a commonly used control group expressing only GFP (or another fluorophore) instead of a light-sensitive opsin. The same applies to a larger extent to chemogenetic experiments, where the agonist might be delivered systemically, rather than locally.

To ensure that principal cell expression does not confound a behavioral experiment, the colocalization between transgene expressing cells and the appropriate interneuron marker should be quantified for all areas where viral transduction occurred. This includes the injection cannula tract. When the transgene is expressed by crossing mouse lines, the expressing fiber distribution throughout the entire brain should be examined carefully. Especially for optogenetic experiments, it would be valuable to additionally check for direct excitatory synaptic transmission. For a specific mouse line, no direct excitatory currents should be detectable. Importantly, the net effect of a direct excitatory connection can be reduced spiking through recruitment of feedforward and feedback inhibition (Buzsáki and Czéh, 1981). Therefore, it is not sufficient to quantify spiking or activity levels in the post-synaptic population to exclude direct excitation. These issues should be considered when using any Cre-mouse line for *in vivo* behavioral experiments, particularly the SST-Cre mouse lines used in the present study.

DATA AVAILABILITY STATEMENT

Datasets are available on request. The raw data supporting the conclusions of this article will be made available by the authors, without undue reservation, to any qualified researcher.

ETHICS STATEMENT

The animal study was reviewed and approved by Landesamt für Natur, Umwelt und Verbraucherschutz Nordrhein Westfalen.

AUTHOR CONTRIBUTIONS

DM-K and HB designed the project and wrote the manuscript. DM-K performed viral injections, SST antibody stainings, patch-clamp recordings and quantification of Allen Brain Institute Data. TO performed viral injections for miniSOG and performed photooxidation. MS acquired EM images and quantified them. SE performed CT-B injections and SST antibody stainings in connection with them. EA performed SST-IRES-Cre experiments and wild type viral injections.

FUNDING

The study was supported by SFB 1089 and the SPP 2041 of the Deutsche Forschungsgemeinschaft to HB.

ACKNOWLEDGMENTS

We acknowledge the support of the Microscopy Core Facility of the University Bonn Medical Center, specifically Hannes Beckert, and the Viral Core Facility, specifically Susanne Schoch-McGovern. We thank Joanna Komorowska-Müller for helpful suggestions on the antibody staining protocol and figure design. We also thank Kristina Piwellek for excellent technical assistance with viral injections for miniSOG labeling. This manuscript has been released as a Pre-Print at https://www.biorxiv.org/content/10.1101/848655v1.

REFERENCES

Buzsáki, G., and Czéh, G. (1981). Commissural and perforant path interactions in the rat hippocampus. *Exp. Brain Res.* 43, 429–438. doi: 10.1007/bf00238387

Buzsáki, G., and Eidelberg, E. (1982). Convergence of associational and commissural pathways on CA1 pyramidal cells of the rat hippocampus. *Brain Res.* 237, 283–295. doi: 10.1016/0006-8993(82)90442-5

Deller, T., Nitsch, R., and Frotscher, M. (1995). Phaseolus vulgaris-leucoagglutinin dentate gyrus: evidence for a previously unknown commissural projection to the outer molecular layer. *J. Comp. Neurol.* 352, 55–68. doi: 10.1002/cne.903520105

Dinkel, A., Aicher, W. K., Warnatz, K., Bürki, K., Eibel, H., and Ledermann, B. (1999). Efficient generation of transgenic BALB/c mice using BALB/c embryonic stem cells. *J. Immunol. Methods* 223, 255–260. doi: 10.1016/s0022-1759(99)00005-8

Eyre, M. D., and Bartos, M. (2019). Somatostatin-expressing interneurons form axonal projections to the contralateral hippocampus. *Front. Neural Circuits* 13:56. doi: 10.3389/fncir.2019.00056

Finnerty, G. T., and Jefferys, J. G. R. (1993). Functional connectivity from ca3 to the ipsilateral and contralateral ca1 in the rat dorsal hippocampus. *Neuroscience* 56, 101–108. doi: 10.1016/0306-4522(93)90566-x

Freund, T. F., and Buzsáki, G. (1996). Interneurons of the hippocampus. *Hippocampus* 6, 347–470. doi: 10.1002/(sici)1098-1063(1996)6:4<347::aid-hipo1>3.0.co;2-i

Garcia, S., Guarino, D., Jaillet, F., Jennings, T., Pröpper, R., Rautenberg, P. L., et al. (2014). Neo: an object model for handling electrophysiology data in multiple formats. *Front. Neuroinform.* 8:10. doi: 10.3389/fninf.2014.00010

Gonzalez, G. A., and Montminy, M. R. (1989). Cyclic AMP stimulates somatostatin gene transcription by phosphorylation of CREB at serine 133. *Cell* 59, 675–680. doi: 10.1016/0092-8674(89)90013-5

Hippenmeyer, S., Vrieseling, E., Sigrist, M., Portmann, T., Laengle, C., Ladle, D. R., et al. (2005). A developmental switch in the response of DRG neurons to ETS transcription factor signaling. *PLoS Biol.* 3:e159. doi: 10.1371/journal.pbio.0030159

Hu, H., Cavendish, J. Z., and Agmon, A. (2013). Not all that glitters is gold: off-target recombination in the somatostatin-IRES-Cre mouse line

labels a subset of fast-spiking interneurons. *Front. Neural Circuits* 7:195. doi: 10.3389/fncir.2013.00195

Hunter, J. D. (2007). Matplotlib: a 2D graphics environment. *Comput. Sci. Eng.* 9, 90–95. doi: 10.1109/mcse.2007.55

Jankowsky, J. L., Fadale, D. J., Anderson, J., Xu, G. M., Xu, G. M., Gonzales, V., et al. (2004). Mutant presenilins specifically elevate the levels of the 42 residue β-amyloid peptide *in vivo*: evidence for augmentation of a 42-specific γ secretase. *Human Mol. Gen.* 13, 159–170. doi: 10.1093/hmg/ddh019

Lovett-Barron, M., Turi, G. F., Kaifosh, P., Lee, P. H., Bolze, F., Sun, X.-H., et al. (2012). Regulation of neuronal input transformations by tunable dendritic inhibition. *Nat. Neurosci.* 15, 423–430, S1–S3. doi: 10.1038/nn.3024

Lowe, W. L. Jr., Schaffner, A. E., Roberts, C. T. Jr., and Leroith, D. (1987). Developmental regulation of somatostatin gene expression in the brain is region specific. *Mol. Endocrinol.* 1, 181–187. doi: 10.1210/mend-1-2-181

Mikulovic, S., Restrepo, C. E., Hilscher, M. M., Kullander, K., and Leão, R. N. (2015). Novel markers for OLM interneurons in the hippocampus. *Front. Cell. Neurosci.* 9:201. doi: 10.3389/fncel.2015.00201

Oh, S. W., Harris, J. A., Ng, L., Winslow, B., Cain, N., Mihalas, S., et al. (2014). A mesoscale connectome of the mouse brain. *Nature* 508, 207–214. doi: 10.1038/nature13186

Pelkey, K. A., Chittajallu, R., Craig, M. T., Tricoire, L., Wester, J. C., and McBain, C. J. (2017). Hippocampal GABAergic inhibitory interneurons. *Physiol. Rev.* 97, 1619–1747. doi: 10.1152/physrev.00007.2017

Pouille, F., and Scanziani, M. (2001). Enforcement of temporal fidelity in pyramidal cells by somatic feed-forward inhibition. *Science* 293, 1159–1163. doi: 10.1126/science.1060342

Risold, P., and Swanson, L. (1997). Connections of the rat lateral septal complex. *Brain Res. Rev.* 24, 115–195. doi: 10.1016/s0165-0173(97)00009-x

Savanthrapadian, S., Meyer, T., Elgueta, C., Booker, S. A., Vida, I., and Bartos, M. (2014). Synaptic properties of SOM- and CCK-expressing cells in dentate gyrus interneuron networks. *J. Neurosci.* 34, 8197–8209. doi: 10.1523/JNEUROSCI.5433-13.2014

Schindelin, J., Arganda-Carreras, I., Frise, E., Kaynig, V., Longair, M., Pietzsch, T., et al. (2012). Fiji: an open-source platform for biological-image analysis. *Nat. Methods* 9, 676–682. doi: 10.1038/nmeth.2019

Shu, X., Lev-Ram, V., Deerinck, T. J., Qi, Y., Ramko, E. B., Davidson, M. W., et al. (2011). A genetically encoded tag for correlated light and electron microscopy of intact cells, tissues and organisms. *PLoS Biol.* 9:e1001041. doi: 10.1371/journal.pbio.1001041

Taniguchi, H., He, M., Wu, P., Kim, S., Paik, R., Sugino, K., et al. (2011). A resource of cre driver lines for genetic targeting of GABAergic neurons in cerebral cortex. *Neuron* 71, 995–1013. doi: 10.1016/j.neuron.2011.07.026

van der Walt, S., Colbert, S. C., and Varoquaux, G. (2011). The NumPy array: a structure for efficient numerical computation. *Comput. Sci. Eng.* 13, 22–30. doi: 10.1109/mcse.2011.37

Xiang, Z., Jiang, L., and Kang, Z. (2001). Transient expression of somatostatin mRNA in developing ganglion cell layers of rat retina. *Dev. Brain Res.* 128, 25–33. doi: 10.1016/s0165-3806(01)00145-6

Zappone, C. A., and Sloviter, R. S. (2001). Commissurally projecting inhibitory interneurons of the rat hippocampal dentate gyrus: a colocalization study of neuronal markers and the retrograde tracer Fluoro-Gold. *J. Comp. Neurol.* 441, 324–344. doi: 10.1002/cne.1415

Zingg, H. H., Goodman, R. H., and Habener, J. F. (1984). Developmental expression of the rat somatostatin gene. *Endocrinology* 115, 90–94. doi: 10.1210/endo-115-1-90

Conflict of Interest: The authors declare that the research was conducted in the absence of any commercial or financial relationships that could be construed as a potential conflict of interest.

5.3 Summary

We found that most cells that are transduced in the PCL are Sst-Ab negative. Contralateral fibers and excitatory postsynaptic currents in contralateral CA1 suggest that these cells are CA3 pyramidal cells. Fortunately, this nonspecific SST-Cre mouse line is not widely used and the more common SST-ires-cre mouse line appears to be more specific as far as Sst-Ab colocalization is concerned. However, our findings have important implications for the validation of Cre mouse lines.

The SST-Cre mouse line was considered Sst specific. This is probably due to the fact that it was primarily validated in the DG, where nearly all expressing cells are indeed Sst-Ab positive. We were only able to find out that it is nonspecific because we specifically investigated the CA3 pyramidal cell layer. Mouse lines can be specific in one brain area but nonspecific in another. This means that mouse line validations should only be accepted when they are validated for the specific brain area and layer of interest.

Another crucial finding was the difference between genetic expression through a reporter mouse line and viral transduction. In the SST-Cre mouse line, nonspecific expression was more severe under genetic expression as opposed to viral. It is not clear whether this is a general rule or what the mechanism is. However, these findings suggest, that validations from one expression strategy do not necessarily transfer to another expression strategy.

Transgenic animals are useful if they are properly validated for their purpose because they allow for optogenetic control of a neuronal population. This kind of control can afford insights into the quantitative properties of neuronal circuits. In the following paper we describe some of the quantitative properties of feedback inhibition in the dentate gyrus. In a computational model we investigate these quantitative features in the context of pattern separation. Pattern separation important for precise memory formation during novelty behavior and our findings make predictions that can be tested in behavioral experiments.

6 Quantitative properties of a feedback circuit predict frequency-dependent pattern separation

6.1 Introduction

Feedback inhibition is found in many brain areas and species. It is driven by the principal cells of a microcircuit and inhibits those same principal cells. In this way, principal cells control their own activity, which is important to avoid overly excitable network states. Excitability is also relevant for pattern separation, a neuronal computation that helps with distinguishing similar patterns. A sparse network where few cells are active at a time and produce few action potentials is usually a good pattern separator. The dentate gyrus is known for pattern separation during behavioral tasks (Leutgeb et al., 2007) and its in vivo activity is sparse.

Feedback inhibition is particularly interesting for pattern separation because it has a complex temporal structure. We therefore incorporated frequency modulation into our model of the dentate gyrus inputs. We found that input patterns are better separated when they have a modulation frequency above 10Hz. This is behaviorally relevant because the input area of the dentate gyrus changes its population frequency and our model predicts that interfering with population frequencies above 10Hz would decrease performance during pattern separation dependent behaviors.

We furthermore found that the input frequency lost relevance for pattern separation when we removed feedback inhibition from our model. Importantly, we experimentally constrained the quantitative properties of feedback inhibition using in-vitro experiments. Removing feed-forward inhibition on the other hand had not effect on the frequency dependent component of pattern separation. These data predict that the two types of inhibition could have dissociable effects on pattern separation behaviors.

RESEARCH ARTICLE

Quantitative properties of a feedback circuit predict frequency-dependent pattern separation

Oliver Braganza[1]*, Daniel Mueller-Komorowska[1,2], Tony Kelly[1], Heinz Beck[1,3]*

[1]Institute for Experimental Epileptology and Cognition Research, University of Bonn, Bonn, Germany; [2]International Max Planck Research School for Brain and Behavior, University of Bonn, Bonn, Germany; [3]Deutsches Zentrum für Neurodegenerative Erkrankungen e.V., Bonn, Germany

Abstract Feedback inhibitory motifs are thought to be important for pattern separation across species. How feedback circuits may implement pattern separation of biologically plausible, temporally structured input in mammals is, however, poorly understood. We have quantitatively determined key properties of *net*feedback inhibition in the mouse dentate gyrus, a region critically involved in pattern separation. Feedback inhibition is recruited steeply with a low dynamic range (0% to 4% of active GCs), and with a non-uniform spatial profile. Additionally, net feedback inhibition shows frequency-dependent facilitation, driven by strongly facilitating mossy fiber inputs. Computational analyses show a significant contribution of the feedback circuit to pattern separation of theta modulated inputs, even within individual theta cycles. Moreover, pattern separation was selectively boosted at gamma frequencies, in particular for highly similar inputs. This effect was highly robust, suggesting that frequency-dependent pattern separation is a key feature of the feedback inhibitory microcircuit.

***For correspondence:**
oliver.braganza@ukbonn.de (OB);
heinz.beck@ukbonn.de (HB)

Competing interests: The authors declare that no competing interests exist.

Funding: See page 25

Received: 29 October 2019
Accepted: 20 January 2020
Published: 20 February 2020

Reviewing editor: Inna Slutsky, Tel Aviv University, Israel

Introduction

Efficiently discriminating similar percepts or experiences is a central capability common to invertebrate and vertebrate species. In general terms, such discrimination can be achieved by decreasing the overlap in representations by neuronal ensembles between input and output patterns, a process termed 'pattern separation' (***Cayco-Gajic and Silver, 2019***; ***Marr, 1971***; ***McNaughton and Morris, 1987***; ***Rolls, 2013***). Numerous studies have proposed cellular and circuit mechanisms that support this computation. For instance, sparse divergent inputs, specialized intrinsic properties and feedforward inhibition are thought to generally contribute (***Cayco-Gajic et al., 2017***; ***Cayco-Gajic and Silver, 2019***; ***Krueppel et al., 2011***; ***Mircheva et al., 2019***). Another common feature of most of these models and experimental studies is a critical role of feedback inhibition (***Cayco-Gajic et al., 2017***; ***Rolls, 2013***). Feedback circuits differ from the above mechanisms in that they can i) implement direct competition between active cells through lateral inhibition and ii) integrate information about the actual global activity level in a population allowing efficient normalization (***Braganza and Beck, 2018***; ***Wick et al., 2010***; ***Wiechert et al., 2010***). Indeed, in the insect olfactory system a critical role of such a circuit has been causally demonstrated (***Lin et al., 2014***; ***Papadopoulou et al., 2011***).

In mammals, substantial evidence points toward a role of the hippocampal dentate gyrus (DG) for pattern separation during memory formation and spatial discrimination (***Bakker et al., 2008***; ***Berron et al., 2016***; ***Gilbert et al., 2001***; ***Leal and Yassa, 2018***; ***Leutgeb et al., 2007***; ***McHugh et al., 2007***; ***Neunuebel and Knierim, 2014***; ***Stefanelli et al., 2016***; ***van Dijk and Fenton, 2018***). The DG is thought to subserve this task by converting different types of inputs to sparse,

eLife digest You can probably recall where you left your car this morning without too much trouble. But assuming you use the same busy parking lot every day, can you remember which space you parked in yesterday? Or the day before that? Most people find this difficult not because they cannot remember what happened two or three days ago, but because it requires distinguishing between very similar memories. The car, the parking lot, and the time of day were the same on each occasion. So how do you remember where you parked this morning?

This ability to distinguish between memories of similar events depends on a brain region called the hippocampus. A subregion of the hippocampus called the dentate gyrus generates different patterns of activity in response to events that are similar but distinct. This process is called pattern separation, and it helps ensure that you do not look for your car in yesterday's parking space.

Pattern separation in the dentate gyrus is thought to involve a form of negative feedback called feedback inhibition, a phenomenon where the output of a process acts to limit or stop the same process. To test this idea, Braganza et al. studied feedback inhibition in the dentate gyrus of mice, before building a computer model simulating the inhibition process and supplying the model with two types of realistic input. The first consisted of low-frequency theta brainwaves, which occur, for instance, in the dentate gyrus when animals explore their environment. The second consisted of higher frequency gamma brainwaves, which occur, for example, when animals experience something new.

Testing the model showed that feedback inhibition contributes to pattern separation with both theta and gamma inputs. However, pattern separation is stronger with gamma input. This suggests that high frequency brainwaves in the hippocampus could help animals distinguish new events from old ones by promoting pattern separation.

Various brain disorders, including Alzheimer's disease, schizophrenia and epilepsy, involve changes in the dentate gyrus and altered brain rhythms. The current findings could help reveal how these changes contribute to memory impairments and to a reduced ability to distinguish similar experiences.

non-overlapping activity patterns of granule cells (GCs). However, in contrast to the insect olfactory system, the DG feedback circuit is extremely complex, comprising numerous interconnected interneuron types (Supplementary Table 1) (***Bartos et al., 2002***; ***Dasgupta and Sikdar, 2015***; ***Espinoza et al., 2018***; ***Ewell and Jones, 2010***; ***Freund and Buzsáki, 1996***; ***Geiger et al., 1997***; ***Harney and Jones, 2002***; ***Hefft and Jonas, 2005***; ***Kraushaar and Jonas, 2000***; ***Larimer and Strowbridge, 2008***; ***Lee et al., 2016***; ***Liu et al., 2014***; ***Lysetskiy et al., 2005***; ***Sambandan et al., 2010***; ***Savanthrapadian et al., 2014***; ***Sik et al., 1997***; ***Yu et al., 2015***; ***Yuan et al., 2017***; ***Zhang et al., 2009***). For instance, interneurons subserving feedback inhibition are also incorporated into circuits mediating feedforward inhibition (***Ewell and Jones, 2010***; ***Hsu et al., 2016***; ***Lee et al., 2016***) and disinhibition (***Savanthrapadian et al., 2014***; ***Yuan et al., 2017***). This makes it difficult to predict the *net* inhibition arising from GC activity.

We reasoned that to assess if feedback inhibition is indeed suitable for the purpose of pattern separation in the DG, it is necessary to determine how efficiently the activity of sparse GC ensembles recruits *net* inhibition, that is the dynamic range and gain of the feedback inhibitory microcircuit. It is furthermore necessary to quantify the spatial and temporal properties of the elicited inhibition, in order to investigate its impact on biologically plausible, temporally structured input. For instance, the DG shows prominent theta oscillations during exploration and distinctive slow-gamma activity during associative memory encoding (***Hsiao et al., 2016***; ***Lasztóczi and Klausberger, 2017***; ***Pernía-Andrade and Jonas, 2014***; ***Sasaki et al., 2018***; ***Trimper et al., 2017***). Importantly, both sparsity and temporal oscillations will critically affect a proposed pattern separation function. For instance, feedback inhibition must by definition occur with a delay, a property frequently abstracted away in computational models (***Myers and Scharfman, 2009***; ***Rolls, 2016***), but potentially critical during oscillatory activity.

Here, we combine patch-clamp recordings, multiphoton imaging and optogenetics to provide a first quantitative, empirical description of the *net* input-output function of a feedback inhibitory

microcircuit. This includes the spatiotemporal organization of *net* feedback inhibition elicited by a spatially restricted GC population and the *net* short-term dynamics within the feedback microcircuit. Finally, we integrate our data into a biophysically realistic computational model and probe its ability to perform pattern separation. We find a moderate feedback inhibition mediated pattern separation effect during theta modulated input but a substantial separation, particularly of highly similar inputs, during gamma oscillations.

Results

Input-output relation of the feedback inhibitory microcircuit

We reasoned that the ultimately relevant parameter for the putative pattern separation effect of feedback inhibition is the *net* inhibition arriving at GCs. We therefore treated the feedback microcircuit as a black-box striving to relate only its *net* input (fraction of GCs active) to its *net* output (feedback inhibition in GCs). To this end, we antidromically recruited feedback inhibitory circuits, while simultaneously recording GC inhibition and population activity (see schematic in ***Figure 1A***). Electrical stimulation reliably evoked graded IPSCs in dentate GCs, that increased with stimulation strength (maximal amplitude of 324.1 ± 99.2 pA, n = 8; ***Figure 1B***). Feedback IPSCs were completely blocked by 10 µM GABAzine (to 1.5 ± 0.9%, n = 7 cells, P(df = 6, t = 117.4)<0.001, one-sided t-test), as expected (***Figure 1C***). To ascertain that IPSCs were mediated by synaptically activated interneurons rather than interneurons directly recruited by electrical stimulation, we only included slices where inhibition was successfully blocked by glutamatergic antagonists (25 µM CNQX and 50 µM D-APV, 8 of 21 experiments, ***Figure 1C***). We also tested if inhibition of glutamate release from mossy fibers, which can be specifically achieved via mGluR2/3 activation by DCG-IV (***Doherty and Dingledine, 1998***; ***Toth et al., 2000***), reduces feedback IPSCs. Indeed, we found that IPSCs were reduced to 16.3 ± 6.1% by 0.5 µM DCG-IV (n = 4 cells, P(df = 3, t = 13.73)<0.001, one-sided t-test, ***Figure 1C***).

In order to relate the measured IPSCs to the fraction of GCs activated by a given stimulation strength, we used population Ca^{2+} imaging with multibeam two-photon microscopy (***Figure 1A***, see Materials and methods). After bolus-loading GCs with the Ca^{2+} indicator OGB-1-AM (see Materials and methods), antidromic stimulation caused action potential associated Ca^{2+} elevations in a subset of GCs (***Figure 1D***, transients indicated by *). Before quantifying population activity, we verified the reliable detection of single action potentials under our conditions using simultaneous cell-attached recordings from dentate GCs (***Figure 1E***; ***Figure 1—figure supplement 1***). Briefly, cells were differentiated into true responders or non-responders on the basis of cell-attached recordings (***Figure 1E,F***; responders green, non-responders grey). A histogram of the peak ΔF/F of non-responders upon a single stimulus was fitted with a Gaussian (***Figure 1F*** right, grey dots, grey bars, n = 33) and the threshold set to the quadruple standard deviation of this fit (0.94% ΔF/F, dashed line in ***Figure 1F***). We estimated that this threshold would yield approximately equal numbers of false positives and false negatives (***Figure 1—figure supplement 1F***). We additionally controlled for possible errors through variable dye loading and the overestimation of the active cell-fraction through accidental detection of adjacent active cells (***Figure 1—figure supplement 1G,H***, respectively).

Orientation of hippocampal slices may be a critical feature in determining the extent of feedback connectivity. We therefore systematically assessed the magnitude of feedback activation of GCs using imaging in slices obtained from different dorso-ventral levels of the hippocampus (see inset of ***Figure 1G***). We found a clear connectivity maximum within horizontal slices obtained at a distance of ~1750 µm from the temporal pole (***Figure 1G,H***; ***Bischofberger et al., 2006***). In these and all following experiments we therefore used exclusively slices obtained at 1400–2100 µm from the temporal pole, where the orientation of hippocampal slices matches the orientation of mossy fibers.

Combining the IPSC recordings with population Ca^{2+} imaging allowed us to probe the input-output relationship of the feedback inhibitory microcircuit. Inhibition was recorded in a GC within or immediately adjacent to the imaging field, and stimulation strength was increased gradually (***Figure 1I***). The IPSC saturated at 300µA stimulation strength, where the mean active cell fraction was 2.2 ± 0.7% and the mean IPSC reached 93.1 ± 3.4% of the maximal IPSC (***Figure 1I,J***, n = 20 for imaging, n = 8 for IPSCs including six slices with both). Plotting the IPSC magnitude vs. the cell

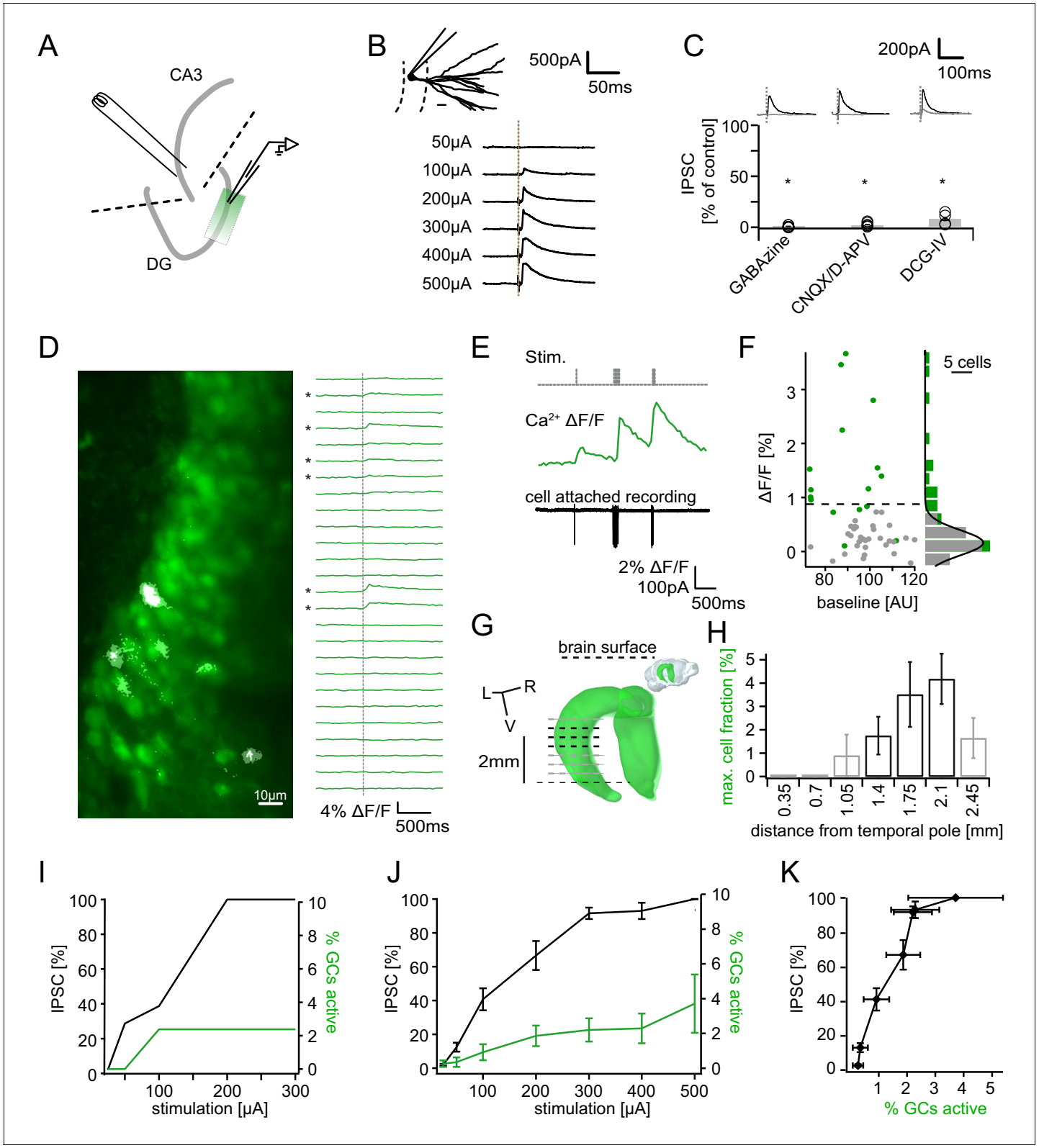

Figure 1. Recruitment of feedback inhibition assessed using population Ca^{2+} imaging. Combined population Ca^{2+} imaging and IPSC recordings of GCs during antidromic electrical stimulation. (**A**) Schematic illustration of the experimental setup. Dashed lines represent cuts to sever CA3 backprojections. (**B**) Top: reconstruction of the dendritic tree of a representative GC. Bottom: Feedback IPSC at increasing stimulation strength during stratum lucidum stimulation. (**C**) IPSCs were completely blocked by GABAzine and CNQX + D-APV and largely by DCG-IV. (**D**) Left: overlay of exemplary OGB1-AM-loaded GC population (green) with a ΔF/F map (white). right: traces of ΔF/F over time of a subpopulation of cells depicted on the

Figure 1 continued on next page

Figure 1 continued

left. (**E**) Simultaneous cell attached recording and calcium imaging to measure the action potential induced somatic calcium transient amplitude. (**F**) Scatterplot and histogram of the calcium fluorescence peaks of cells which either did (green) or did not (grey) fire action potentials, as assessed by cell attached recordings. (**G**) Illustration of the anatomical localization of maximum connectivity plane slices. Short black dashed lines indicate depth at which the slice plane is aligned to the dorsal brain surface. (**H**) Antidromic stimulation elicited Ca^{2+} transients primarily at this depth (black bars). (**I**) Normalized IPSC amplitude and activated cell fraction both increase with increasing stimulation strength (example from a single slice). (**J**) Summary of all slices (**K**) Summary data plotted to show the increase of inhibition as a function of the active GC fraction.
The online version of this article includes the following figure supplement(s) for figure 1:

Figure supplement 1. Detection of single action potential induced calcium transients.

fraction showed that the magnitude of feedback inhibition rises steeply, reaching ~90% with less than 3% of GCs active and complete saturation at 3.7 ± 1.7% of cells (***Figure 1K***).

Optogenetic quantification of the recruitment of feedback inhibition

These experiments yielded a first quantitative estimate of the input-output relation of the feedback-inhibitory microcircuit in the DG. We then decided to verify these findings using an alternative method, which allowed spatially controlled and less synchronous GC activation. Mice selectively expressing $ChR2^{(H134R)}$-eYFP in GCs were created by crossing Prox1-Cre mice with Ai32-mice (***Figure 2A***, see Materials and methods). Focal optogenetic stimulation was achieved through a laser coupled into the microscope light path, yielding an 8 µm stimulation spot (***Figure 2B***). Brief (20 ms, 473 nm) light pulses within the molecular layer approximately 40 µm from the dentate GC layer elicited reliable IPSCs in GCs (***Figure 2C***). Increasing the light intensity evoked larger IPSCs that showed clear saturation (***Figure 2C,D***, Power = 7 AU corresponding to 1.7 mW, see Materials and methods). Inhibition was completely blocked by combined application of 40 µM CNQX and 50 µM D-APV (***Figure 2E***, n = 9), confirming that it is recruited via glutamatergic collaterals. The maximal IPSC amplitude obtained optically vs. electrically in experiments in which both stimulations were performed were similar (***Figure 2F***, paired t-test, P(df = 3, t = 1.568)=0.2148, n = 4), indicating that similar maximal inhibition is recruited despite the differences in the activated GC population (distributed vs local; synchronous vs. less synchronous).

In order to relate feedback inhibition to the underlying GC activity levels, we performed systematic cell attached recordings of GCs in the same slices in which inhibition was recorded (~2 cells per slice, ***Figure 2—figure supplement 1***). Briefly, we recorded the spatial firing probability distribution in response to focal stimulation for each laser power. We then estimated the mean firing probability of GCs throughout the section, which is equivalent to the expected active GC fraction, by incorporating measurements of the light intensity distribution throughout the slice (***Figure 2G***, black). We additionally estimated an upper and lower bound by assuming either no decay of firing probability with slice depth or isometric decay (***Figure 2G***, grey dashed lines). Combining the input-output relations of IPSCs (***Figure 2D***) and the estimated active cell fraction (***Figure 2G***) again revealed that inhibition is recruited steeply, saturating when approximately 4% of GC are active (***Figure 2H***). Importantly, the resulting recruitment function of inhibition is unlikely to be affected by voltage escape errors (***Figure 2—figure supplement 2***). This is because such errors scale linearly with synaptic conductance and will thus affect the absolute but not the relative amplitude of the somatically measured IPSC. Next, we compared the focal light activation with global activation via a light fiber positioned over the surface of the slice (with powers up to 50 mW, ***Figure 2I***). Under global stimulation all cells tested fired APs with 100% reliability and independent of location, even though focal stimulation in direct proximity to the cell led to much lower maximal firing probabilities (***Figure 2I***, middle, 100.0 ± 0.0 versus 31.2 ± 7.1% respectively, paired t-test, P(df = 7, t = 9.74)<0.001, n = 8). At the same time, the maximal IPSC amplitude did not increase further upon global stimulation (***Figure 2I***, right, 356.9 ± 76.2 versus 344.3 ± 77.5 pA, paired t-test, P(df = 9, t = 1.112)=0.29, n = 10). This implies that additional activation of remote GCs cannot recruit interneurons beyond those activated by local GC populations. Thus, the recruitment of feedback inhibition in the DG is steep, with a dynamic range tuned to sparse populations of GCs (up to 3–4% of cells).

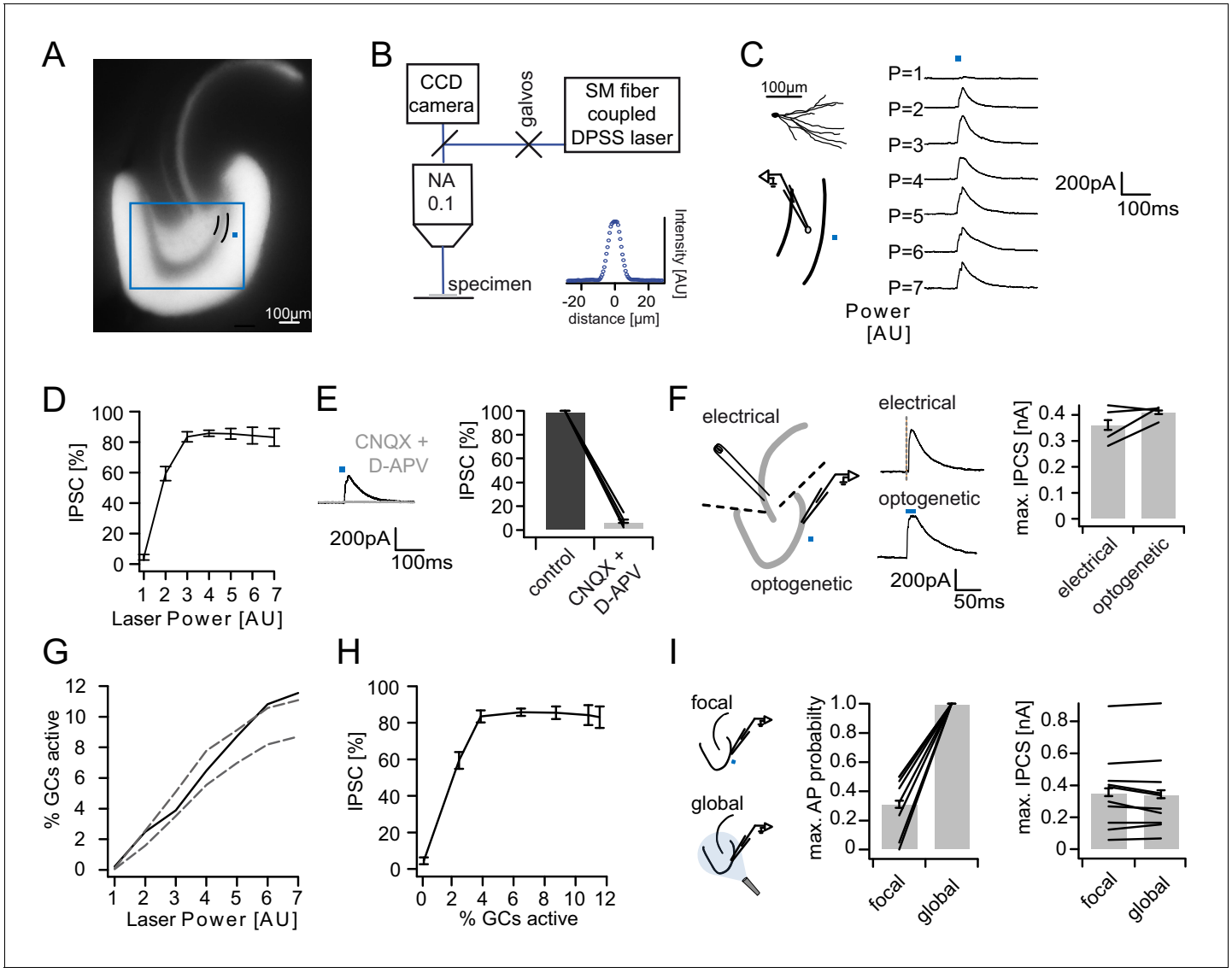

Figure 2. Recruitment of feedback inhibition assessed optogenetically. (**A**) EYFP fluorescence in dentate GCs of Prox1/ChR2(H134R)-EYFP transgenic mice. The field of view for rapid focal optogenetic stimulation is indicated by a blue square. A typical stimulation site approx. 40 µm from the GC layer (two short black lines) is indicated by a blue dot. (**B**) Schematic of the microscope setup used to achieve spatially controlled illumination. The inset shows the intensity profile of the laser spot. (**C**) Top left, reconstruction of an Alexa594 filled GC. Left, illustration of optical stimulation. Right, IPSCs following 20 ms light pulses at increasing laser power (p=1 to 7 AU). Each trace represents an average of three trials. (**D**) Summary of IPSC amplitudes from cells in the superior blade (n = 7 cells). IPSC amplitudes were normalized to the maximum amplitude within each cell. (**E**) Optogenetically elicited IPSCs are abolished by glutamatergic blockers (40 µM CNQX + 50 µM D-APV, n = 9). (**F**) Left, Schematic of focal optical and electrical stimulation. Dashed lines indicate cuts to sever CA3 backprojections. Middle, Example traces for IPSCs following electrical or focal optogenetic stimulation. Right, maximal IPSC amplitude for the two stimulation paradigms (361 ± 37 vs. 410 ± 13 pA for electrical and optogenetic stimulation respectively, paired t-test, p=0.28, n = 4) (**G**) The optogenetically activated GC fraction responsible for recruiting the IPSC at the respective laser powers was estimated from systematic cell attached recordings (see ***Figure 2—figure supplement 1*** for details). The best estimate (black) incorporates measurements of the 3D light intensity profile in the acute slice. Upper and lower bounds were estimated by assuming no firing probability decay with increasing slice depth (upper grey dashed line) or isometric firing probability decay (lower grey dashed line. (**H**) Data from (**D**) and (**H**, best estimate) plotted to show the recruitment of feedback inhibition. (**I**) Comparison of focal optogenetic stimulation to global (light fiber mediated) optogenetic stimulation. Left, Schematic illustration. Middle, Comparison of the AP probability of individual GCs at maximal stimulation power for focal and global stimulation assessed by cell attached recordings. Right, Comparison of the maximal IPSC amplitude under focal and global stimulation for individual GCs.
The online version of this article includes the following figure supplement(s) for figure 2:

Figure supplement 1. Optogenetically activated cell fraction.
Figure supplement 2. Error in somatic IPSC measurements with increasing inhibitory conductance.
Figure supplement 3. Absence of single GC induced feedback inhibition.

Lower limit of feedback recruitment

Previous work has addressed the lower limit of the recruitment of feedback inhibition in various cortical areas (**Jouhanneau et al., 2018**; **Kapfer et al., 2007**; **Miles, 1990**; **Silberberg and Markram, 2007**). The authors report the ability of even a single principal cell to activate feedback inhibitory interneurons and a supralinear increase of inhibition as the second and third principal cells are co-activated (**Kapfer et al., 2007**). Given our findings so far we asked whether single GCs might also suffice to elicit feedback inhibition in the DG. To this end, we performed dual patch clamp recordings and elicited short trains of 10 action potentials at 100 Hz in one cell while monitoring inhibition in the other (**Figure 2—figure supplement 3**, n = 15). However, in contrast to the neocortex (**Kapfer et al., 2007**; **Silberberg and Markram, 2007**) and area CA3 (**Miles, 1990**), we did not find single GC-induced feedback inhibition in any of these experiments, consistent with a recent large scale study reporting that such connections are extremely sparse (0.124%) (**Espinoza et al., 2018**).

Spatial distribution of feedback inhibition

Recent evidence indicates that inhibition by individual PV^+ fast spiking hilar border interneurons is non-uniformly distributed over space, with decreasing connectivity and inhibition at greater distances from the interneuron (**Espinoza et al., 2018**; **Strüber et al., 2015**). To test whether feedback inhibition by the entire ensemble of feedback inhibitory interneurons also displays a spatial gradient, we activated cell populations at 100 µm intervals along the GC layer while recording inhibition in individual GCs (**Figure 3A**). Spatial profiles were recorded for increasing laser powers in cells in the superior as well as inferior blade of the DG (**Figure 3B,C** respectively; n = 8 cells for each blade). IPSC amplitudes across locations and powers were normalized to the maximal IPSC amplitude in each respective cell. This maximal amplitude did not differ between cells in different blades (366 ± 40 vs 390 ± 84 pA for superior and inferior blades, respectively; t-test, P(df = 14, t = 0.258) =0.0686). Next, we investigated the spatial organization of feedback inhibition at stimulation powers at which inhibition had saturated (**Figure 3D,E**). In all GCs tested, the inhibition was greatest when stimulating in the direct vicinity of the recorded cell. Activating cells at increasing distances led to monotonically decreasing IPSC amplitudes for both blades. Importantly, the term distance here refers to the functional distance along the GC layer and not to Euclidean distance. However, inhibition was observed even at the most remote stimulation sites, indicating that even the most remote cells from the contralateral blade can contribute to the activation of feedback inhibition in a given GC. In order to statistically compare the relation of local versus remote inhibition between blades, we defined a remote location in the contralateral blade at 800 µm from the recorded cell (measured along the GC layer and equidistant in all slices; **Figure 3D,E**; grey lines) and compared it to the local IPSC (black lines). Remote inhibition was significantly smaller than local inhibition while no difference between blades or significant interaction was observed (**Figure 3F**; two-way RM ANOVA; Distance: F(1,14)=3.341, p<0.001; Blade: F(1,14)=2.615, p=0.128; Interaction: F(1,14)=3.341, p=0.089). Post-tests suggested inhibition of inferior GCs by superior activation might be greater than vice versa. However, the difference was not significant (Sidak's multiple comparison corrected posttest, P (df = 28)=0.932, P(df = 28)=0.051 for local and remote, respectively).

Next, we investigated whether there are differences in the steepness of recruitment of local versus remote inhibition between blades (black and grey, respectively; **Figure 3G,H**). To this end, we calculated the active cell fraction which produces half-maximal inhibition during local or remote stimulation for each individual slice. Comparison of the recruitment between the four groups revealed no differences between blades (**Figure 3I**, two-way RM ANOVA; Distance: F(1,14)=7.889, p=0.014; Blade: F(1,14)=0.5506, p=0.470; Interaction: F(1,14)=0.0976, p=0.759). However, local inhibition was significantly more steeply recruited than remote inhibition (1.99 ± 0.22% vs. 3.17 ± 0.57% active cells for half-maximal inhibition).

Next, we tested if IPSCs elicited by increasing active GC populations differed between local and remote activation with respect to their kinetic properties. Since all previous data showed no indication of blade specific differences the analysis of the kinetics of feedback IPSCs were performed on the pooled data for both blades. Interestingly, local and remote inhibition differed in all tested respects (**Figure 3J–M**, two-way RM ANOVAs with $df_{Distance}$ = 1,183, $df_{cell\ fraction}$ = 6,183 and $df_{interaction}$ = 6,183). Local IPSCs occurred with shorter latency and lower jitter than remote IPSCs (**Figure 3J,K**; Latency: p<0.001, <0.001 and =0.031 for distance, cell fraction and interaction,

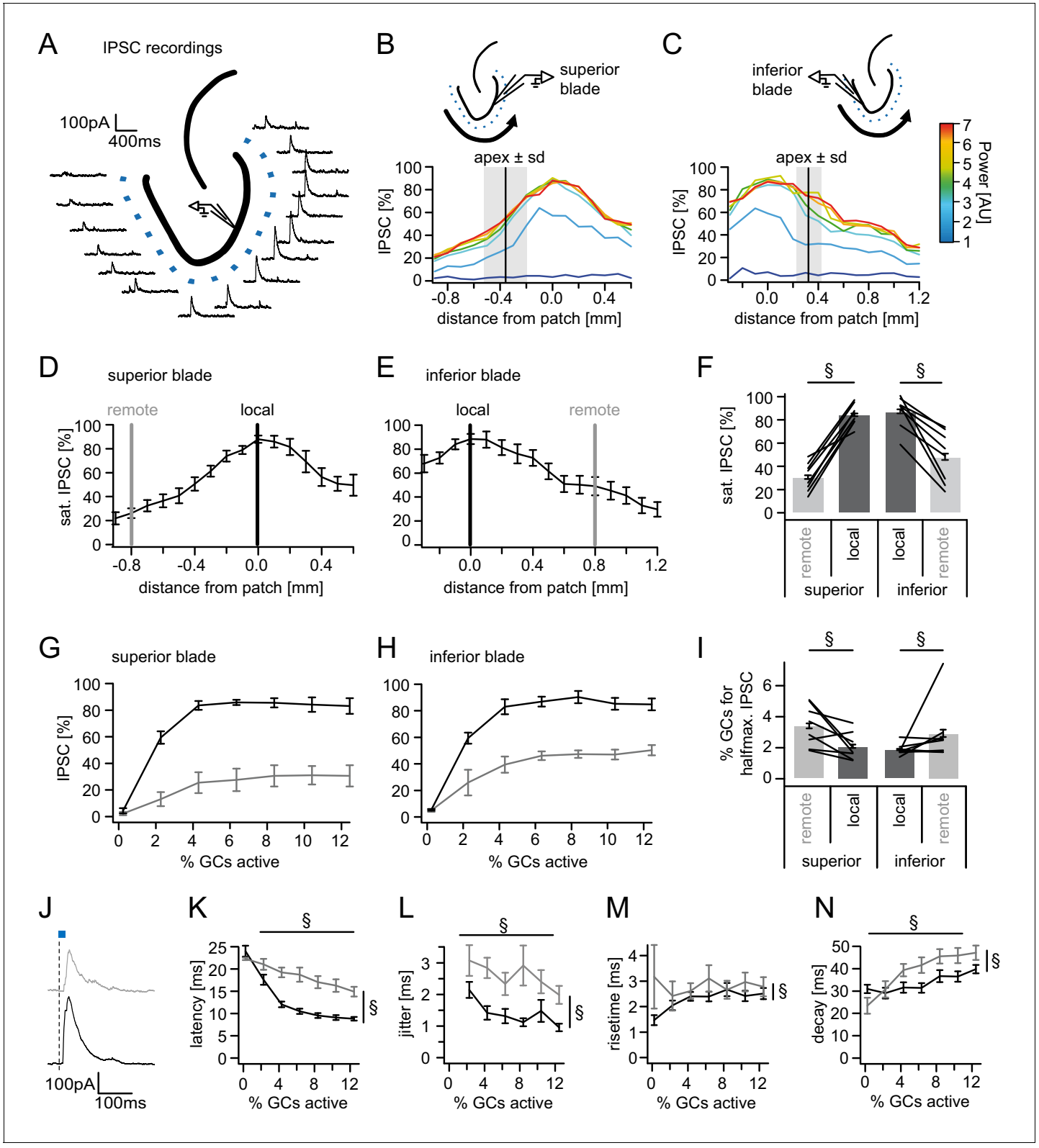

Figure 3. Spatial organization of feedback inhibition. Feedback IPSCs recorded from an individual GC while GCs at varying distances were activated. (**A**) Schematic illustration of the stimulation paradigm and example IPSC traces of an individual trial (p=3). (**B, C**) Distribution of normalized IPSC amplitudes as a function of laser power and distance from stimulation spot for superior and inferior blade GCs (n = 8 for each blade). The relative location of the DG apex ± standard deviation is indicated by the black bar and grey area respectively. (**D, E**) IPSC distribution over space at saturation (p≥5). Black and grey bars indicate a local and a remote location at 800 µm from the recorded cell respectively. (**F**) Comparison of the amplitude of the

Figure 3 continued on next page

Figure 3 continued

locally and remotely activated IPSCs at saturation (two-way RM ANOVA, overall test significance indicated by §). (**G, H**) Comparison of the recruitment curves during local (black) or remote (grey) stimulation for superior and inferior blade respectively. (**I**) Comparison of the cell fraction required for halfmaximal IPSC activation between stimulation sites and blades (two-way RM ANOVA overall test significance indicated by §). (**J–M**) Temporal properties of IPSCs between local (black) and remote (grey) stimulation. To test for systematic variations of kinetic parameters with increasing active cell fractions as well as stimulation site two-way RM ANOVAs with no post tests were performed. Overall significance indicated by §. (**K**) Latency from beginning of light pulse to IPSC (**L**) temporal jitter of IPSCs (SD of latency within cells) (**M**) 20% to 80% rise time (**N**) IPSC decay time constant.

respectively; Jitter: $p<0.001$, =0.037 and =0.707 for distance, cell fraction and interaction, respectively). Furthermore, both latency and jitter decreased as larger populations were activated. IPSCs were also significantly slower in remote versus local inhibition. IPSC rise time was slightly shorter in the larger local IPSCs but did not correlate with the active cell fraction (***Figure 3L***: p=0.010, =0.633 and =0.388 for distance, cell fraction and interaction, respectively). Similarly, decay times were significantly shorter in local versus remote inhibition while they progressively increased with increasing stimulation power (***Figure 3M***; $p<0.001$, <0.001 and =0.124 for distance, cell fraction and interaction, respectively). These data demonstrate that remote inhibition shows greater delay, greater jitter and slower kinetics than local inhibition.

Short-term dynamics in the feedback inhibitory microcircuit

Different connections within the feedback inhibitory microcircuit have been shown to variably facilitate or depress during trains of activity (***Savanthrapadian et al., 2014***) (Tabular overview provided in ***supplementary file 1***). This makes it difficult to predict the net effect on the short-term dynamics of GC feedback inhibition. We therefore characterized the frequency-dependence of net feedback inhibition using antidromic electrical stimulation as described above (***Figure 4A–C***). In marked contrast to the CA1 region of the hippocampus (***Pothmann et al., 2014***), feedback IPSCs showed strong frequency-dependent facilitation (***Figure 4C***, n = 10 cells, one-way RM ANOVA; Frequency: $F(2.69, 29.54)=13.99$, $p<0.001$; Wilcoxon signed rank tests for deviation from unity at each frequency with Bonferroni corrected p-values; $p>0.99$, p=0.004, p=0.002 and p=0.002 for 1, 10, 30 and 50 Hz, respectively). Furthermore, the facilitation indices significantly increased with increasing stimulation frequency (1 Hz: 0.99 ± 0.07; 10 Hz: 1.41 ± 0.11; 30 Hz: 1.83 ± 0.16; 50 Hz: 2.09 ± 0.19; posttest for linear trend: $p<0.0001$, $R^2=0.436$). We found no evidence for a spatial gradient of net feedback inhibitory short-term dynamics (***Figure 4—figure supplement 1***).

Because this unusual degree of facilitation may be important in allowing sparse activity of GCs to recruit significant inhibition over time, we further examined the underlying circuit mechanisms. Interestingly, dentate interneuron inputs to GCs appear to be generally depressing (***Supplementary file 1***, blue rows), rendering our finding of pronounced facilitation at the circuit level even more striking. We reasoned that a facilitating excitatory synapse driving feedback interneurons could underlie circuit level facilitation. We therefore measured feedback excitation of hilar neurons by stimulating mossy fiber axons as described above (***Figure 4D–L***). Mossy cells and interneurons were classified according to their morpho-functional properties (***Larimer and Strowbridge, 2008***) (***Figure 4D,E,G, H,J,K***). Cell classification was confirmed using unbiased k-means clustering (***Figure 4K***). We found that feedback excitation of hilar cells displayed marked facilitation, which was similar for both INs and MCs (***Figure 4F,I,L***; n = 9, 12 respectively, two-way RM-ANOVA, Frequency: $F(3,57)=6.642$, $p<0.001$; Cell type: $F(1,19)=0.0075$, p=0.932; Interaction: $F(3,57)=0.743$, p=0.531). Facilitation indices of hilar cells significantly deviated from one for all frequencies tested (***Figure 4E,F***; n = 23 cells; Wilcoxon signed rank tests with Bonferroni corrected p-values; $p<0.001$ for all frequencies). These data demonstrate a pronounced frequency-dependent net facilitation of the feedback inhibitory microcircuit, which is supported by strongly facilitating mossy fiber inputs to hilar cells.

Quantitative properties of the feedback circuit predict frequency-dependent pattern separation

Together, these data indicate that the dentate feedback circuit is able to deliver strong, spatially graded inhibition with a high gain and the ability for temporal integration. To probe how these quantitative properties of the feedback circuit affect the pattern separation capability of the DG, we incorporated them into a biophysically realistic model of the lamellar microcircuit (***Figure 5***) based

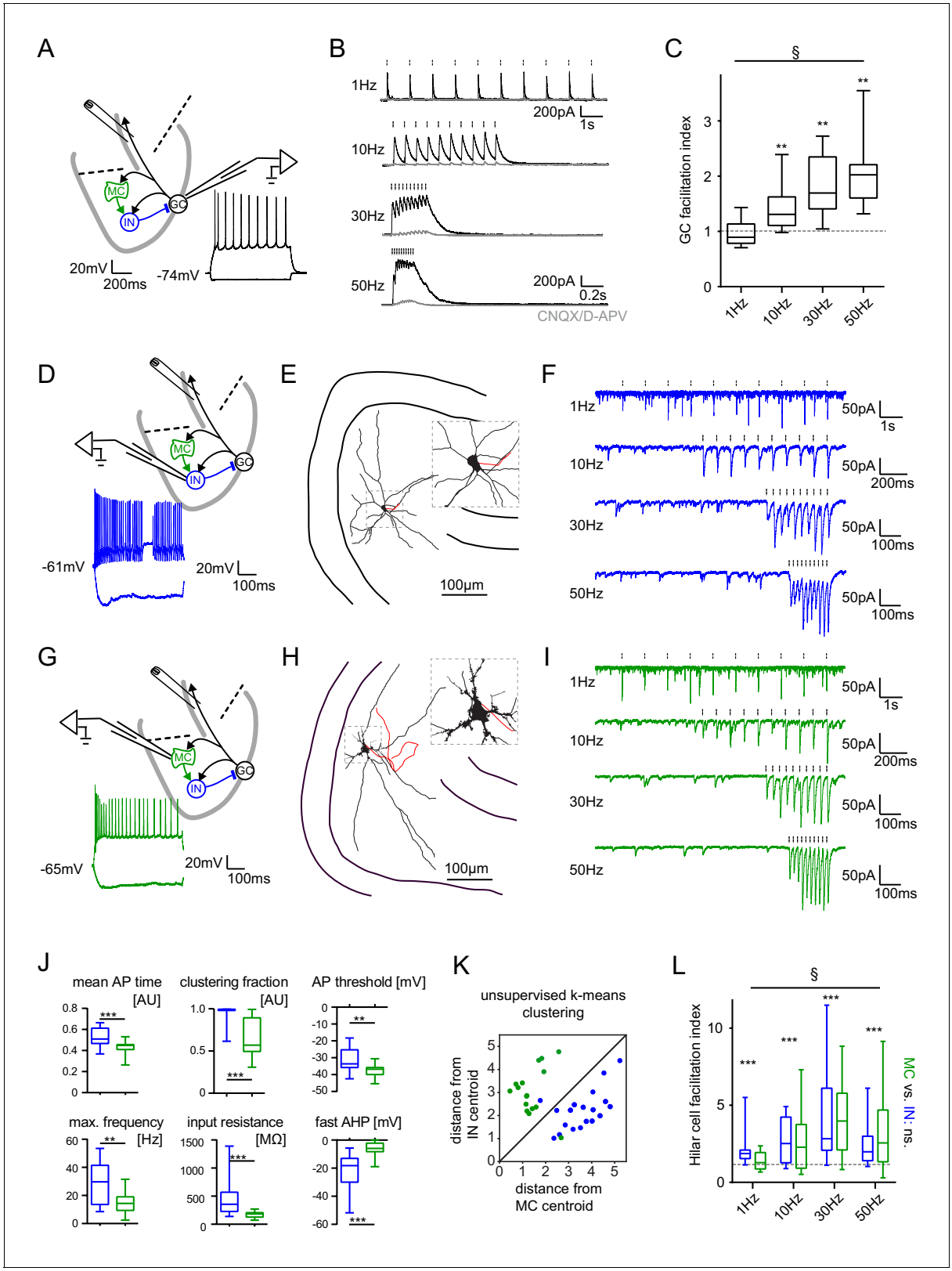

Figure 4. Short-term dynamics in the feedback inhibitory microcircuit. Trains of ten antidromic electrical stimulations at 1, 10, 30 or 50 Hz were applied to elicit disynaptic feedback inhibition or excitation of hilar cells (electrical stimulation artifacts were removed in all traces). (**A, D, G**) Schematic illustration of the experimental setup and example traces of voltage responses to positive and negative current injections of GC and hilar cells (dashed lines indicate cuts to sever CA3 backprojections). (**B**) Exemplary GC feedback IPSCs before (black) and after (grey) glutamatergic block (n = 7). (**C**)

Figure 4 continued on next page

Figure 4 continued

Facilitation indices (mean of the last three IPSCs normalized to the first; n = 10 cells). (**D-L**) Hilar cells were manually classified into putative interneurons (blue) or mossy cells (green) based on their morpho-functional properties. (**E**) Reconstruction of biocytin filled hilar interneuron (axon in red). (**F**) Interneuron EPSCs in response to stimulation trains. (**H**) Reconstruction of biocytin filled mossy cell (axon in red). (**I**) Mossy cell EPSCs in response to stimulation trains. (**J**) Quantification of intrinsic properties of hilar cells (see Materials and methods). (**K**) k-means clustering based on intrinsic properties of hilar cells (coloring according to manual classification). (**L**) Facilitation indices of classified hilar cells. (§ indicates significance in one-way RM ANOVA, * show significance in Bonferroni corrected Wilcoxon signed rank tests for deviation from 1).
The online version of this article includes the following figure supplement(s) for figure 4:

Figure supplement 1. Frequency dependence of feedback inhibition over space.

on ***Santhakumar et al. (2005)***; ***Yim et al. (2015)***, making use of their carefully experimentally constrained DG cell-types (***Figure 5A***; ***Figure 5—figure supplement 1A***). To maximize our models inferential value we clearly separated a tuning phase, in which we constrained the model by our experimental data, and an experimental phase, in which pattern separation was tested without further changes to the model. In the tuning phase, we first scaled up the model four-fold to contain 400 perforant path afferents (PPs), 2000 GCs, 24 basket cells (BCs), 24 hilar perforant path associated cells (HC) and 60 MCs (***Figure 5A,B***). BCs, HCs and MCs comprise the feedback inhibitory circuit and BCs receive direct PP input thereby additionally mediating feedforward inhibition (***Ewell and Jones, 2010***). We then adapted the spatial extent of the target pools of BC and HC outputs to produce local and global inhibition, respectively, reproducing the experimentally determined spatial tuning of *net* feedback inhibition (***Figure 5C***). We further adjusted synaptic decay time constants and weights in order to reproduce the measured PSCs of hilar neurons and GCs and the empirical recruitment curves (***Figure 5D***, ***Figure 5—figure supplement 1***). Finally, we incorporated

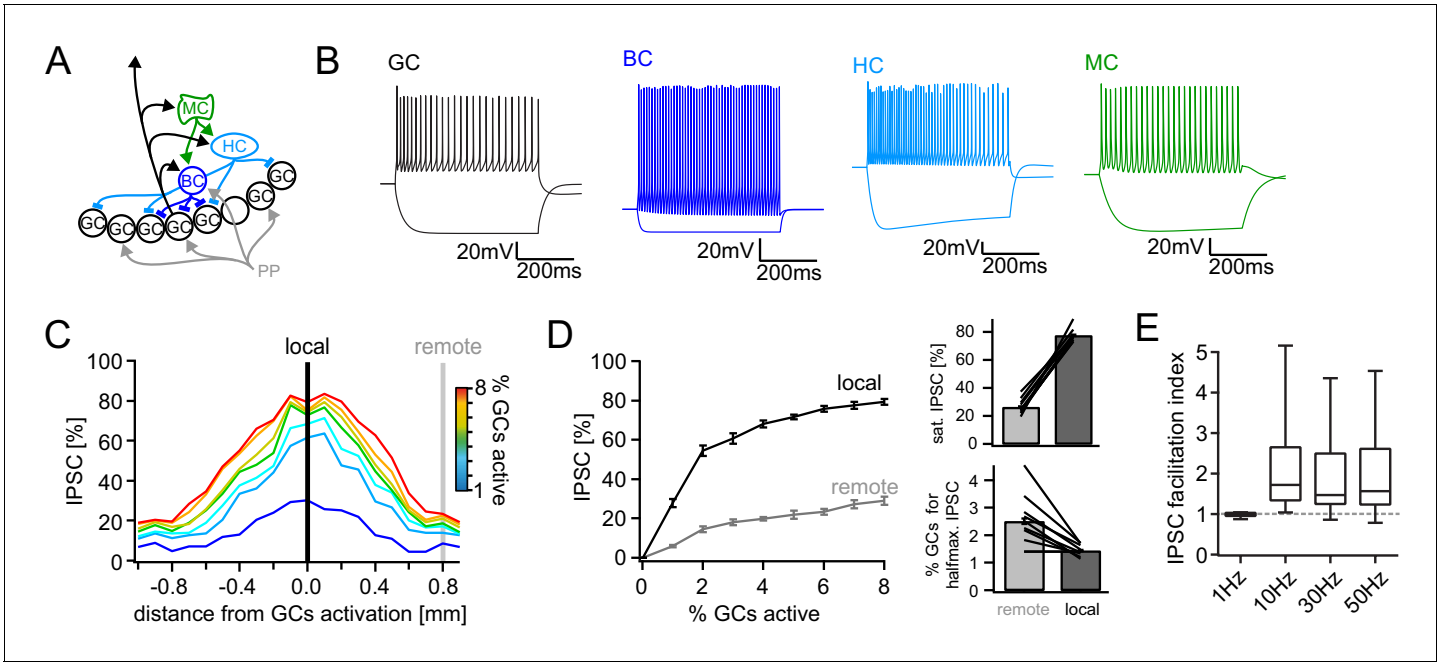

Figure 5. Computational model of the DG feedback circuit. A biophysically realistic model of DG was tuned to capture the key quantitative features of the feedback circuit. All analyses were performed as for the real data (including IPSC normalization to maximal IPSC over space and power within each respective cell) (**A**) Schematic of the model circuit. GC: granule cell, BC: basket cell, HC: hilar perforant path associated cell, MC; mossy cell. (**B**) Intrinsic responses of model cell types to positive and negative current injections. (**C**) Spatially graded net feedback inhibition following simulated focal GC activation. (**D**) Local and remote recruitment curves of the feedback inhibitory circuit (left) and the resulting saturated IPSC amplitudes and GC fractions recruiting halfmaximal inhibition (right). (**E**) Facilitation indices resulting from simulated, 10 pulse, frequency stimulation of GCs as above.
The online version of this article includes the following figure supplement(s) for figure 5:

Figure supplement 1. Model tuning and validation.

facilitation of the experimentally determined magnitude into feedback excitatory mossy-fiber outputs, leading to GC IPSC facilitation in the experimentally observed range (***Figure 5E***, ***Figure 5—figure supplement 1B***). Together, these minimal adaptations resulted in a model with remarkably similar properties to our experimental findings (***Figure 5C–E***). We therefore concluded the tuning phase of the model and proceeded to an in silico pattern separation experiment without further changes to the model.

To investigate the implications for pattern separation, we probed the ability of this model to separate PP input patterns with behaviorally relevant temporal structure and varying degrees of overlap (***Myers and Scharfman, 2009***; ***Yim et al., 2015***). Specifically, we created input trains with constant mean rate, but with either theta (10 Hz) or slow-gamma (30 Hz) modulation (***Figure 5—figure supplement 1C***), which are prominent during exploration and novelty exposure, respectively (***Sasaki et al., 2018***; ***Trimper et al., 2017***). To model rapid pattern separation in a behaviorally relevant timescale we chose an input duration of approximately five theta cycles (600 ms, corresponding to the approximate duration of place cell spiking during traversal of its place field). To obtain a range of input similarities, we generated input patterns in which 24 of 400 PP afferents were activated (***Figure 6A***) and compared pairs of such patterns ranging from no overlap (two separate sets of afferents) to complete overlap (identical trains in the same 24 afferents in both patterns). Each model network was run with 25 input patterns leading to a total of 325 comparisons (data points in ***Figure 6C***). To quantify pattern separation we compared input correlation (R_{in}) to output correlation (R_{out}; ***Figure 6B***) both measured as Pearson's R between the population rate vectors over the full 600 ms time window (***Leutgeb et al., 2007***; ***Wiechert et al., 2010***).

Our full, tuned model reliably decreased the population vector correlations for similar patterns ($0 < R_{in} < 1$) thereby demonstrating robust pattern separation over the whole range of input similarities ($R_{out} < R_{in}$; ***Figure 6C***, left). Next, we isolated the contribution of feedback inhibition to pattern separation by rerunning the same input pattern combinations on the network in which mossy fiber outputs to interneurons were removed (***Figure 6C***, middle). As expected this manipulation decreased interneuron activity and GC sparsity (***Figure 6—figure supplement 1C,D***) leading to impaired pattern separation (***Figure 6D***, noFB). Note that removing mossy fiber outputs also eliminates BC activity through cooperative activation of summating feedforward and feedback inputs (***Ewell and Jones, 2010***). Removal of all inhibitory outputs led to a further decrease in pattern separation, demonstrating the effect of additionally removing feedforward inhibition (***Figure 6C***, right). As expected, each of these manipulations increased both the fraction of active GCs and the activity per GC (***Figure 6—figure supplement 1C,D***). In order to quantify the respective pattern separation effects over the full range of input similarity, we computed the bin wise mean R_{out} (***Figure 6C***, R_{in} bin-width: 0.1, dashed line) and measured the area to the identity line (***Figure 6C***, black lines). The resulting mean ΔR_{out} was calculated for seven separate random networks, each challenged with theta as well as slow-gamma modulated inputs in each of the three conditions. Both the frequency of the input modulation as well as network manipulations significantly affected pattern separation (***Figure 6D***; two-way RM ANOVA with both factors matching, condition: $F(2,12)=145.1$, $p<0.001$; frequency: $F(1,6)=31.48$, $p=0.001$; interaction: $F(2,12)=11.77$, $p=0.002$; n = 7 random network seeds for these and all subsequent analyses). Specifically, both feedback and feedforward inhibition significantly contributed to pattern separation (Sidak's multiple comparison posttest, $P(df = 12, t = 11.33) <0.001$ and $P(df = 12, t = 5.36)<0.001$, respectively). These results are consistent with the standard account, by which any source of inhibition supports pattern separation by decreasing GC activity (***Figure 6—figure supplement 1C,D***). Notably, the effect of inhibition on GC sparseness was more pronounced during gamma than theta modulated activity, translating to improved pattern separation in the sparser gamma regime (***Figure 6D***, ***Figure 6—figure supplement 1C,D***). Remarkably, this increased sparsity in the gamma domain was achieved despite the same excitatory drive from perforant path (***Figure 6—figure supplement 1A,B***), and with less interneuron activity (***Figure 6—figure supplement 1C,D***).

Next, we more closely investigated the isolated pattern separation effects of feedback and feedforward inhibition. To this end, we computed the difference in R_{out} between the respective conditions for each individual comparison (i.e. data point in ***Figure 6C***). For instance, the individual comparison shown in ***Figure 6A***, will lead to a single R_{out} value in the network with MF inputs to interneurons (full model), which is subtracted from the corresponding R_{out} value in the same network without this input (no FB). This procedure isolates the effect of interest (ΔR_{out}) for each individual

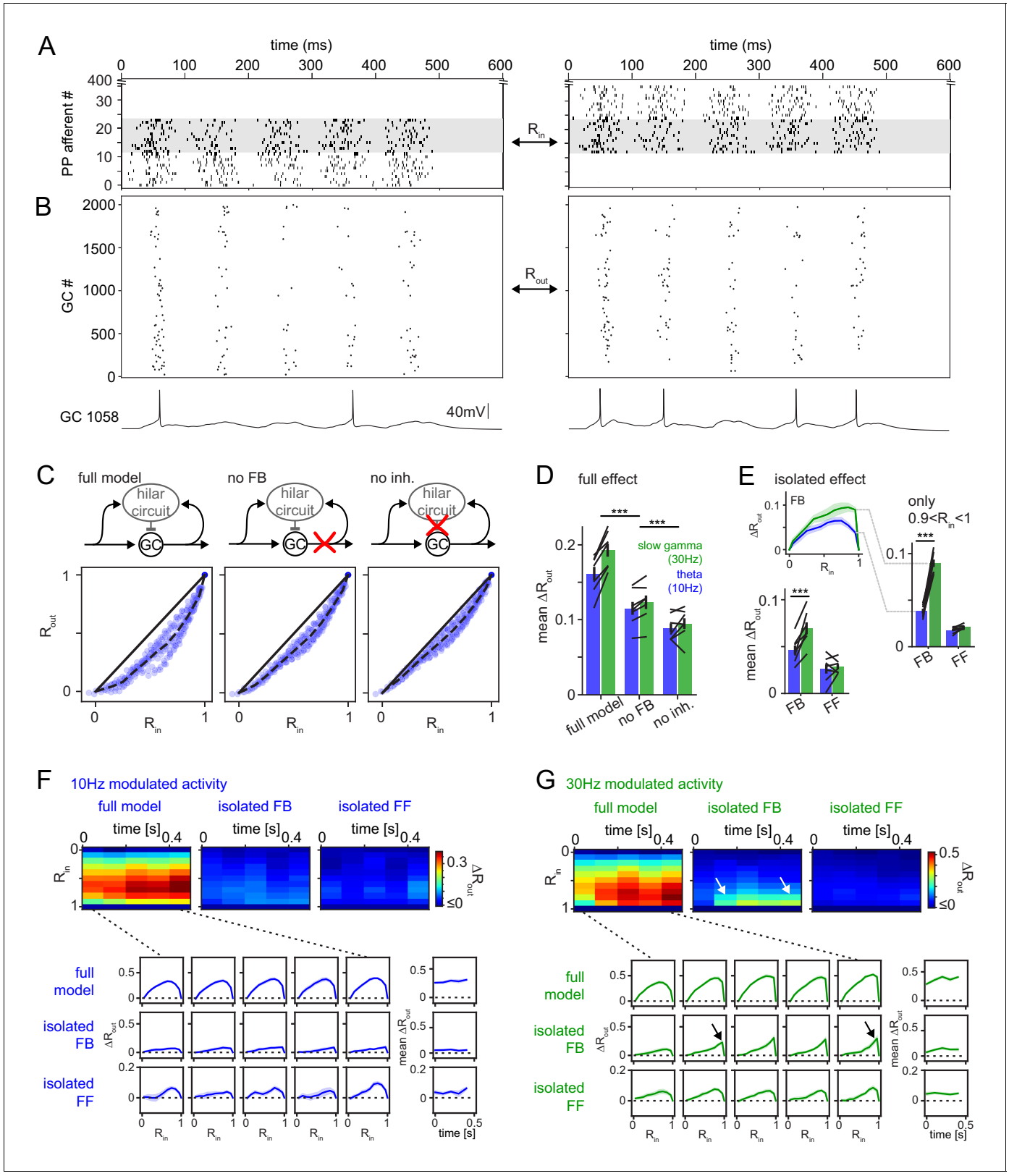

Figure 6. Frequency dependent pattern separation of temporally structured inputs. The quantitative DG model was challenged with theta (10 Hz) or slow gamma (30 Hz) modulated input patterns with defined overlap to probe its pattern separation ability. (**A**) Pair of theta modulated perforant path input patterns in which 50% of afferents overlap (grey area). (**B**) Resulting pair of GC output patterns of the full tuned network. Bottom: Representative individual GC underlying the observed patterns. (**C**) Comparison of 325 input pattern pairs and their resulting output pattern pairs. Each pair is

Figure 6 continued on next page

Figure 6 continued

characterized by its rate vector correlation for inputs (R_{in}) and outputs (R_{out}), where rates are measured over the full 600 ms time window. Dashed black lines represent the bin-wise mean R_{out} (in R_{in} bins of 0.1). Left: full tuned model, middle: model without mossy fiber inputs to interneurons, right: model without inhibitory synapses. (**D**) Full pattern separation effects (mean ΔR_{out}) of all three conditions for both frequency domains quantified as the area enclosed by the dashed and unity lines in (**C**). Black lines represent individual network seeds. Two-way RM ANOVA indicated significance of condition, frequency and interaction, * indicate significance in Sidak's posttests between individual conditions. (**E**) Isolated effects of feedback and feedforward motifs obtained by pairwise subtraction of R_{out} between conditions for each individual comparison. The inset shows the resulting ΔR_{out} for each R_{in} bin. The area under the curve quantifies the mean ΔR_{out} as in (**D**). Two-way RM ANOVA indicated significance of condition, frequency and interaction. *** indicate p<0.001 in Sidak's posttest. (**F**). 100 ms time-resolved pattern separation effects of the full model, isolated FB or FF inhibition for theta modulated input (10 Hz). All analyses were performed as above but with rate vector correlations computed for 100 ms time windows. The bottom insets show ΔR_{out} as a function of input similarity for each time window. The bottom right insets show the evolution of the mean ΔR_{out} over time. (**G**) Same as (**F**) but for slow gamma (30 Hz) modulated inputs. Arrow indicate the region of selectively increased pattern separation. Data in D-G represent mean ± SEM of n = 7 random network seeds.

The online version of this article includes the following figure supplement(s) for figure 6:

Figure supplement 1. Activity levels and pattern separation.
Figure supplement 2. Robustness over different Similarity Metrics.
Figure supplement 3. Isolated pattern separation effects of spatial tuning and MF facilitation.
Figure supplement 4. Robustness for shorter analysis time-window.
Figure supplement 5. Robustness over various IPSC decay time-constants and over the full gamma range.
Figure supplement 6. Robustness for increased feedforward inhibition.
Figure supplement 7. Robustness for increased perforant path (PP) drive.

comparison, controlling for other sources of variability. A single pattern separation measure was then obtained as before, as the area under the curve of bin-wise means of these ΔR_{out} values (***Figure 6E***, bottom). We found a significant effect of both inhibitory motif and frequency domain (***Figure 6E***; two-way RM ANOVA with both factors matching, Motif: F(1,6)=15.58, p=0.008; Frequency: F(1,6)=9.91, p=0.020; Interaction: F(1,6)=76.37, p<0.001). Posttests revealed that the frequency dependence of pattern separation was driven by feedback inhibition (Sidak's multiple comparison posttest: FB: P(df = 6, t = 13.68)<0.001; FF: P(df = 6, t = 1.33)=0.412. Interestingly, this frequency dependence of feedback inhibition mediated pattern separation was particularly pronounced for highly similar input patterns ($0.9 < R_{in} < 1$; ***Figure 6E***, right; Motif: F(1,6)=261.7, p<0.001; Frequency: F(1,6)=108.1, p<0.001; Interaction: F(1,6)=109.5, p<0.001; Sidak's multiple comparison posttest: FB: P(df = 6, t = 15.78)<0.001; FF: P(df = 6, t = 0.98)=0.595). Indeed, feedback inhibitory pattern separation for highly similar input at 30 Hz compared to 10 Hz was more than doubled (from 0.04 ± 0.01 to 0.09 ± 0.01, mean ± SD, Cohen's d = 4.1, ***Figure 6E***, right). This again demonstrates feedback inhibitory pattern separation effects beyond those explainable by decreases in GC activity, since comparisons for highly similar inputs are computed on the exact same model runs as comparisons for less similar inputs and thus by definition have the same GC activity levels (also see ***Figure 6F,G***, arrows).

It has recently been emphasized, that the assessment of pattern separation can depend critically on the similarity measure used (***Madar et al., 2019***; ***Wick et al., 2010***). Therefore, we tested the robustness of this result for two alternative similarity measures, namely normalized dot product (NDP, also known as cosine similarity) and pattern overlap (# of coactive/ # of totally active cells; ***Figure 6—figure supplement 2***). The frequency dependence of feedback inhibition-mediated pattern separation, especially for highly similar inputs, proved robust for all three similarity measures.

Effect of spatial tuning and facilitation of net feedback inhibition

Next, we investigated the specific effects of two interesting empirical findings of the present study, 1) the spatial tuning and 2) the facilitation of the feedback circuit (***Figure 6—figure supplement 3***). To this end, we undertook two targeted, minimal manipulations of the full tuned network. To probe the effect of spatially graded inhibition, we redistributed BC output synapses to a global target pool (the whole GC population), leading to spatially uniform inhibition (global FB; ***Figure 6—figure supplement 3B,E***). To probe the effect of facilitation, we removed facilitation from mossy fiber outputs (***Figure 6—figure supplement 3C,E***). We isolated the effects of these manipulations by pairwise comparison to the corresponding full tuned networks as described above (***Figure 6—figure***

supplement 3F–I). The results showed a small but significant contribution of facilitation (~20% of the isolated FB effect for both frequency paradigms), but not spatial tuning to pattern separation (*Figure 6—figure supplement 3G*, left; Wilcoxon signed rank test for deviation from 0, n = 7, Bonferroni corrected p-values: p=0.031 and p=1 respectively for 10 Hz; p=0.031 and p=1 respectively for 30 Hz). We noted that while spatial tuning did not affect mean pattern separation, it appeared to reduce its variability (CoV) for a given input similarity, although the effect was again small (*Figure 6—figure supplement 3G*, right; Wilcoxon signed rank test for deviation from 0, n = 7, Bonferroni corrected p-values: p=0.031 and p=0.750 for tuning and facilitation respectively at 10 Hz; p=0.438 and p>0.999 respectively at 30 Hz).

Frequency-dependent pattern separation is robust over analysis scales and input strengths

So far, all pattern separation analyses were conducted on the population rate vectors during a 600 ms time window. However, many neural computations are likely to occur on shorter timescales, such as within individual theta (~100 ms) and gamma (~10–33 ms) cycles (*Buzsáki, 2010*; *van Dijk and Fenton, 2018*). Indeed, the time window in which correlation is recorded can nontrivially affect the resulting correlation, depending on the timing of spikes within it (*Madar et al., 2019*). We therefore first computed the networks pattern separation ability within 100 ms time windows, revealing i) the pattern separation ability within such short timescales and ii) the temporal evolution of pattern separation throughout a 600 ms stimulus presentation (*Figure 6F,G*). We find that pattern separation occurs even within a single theta cycle, including a contribution of feedback inhibition in both frequency paradigms (mean $\Delta R_{out} > 0$ within the first 100 ms bin, Wilcoxon signed rank test with Bonferroni corrected p-values: p=0.031,=0.031 for full and FB effect respectively in both paradigms). While mean ΔR_{out} did not differ between frequency paradigms within this first time window, it was significantly elevated in the 30 Hz paradigm in all subsequent time windows (full model effect, two-way RM ANOVA, p<0.001,<0.001 and=0.004 for time-bin, frequency and interaction respectively, Sidak's posttest p=0.234 for 1st bin and p<0.001 for all subsequent bins). Again, the selective increase during slow-gamma modulated inputs was driven by feedback inhibition (isolated FB effect, two-way RM ANOVA, p=0.007,<0.001 and=0.041 for time-bin, frequency and interaction respectively, Sidak's posttest p=0.708 for 1st bin and p<0.002 for all subsequent bins), including a contribution from MF facilitation (*Figure 6—figure supplement 3*). As above, the effect was predominantly driven by the separation of highly similar input patterns (isolated FB effect, R_{in} >0.5; two-way RM ANOVA on last time-bin, p<0.001,=0.010 and<0.001 for R_{in}-bin, frequency and interaction respectively, Sidak's posttest on differences between frequency paradigms for each input similarity: p=1 for R_{in} <0.6 and p=0.032 to p<0.001 for R_{in} = 0.6 to 0.9). These results were robust when analysis time windows were decreased even further (to the duration of a slow gamma cycle, 33 ms, *Figure 6—figure supplement 4*). This 33 ms resolved analysis additionally reveals that the pattern separation effect, particularly of feedback inhibition, ramps up within a 100 ms window, becoming effective only at the end of a theta cycle (*Figure 6—figure supplement 4A*).

Next, we asked if the frequency dependence of feedback inhibitory pattern separation was sensitive to variations of the inhibitory decay time constants and if there might be an interaction between these decay time constants and the frequency range at which pattern separation is most effective (*Figure 6—figure supplement 5*). Remarkably, we found the differential effect between 10 and 30 Hz to be highly robust across a range of different decay time-constants (0.5x to 5x of the experimentally matched decay, *Figure 6—figure supplement 5A–C*, *Supplementary file 2*). Furthermore, the selective enhancement of feedback inhibitory pattern separation of highly similar inputs was robust over the entire gamma range (up to 100 Hz, *Figure 6—figure supplement 5D,E*).

Next, we tested if our main results were robust to alterations in the relative strengths of feedforward vs. feedback inhibition. Since, our model is closely constrained with respect to the recruitment and functional properties of the feedback circuit, we are confident about the resulting computational inferences concerning this circuit. However, the model does not allow strong inferences about the relative roles of feedback and feedforward inhibition, and it is thus necessary to probe if extremely powerful feedforward inhibition might occlude the effects described here. We therefore selectively enhanced the feedforward inhibitory circuit in our model by increasing the PP to BC circuit 2x (*Figure 6—figure supplement 6*). This robustly increased the feedforward inhibitory contribution to pattern separation above that of feedback inhibition (*Figure 6—figure supplement 6B*). However, it

did not affect the frequency dependence of the feedback inhibitory effect. Indeed, for highly similar input patterns, the feedback inhibitory effect was so prominently enhanced during gamma input, as to again dominate the feedforward inhibitory effect (***Figure 6—figure supplement 6C***).

Finally, we probed the robustness of our findings for various perforant path input strengths (***Figure 6—figure supplement 7***). We found that frequency-dependent pattern separation by the feedback circuit occurred over a large range of PP-input strengths and resulting mean sparsities of the GC population (***Figure 6—figure supplement 7B–D***). These data additionally suggest that for highly similar input patterns, the more efficient sparsification of the GC population at 30 Hz did not fully account for the gains in pattern separation (***Figure 6—figure supplement 7F***). Specifically, selecting a PP-input strength at 10 Hz that produced the same sparsity as during 30 Hz did not allow to reach similar pattern separation (***Figure 6—figure supplement 7F***). This result suggests that the feedback circuit mediates direct assembly competition, allowing pattern separation beyond a pure sparsification effect.

Together these results suggest that frequency dependence is a key feature of the feedback inhibitory microcircuits and predict that feedback inhibition selectively boosts the separation of highly similar input patterns during gamma oscillations.

Discussion

Across brain regions and species, inhibitory circuits contribute critically to regulating the sparsity and overlap of neural representations (***Cayco-Gajic and Silver, 2019***; ***Lin et al., 2014***; ***Papadopoulou et al., 2011***; ***Stefanelli et al., 2016***). In most, if not all brain regions, feedback inhibition is viewed as important in these capabilities, by directly mediating competition between active cell ensembles (***de Almeida et al., 2009***; ***Myers and Scharfman, 2009***; ***Rolls, 2010***). In the mammalian DG, feedback inhibition is implemented by an intricate network of interneurons that is capable of delivering spatiotemporally defined inhibition to the principal cell population. How *net* feedback inhibition is functionally organized in mammals, and how it may contribute to pattern separation of biologically relevant, temporally structured input patterns is, however, incompletely understood.

Quantitative physiological properties of DG feedback inhibition

We have therefore quantitatively described the recruitment of *net* feedback inhibition by defined GC population sizes in space and time in the hippocampal DG, a structure in which sparse activity and inhibition are thought to critically contribute to the function of pattern separation (***Gilbert et al., 2001***; ***Hunsaker et al., 2008***; ***Leal and Yassa, 2018***; ***McHugh et al., 2007***; ***Stefanelli et al., 2016***). The proposed role of the feedback inhibitory circuit depends critically on its dynamic range, that is the relation between the number of active principal cells and the resulting feedback inhibition. This property of the feedback circuit is determined by complex, mainly hilar cellular connectivity patterns including the synaptic and intrinsic properties of all participating cells (see e.g. ***Espinoza et al., 2018***; ***Savanthrapadian et al., 2014***), tabular overview in ***Supplementary file 1***). While delving into detailed cell-cell connectivities is clearly important, such studies do not allow the quantitative determination of the gain and dynamic range of *net* feedback inhibition (***Kapfer et al., 2007***; ***Silberberg and Markram, 2007***). Using two complementary experimental approaches, we found that *net* feedback inhibition is steeply recruited by sparse populations of GCs (<4%). This is in good agreement with the sparse range of GC activity reported in vivo (***Diamantaki et al., 2016***; ***Hainmueller and Bartos, 2018***; ***Pernía-Andrade and Jonas, 2014***; ***Pilz et al., 2016***; ***Schmidt et al., 2012***). In these studies, different time windows were used to define active vs. non-active granule cell populations (one to tens of minutes for electrophysiological, imaging or immediate-early gene studies). The relevant window for assembly competition, however, is much shorter. If we assume random Poisson firing, the electrophysiologically determined rates by ***Pernía-Andrade and Jonas (2014)*** and ***Diamantaki et al. (2016)***, suggest active GCs fractions of <2% for realistic assembly competition time windows of <100 ms. Accordingly, the gain and sensitivity of the circuit are well suited to strongly modulate feedback inhibition within the range of GC activity reported in vivo.

Frequency-dependent effects of feedback inhibition on pattern separation

In addition to steep recruitment, we have described the temporal and spatial distribution of net inhibition delivered by feedback circuits in the DG. How do these properties influence the pattern separation capability of the dentate gyrus? To address this question, we adapted an established biophysically realistic computational model of the DG circuitry (**Santhakumar et al., 2005**; **Yim et al., 2015**). We first carefully constrained the model to match the spatial and temporal properties of *net* feedback inhibition as assessed in our physiological data. We then fixed all model parameters, and proceeded to probe the ability of this circuit to perform pattern separation on temporally complex oscillatory inputs. The major, highly robust, result of this computational study was that the impact of feedback inhibition on pattern separation is frequency-dependent. Specifically, we find that the separation of input patterns during gamma oscillations > 30 Hz is powerfully and selectively enhanced by the feedback circuit. Remarkably, this mechanism involved decreased interneuron activity and was particularly efficient for very similar input patterns. Such an effect has not been discovered in earlier modeling studies, because most models have discretized time, calculating the pre-inhibition population activity, the resulting inhibition, and the inhibition-corrected population activity in a single time step, sometimes assuming an average corrected population rate within this time step (**Myers and Scharfman, 2009**; **Rolls and Treves, 1998**; **Trappenberg, 2010**). Thus, they do not capture temporal features of feedback circuits. On the other hand, a number of spike based, temporally resolved models have considered only temporally unstructured (Poisson) inputs (**Chavlis et al., 2017**; **Hendrickson et al., 2015**; **Hummos et al., 2014**; **Yim et al., 2015**). We suggest that the precise spatiotemporal organization of the feedback circuit, together with the temporal structure of DG inputs is a crucial determinant of pattern separation. Indeed, the DG and its inputs have a strong, behaviorally relevant, temporal structure (**Lasztóczi and Klausberger, 2017**; **Mizuseki et al., 2009**; **Pernía-Andrade and Jonas, 2014**; **Skaggs et al., 1996**). Novelty experience can induce increased gamma and beta range activity (**Berke et al., 2008**; **Rangel et al., 2015**; **Trimper et al., 2017**), and explorative activity with rearing is also associated with increased gamma oscillations (**Barth et al., 2018**). A previous model has addressed how fast, rhythmic gamma-frequency feedback inhibition may implement a type of 'k-winners-take-all' operation, a basic computational component of pattern separation models (**de Almeida et al., 2009**), although this model relies on faster synaptic timescales than we observed in our compound IPSCs. Perhaps most interestingly, the occurrence of oscillations in the slow-gamma range has recently been reported to be causally related to associative memory formation (**Sasaki et al., 2018**; **Trimper et al., 2017**), a process thought to require pattern separation. Consistent with this finding, **Hsiao et al. (2016)** report DG driven gamma entrainment of CA3, the presumed primary storage location of associative memories. Together, this suggests that the dentate pattern separator may be optimized to rapidly detect subtle degrees of difference within the environment in gamma-dominated exploratory brain states, a capability likely to support successful memory encoding of novel environmental features, and potentially aiding in rapid discrimination during recall.

Importantly, the frequency-dependency of pattern separation was driven by the feedback circuit. This effect was highly robust when varying the decay time constants of the inhibitory synaptic conductances, the time windows of analysis, the similarity measure, or the PP input strength. By contrast, feedforward inhibition and anatomical pattern separation was robustly independent of frequency modulation. Together this suggests that frequency-dependent pattern separation is a key property of the local inhibitory feedback circuit. Importantly, this does not preclude that additional, long range projections may add further complexity (**Szabo et al., 2017**). Also note that in addition to the instantaneous pattern separation mechanisms investigated here, potentially complementary mechanisms at much longer time scales have been proposed involving ongoing neurogenesis (**Aimone et al., 2011**; **Clelland et al., 2009**; **Li et al., 2017**; **Sahay et al., 2011**; **Severa et al., 2017**; **Temprana et al., 2015**).

Spatiotemporal organization of inhibition and pattern separation

The model also allowed us to examine the impact of the spatiotemporal organization of inhibition on pattern separation. Facilitation of feedback circuits produced a small but robust enhancement of pattern separation, while spatial tuning of feedback inhibition did not. The facilitation of feedback

inhibition is a remarkable feature of the DG, which we to our knowledge have described for the first time. It is in marked contrast to area CA1, where somatically measured feedback inhibition shows strong depression (**Pothmann et al., 2014**; **Pouille and Scanziani, 2004**) and is particularly surprising given the prevalence of depression in the literature on pairwise connections (**Supplementary file 1**). Our experimental and modeling data suggest that the strong facilitation of the mossy fiber input to the feedback circuit is the principal mediator of this net facilitation. Physiologically, facilitation may aid sparse GC spiking to efficiently recruit inhibition, particularly during burst-like activity (**Pernía-Andrade and Jonas, 2014**).

In our model, spatial tuning of feedback inhibition had no effects on pattern separation. This may derive from the fact that PP inputs were spatially broad and random, as suggested by anatomical studies (**Tamamaki, 1997**; **Tamamaki and Nojyo, 1993**). In general, the effect of localized inhibition could be more relevant if synchronously activated populations of GCs are locally clustered (**Feldt Muldoon et al., 2013**). For instance, GCs in the inferior and superior blades of the DG are known to be differentially active (**Alme et al., 2010**; **Chawla et al., 2005**). Accordingly, localized inhibition might be important for independent processing between the two blades. An alternative function of spatially graded inhibition has been proposed by **Strüber et al. (2015)**, who suggest that it is more effective in promoting synchronous gamma oscillations. Accordingly, spatial tuning may play a role in creating the oscillatory dynamics, found here to critically impact the feedback inhibitory pattern separation performance.

In conclusion, this study provides the first comprehensive, quantitative description of the spatiotemporal properties of the DG feedback inhibitory microcircuit, and predicts that these properties will selectively enhance the separation of highly similar input patterns during learning-related gamma oscillations. This mechanism may be relevant for understanding disease states in which there is a coincidence of dentate gyrus-centered pathology with abnormal oscillatory activity, and memory and pattern separation deficits such as temporal lobe epilepsy, Alzheimer's disease or schizophrenia (**Andrews-Zwilling et al., 2012**; **Gillespie et al., 2016**; **Leal and Yassa, 2018**; **Verret et al., 2012**).

Materials and methods

Key resources table

Reagent type (species) or resource	Designation	Source or reference	Identifiers	Additional information
Strain, strain background (*Mus musculus*)	C57BL/6N	Charles River	Strain Code 027	
Strain, strain background (*Mus musculus*)	Prox1-Cre	MMRRC-UCD	RRID: MMRRC_036632-UCD	obtained as cryopreserved sperm and rederived in the local facility
Strain, strain background (*Mus musculus*)	Ai32-ChR-eYFP	Jackson Laboratory	RRID: IMSR_JAX:012569	
Other	UGA-40	RAPP Optoelectronics		Galvanometric, focal laser stimulation device
Software, algorithm	Igor Pro 6.3	Wavemetrics		
Software, algorithm	Python 3.5 scikit learn	**Pedregosa et al. (2011)**		https://scikit-learn.org/stable/
Software, algorithm	ouropy	Custom Python code. This Paper		https://github.com/danielmk/ouropy
Software, algorithm	pyDentate	Custom Python code, This Paper		https://github.com/danielmk/pyDentateeLife2020
Software, algorithm	Neuron 7.4	**Carnevale and Hines, 2006**		
Software, algorithm	Prism 6	Graphpad		

Animals and slice preparation

All experimental procedures were conducted in accordance to federal law of the state of North Rhine-Westphalia (Aktenzeichen 84–02.04.2014.A254), minimizing unnecessary pain and discomfort. Experiments were performed on horizontal hippocampal slices of 21- to 97-day-old mice. Ca^{2+} imaging and a subset of dual recording experiments were performed in C57/Bl6 mice obtained from

Charles River Laboratories (Wilmington, MA). Optogenetic experiments and the remaining dual recording experiments were performed on double transgenic offspring of Tg(Prox1-cre)SJ39Gsat/Mmucd, MMRRC Cat# 036632-UCD, RRID: MMRRC_036632-UCD) obtained as cryopreserved sperm and rederived in the local facility (**Gong et al., 2007**; **Gong et al., 2003**) and Ai32-mice (B6;129S-Gt(ROSA)26Sor$^{tm32(CAG-COP4*H134R/EYFP)Hze}$/J, IMSR Cat# JAX:012569, RRID: IMSR_JAX:012569). For preparation the animals were deeply anesthetized with Isoflurane (Abbott Laboratories, Abbot Park, USA) and decapitated. The head was instantaneously submerged in ice-cold carbogen saturated artificial cerebrospinal fluid (containing in mM: NaCl, 60; sucrose, 100; KCl, 2.5; NaH_2PO_4, 1.25; $NaHCO_3$, 26; $CaCl_2$, 1; $MgCl_2$, 5; glucose, 20) and the brain removed.

Horizontal 350 µm thick sections were cut with a vibratome (VT1200 S, Leica, Wetzlar, Germany, 300 µm sections for hilar recordings). To obtain maximum-connectivity-plane slices the brain was glued to its dorsal surface (compare **Bischofberger et al., 2006**). The slicing depth at which the temporal pole of the hippocampus first became visible was noted (depth = 0 µm). From here the first four sections were discarded (up to a depth of 1400 µm). The following two to three sections were secured such that one further section before the beginning of the dorsal hippocampus (approximately 2400 µm) could be discarded. Slices were incubated at 35˚C for 20 to 40 min and then stored in normal ACSF (containing in mM: NaCl, 125; KCl, 3.5; NaH_2PO_4, 1.25; $NaHCO_3$, 26; $CaCl_2$, 2.0; $MgCl_2$, 2.0; glucose, 15) at room temperature. Recordings were performed in a submerged recording chamber at 33–35˚C under constant superfusion with carbogen saturated ACSF (3 ml/min). Experiments were performed in the superior blade unless otherwise indicated.

Electrophysiological recordings

Hippocampal dentate GCs were visually identified using infrared oblique illumination contrast microscopy in a 20x or 60x water immersion objective (Olympus, XLumPlanFl, NA0.95W or Nikon, N60X-NIR Apo, NA1.0W) on an upright microscope (TriMScope, LaVision Biotech, Bielefeld, Germany or Nikon Eclipse FN1, Tokyo, Japan). For IPSC measurements the whole-cell patch-clamp configuration was established with a low chloride cesium-methane-sulfonate based intracellular solution (intracellular solution containing in mM: CH_3O_3SCs, 140; 4-(2-hydroxyethyl)−1-piperazineethanesulfonic acid (HEPES-acid), 5; ethylene glycol tetraacetic acid (EGTA), 0.16; $MgCl_2$, 0.5; sodium phosphocreatine, 5; glucose, 10). For GC current clamp experiments a low-chloride solution (CC-intracellular solution containing in mM: K-gluconate, 140; 4-(2-hydroxyethyl)−1-piperazineethanesulfonic acid (HEPES-acid), 5; ethylene glycol tetraacetic acid (EGTA), 0.16; $MgCl_2$, 0.5; sodium phosphocreatine, 5) was used. GCs with input resistances greater than 300 MΩ were discarded in order to exclude immature GCs (**Schmidt-Hieber et al., 2004**). Hilar cells were recorded with intracellular solution containing in mM: K-gluconate, 140; KCL, 5; HEPES-acid, 10; EGTA, 0.16; Mg-ATP, 2; Na_2-ATP, 2; pH adjusted to 7.25; 277 mmol/kg without biocytin. 0.3% biocytin (Sigma-Aldrich, B4261). In all imaging experiments and a subset of optogenetic experiments, the intracellular solution additionally contained 100 µM Alexa 594 hydrazide sodium salt (Life Technologies, Carlsbad, USA). The identity of visually and electrophysiologically identified mature GC was confirmed by their dendritic morphology after dye filling in every case tested. Pipette resistance of the patch pipettes was 3–7 MΩ. Voltage-clamp recordings were performed with a Multiclamp 700B (Molecular Devices, Sunnyvale) or a BVC-700A amplifier (Dagan Corporation, Minneapolis). Current-clamp recordings were performed with a Multiclamp 700B. Voltage or current signals were digitized with a Digidata 1322A (Molecular Devices) or (Instrutech ITC-16, Heka Electronics, Ludwigshafen, Germany) at 10 or 50 kHz and recorded using Clampex 10.2 (Molecular Devices) or Igor Pro 6 (Wavemetrics, Lake Oswego) on a PC running Windows XP. All electrophysiological recordings were obtained at least in triplicate, then averaged and counted as a single biological replicate. For IPSC measurements, cells were held at 0 mV including liquid-junction potential correction (estimated at 16 mV). To aid the voltage clamp throughout the cell, this depolarized membrane potential was slowly approached during a 15 min pre-equilibration period, during which Cs^+ entered the cell. For CC-recordings liquid junction potential was not corrected. IPSCs were normalized to the maximally elicited IPSC over space and power for each respective cell. Importantly, this normalization does not require prespecification of the location or power at which a respective cell's maximum occurs. Note, that due to this procedure all normalized IPSC values are by definition below 100%. Chemicals for electrophysiological experiments were obtained from Sigma-Aldrich (St. Louis). All drugs were purchased from Tocris Bioscience (Bristol, UK).

Dual patch experiments

Two GCs within 100 µm of each other were recorded. To test for single GC-induced feedback inhibition 10 to 15 trains of 10 APs at 100 Hz were elicited by brief (3 ms) current injections in one cell. Inhibition was monitored either in VC, while holding the cell at 0 mV to allow the detection of small IPSCs (***Figure 2—figure supplement 3***, n = 7 cell pairs, seven directions) or current clamp while holding the cell at −60 mV, allowing to probe for inhibition in both directions (not shown, n = 4 cell pairs, eight directions).

Ca^{2+} imaging

Dye loading was modified from ***Garaschuk et al. (2006)*** and performed in the submerged chamber at 35˚C under constant superfusion. Briefly, a dye solution containing: 1 mM Oregon Green 488 BAPTA-1 acetoxy-methyl ester (OGB-1 AM); 2% pluronic F-127; 150 mM; 2.5 mM KCl; 10 mM HEPES). The dye was injected into the slice along the superior blade of the GC layer using standard patch pipettes (4–5 locations, 100 µm intervals, 30 µm depth, 3 min at 500 mbar per location). Recordings were started at least 45 min after the staining procedure. Population Ca^{2+} Imaging was performed using a multibeam two-photon fluorescence microscope (TriMScope, LaVision Biotech, Bielefeld, Germany) with excitation light at 810 nm. Images were acquired with a digital CMOS camera (ORCA-Flash, Hamamatsu) through a high numerical aperture 20x water immersion Objective (XLumPlanFl, NA-0.95, Olympus). This allowed imaging of a large field of view (320 × 240 µm) with high spatial and temporal resolution (1920 × 1440 pixels, 20 Hz) at acceptable signal to noise ratios. Time series were processed with ImageJ 1.48o and IGOR Pro 6.3 in a semiautomatic manner. Regions of interest were manually placed onto all well loaded cells which remained visible throughout the experiment. Ca^{2+} fluorescence increase normalized to baseline (ΔF/F) traces of individual cells were calculated without background subtraction. The fraction of responders for each time series was extracted by automatic thresholding at ΔF/F = 0.94%. The threshold was determined by combined cell-attached and Ca^{2+} imaging experiments. Note, that for these experiments the stimulation electrode was placed into the hilus in order to obtain a sufficient number of true positive responders. The imaged cell population comprised on average 46 ± 18 (standard deviation) cells (n = 23 slices). The active cell fraction corresponds to the fraction of responders normalized to the dye-loaded population within each section. To assess the spatial distribution of cell activation in imaging experiments, ΔF/F projections were created by averaging and smoothing four frames during the transient and four frames at baseline fluorescence and then calculating the pixel wise ΔF/F.

Antidromic electrical stimulation was achieved using a bipolar cluster microelectrode (FHC, Bowdoin) connected to a digital stimulus isolator (AM-systems, Sequim), placed into stratum lucidum in the CA3 region. IPSCs at individual powers were elicited 5 to 13 times at 0.1 Hz and averaged (0.1 ms pulse time). The amplitude beyond which the stimulus isolator could not pass the full current, determined the maximal stimulation amplitude for each experiment.

In order to obtain the input-output relationships of the feedback inhibitory circuit data, each variable was averaged over slices by power. This was necessary since only a small subset of experiments in which inhibition was completely blocked could also be successfully imaged (6 of 8 sections). Due to the small numbers of active cells within individual slices with sufficient dye loading (n = 23 slices) analysis of only these six slices leads to a very piecemeal recruitment curve. A more accurate estimation of the recruitment of feedback inhibition was obtained by averaging the cell activation and inhibition over all appropriate slices and relating them by power, respectively. Note that while the fraction of activated cells in non-MCP sections (not included in the quantitative analysis) was mostly zero, IPSCs were almost always present (in 28 of 29 cells in non-MCP sections).

Optogenetic stimulation

Focal optogenetic stimulation was achieved through a galvanometer driven spot illumination device coupled to a 473 nm DPSS Laser (UGA-40, DL-473, Rapp Optoelectronics, Hamburg, Germany) on an upright microscope (Nikon Eclipse FN1, Tokyo, Japan). The width of the resulting stimulation spot at the focal plane was 8.36 ± 0.04 µm (full width at half max; Nikon 10X Plan Fluor, NA 0.3 Laser powers are given in arbitrary units from 1 to 7 corresponding to 15 ± 1 µW, 107 ± 14 µW, 292 ± 42 µW, 762 ± 105 µW, 1433 ± 49 µW, 1729 ± 165 µW and 1660 ± 163 µW at the objective (n = 5

measurements). All illumination spots were placed at approximately 40 µm into the ML at the slice surface. Stimulation pulses were of 20 ms duration.

Light intensity distribution

To measure the light intensity distribution throughout a slice the setup was modified to image the slice from below while the laser beam was focused to its surface (***Figure 2—figure supplement 1C–F***). This was achieved by focusing a surgical Microscope with 36x magnification (M695, Leica Microsystems, Wetzlar, Germany) to the lower slice surface. Images were taken with a CCD camera (Nikon D60). Acute sections of 100, 150, 200, 250, 300 and 350 µm thickness were cut from Prox1-ChR-eYPF mice as described above. The laser was focused to the surface of the slice in the molecular layer and an image was taken at every laser power (p=1 to 7 AU). The stage was moved for every image to avoid bleaching or phototoxicity. Linear profiles of the resulting isometric light distribution were measured in several directions and averaged to obtain an x profile per section. The x-profiles of slices of different thickness were then stacked to obtain the xz-profile. Values below 100 µm depth were obtained through fitting a Gaussian function in x-direction at 100 µm depth and an exponential function in z-direction. Complete three-dimensional intensity profiles of three different locations of two slices within the dentate molecular layer were averaged.

Calculation of the optogenetically activated cell fraction

To assess the active fraction of GCs, approximately two GCs were recorded in cell-attached mode in each slice in which an IPSC was recorded. Illumination spots were placed along the GC layer at 100 µm intervals (***Figure 2—figure supplement 1***). The entire profile was probed in triplicate with 1 s intervals between individual locations. When the stimulation spot was in sufficient proximity to the recorded cell clear APs were generally visible (in 25 of 26 cells), and otherwise could be induced through simultaneous cell attached depolarization. Cell-attached spikes were detected by automatic thresholding at 6x standard deviation of the baseline. The spatial profile of firing probabilities, centered on the recorded cells, was averaged within each section. To test if cell activation properties differed between blades the maximum firing probabilities (at p=7) as well as the slopes (increase in firing probability from p=1 to 7) when simply averaging over all location of a given cell were compared by t-test (n = 7 sections per blade, p=0.490 and 0.684 for max. AP probability and slope, respectively). Since no difference was observed a single firing probability distribution as a function of the distance along the GC layer (x – distance) was calculated for each power (***Figure 2—figure supplement 1B***, n = 14 sections, seven per blade). However, the firing probability of cells in the vicinity of the illumination spot is likely to increase not only as a function of the laser power and spread at the surface, but also of the penetration depth of the light cone. In order to calculate the firing probabilities throughout the slice, the firing probability distribution at the surface was related to the measured light intensity distribution throughout the slice (***Figure 2—figure supplement 1C–F***; see above) utilizing a 'virtual distance' measure. Since cells were measured at random distances from the molecular layer border, the light intensity distribution, like the firing probabilities were collapsed to two dimensions, x-distance along the GC layer and z-distance with increasing slice depth. The 'virtual distance' was calculated as the mean distance from a given slice-surface pixel to all other pixels of the light intensity distribution weighted by the intensity within those pixels (***Figure 2—figure supplement 1G***). Assigning the firing probabilities of pixels at the slice surface to their respective virtual distance yields the firing probability distribution as a function of virtual distance, which was well approximated by a gaussian fit (***Figure 2—figure supplement 1H***). This fit was used to also calculate the firing probabilities of pixels/cells deeper in the slice using the measured light intensity distribution as input. The active cell fraction then corresponds simply to the mean firing probability throughout the slice. This calculation is independent of the size and number of GC and was performed for every power individually. We noted that a large fraction of the recorded spikes occurred with larger latency than the typical IPSC following the beginning of the 20 ms stimulation pulse (***Figure 2—figure supplement 1I***, example from a single slice). Since only APs preceding the IPSC can participate in its recruitment, we calculated the fraction of total spikes which preceded mean IPSC latency for every power, and fitted the resulting relation with an exponential function (***Figure 2—figure supplement 1J***). All active cell fractions were corrected by this factor (***Figure 2—figure supplement 1J***, bottom). Note that this does not take account of the disynaptic delay between mossy fiber output

and GC input, thereby potentially slightly overestimating the true recruiting population. For comparison, the active cell fraction was also computed with alternative assumptions about the decay of the firing probability with increasing slice depth. If no firing probability decay with increasing depth is assumed, the active cell fraction throughout the slice is given simply by the average of the measured firing probabilities at the slice surface (***Figure 2—figure supplement 1K***, upper grey dashed line). Alternatively, the firing probability decay with depth was assumed to be identical to the measured decay along the slice surface (isometric firing probability distribution; ***Figure 2—figure supplement 1K***, lower grey dashed line). In this case, Gaussian functions were fit to the probability distributions at the surface and these Gaussian functions were then assumed to extend also in the z-dimension. The active GC fraction was then calculated by numerical integration under the two dimensional Gaussian (with the bounds from 0 to 350 µm in z and −888 to 888 µm in x, which corresponds to the mean GC layer length) normalized to the same area with a uniform firing probability of one. The best estimate of the active GC fraction, incorporating light intensity measurements (***Figure 2—figure supplement 1K***, black line), was within these upper and lower bound estimates.

Comparison of focal and global activation

To globally activate the GC population a multimode light fiber (BF-22, Thorlabs, New Jersey) coupled to a 473 nm laser (Omicron Phoxx, Rodgau-Dudenhofen, Germany) was placed above the slice surface, non-specifically illuminating the entire hippocampus. Analogous to focal stimulations, the activated cell fraction was calculated as the firing probability of individual cells following 20 ms pulses. Here, no spatial normalization is necessary since cells were sampled from random locations with respect to the light fiber. Firing probabilities for the focal stimulation in these sections was calculated as the simple average of all stimulation locations.

Spatial distribution of feedback inhibition

The same stimulation paradigm which was used to assess cell activation was used to assess the spatial distribution of feedback inhibition. For individual cells, IPSCs at each location and power were averaged. The entire profile was normalized to the largest measured IPSC of that cell, independent of the power and stimulation location at which it occurred. For analysis, all IPSC profiles were spatially aligned to the recorded cells. The mean distance to apex ± one standard deviation was 356 ± 163 µm and 322 ± 97 µm for cells from the superior and inferior blade, respectively (n = 8 cells in each blade). In order to test whether there were any distinct effects of the apex, such as a steep decay of inhibition, which would be masked by alignment to the recorded cells, we also aligned the profiles to the apex (not shown). However, no such effects were visible. To analyze the saturated IPSC profiles, normalized IPSC amplitudes from p=5 to 7 were averaged for each cell. In order to analyze the effects of local versus remote stimulation for each blade a distance was chosen such that each remote location was still within the DG but in the other blade (800 µm from the recorded cell). Normalized IPSCs of the three locations surrounding the recorded cell or this remote location were averaged within each power to obtain the IPSC amplitudes for further analysis. The cell fraction required for the activation of a half-maximal IPSC in each section was assessed for each cell by linear interpolation between the measured values. Since no differences were found between superior and inferior inhibition, recordings of both blades were pooled to analyze the kinetic properties of IPSCs. All parameters were calculated on the multiple trials of individual cells. The latency was measured as the time from the beginning of the pulse to when the IPSC superseded six fold standard deviation of the baseline. The jitter was calculated as the standard deviation of these latencies for individual cells. The rise time was calculated as the mean 20 to 80 rise time of each cell and the decay time constant was obtained from an exponential fit to the decaying phase of the compound IPSC.

Hilar recordings

Intrinsic properties of hilar cells were quantified based on 4.6 s long depolarizing current steps or 500 ms hyperpolarizing current steps. AP threshold and fast AHP amplitude were measured from the first AP in the first current step in which an AP occurred within the first 10 ms. Clustering fraction and mean AP time were calculated from the current injection that elicited the maximum average AP frequency. The Clustering fraction represents the fraction of APs that occur within 60 ms before or after another AP (***Larimer and Strowbridge, 2008***). Mean AP time was calculated as the mean AP

time point normalized to the duration of the current injection (4.6 s). Input resistance was calculated as the slope of the IO curve from the hyperpolarizing current ladder. Cells were manually classified as mossy cells or interneurons based on these intrinsic properties. To objectively confirm classification, we performed unsupervised k-means clustering using scikit-learn (**Pedregosa et al., 2011**). For clustering all six measures were normalized by mean and variance. Two cells with conflicting classification were not included in further analysis.

After recording, slices were fixed for 1 hr in 4% PFA and stored overnight in 0.25% PBS-T at room temperature. The following day they were transferred to PBS for short term storage or immediately stained. For biocytin staining, sections were washed with PBS and incubated with Streptavidin-Alexa-Fluor-555 Conjugate (Invitrogen, S32355), 1:1000 in 0.25% PBS-T overnight at 4˚C. The following day they were co-stained with DAPI 1:1000 in PBS for 30 min and mounted with Aqua-Poly/Mount. Cells were imaged with the Leica SP8 Confocal Microscope of the Microscopy Core Facility at the University Clinic Bonn using a 40x water immersion objective.

Short-term dynamics

Short-term dynamics of GCs and hilar cells were assessed using antidromic electrical or optogenetic stimulation at minimal power (the smallest stimulation power that yielded reliable responses). Trains of 10 pulses at 1, 10, 30, 50 Hz were delivered in triplicate and averaged (excluding sweeps with action currents for hilar cells). In all GCs and a subset of hilar cells we confirmed that PSCs could be blocked by at least 90% with 40 µM CNQX + 50 µM D-APV (n = 12, 23 for GCs and hilar cells respectively). Facilitation indices were obtained by normalizing the average of the last three PSC peaks to the first.

To test for differential dynamics between local and remote inhibition analogous trains of optogenetic 20 ms pulses at powers below saturation (usually p=2 for local inhibition and p=3 for remote inhibition) were delivered. For each power and frequency, five repeats were recorded and averaged. AP probabilities were assessed by cell-attached recordings with the stimulation site close to the recorded cell. Cell-attached spikes were detected by automatic thresholding as above.

Voltage escape estimation model

A simple multicompartmental passive 'ball and stick' model with number of segments following the d_lambda rule (**Carnevale and Hines, 2006**) and passive properties Ra = 181 Ωcm, Cm = 1 uFcm^{-2} and a leak conductance = 0.0002 Scm^{-2}, which gave an Rin of 165 MΩ, were adopted from **Carnevale and Hines (2006)** and **Krueppel et al. (2011)**. A soma (20 µm diameter) contained one dendrite (3 µm diameter, 200 µm length) with an alpha synapse point mechanism (Erev −90 mV) placed at 180 µm from the soma. The range of synaptic conductances (0.1–50 nS; adopted from **Williams and Mitchell, 2008**) elicited IPSC amplitudes in the model, which covered the range of somatic IPSC amplitudes that were experimentally measured (3 pA – 1nA). Voltage clamp experiments were simulated using a single electrode point mechanism at the soma (Rs 5 MOhms, to model a Rs of 15 MΩ compensated 70%) with a holding potential of 0 mV. The transfer (Zc) and input impedance (Zn) were determined from the model and used to calculate the actual peak IPSC amplitude at the soma for a given synaptic conductance. Simulations were run in the Neuron 7.5 simulation environment.

Biophysically realistic dentate gyrus lamella model

Simulations were run in python 2.7 with NEURON 7.4 (**Carnevale and Hines, 2006**) on Windows 7/10. We created a generic python-NEURON interface (https://github.com/danielmk/ouropy; copy archived at https://github.com/elifesciences-publications/ouropy) which wraps NEURON's python module, into which we ported the conductance based DG model by **Santhakumar et al. (2005)**. Model code is available at https://github.com/danielmk/pyDentateeLife2020 (copy archived at https://github.com/elifesciences-publications/pyDentateeLife2020).

We first tuned the original model to capture our experimentally determined properties in the most parsimonious way. During tuning we also updated some model properties to better reflect current data and our experimental paradigm in an individual DG lamella:

We introduced a T-type Ca^{2+} channel mechanism into MCs to more realistically reflect the depolarizing envelope at the onset of a positive current step observed in real MCs. Furthermore, while

the original model placed the perforant path input at the distal dendrite of GCs, we moved all perforant path synapses to the middle compartment of the dendrite. In order to be able to capture the results of convergent and divergent synaptic inputs in sufficient resolution to produce the empirically observed activity gradations, we up-scaled cell numbers by a factor of four. To model space, we assumed all cell types to be spread out on a 2 mm DG lamella. Since MCs project to GCs primarily outside the lamellar plane, we removed the MC to GC connection. To allow patterned PP input we adapted PP input specifications from ***Yim et al. (2015)***.

We then proceeded in a first phase of model adjustment, and adapted several parameters to reproduce our in vitro findings regarding spatial and temporal feedback inhibition (***Supplementary file 2***). To model frequency-dependent facilitation on mossy fiber outputs, we implemented a simple frequency-dependent synapse model (tmgsyn) (***Tsodyks et al., 1998***), and matched the facilitation time constant as well as the decay time constants of individual PSCs to our experimental observations. As in the original model, each cell gives rise to a fixed number of synaptic connections which are spatially restricted to a target pool of adjacent cells. We tuned the size and spatial extent of this target pool to reproduce our spatial data. To provide local inhibition we implemented a 'local' interneuron type (BC), whose inputs and outputs were spatially restricted to an ~600 µm area (as described by ***Strüber et al., 2015***). To provide global inhibition we implemented a second class of inhibitory interneurons (HC) whose inputs and outputs connect to GCs independent of space. This simple formulation allowed us to reproduce the recruitment curves seen for local, remote and global GC activation paradigms. To achieve plausible activity levels, we further adapted synaptic weights similar to ***Yim et al. (2015)***. We call the network incorporating both spatially restricted BC synapses and mossy fiber facilitation the full tuned network. To isolate the contribution of intrinsic GC properties to pattern separation, we created a disinhibited network by setting the synaptic weight from all interneurons to zero. We also isolated feedforward inhibition by decreasing the mossy fiber to interneuron synaptic weight to zero. To evaluate the effect of spatially constrained inhibition, we created a global network, where the target pool of all interneuron was the entire GC population. To evaluate the effect of mossy fiber facilitation, we set the facilitation time constant to zero, effectively eliminating facilitation. Details on the model parameters are summarized in ***Supplementary file 2***).

To study pattern separation, we generated 400 PP inputs. Each PP synapsed onto 100 randomly chosen GCs with the spatial connection probability being governed by a gaussian probability distribution with standard deviation 1 mm and random peak position, modeling a full, nearly uniform input connectivity of individual afferents (***Tamamaki and Nojyo, 1993***). To generate theta modulated spike patterns, we used the inhomogeneous Poisson generator from Elephant 0.5.0-Electrophysiology-Analysis-Toolkit with a 10 Hz (theta) sinusoidal rate profile with a peak of 100 Hz, a minimum of 0 Hz and a duration of 600 ms. To generate input patterns with varying overlap from PP afferents i = 1 to 400, we activated afferents i to i+23 in increments of i = 1 per run. We performed 25 runs for each condition resulting in 300 unique comparisons, excluding self-comparisons. The random seed was held constant between different runs of the same condition, resulting in differing input patterns being fed into the same network. All randomness was generated with the python module numpy.random.

To quantify pattern similarity, we used Pearson's product moment correlation coefficient R of the population rate vectors for input and output patterns. The population rate vector refers to the vector of the mean firing rates of all cells in the population within the entire 600 ms simulation, or 100 or 33 ms time windows for the time resolved analyses. All statistical analyses of the model were performed with n = 7 different random network seeds. During Model development (tuning phase), we first ported the model by ***Santhakumar et al. (2005)*** with closely constrained DG cell-types, and further constrained it to reproduce our physiological data. We then locked the model and proceeded to an (in silico) experimental phase, in which pattern separation was investigated.

To compute full pattern separation effects (***Figure 6D***), we calculated the mean R_{out} within R_{in} bins of 0.1 and measured the area to the unity line (computed as the mean of the binwise $R_{in} - R_{out}$ differences). To compute isolated pattern separation effects of specific manipulations we subtracted the respective R_{out} values with and without the manipulation, thereby obtaining a ΔR_{out} value for each individual R_{in}. We then again computed the bin-wise mean and quantified the area under the curve, yielding the mean ΔR_{out} analogous to the full effects. Note, that the sequence of averaging and subtracting is irrelevant, and was inverted only to match the figure panels. Data are displayed as

mean ± SEM for each R_{in} bin (***Figure 6E–G***). The coefficient of variance (CoV) was calculated by normalizing the standard deviation of ΔR_{out} within each bin by the mean of that bin, and then averaging over bins, analogous to the previous analyses. However, only bins within $0.2 < R_{in} < 0.8$ were included, since at the borders very small means led to unreliable results. ΔCoV represents the difference between the mean CoV of the global (or nonfacilitating) and the tuned network models. For the temporally resolved pattern separation analysis, all measures were computed as above, but on population vector correlations within 100 or 33 ms time bins.

Statistics and Data Analysis

Analyses were performed using ImageJ, Microsoft Excel, Python and Igor Pro. Fits were performed using Igor Pro. Statistical analyses were performed using GraphPad Prism six or Igor Pro. Comparisons were two-tailed whenever applicable. Replicates refer to cells unless otherwise indicated (slices for imaging experiments and network seeds for modeling data). Given the lack of previous information on effect sizes, sample sizes were chosen according to field norms, such that only large effects can be detected (e.g. Cohen's $d > 1$ for paired tests). A single outlier facilitation index (***Figure 5E***) during model tuning was removed, as it was outside the triple standard deviation (due to a very small initial IPSC). Group allocation was achieved by alternating acquisition between groups. Statistical significance in Analysis of Variance (ANOVA) is indicated by §. F-values and degrees of freedom are given as F(DFn, DFd). When ANOVAs were followed by specific comparisons these are indicated by asterisks, where *p<0.05, **p<0.01 and ***p<0.001. Bargraphs and XY plots show means where error bars indicate standard error of the mean. In boxplots error bars represent the data range and boxes the upper and lower quartiles and the median.

Acknowledgements

This work was supported by the Deutsche Forschungsgemeinschaft (SFB 1089, ebGluNet, SPP2041), the BONFOR program of the University of Bonn Medical Center, the ERANET Neuron grant 'EpiNet' (to HB). We thank Olivia van Ray and Dominik Holtkamp for excellent technical assistance; Thoralf Opitz, Holger Dannenberg, Laura Ewell and Dirk Dietrich for valuable comments and Stefan Remy for access to multi-beam two-photon microscopy. We further acknowledge support by the Microscopy Core Facility of the Medical Faculty.

Additional information

Funding

Funder	Grant reference number	Author
Deutsche Forschungsgemeinschaft	SFB1089	Heinz Beck
Deutsche Forschungsgemeinschaft	ebGluNet	Heinz Beck
European Commission	EpiNet	Heinz Beck

The funders had no role in study design, data collection and interpretation, or the decision to submit the work for publication.

Author contributions

Oliver Braganza, Conceptualization, Resources, Data curation, Software, Formal analysis, Investigation, Visualization, Methodology; Daniel Mueller-Komorowska, Conceptualization, Resources, Software, Validation, Investigation, Methodology; Tony Kelly, Software, Supervision, Investigation, Methodology; Heinz Beck, Conceptualization, Resources, Supervision, Funding acquisition, Project administration

Author ORCIDs

Oliver Braganza https://orcid.org/0000-0001-8508-1070
Daniel Mueller-Komorowska https://orcid.org/0000-0002-2789-6068

Ethics

Animal experimentation: This study was performed in strict accordance with the recommendations of the Landesamt für Natur, Umwelt und Verbraucherschutz Nordrhein-Westfalen (LANUV, Aktenzeichen 84-02.04.2014.A254). All animals were anesthetized with isoflurane prior to euthanasia and organ extraction.

Decision letter and Author response

Decision letter https://doi.org/10.7554/eLife.53148.sa1
Author response https://doi.org/10.7554/eLife.53148.sa2

Additional files

Supplementary files

- Supplementary file 1. Literature review for DG circuit short-term dynamics. Studies reporting short-term dynamics within the DG circuit were reviewed with a main focus on facilitation or depression of synaptic connections defined by pre and postsynaptic cell types. Note the abundance of depressing synapses (quantitative descriptions of depression blue). Also note the complexity of direct connections between Interneurons (lower third of the table).

- Supplementary file 2. Model parameters. Overview of synaptic and intrinsic parameters between model cell-types. First row includes modeled cell number per type. **PP**: perforant path, **GC**: granule cell, **MC**: mossy cell, **BC**: basket cell, **HC**: Hilar perforant path associated cell; Weight: maximal synaptic conductance, Facilitation Max.: maximal fold increase of synaptic conductance, Decay Tau: synaptic decay time constant, Facilit. Tau: facilitation time constant, Delay: latency to postsynaptic event after presynaptic action potential, Target pool: range of n closest cells potentially receiving an output, Divergence: number of output synapses per cell stochastically picked from target pool, Target segments: cellular compartment receiving the synapse. Values in brackets are values for robustness analyses in Figs. S10, S11.

- Transparent reporting form

Data availability

The generic python-NEURON interface is available at https://github.com/danielmk/ouropy (copy archived at https://github.com/elifesciences-publications/ouropy). The model code is available at https://github.com/danielmk/pyDentateeLife2020 (copy archived at https://github.com/elifesciences-publications/pyDentateeLife202).

References

Aimone JB, Deng W, Gage FH. 2011. Resolving new memories: a critical look at the Dentate Gyrus, adult neurogenesis, and pattern separation. *Neuron* **70**:589–596. DOI: https://doi.org/10.1016/j.neuron.2011.05.010, PMID: 21609818

Alme CB, Buzzetti RA, Marrone DF, Leutgeb JK, Chawla MK, Schaner MJ, Bohanick JD, Khoboko T, Leutgeb S, Moser EI, Moser MB, McNaughton BL, Barnes CA. 2010. Hippocampal granule cells opt for early retirement. *Hippocampus* **20**:1109–1123. DOI: https://doi.org/10.1002/hipo.20810, PMID: 20872737

Andrews-Zwilling Y, Gillespie AK, Kravitz AV, Nelson AB, Devidze N, Lo I, Yoon SY, Bien-Ly N, Ring K, Zwilling D, Potter GB, Rubenstein JL, Kreitzer AC, Huang Y. 2012. Hilar GABAergic interneuron activity controls spatial learning and memory retrieval. *PLOS ONE* **7**:e40555. DOI: https://doi.org/10.1371/journal.pone.0040555, PMID: 22792368

Bakker A, Kirwan CB, Miller M, Stark CE. 2008. Pattern separation in the human hippocampal CA3 and dentate gyrus. *Science* **319**:1640–1642. DOI: https://doi.org/10.1126/science.1152882, PMID: 18356518

Barth AM, Domonkos A, Fernandez-Ruiz A, Freund TF, Varga V. 2018. Hippocampal network dynamics during rearing episodes. *Cell Reports* **23**:1706–1715. DOI: https://doi.org/10.1016/j.celrep.2018.04.021, PMID: 29742427

Bartos M, Vida I, Frotscher M, Meyer A, Monyer H, Geiger JR, Jonas P. 2002. Fast synaptic inhibition promotes synchronized gamma oscillations in hippocampal interneuron networks. *PNAS* **99**:13222–13227. DOI: https://doi.org/10.1073/pnas.192233099, PMID: 12235359

Berke JD, Hetrick V, Breck J, Greene RW. 2008. Transient 23-30 hz oscillations in mouse Hippocampus during exploration of novel environments. *Hippocampus* **18**:519–529. DOI: https://doi.org/10.1002/hipo.20435, PMID: 18398852

Berron D, Schütze H, Maass A, Cardenas-Blanco A, Kuijf HJ, Kumaran D, Düzel E. 2016. Strong evidence for pattern separation in human dentate gyrus. *Journal of Neuroscience* **36**:7569–7579. DOI: https://doi.org/10.1523/JNEUROSCI.0518-16.2016, PMID: 27445136

Bischofberger J, Engel D, Li L, Geiger JR, Jonas P. 2006. Patch-clamp recording from mossy fiber terminals in hippocampal slices. *Nature Protocols* **1**:2075–2081. DOI: https://doi.org/10.1038/nprot.2006.312, PMID: 17487197

Braganza O, Beck H. 2018. The circuit motif as a conceptual tool for multilevel neuroscience. *Trends in Neurosciences* **41**:128–136. DOI: https://doi.org/10.1016/j.tins.2018.01.002, PMID: 29397990

Buzsáki G. 2010. Neural syntax: cell assemblies, synapsembles, and readers. *Neuron* **68**:362–385. DOI: https://doi.org/10.1016/j.neuron.2010.09.023, PMID: 21040841

Carnevale NT, Hines ML. 2006. *The NEURON Book*. Cambridge: Cambridge University Press. DOI: https://doi.org/10.1017/CBO9780511541612

Cayco-Gajic NA, Clopath C, Silver RA. 2017. Sparse synaptic connectivity is required for decorrelation and pattern separation in feedforward networks. *Nature Communications* **8**:1116. DOI: https://doi.org/10.1038/s41467-017-01109-y, PMID: 29061964

Cayco-Gajic NA, Silver RA. 2019. Re-evaluating circuit mechanisms underlying pattern separation. *Neuron* **101**:584–602. DOI: https://doi.org/10.1016/j.neuron.2019.01.044, PMID: 30790539

Chavlis S, Petrantonakis PC, Poirazi P. 2017. Dendrites of dentate gyrus granule cells contribute to pattern separation by controlling sparsity. *Hippocampus* **27**:89–110. DOI: https://doi.org/10.1002/hipo.22675, PMID: 27784124

Chawla MK, Guzowski JF, Ramirez-Amaya V, Lipa P, Hoffman KL, Marriott LK, Worley PF, McNaughton BL, Barnes CA, a BC. 2005. Sparse, environmentally selective expression ofArc RNA in the upper blade of the rodent fascia dentata by brief spatial experience. *Hippocampus* **15**:579–586. DOI: https://doi.org/10.1002/hipo.20091

Clelland CD, Choi M, Romberg C, Clemenson GD, Fragniere A, Tyers P, Jessberger S, Saksida LM, Barker RA, Gage FH, Bussey TJ. 2009. A functional role for adult hippocampal neurogenesis in spatial pattern separation. *Science* **325**:210–213. DOI: https://doi.org/10.1126/science.1173215, PMID: 19590004

Dasgupta D, Sikdar SK. 2015. Calcium permeable AMPA receptor-dependent long lasting plasticity of intrinsic excitability in fast spiking interneurons of the dentate gyrus decreases inhibition in the granule cell layer. *Hippocampus* **25**:269–285. DOI: https://doi.org/10.1002/hipo.22371, PMID: 25252134

de Almeida L, Idiart M, Lisman JE. 2009. A second function of gamma frequency oscillations: an E%-max winner-take-all mechanism selects which cells fire. *The Journal of Neuroscience* **29**:7497–7503. DOI: https://doi.org/10.1523/JNEUROSCI.6044-08.2009, PMID: 19515917

Diamantaki M, Frey M, Berens P, Preston-Ferrer P, Burgalossi A. 2016. Sparse activity of identified dentate granule cells during spatial exploration. *eLife* **5**:e20252. DOI: https://doi.org/10.7554/eLife.20252, PMID: 27692065

Doherty J, Dingledine R. 1998. Differential regulation of synaptic inputs to dentate hilar border interneurons by metabotropic glutamate receptors. *Journal of Neurophysiology* **79**:2903–2910. DOI: https://doi.org/10.1152/jn.1998.79.6.2903, PMID: 9636096

Espinoza C, Guzman SJ, Zhang X, Jonas P. 2018. Parvalbumin^{+} interneurons obey unique connectivity rules and establish a powerful lateral-inhibition microcircuit in Dentate Gyrus. *Nature Communications* **9**:4605. DOI: https://doi.org/10.1038/s41467-018-06899-3, PMID: 30389916

Ewell LA, Jones MV. 2010. Frequency-tuned distribution of inhibition in the dentate gyrus. *Journal of Neuroscience* **30**:12597–12607. DOI: https://doi.org/10.1523/JNEUROSCI.1854-10.2010, PMID: 20861366

Feldt Muldoon S, Soltesz I, Cossart R. 2013. Spatially clustered neuronal assemblies comprise the microstructure of synchrony in chronically epileptic networks. *PNAS* **110**:3567–3572. DOI: https://doi.org/10.1073/pnas.1216958110, PMID: 23401510

Freund TF, Buzsáki G. 1996. Interneurons of the hippocampus. *Hippocampus* **6**:347–470. DOI: https://doi.org/10.1002/(SICI)1098-1063(1996)6:4<347::AID-HIPO1>3.0.CO;2-I, PMID: 8915675

Garaschuk O, Milos RI, Konnerth A. 2006. Targeted bulk-loading of fluorescent indicators for two-photon brain imaging in vivo. *Nature Protocols* **1**:380–386. DOI: https://doi.org/10.1038/nprot.2006.58, PMID: 17406260

Geiger JR, Lübke J, Roth A, Frotscher M, Jonas P. 1997. Submillisecond AMPA receptor-mediated signaling at a principal neuron-interneuron synapse. *Neuron* **18**:1009–1023. DOI: https://doi.org/10.1016/S0896-6273(00)80339-6, PMID: 9208867

Gilbert PE, Kesner RP, Lee I. 2001. Dissociating hippocampal subregions: double dissociation between dentate gyrus and CA1. *Hippocampus* **11**:626–636. DOI: https://doi.org/10.1002/hipo.1077, PMID: 11811656

Gillespie AK, Jones EA, Lin YH, Karlsson MP, Kay K, Yoon SY, Tong LM, Nova P, Carr JS, Frank LM, Huang Y. 2016. Apolipoprotein E4 causes Age-Dependent disruption of slow gamma oscillations during hippocampal Sharp-Wave ripples. *Neuron* **90**:740–751. DOI: https://doi.org/10.1016/j.neuron.2016.04.009, PMID: 27161522

Gong S, Zheng C, Doughty ML, Losos K, Didkovsky N, Schambra UB, Nowak NJ, Joyner A, Leblanc G, Hatten ME, Heintz N. 2003. A gene expression atlas of the central nervous system based on bacterial artificial chromosomes. *Nature* **425**:917–925. DOI: https://doi.org/10.1038/nature02033, PMID: 14586460

Gong S, Doughty M, Harbaugh CR, Cummins A, Hatten ME, Heintz N, Gerfen CR. 2007. Targeting cre recombinase to specific neuron populations with bacterial artificial chromosome constructs. *Journal of Neuroscience* **27**:9817–9823. DOI: https://doi.org/10.1523/JNEUROSCI.2707-07.2007, PMID: 17855595

Hainmueller T, Bartos M. 2018. Parallel emergence of stable and dynamic memory engrams in the Hippocampus. *Nature* **558**:292–296. DOI: https://doi.org/10.1038/s41586-018-0191-2, PMID: 29875406

Harney SC, Jones MV. 2002. Pre- and postsynaptic properties of somatic and dendritic inhibition in dentate gyrus. *Neuropharmacology* **43**:584–594. DOI: https://doi.org/10.1016/S0028-3908(02)00169-7, PMID: 12367604

Hefft S, Jonas P. 2005. Asynchronous GABA release generates long-lasting inhibition at a hippocampal interneuron-principal neuron synapse. *Nature Neuroscience* **8**:1319–1328. DOI: https://doi.org/10.1038/nn1542, PMID: 16158066

Hendrickson PJ, Yu GJ, Song D, Berger TW. 2015. Interactions between inhibitory interneurons and excitatory associational circuitry in determining Spatio-Temporal dynamics of hippocampal dentate granule cells: a Large-Scale computational study. *Frontiers in Systems Neuroscience* **9**:155. DOI: https://doi.org/10.3389/fnsys.2015.00155, PMID: 26635545

Hsiao YT, Zheng C, Colgin LL. 2016. Slow gamma rhythms in CA3 are entrained by slow gamma activity in the dentate gyrus. *Journal of Neurophysiology* **116**:2594–2603. DOI: https://doi.org/10.1152/jn.00499.2016, PMID: 27628206

Hsu TT, Lee CT, Tai MH, Lien CC. 2016. Differential recruitment of dentate gyrus interneuron types by commissural versus perforant pathways. *Cerebral Cortex* **26**:2715–2727. DOI: https://doi.org/10.1093/cercor/bhv127, PMID: 26045570

Hummos A, Franklin CC, Nair SS. 2014. Intrinsic mechanisms stabilize encoding and retrieval circuits differentially in a hippocampal network model. *Hippocampus* **24**:1430–1448. DOI: https://doi.org/10.1002/hipo.22324, PMID: 24978936

Hunsaker MR, Rosenberg JS, Kesner RP. 2008. The role of the Dentate Gyrus, CA3a,b, and CA3c for detecting spatial and environmental novelty. *Hippocampus* **18**:1064–1073. DOI: https://doi.org/10.1002/hipo.20464, PMID: 18651615

Jouhanneau JS, Kremkow J, Poulet JFA. 2018. Single synaptic inputs drive high-precision action potentials in Parvalbumin expressing GABA-ergic cortical neurons in vivo. *Nature Communications* **9**:1540. DOI: https://doi.org/10.1038/s41467-018-03995-2, PMID: 29670095

Kapfer C, Glickfeld LL, Atallah BV, Scanziani M. 2007. Supralinear increase of recurrent inhibition during sparse activity in the somatosensory cortex. *Nature Neuroscience* **10**:743–753. DOI: https://doi.org/10.1038/nn1909, PMID: 17515899

Kraushaar U, Jonas P. 2000. Efficacy and stability of quantal GABA release at a hippocampal interneuron-principal neuron synapse. *The Journal of Neuroscience* **20**:5594–5607. DOI: https://doi.org/10.1523/JNEUROSCI.20-15-05594.2000, PMID: 10908596

Krueppel R, Remy S, Beck H. 2011. Dendritic integration in hippocampal dentate granule cells. *Neuron* **71**:512–528. DOI: https://doi.org/10.1016/j.neuron.2011.05.043, PMID: 21835347

Larimer P, Strowbridge BW. 2008. Nonrandom local circuits in the dentate gyrus. *Journal of Neuroscience* **28**:12212–12223. DOI: https://doi.org/10.1523/JNEUROSCI.3612-08.2008, PMID: 19020015

Lasztóczi B, Klausberger T. 2017. Distinct gamma oscillations in the distal dendritic fields of the dentate gyrus and the CA1 area of mouse Hippocampus. *Brain Structure and Function* **222**:3355–3365. DOI: https://doi.org/10.1007/s00429-017-1421-3, PMID: 28391402

Leal SL, Yassa MA. 2018. Integrating new findings and examining clinical applications of pattern separation. *Nature Neuroscience* **21**:163–173. DOI: https://doi.org/10.1038/s41593-017-0065-1, PMID: 29371654

Lee CT, Kao MH, Hou WH, Wei YT, Chen CL, Lien CC. 2016. Causal evidence for the role of specific GABAergic interneuron types in entorhinal recruitment of dentate granule cells. *Scientific Reports* **6**:36885. DOI: https://doi.org/10.1038/srep36885, PMID: 27830729

Leutgeb JK, Leutgeb S, Moser MB, Moser EI. 2007. Pattern separation in the dentate gyrus and CA3 of the Hippocampus. *Science* **315**:961–966. DOI: https://doi.org/10.1126/science.1135801, PMID: 17303747

Li L, Sultan S, Heigele S, Schmidt-Salzmann C, Toni N, Bischofberger J. 2017. Silent synapses generate sparse and orthogonal action potential firing in adult-born hippocampal granule cells. *eLife* **6**:e13612. DOI: https://doi.org/10.7554/eLife.23612

Lin AC, Bygrave AM, de Calignon A, Lee T, Miesenböck G. 2014. Sparse, decorrelated odor coding in the mushroom body enhances learned odor discrimination. *Nature Neuroscience* **17**:559–568. DOI: https://doi.org/10.1038/nn.3660, PMID: 24561998

Liu YC, Cheng JK, Lien CC. 2014. Rapid dynamic changes of dendritic inhibition in the dentate gyrus by presynaptic activity patterns. *Journal of Neuroscience* **34**:1344–1357. DOI: https://doi.org/10.1523/JNEUROSCI.2566-13.2014, PMID: 24453325

Lysetskiy M, Földy C, Soltesz I. 2005. Long- and short-term plasticity at mossy fiber synapses on mossy cells in the rat dentate gyrus. *Hippocampus* **15**:691–696. DOI: https://doi.org/10.1002/hipo.20096, PMID: 15986406

Madar AD, Ewell LA, Jones MV. 2019. Temporal pattern separation in hippocampal neurons through multiplexed neural codes. *PLOS Computational Biology* **15**:e1006932. DOI: https://doi.org/10.1371/journal.pcbi.1006932, PMID: 31009459

Marr D. 1971. Simple memory: a theory for archicortex. *Philosophical Transactions of the Royal Society B: Biological Sciences* **262**:23–81. DOI: https://doi.org/10.1098/rstb.1971.0078

McHugh TJ, Jones MW, Quinn JJ, Balthasar N, Coppari R, Elmquist JK, Lowell BB, Fanselow MS, Wilson MA, Tonegawa S. 2007. Dentate gyrus NMDA receptors mediate rapid pattern separation in the hippocampal network. *Science* **317**:94–99. DOI: https://doi.org/10.1126/science.1140263, PMID: 17556551

McNaughton BL, Morris RGM. 1987. Hippocampal synaptic enhancement and information storage within a distributed memory system. *Trends in Neurosciences* **10**:408–415. DOI: https://doi.org/10.1016/0166-2236(87)90011-7

Miles R. 1990. Synaptic excitation of inhibitory cells by single CA3 hippocampal pyramidal cells of the guinea-pig in vitro. *The Journal of Physiology* **428**:61–77. DOI: https://doi.org/10.1113/jphysiol.1990.sp018200, PMID: 2231426

Mircheva Y, Peralta MR, Tóth K. 2019. Interplay of entorhinal input and local inhibitory network in the Hippocampus at the origin of slow inhibition in granule cells. *The Journal of Neuroscience* **39**:6399–6413. DOI: https://doi.org/10.1523/JNEUROSCI.2976-18.2019, PMID: 31182636

Mizuseki K, Sirota A, Pastalkova E, Buzsáki G. 2009. Theta oscillations provide temporal windows for local circuit computation in the entorhinal-hippocampal loop. *Neuron* **64**:267–280. DOI: https://doi.org/10.1016/j.neuron.2009.08.037, PMID: 19874793

Myers CE, Scharfman HE. 2009. A role for hilar cells in pattern separation in the dentate gyrus: a computational approach. *Hippocampus* **19**:321–337. DOI: https://doi.org/10.1002/hipo.20516, PMID: 18958849

Neunuebel JP, Knierim JJ. 2014. CA3 retrieves coherent representations from degraded input: direct evidence for CA3 pattern completion and dentate gyrus pattern separation. *Neuron* **81**:416–427. DOI: https://doi.org/10.1016/j.neuron.2013.11.017, PMID: 24462102

Papadopoulou M, Cassenaer S, Nowotny T, Laurent G. 2011. Normalization for sparse encoding of odors by a wide-field interneuron. *Science* **332**:721–725. DOI: https://doi.org/10.1126/science.1201835, PMID: 21551062

Pedregosa F, Varoquaux G, Gramfort A, Michel V, Thirion B, Grisel O, Blondel M, Prettenhofer P, Weiss R, Dubourg V, Vanderplas J, Passos A, Cournapeau D, Brucher M, Perrot M, É D. 2011. Scikit-learn: machine learning in Python. *Journal of Machine Learning Research : JMLR* **12**:2825–2830.

Pernía-Andrade AJ, Jonas P. 2014. Theta-gamma-modulated synaptic currents in hippocampal granule cells in vivo define a mechanism for network oscillations. *Neuron* **81**:140–152. DOI: https://doi.org/10.1016/j.neuron.2013.09.046, PMID: 24333053

Pilz GA, Carta S, Stäuble A, Ayaz A, Jessberger S, Helmchen F. 2016. Functional imaging of dentate granule cells in the adult mouse Hippocampus. *Journal of Neuroscience* **36**:7407–7414. DOI: https://doi.org/10.1523/JNEUROSCI.3065-15.2016, PMID: 27413151

Pothmann L, Müller C, Averkin RG, Bellistri E, Miklitz C, Uebachs M, Remy S, Menendez de la Prida L, Beck H. 2014. Function of inhibitory micronetworks is spared by na+ channel-acting anticonvulsant drugs. *Journal of Neuroscience* **34**:9720–9735. DOI: https://doi.org/10.1523/JNEUROSCI.2395-13.2014, PMID: 25031410

Pouille F, Scanziani M. 2004. Routing of spike series by dynamic circuits in the Hippocampus. *Nature* **429**:717–723. DOI: https://doi.org/10.1038/nature02615, PMID: 15170216

Rangel LM, Chiba AA, Quinn LK. 2015. Theta and beta oscillatory dynamics in the dentate gyrus reveal a shift in network processing state during cue encounters. *Frontiers in Systems Neuroscience* **9**:96. DOI: https://doi.org/10.3389/fnsys.2015.00096, PMID: 26190979

Rolls ET. 2010. A computational theory of episodic memory formation in the Hippocampus. *Behavioural Brain Research* **215**:180–196. DOI: https://doi.org/10.1016/j.bbr.2010.03.027, PMID: 20307583

Rolls ET. 2013. The mechanisms for pattern completion and pattern separation in the Hippocampus. *Frontiers in Systems Neuroscience* **7**:74. DOI: https://doi.org/10.3389/fnsys.2013.00074, PMID: 24198767

Rolls ET. 2016. Pattern separation, completion, and categorisation in the Hippocampus and neocortex. *Neurobiology of Learning and Memory* **129**:4–28. DOI: https://doi.org/10.1016/j.nlm.2015.07.008, PMID: 26190832

Rolls ET, Treves A. 1998. Competitive networks. In: *Neural Networks and Brain Function*. Oxford University Press. DOI: https://doi.org/10.1093/acprof:oso/9780198524328.001.0001

Sahay A, Scobie KN, Hill AS, O'Carroll CM, Kheirbek MA, Burghardt NS, Fenton AA, Dranovsky A, Hen R. 2011. Increasing adult hippocampal neurogenesis is sufficient to improve pattern separation. *Nature* **472**:466–470. DOI: https://doi.org/10.1038/nature09817, PMID: 21460835

Sambandan S, Sauer JF, Vida I, Bartos M. 2010. Associative plasticity at excitatory synapses facilitates recruitment of fast-spiking interneurons in the dentate gyrus. *Journal of Neuroscience* **30**:11826–11837. DOI: https://doi.org/10.1523/JNEUROSCI.2012-10.2010, PMID: 20810902

Santhakumar V, Aradi I, Soltesz I. 2005. Role of mossy fiber sprouting and mossy cell loss in Hyperexcitability: a network model of the dentate gyrus incorporating cell types and axonal topography. *Journal of Neurophysiology* **93**:437–453. DOI: https://doi.org/10.1152/jn.00777.2004, PMID: 15342722

Sasaki T, Piatti VC, Hwaun E, Ahmadi S, Lisman JE, Leutgeb S, Leutgeb JK. 2018. Dentate network activity is necessary for spatial working memory by supporting CA3 sharp-wave ripple generation and prospective firing of CA3 neurons. *Nature Neuroscience* **21**:258–269. DOI: https://doi.org/10.1038/s41593-017-0061-5, PMID: 29335604

Savanthrapadian S, Meyer T, Elgueta C, Booker SA, Vida I, Bartos M. 2014. Synaptic properties of SOM- and CCK-expressing cells in dentate gyrus interneuron networks. *Journal of Neuroscience* **34**:8197–8209. DOI: https://doi.org/10.1523/JNEUROSCI.5433-13.2014, PMID: 24920624

Schmidt B, Marrone DF, Markus EJ. 2012. Disambiguating the similar: the dentate gyrus and pattern separation. *Behavioural Brain Research* **226**:56–65. DOI: https://doi.org/10.1016/j.bbr.2011.08.039, PMID: 21907247

Schmidt-Hieber C, Jonas P, Bischofberger J. 2004. Enhanced synaptic plasticity in newly generated granule cells of the adult Hippocampus. *Nature* **429**:184–187. DOI: https://doi.org/10.1038/nature02553, PMID: 15107864

Severa W, Parekh O, James CD, Aimone JB. 2017. A combinatorial model for dentate gyrus sparse coding. *Neural Computation* **29**:94–117. DOI: https://doi.org/10.1162/NECO_a_00905, PMID: 27764589

Sik A, Penttonen M, Buzsáki G. 1997. Interneurons in the hippocampal dentate gyrus: an in vivo intracellular study. *European Journal of Neuroscience* **9**:573–588. DOI: https://doi.org/10.1111/j.1460-9568.1997.tb01634.x, PMID: 9104599

Silberberg G, Markram H. 2007. Disynaptic inhibition between neocortical pyramidal cells mediated by martinotti cells. *Neuron* **53**:735–746. DOI: https://doi.org/10.1016/j.neuron.2007.02.012, PMID: 17329212

Skaggs WE, McNaughton BL, Wilson MA, Barnes CA. 1996. Theta phase precession in hippocampal neuronal populations and the compression of temporal sequences. *Hippocampus* **6**:149–172. DOI: https://doi.org/10.1002/(SICI)1098-1063(1996)6:2<149::AID-HIPO6>3.0.CO;2-K, PMID: 8797016

Stefanelli T, Bertollini C, Lüscher C, Muller D, Mendez P. 2016. Hippocampal somatostatin interneurons control the size of neuronal memory ensembles. *Neuron* **89**:1074–1085. DOI: https://doi.org/10.1016/j.neuron.2016.01.024, PMID: 26875623

Strüber M, Jonas P, Bartos M. 2015. Strength and duration of perisomatic GABAergic inhibition depend on distance between synaptically connected cells. *PNAS* **112**:1220–1225. DOI: https://doi.org/10.1073/pnas.1412996112, PMID: 25583495

Szabo GG, Du X, Oijala M, Varga C, Parent JM, Soltesz I. 2017. Extended interneuronal network of the dentate gyrus. *Cell Reports* **20**:1262–1268. DOI: https://doi.org/10.1016/j.celrep.2017.07.042, PMID: 28793251

Tamamaki N. 1997. Organization of the entorhinal projection to the rat dentate gyrus revealed by dil anterograde labeling. *Experimental Brain Research* **116**:250–258. DOI: https://doi.org/10.1007/PL00005753, PMID: 9348124

Tamamaki N, Nojyo Y. 1993. Projection of the entorhinal layer II neurons in the rat as revealed by intracellular pressure-injection of neurobiotin. *Hippocampus* **3**:471–480. DOI: https://doi.org/10.1002/hipo.450030408, PMID: 8269038

Temprana SG, Mongiat LA, Yang SM, Trinchero MF, Alvarez DD, Kropff E, Giacomini D, Beltramone N, Lanuza GM, Schinder AF. 2015. Delayed coupling to feedback inhibition during a critical period for the integration of adult-born granule cells. *Neuron* **85**:116–130. DOI: https://doi.org/10.1016/j.neuron.2014.11.023, PMID: 25533485

Toth K, Suares G, Lawrence JJ, Philips-Tansey E, McBain CJ. 2000. Differential mechanisms of transmission at three types of mossy fiber synapse. *The Journal of Neuroscience* **20**:8279–8289. DOI: https://doi.org/10.1523/JNEUROSCI.20-22-08279.2000, PMID: 11069934

Trappenberg TP. 2010. *Fundamentals of Computational Neuroscience*. Oxford University Press.

Trimper JB, Galloway CR, Jones AC, Mandi K, Manns JR. 2017. Gamma oscillations in rat hippocampal subregions Dentate Gyrus, CA3, CA1, and subiculum underlie associative memory encoding. *Cell Reports* **21**:2419–2432. DOI: https://doi.org/10.1016/j.celrep.2017.10.123, PMID: 29186681

Tsodyks M, Pawelzik K, Markram H. 1998. Neural networks with dynamic synapses. *Neural Computation* **10**:821–835. DOI: https://doi.org/10.1162/089976698300017502, PMID: 9573407

van Dijk MT, Fenton AA. 2018. On how the dentate gyrus contributes to memory discrimination. *Neuron* **98**:832–845. DOI: https://doi.org/10.1016/j.neuron.2018.04.018, PMID: 29731252

Verret L, Mann EO, Hang GB, Barth AM, Cobos I, Ho K, Devidze N, Masliah E, Kreitzer AC, Mody I, Mucke L, Palop JJ. 2012. Inhibitory interneuron deficit links altered network activity and cognitive dysfunction in alzheimer model. *Cell* **149**:708–721. DOI: https://doi.org/10.1016/j.cell.2012.02.046, PMID: 22541439

Wick SD, Wiechert MT, Friedrich RW, Riecke H. 2010. Pattern orthogonalization via channel decorrelation by adaptive networks. *Journal of Computational Neuroscience* **28**:29–45. DOI: https://doi.org/10.1007/s10827-009-0183-1, PMID: 19714457

Wiechert MT, Judkewitz B, Riecke H, Friedrich RW. 2010. Mechanisms of pattern decorrelation by recurrent neuronal circuits. *Nature Neuroscience* **13**:1003–1010. DOI: https://doi.org/10.1038/nn.2591, PMID: 20581841

Williams SR, Mitchell SJ. 2008. Direct measurement of somatic voltage clamp errors in central neurons. *Nature Neuroscience* **11**:790–798. DOI: https://doi.org/10.1038/nn.2137, PMID: 18552844

Yim MY, Hanuschkin A, Wolfart J. 2015. Intrinsic rescaling of granule cells restores pattern separation ability of a dentate gyrus network model during epileptic hyperexcitability. *Hippocampus* **25**:297–308. DOI: https://doi.org/10.1002/hipo.22373, PMID: 25269417

Yu J, Swietek B, Proddutur A, Santhakumar V. 2015. Dentate total molecular layer interneurons mediate cannabinoid-sensitive inhibition. *Hippocampus* **25**:884–889. DOI: https://doi.org/10.1002/hipo.22419

Yuan M, Meyer T, Benkowitz C, Savanthrapadian S, Ansel-Bollepalli L, Foggetti A, Wulff P, Alcami P, Elgueta C, Bartos M. 2017. Somatostatin-positive interneurons in the dentate gyrus of mice provide local- and long-range septal synaptic inhibition. *eLife* **6**:e21105. DOI: https://doi.org/10.7554/eLife.21105, PMID: 28368242

Zhang W, Yamawaki R, Wen X, Uhl J, Diaz J, Prince DA, Buckmaster PS. 2009. Surviving hilar somatostatin interneurons enlarge, sprout axons, and form new synapses with granule cells in a mouse model of temporal

lobe epilepsy. *Journal of Neuroscience* **29**:14247–14256. DOI: https://doi.org/10.1523/JNEUROSCI.3842-09.2009, PMID: 19906972

RESEARCH ARTICLE

Figures and figure supplements

Quantitative properties of a feedback circuit predict frequency-dependent pattern separation

Oliver Braganza *et al*

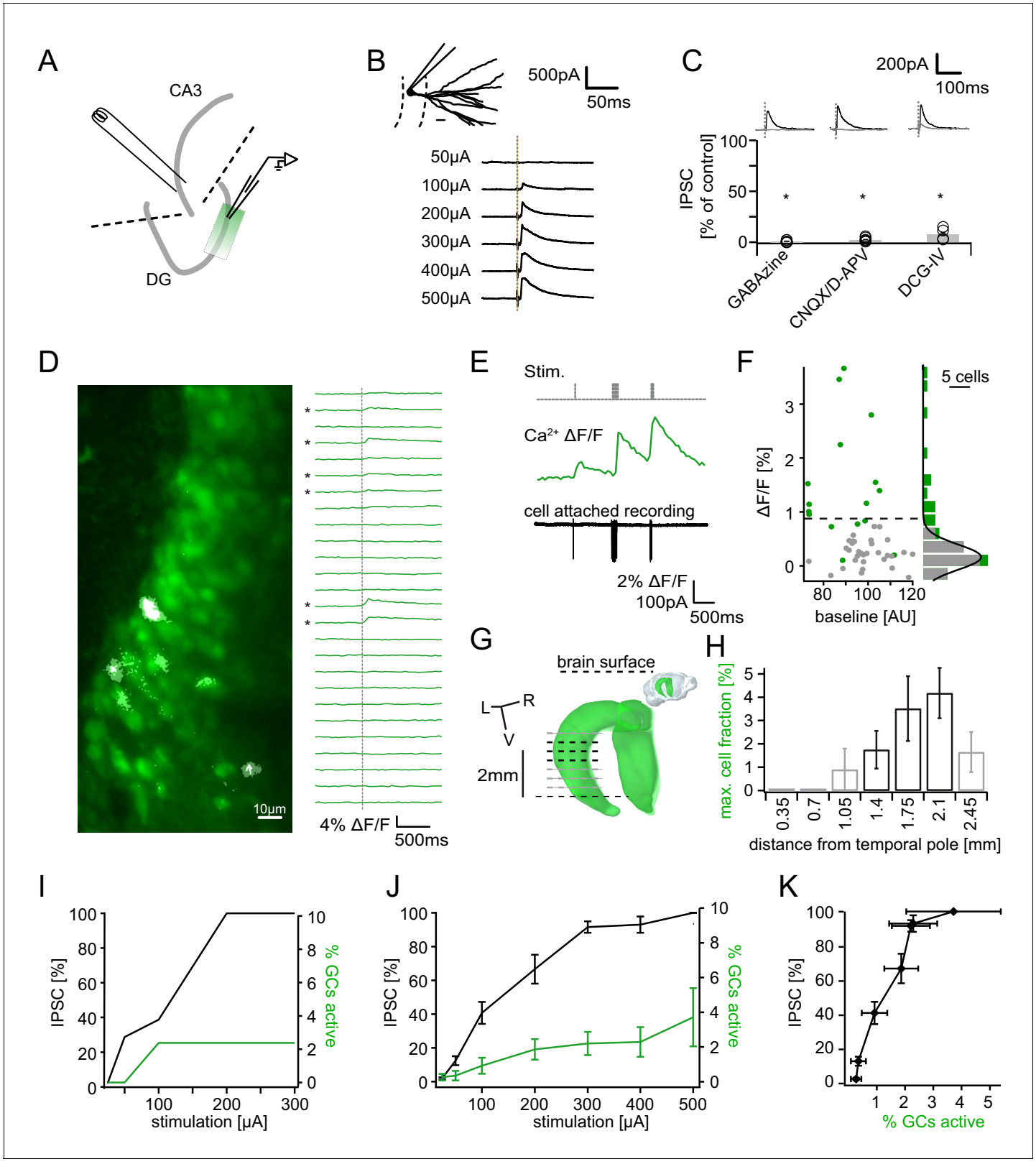

Figure 1. Recruitment of feedback inhibition assessed using population Ca^{2+} imaging. Combined population Ca^{2+} imaging and IPSC recordings of GCs during antidromic electrical stimulation. (**A**) Schematic illustration of the experimental setup. Dashed lines represent cuts to sever CA3 backprojections. (**B**) Top: reconstruction of the dendritic tree of a representative GC. Bottom: Feedback IPSC at increasing stimulation strength during stratum lucidum stimulation. (**C**) IPSCs were completely blocked by GABAzine and CNQX + D-APV and largely by DCG-IV. (**D**) Left: overlay of

Figure 1 continued on next page

Figure 1 continued

exemplary OGB1-AM-loaded GC population (green) with a ΔF/F map (white). right: traces of ΔF/F over time of a subpopulation of cells depicted on the left. (**E**) Simultaneous cell attached recording and calcium imaging to measure the action potential induced somatic calcium transient amplitude. (**F**) Scatterplot and histogram of the calcium fluorescence peaks of cells which either did (green) or did not (grey) fire action potentials, as assessed by cell attached recordings. (**G**) Illustration of the anatomical localization of maximum connectivity plane slices. Short black dashed lines indicate depth at which the slice plane is aligned to the dorsal brain surface. (**H**) Antidromic stimulation elicited Ca^{2+} transients primarily at this depth (black bars). (**I**) Normalized IPSC amplitude and activated cell fraction both increase with increasing stimulation strength (example from a single slice). (**J**) Summary of all slices (**K**) Summary data plotted to show the increase of inhibition as a function of the active GC fraction.

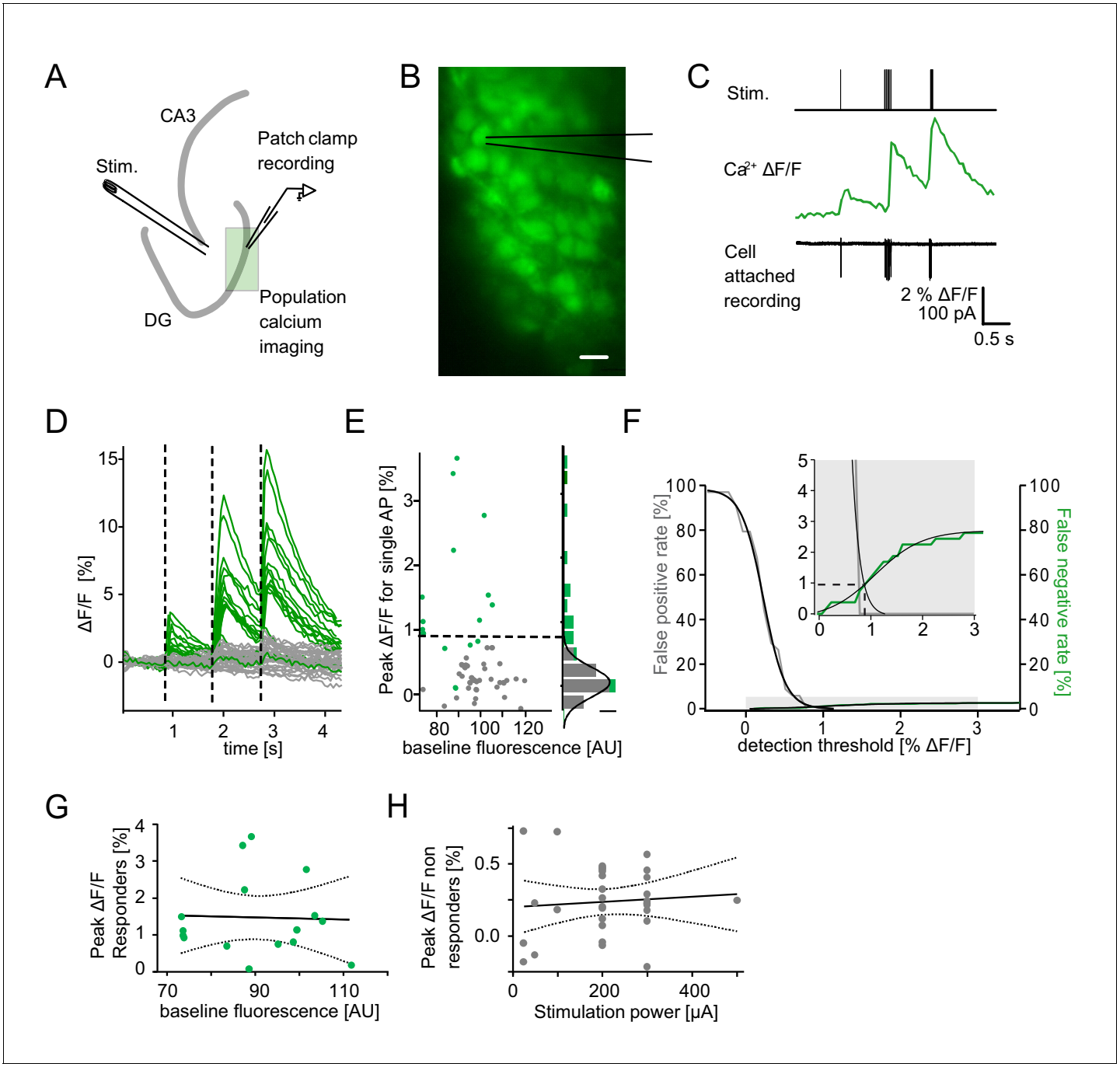

Figure 1—figure supplement 1. Detection of single action potential induced calcium transients. A section of the dentate gyrus was loaded with OGB1-AM and imaged with multibeam two-photon microscopy while antidromically eliciting action potentials and recording from individual cells in cell-attached mode. (**A**) A schematic illustration of the experimental setup. (**B**) Example of OGB1-AM loaded GCs. Scale bar: 10 µm (**C**) Cells were stimulated with a single pulse (left) or bursts of 5 pulses at 30 Hz (middle) or 100 Hz (right). Cell attached recordings revealed the exact number of induced action potentials (bottom), which could then be correlated with the intracellular calcium signal (middle). (**D**) Superposition of the calcium fluorescence traces of 49 recorded cells constituted of cells identified as responders (green) or non-responders (grey) by cell attached recordings. (**E**) Peak ΔF/F for single APs of identified responders and non-responders plotted against their respective baseline fluorescence (left). A histogram of the peak ΔF/F of both groups fitted with a Gaussian distribution of the non-responders (right, scale bar = 5 cells). The dashed line indicates detection threshold at the quadruple standard deviation of this fit (0.94% ΔF/F). (**F**) False-positive (gray) and false-negative (green) rates were plotted as a function of the detection threshold and fitted with sigmoidal functions. A detection threshold of 0.94% leads to exactly equal numbers of false positives and false negatives if the actually active fraction of GCs is 3% (inset, dashed lines). (**G**) To test for potential effects of variable dye loading on detection efficacy, we tested for a correlation between peak ΔF/F of responders and baseline fluorescence intensity ($p>0.05$). (**H**) To test if increasing numbers of

Figure 1—figure supplement 1 continued on next page

Figure 1—figure supplement 1 continued

responders at increasing stimulation power led to increases of false positives in the densely packed GC layer, we correlated peak ΔF/F of non-responders with stimulation power ($p>0.05$). Dashed lines in (**G**) and (**H**) represent the 95% confidence intervals of linear regressions.

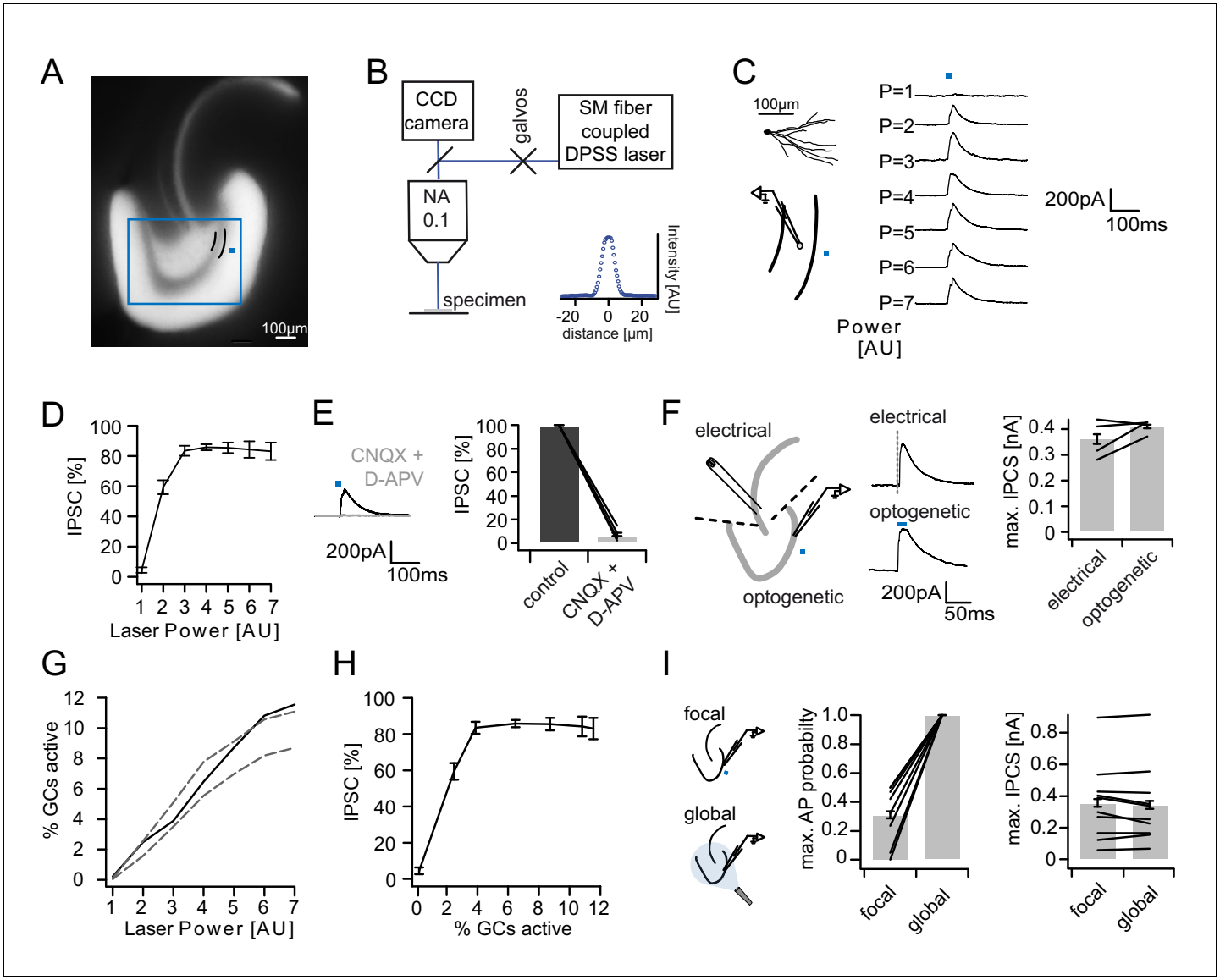

Figure 2. Recruitment of feedback inhibition assessed optogenetically. (**A**) EYFP fluorescence in dentate GCs of Prox1/ChR2(H134R)-EYFP transgenic mice. The field of view for rapid focal optogenetic stimulation is indicated by a blue square. A typical stimulation site approx. 40 µm from the GC layer (two short black lines) is indicated by a blue dot. (**B**) Schematic of the microscope setup used to achieve spatially controlled illumination. The inset shows the intensity profile of the laser spot. (**C**) Top left, reconstruction of an Alexa594 filled GC. Left, illustration of optical stimulation. Right, IPSCs following 20 ms light pulses at increasing laser power (p=1 to 7 AU). Each trace represents an average of three trials. (**D**) Summary of IPSC amplitudes from cells in the superior blade (n = 7 cells). IPSC amplitudes were normalized to the maximum amplitude within each cell. (**E**) Optogenetically elicited IPSCs are abolished by glutamatergic blockers (40 µM CNQX + 50 µM D-APV, n = 9). (**F**) Left, Schematic of focal optical and electrical stimulation. Dashed lines indicate cuts to sever CA3 backprojections. Middle, Example traces for IPSCs following electrical or focal optogenetic stimulation. Right, maximal IPSC amplitude for the two stimulation paradigms (361 ± 37 vs. 410 ± 13 pA for electrical and optogenetic stimulation respectively, paired t-test, p=0.28, n = 4) (**G**) The optogenetically activated GC fraction responsible for recruiting the IPSC at the respective laser powers was estimated from systematic cell attached recordings (see ***Figure 2—figure supplement 1*** for details). The best estimate (black) incorporates measurements of the 3D light intensity profile in the acute slice. Upper and lower bounds were estimated by assuming no firing probability decay with increasing slice depth (upper grey dashed line) or isometric firing probability decay (lower grey dashed line. (**H**) Data from (**D**) and (**H**, best estimate) plotted to show the recruitment of feedback inhibition. (**I**) Comparison of focal optogenetic stimulation to global (light fiber mediated) optogenetic stimulation. Left, Schematic illustration. Middle, Comparison of the AP probability of individual GCs at maximal stimulation power for focal and global stimulation assessed by cell attached recordings. Right, Comparison of the maximal IPSC amplitude under focal and global stimulation for individual GCs.

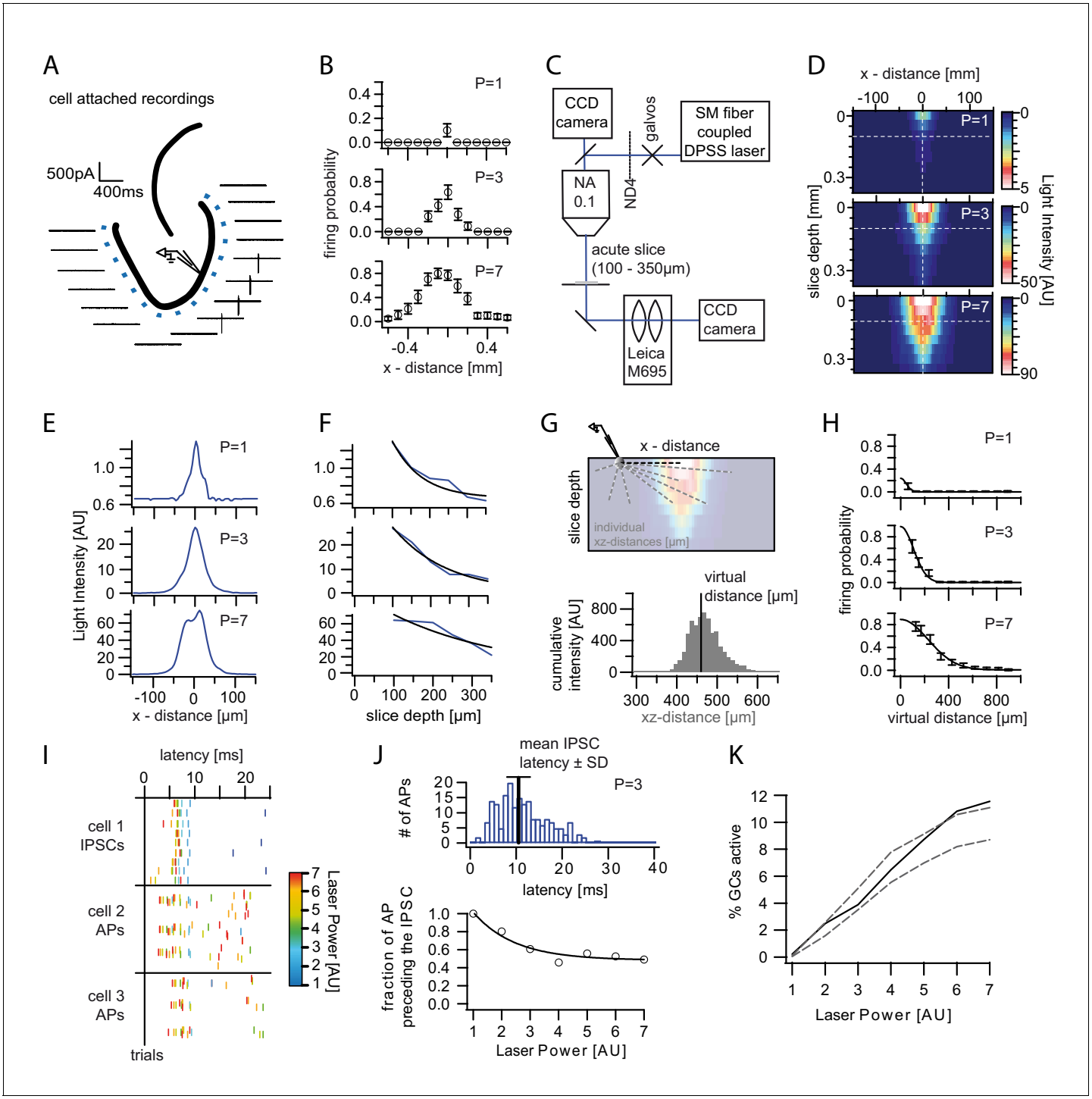

Figure 2—figure supplement 1. Optogenetically activated cell fraction. (**A**) Schematic illustration of the experimental setup. Cells were recorded in cell attached mode (two per slice), while systematically stimulating at varying distances. Traces from a representative trial at p=3. (**B**) Mean firing probability of every location over trials and cells for each laser power (three example powers shown). (**C**) Schematic of the modified setup to record the three dimensional light intensity profile in an acute slice. In order to avoid saturation a neutral density filter (ND4) was inserted into the light path. (**D**) Cross-section of the light intensity profile of the laser spot at increasing slice depth. The dashed white lines indicate the location of the cross sections shown in (**E**) and (**F**). Depths below 100 µm were extrapolated from fits to (**E**) and (**F**). (**G**) Top, Illustration of the calculation of the virtual distance for a particular cell/pixel 440 µm lateral to the laser focus. The distances between the given cell/pixel and all other pixels (individual xz-distances) were weighted by the intensity at those pixels. Bottom, this weighting is illustrated by a histogram displaying the intensities for each respective xz-distance. The virtual distance corresponds to the intensity weighted mean of xz-distances. (**H**) The measured firing probabilities were assigned to the respective

Figure 2—figure supplement 1 continued on next page

Figure 2—figure supplement 1 continued

virtual distances. The resulting firing probability distribution was well approximated by a Gaussian fit (black lines). (**I**) Example of the IPSC and AP latencies upon a stimulation pulse from an individual slice. Laser Powers are color coded. (**J**) Top, Example Histogram of the distribution of all AP latencies for p=3 (blue). The black bar indicates the mean IPSC latency ± standard deviation at that power. Bottom, The fraction of action potentials that precede the mean IPSC for each power was well approximated by an exponential fit (black line). Light stimulation in (**I**) and (**J**) was from 0 to 20 ms. (**K**, black) Estimated active cell fraction in the slice calculated from the light intensity profiles in (**D**) and the virtual firing probability distributions in (**H**) and corrected by the fraction of APs occurring after the mean IPSC (**J**). The estimated active cell fraction is identical to the mean firing probability throughout the slice. For comparison, the cell fraction was also estimated assuming no firing probability decay with increasing depth (upper grey dashed line) or assuming isometric decay (lower grey dashed line).

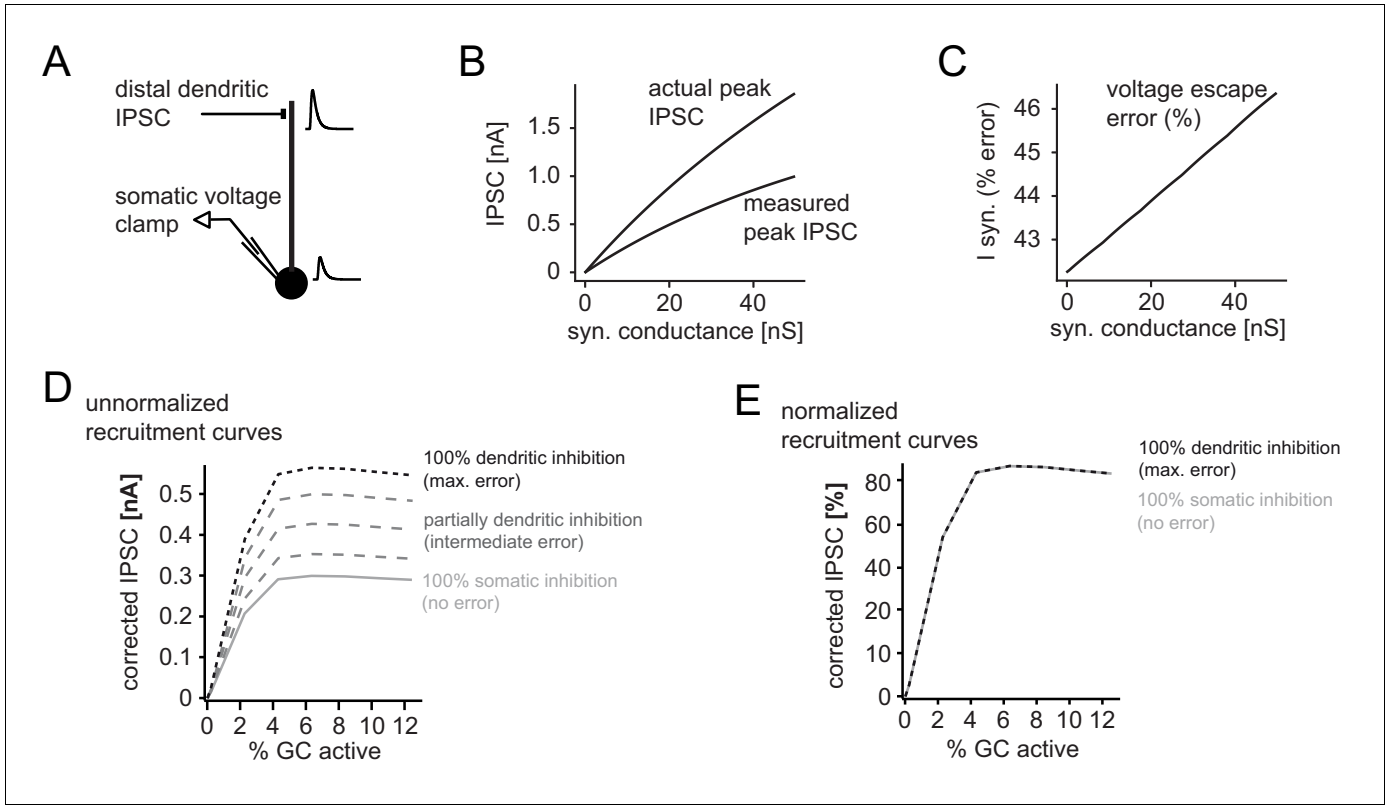

Figure 2—figure supplement 2. Error in somatic IPSC measurements with increasing inhibitory conductance. A simple ball and stick model was used to estimate the impact of voltage escape errors for dendritic IPSCs (soma diameter 20um; dendrite diameter and length 3 µm and 200 µm, respectively). To estimate the maximum errors the inhibitory synapse was placed at a distal site (180 µm from the soma) and inhibitory currents were measured using a single electrode voltage-clamp at the soma. (**A**) Illustration of the model and an attenuated somatic IPSC measurement. (**B**) Peak amplitudes of the measured IPSC over a range of distal synaptic conductances (measured peak IPSC), as well as the actual peak IPSC in the absence of voltage errors, calculated from the transfer and input impedances of the model. (**C**) Error in somatically measured peak IPSC as percentage of the actual peak IPSC (I syn, % error) at a given synaptic conductance. Errors in estimating synaptic inhibitory currents were linear. (**D**) Illustration of corrected and uncorrected recruitment curves of absolute IPSC amplitudes for varying degrees of voltage error (using data from the recruitment curve in ***Figure 2H***). Note that due to the linearity of voltage escape errors, absolute IPSC amplitudes change, but the saturation point does not. (**E**) This is illustrated by the normalized recruitment curves, as shown throughout the manuscript (see ***Figure 2H***). Note that normalized curves are practically unaffected by voltage escape errors.

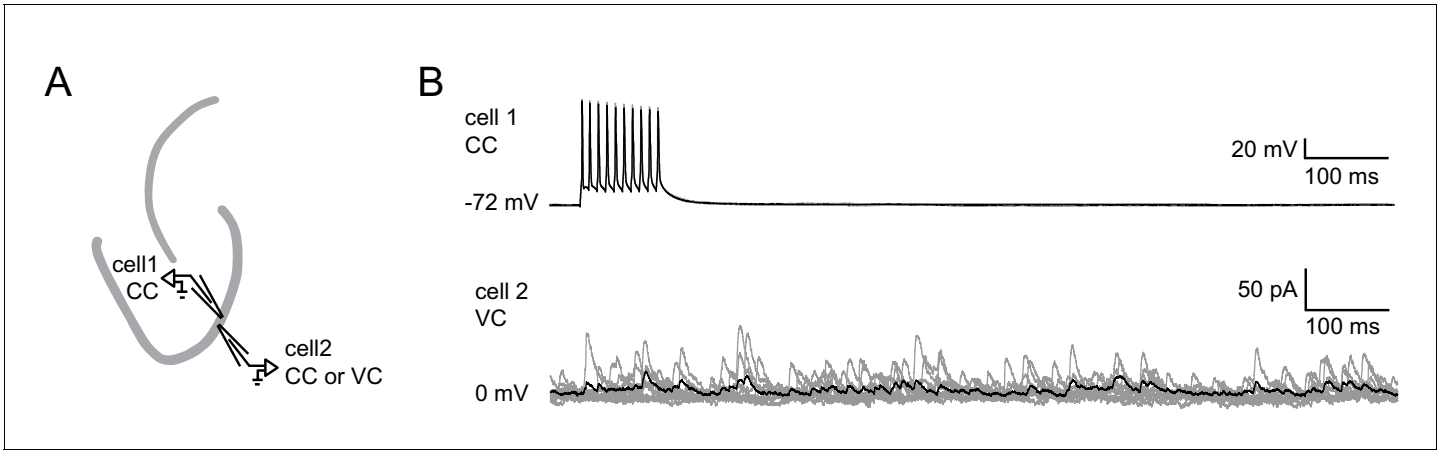

Figure 2—figure supplement 3. Absence of single GC induced feedback inhibition. Pairs of juxtaposed GCs (<100 µm distance) were recorded to test for single GC induced feedback inhibition. (**A**) Schematic illustration of the experimental setup. (**B**) Example of a paired recording where cell one is fired at 100 Hz in current clamp mode while cell two is recorded in voltage clamp mode in order to detect IPSCs. (gray, 10 individual trials; black, average).

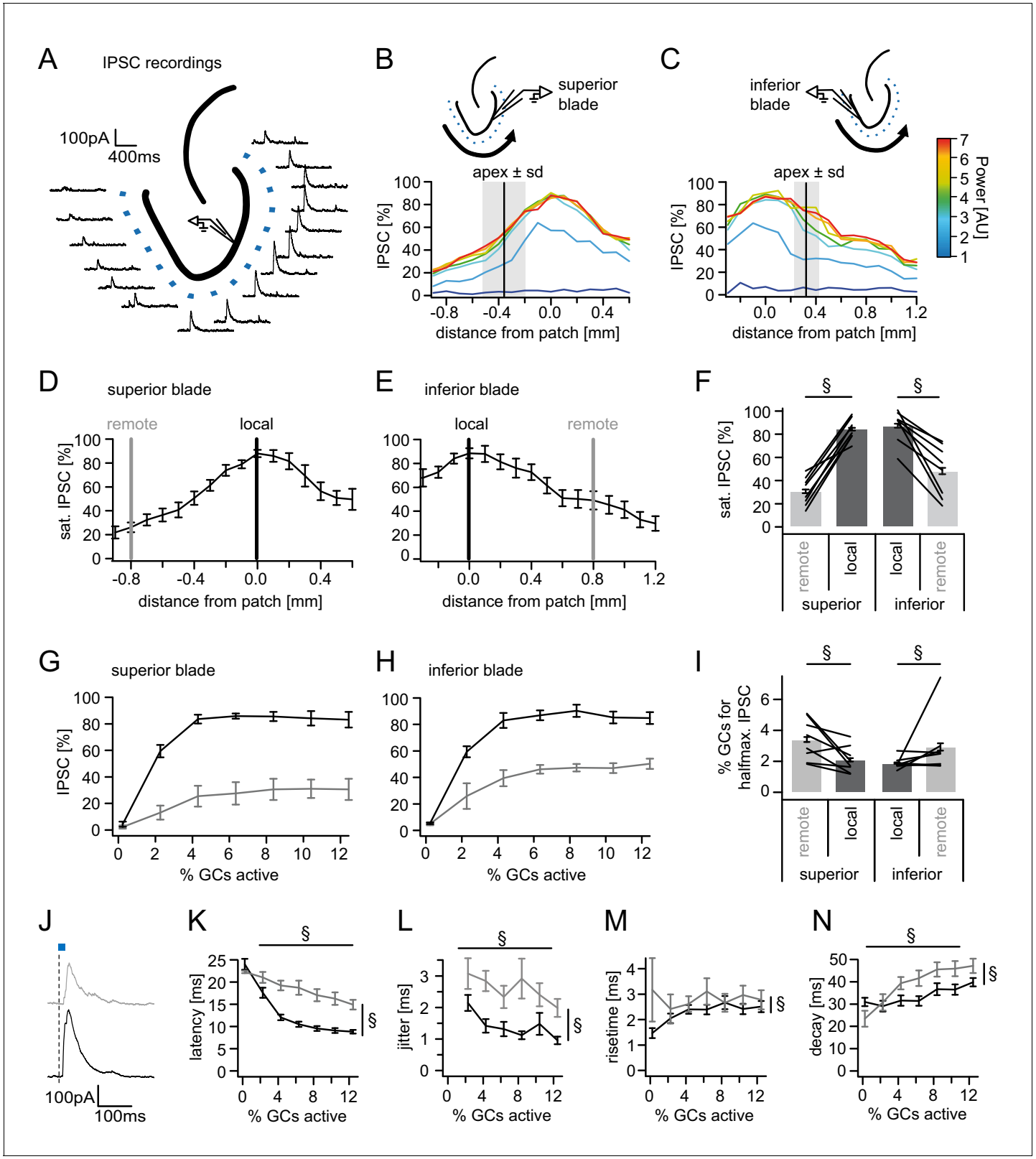

Figure 3. Spatial organization of feedback inhibition. Feedback IPSCs recorded from an individual GC while GCs at varying distances were activated. (**A**) Schematic illustration of the stimulation paradigm and example IPSC traces of an individual trial (p=3). (**B, C**) Distribution of normalized IPSC amplitudes as a function of laser power and distance from stimulation spot for superior and inferior blade GCs (n = 8 for each blade). The relative location of the DG apex ± standard deviation is indicated by the black bar and grey area respectively. (**D, E**) IPSC distribution over space at saturation

Figure 3 continued on next page

Figure 3 continued

($p \geq 5$). Black and grey bars indicate a local and a remote location at 800 µm from the recorded cell respectively. (**F**) Comparison of the amplitude of the locally and remotely activated IPSCs at saturation (two-way RM ANOVA, overall test significance indicated by §). (**G, H**) Comparison of the recruitment curves during local (black) or remote (grey) stimulation for superior and inferior blade respectively. (**I**) Comparison of the cell fraction required for halfmaximal IPSC activation between stimulation sites and blades (two-way RM ANOVA overall test significance indicated by §). (**J–M**) Temporal properties of IPSCs between local (black) and remote (grey) stimulation. To test for systematic variations of kinetic parameters with increasing active cell fractions as well as stimulation site two-way RM ANOVAs with no post tests were performed. Overall significance indicated by §. (**K**) Latency from beginning of light pulse to IPSC (**L**) temporal jitter of IPSCs (SD of latency within cells) (**M**) 20% to 80% rise time (**N**) IPSC decay time constant.

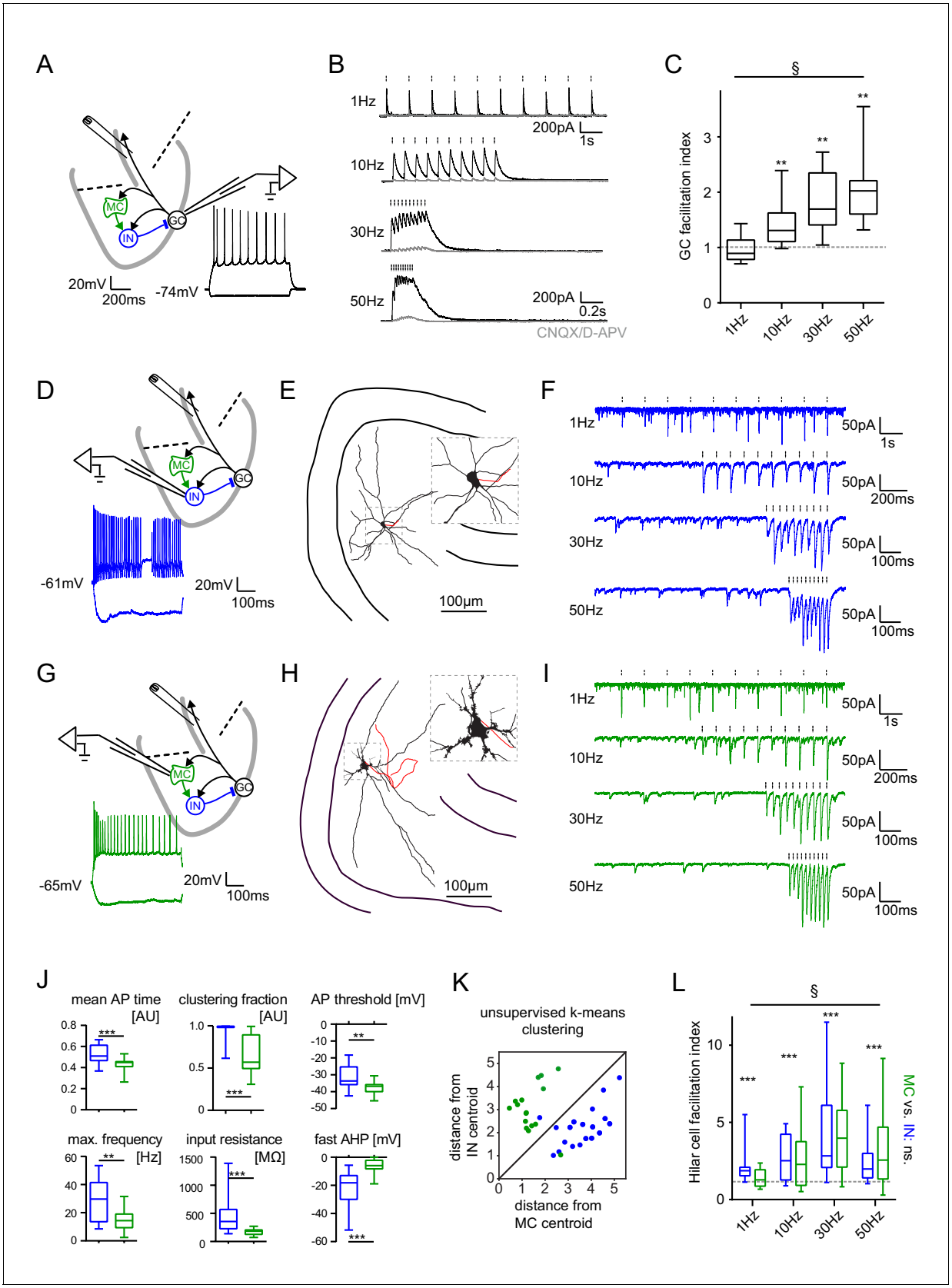

Figure 4. Short-term dynamics in the feedback inhibitory microcircuit. Trains of ten antidromic electrical stimulations at 1, 10, 30 or 50 Hz were applied to elicit disynaptic feedback inhibition or excitation of hilar cells (electrical stimulation artifacts were removed in all traces). (**A, D, G**) Schematic

Figure 4 continued on next page

Figure 4 continued

illustration of the experimental setup and example traces of voltage responses to positive and negative current injections of GC and hilar cells (dashed lines indicate cuts to sever CA3 backprojections). (**B**) Exemplary GC feedback IPSCs before (black) and after (grey) glutamatergic block (n = 7). (**C**) Facilitation indices (mean of the last three IPSCs normalized to the first; n = 10 cells). (**D-L**) Hilar cells were manually classified into putative interneurons (blue) or mossy cells (green) based on their morpho-functional properties. (**E**) Reconstruction of biocytin filled hilar interneuron (axon in red). (**F**) Interneuron EPSCs in response to stimulation trains. (**H**) Reconstruction of biocytin filled mossy cell (axon in red). (**I**) Mossy cell EPSCs in response to stimulation trains. (**J**) Quantification of intrinsic properties of hilar cells (see Materials and methods). (**K**) k-means clustering based on intrinsic properties of hilar cells (coloring according to manual classification). (**L**) Facilitation indices of classified hilar cells. (§ indicates significance in one-way RM ANOVA, * show significance in Bonferroni corrected Wilcoxon signed rank tests for deviation from 1).

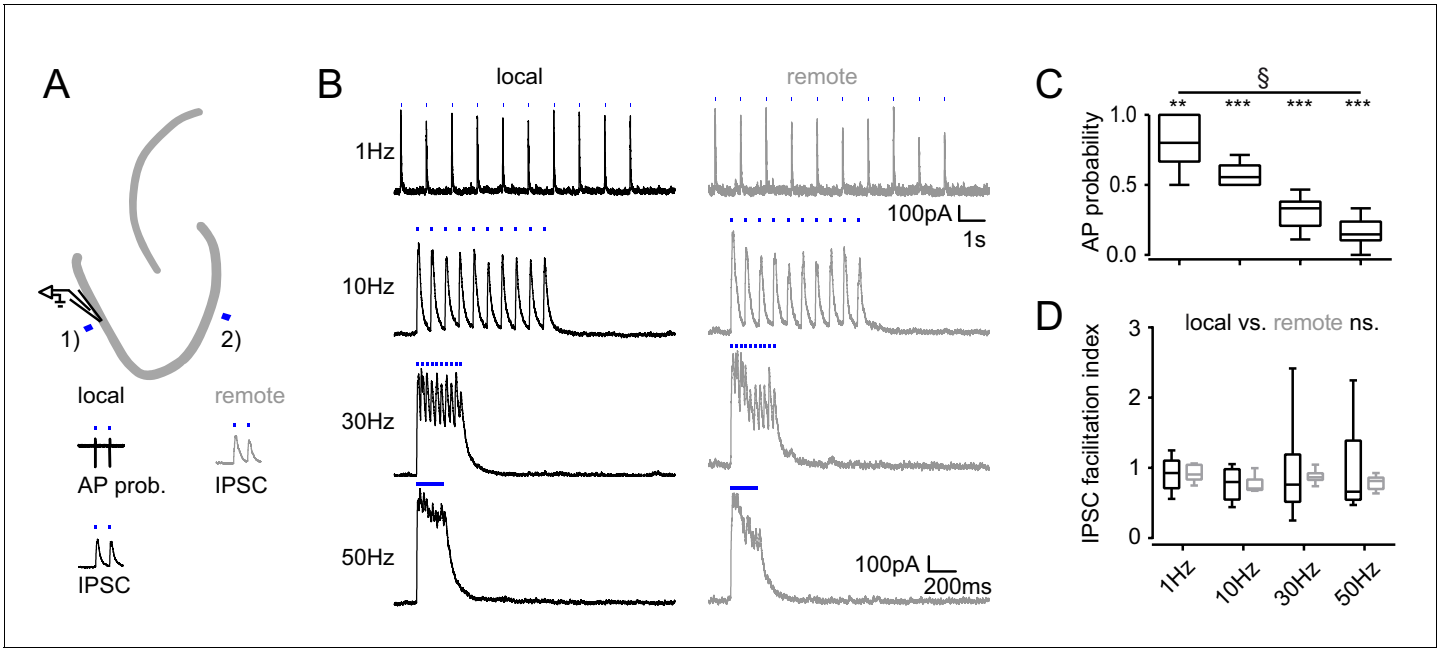

Figure 4—figure supplement 1. Frequency dependence of feedback inhibition over space. Trains of 10 focal optic stimulations (20 ms duration) were applied either locally (1) or remotely (2) to elicit feedback inhibition. (**A**) Schematic of the experimental paradigm and example traces of elicited cell attached spikes or IPSCs. (**B**) Example traces for stimulation at 1, 10, 30 Hz or continuously for 200 ms of a local or remote GC populations (black and grey, respectively). (**C**) The AP probability index (mean probability during the last three pulses normalized to the first pulse (one-way RM ANOVA, $p < 0.001$ for frequency, Bonferroni corrected Wilcoxon signed rank test for deviation from 1; $p = 0.024$, $= 0.008$, $= 0.008$ and $= 0.008$ for 1 Hz, 10 Hz, 30 Hz and continuous stimulation, respectively). (**D**) Facilitation indices of local (dark grey) and remote (light grey) stimulation (two-way RM ANOVA; $p = 0.635$, $= 0.314$ and $= 0.687$ for location, frequency and interaction, respectively).

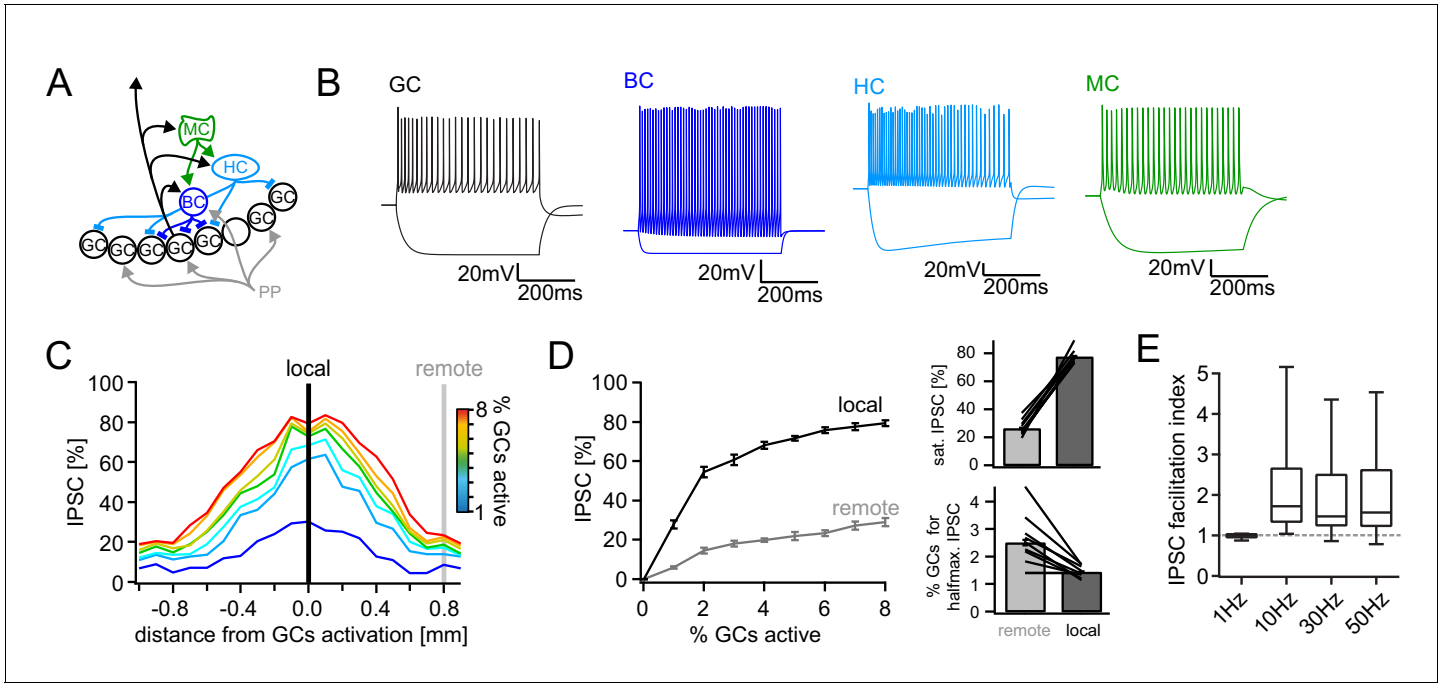

Figure 5. Computational model of the DG feedback circuit. A biophysically realistic model of DG was tuned to capture the key quantitative features of the feedback circuit. All analyses were performed as for the real data (including IPSC normalization to maximal IPSC over space and power within each respective cell) (**A**) Schematic of the model circuit. GC: granule cell, BC: basket cell, HC: hilar perforant path associated cell, MC; mossy cell. (**B**) Intrinsic responses of model cell types to positive and negative current injections. (**C**) Spatially graded net feedback inhibition following simulated focal GC activation. (**D**) Local and remote recruitment curves of the feedback inhibitory circuit (left) and the resulting saturated IPSC amplitudes and GC fractions recruiting halfmaximal inhibition (right). (**E**) Facilitation indices resulting from simulated, 10 pulse, frequency stimulation of GCs as above.

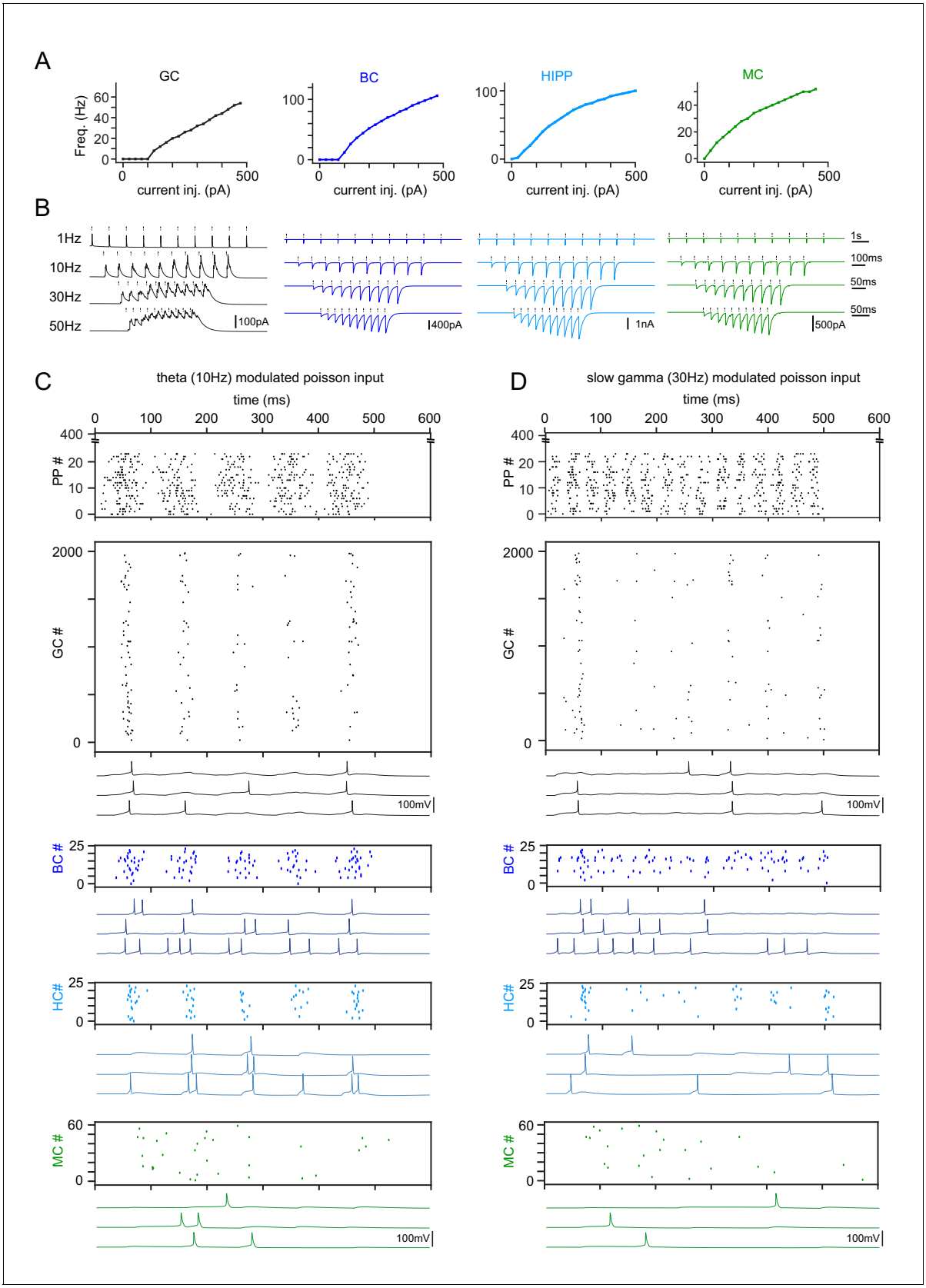

Figure 5—figure supplement 1. Model tuning and validation. (**A**) Frequency responses to somatic current injections of model cell types (GC: granule cells, BC: basket cells, HC: hilar perforant path associated cells, MC: mossy cells). All model cells were matched to data by ***Santhakumar et al. (2005)***.

Figure 5—figure supplement 1 continued on next page

Figure 5—figure supplement 1 continued

(**B**) Simulation of synchronous frequency stimulation of GCs and the resulting PSCs in modeled cell types, analogous to ***Figure 4***. (**C**) Representative theta modulated PP input and population responses (scatterplots) of all modeled cell types. Following each scatterplot are three examples of spiking cells of the respective type. (**D**) Same as (**C**) but for slow gamma modulated inputs.

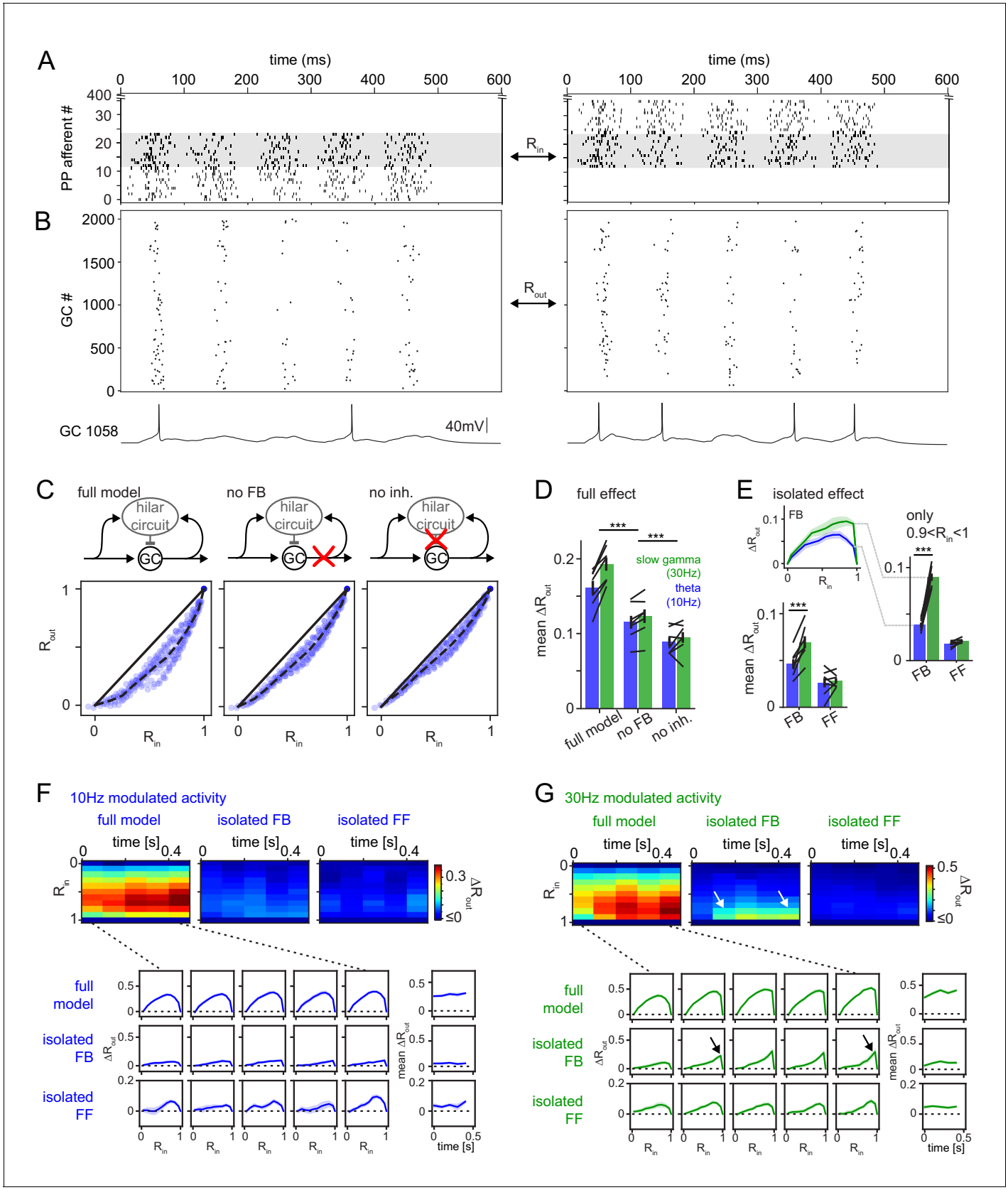

Figure 6. Frequency dependent pattern separation of temporally structured inputs. The quantitative DG model was challenged with theta (10 Hz) or slow gamma (30 Hz) modulated input patterns with defined overlap to probe its pattern separation ability. (**A**) Pair of theta modulated perforant path

Figure 6 continued on next page

Figure 6 continued

input patterns in which 50% of afferents overlap (grey area). (**B**) Resulting pair of GC output patterns of the full tuned network. Bottom: Representative individual GC underlying the observed patterns. (**C**) Comparison of 325 input pattern pairs and their resulting output pattern pairs. Each pair is characterized by its rate vector correlation for inputs (R_{in}) and outputs (R_{out}), where rates are measured over the full 600 ms time window. Dashed black lines represent the bin-wise mean R_{out} (in R_{in} bins of 0.1). Left: full tuned model, middle: model without mossy fiber inputs to interneurons, right: model without inhibitory synapses. (**D**) Full pattern separation effects (mean ΔR_{out}) of all three conditions for both frequency domains quantified as the area enclosed by the dashed and unity lines in (**C**). Black lines represent individual network seeds. Two-way RM ANOVA indicated significance of condition, frequency and interaction, * indicate significance in Sidak's posttests between individual conditions. (**E**) Isolated effects of feedback and feedforward motifs obtained by pairwise subtraction of R_{out} between conditions for each individual comparison. The inset shows the resulting ΔR_{out} for each R_{in} bin. The area under the curve quantifies the mean ΔR_{out} as in (**D**). Two-way RM ANOVA indicated significance of condition, frequency and interaction. *** indicate $p<0.001$ in Sidak's posttest. (**F**). 100 ms time-resolved pattern separation effects of the full model, isolated FB or FF inhibition for theta modulated input (10 Hz). All analyses were performed as above but with rate vector correlations computed for 100 ms time windows. The bottom insets show ΔR_{out} as a function of input similarity for each time window. The bottom right insets show the evolution of the mean ΔR_{out} over time. (**G**) Same as (**F**) but for slow gamma (30 Hz) modulated inputs. Arrow indicate the region of selectively increased pattern separation. Data in D-G represent mean ± SEM of n = 7 random network seeds.

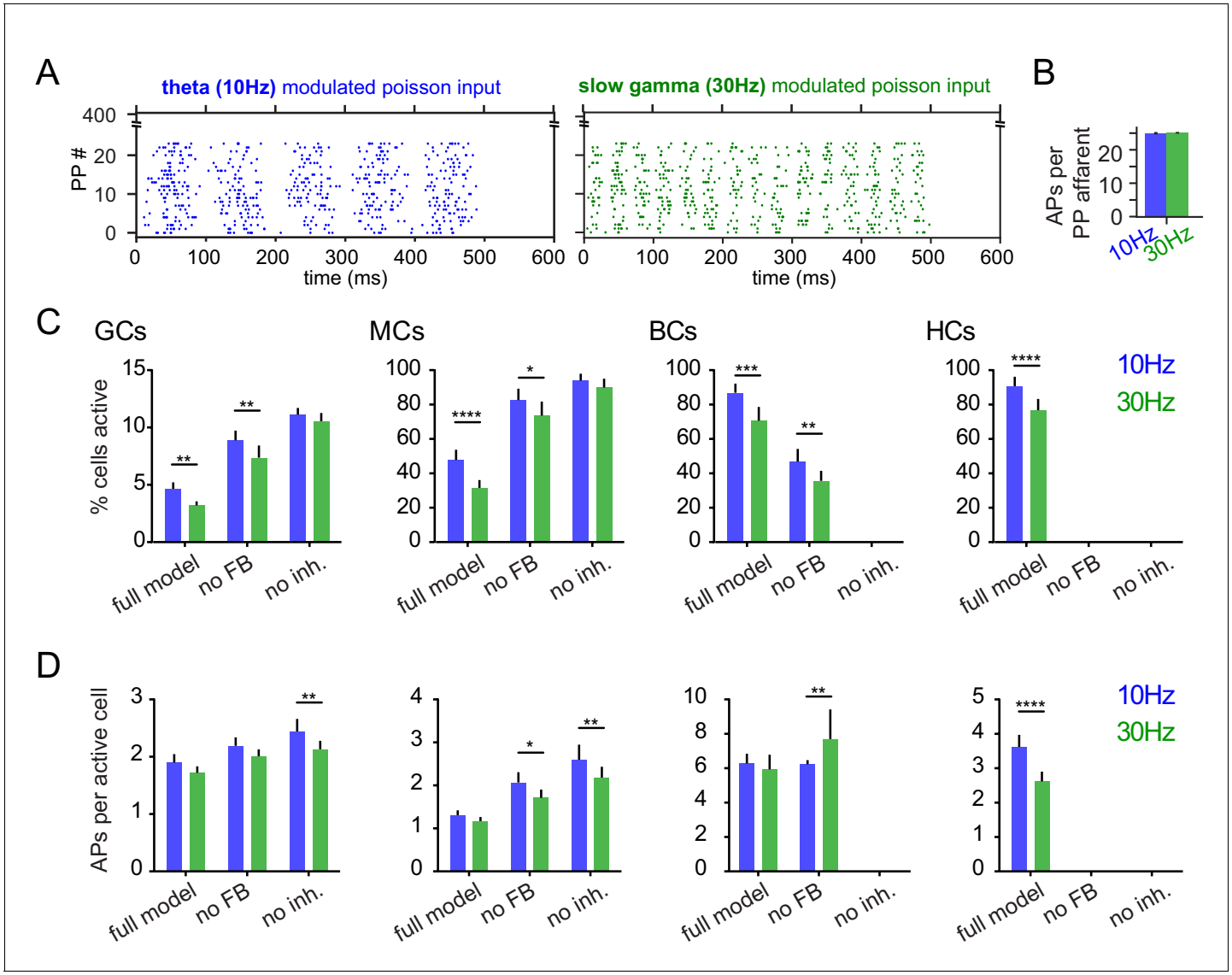

Figure 6—figure supplement 1. Activity levels and pattern separation. (GCs: granule cells; MCs: mossy cells; BCs: basket cells; HCs: HIPP cells; n = 7 model runs). (**A**) Exemplary raster plots of 10 Hz and 30 Hz modulated inputs. (**B**) Mean number of action potentials per active perforant path afferent. (**C**) Percentages of active cells within the model. (**D**) Mean number of action potentials per active cell within the model. Activity rates (**A, B**) were tested with two-way ANOVAs followed by Sidak's posttests for differences between frequencies. Asterisks indicate significance in posttests given significant overall effects (*p<0.05, **p<0.01, ***p<0.001, ****p<0.0001).

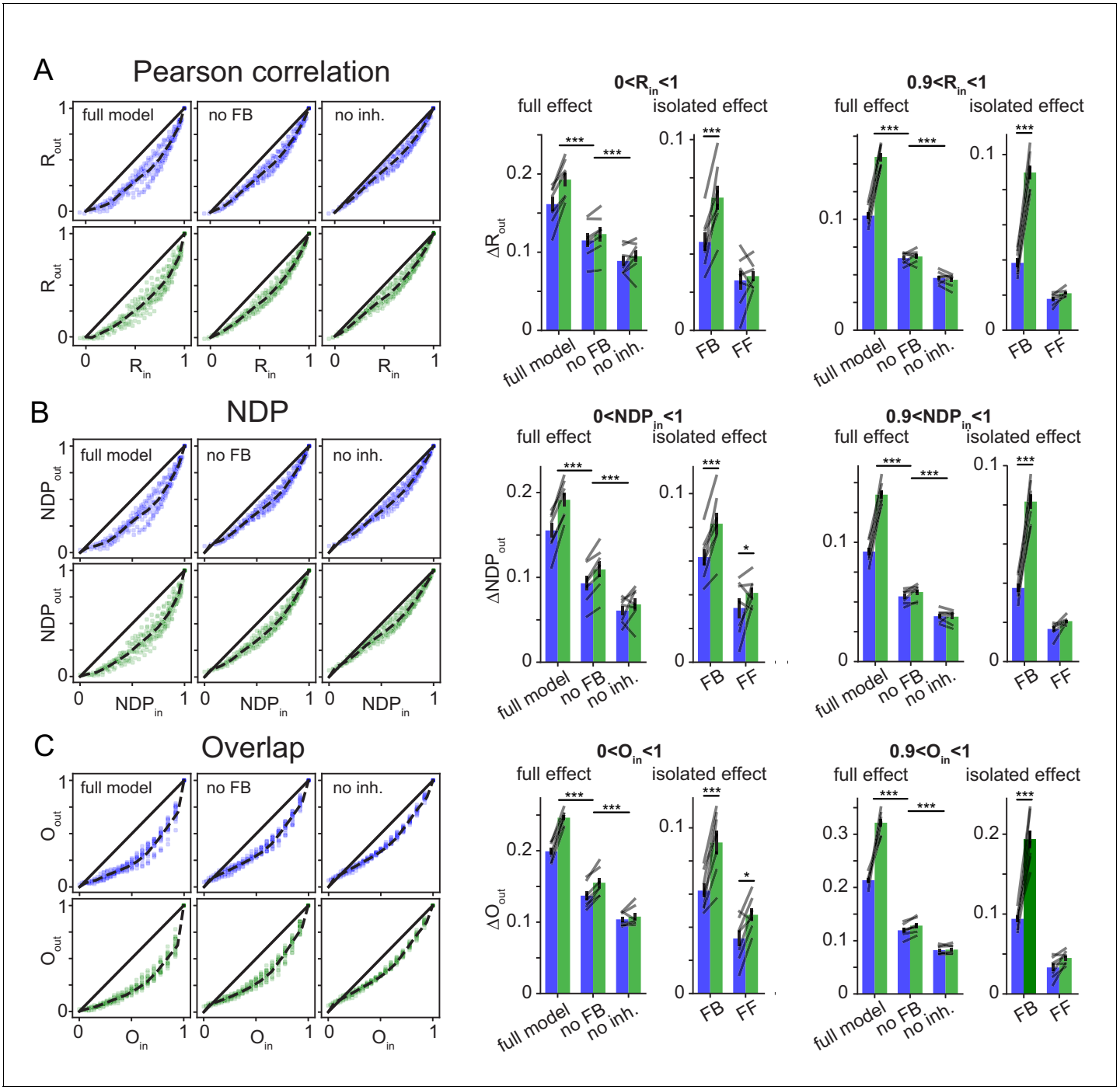

Figure 6—figure supplement 2. Robustness over different Similarity Metrics. To test if the main finding of frequency dependent pattern separation, particularly for highly similar inputs, depended on the similarity metric used, the original data was reanalyzed with two alternative similarity metrics. As in the main figures data points in bar graphs represent the seven independent network seeds. For each network (seed), we ran sets of patterns for the full model, a network without feedback inhibition (no FB) and a model with no inhibition (no inh.). (**A**) Pearson's correlation coefficient R (as in ***Figure 6***) left: exemplary scatterplots of pattern separation effects. right: bargraphs of the mean pattern separation effect over the full input similarity range ($0 < R_{in}1$) or only highly similar input patterns ($0.9 < R_{in} < 1$). Full effects measure the mean pattern separation effect for each network condition: full model, no feedback (no FB) and no inhibition (no inh.). Isolated effects measure the pattern separation contribution of individual circuit motifs: feedback inhibition (FB) and feedforward inhibition (FF). (**B**) Same as (**A**) but using normalized dot product (NDP) as similarity metric for input and output comparisons. (**C**) Same as (**A**) but using population overlap as similarity metric. Overlap is defined as the number of cells active in both patterns (logical and) divided by the number of cells active in either pattern (logical or). The full effects were tested with 2 × 3 ANOVAs followed by Sidak's posttests for differences between conditions. Isolated effects were tested with 2 × 2 ANOVAs followed by Tukey posttests for differences between frequencies. Asterisks indicate significance in posttests given significant overall effects (*p<0.05,**p<0.01,***p<0.001).

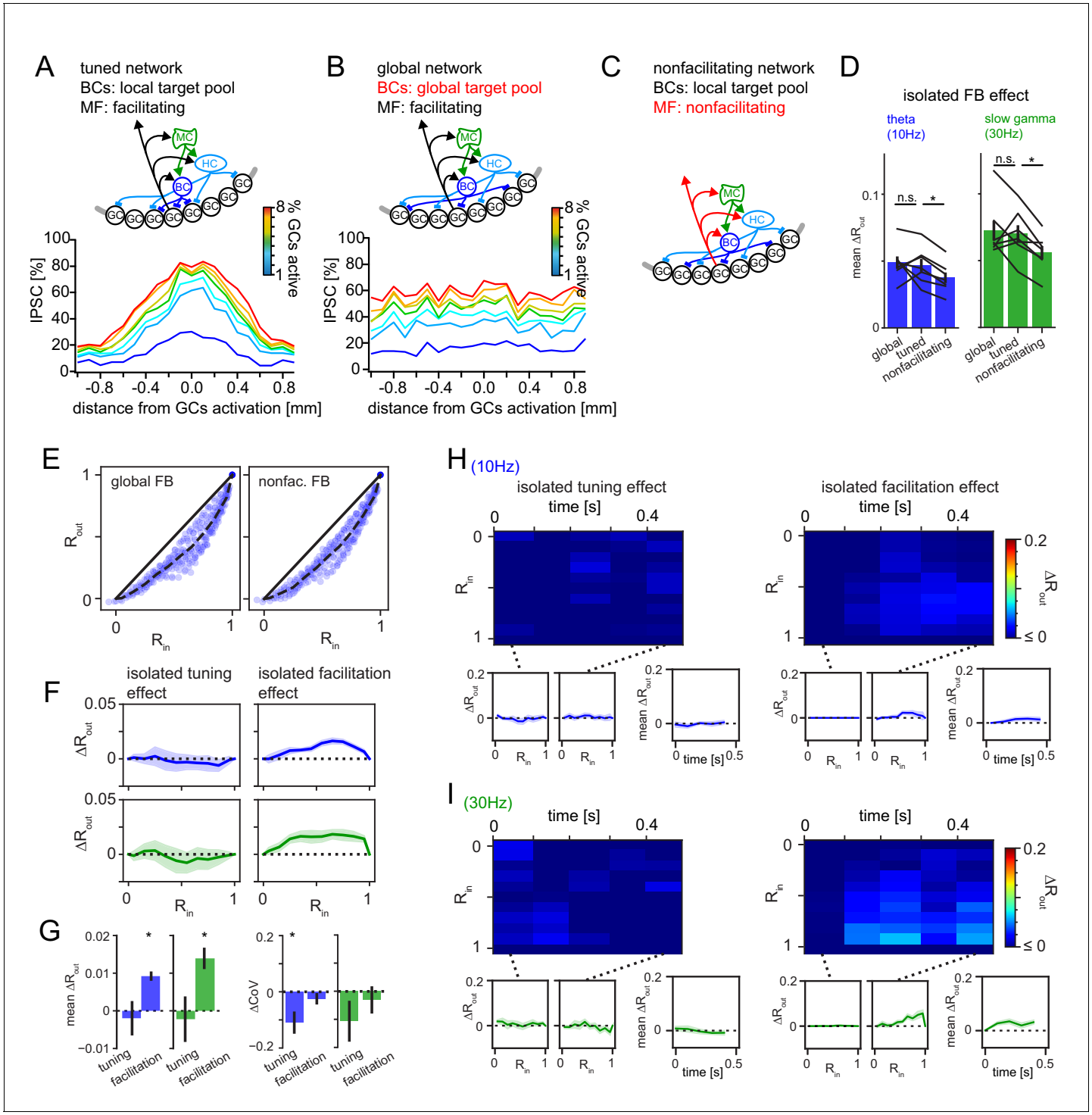

Figure 6—figure supplement 3. Isolated pattern separation effects of spatial tuning and MF facilitation. Effects of isolated manipulations were computed for the DG model as in ***Figure 6***. (**A**) Schematic of the full tuned network and the resulting spatial profile of inhibition (as in ***Figure 5***). (**B**) Schematic of the global network (with unrestricted BC target pool) and the resulting spatial profile of inhibition. (**C**) Schematic of the non-facilitating network. (**D**) Isolated mean feedback effects of the global, tuned and non-facilitating models. Two-way RM ANOVA showed: $p < 0.001$, $= 0.020$, $= 0.402$ for frequency, condition and interaction respectively with * indicating significance in Dunnett's posttest against the full tuned effect. $p = 0.742$ and 0.020 for global and non-facilitating, respectively at 10 Hz; $p = 0.650$ and 0.001 for global and non-facilitating, respectively at 30 Hz. (**E**) Exemplary pattern separation plots of theta modulated inputs when spatial tuning (left) or MF facilitation (right) was removed. (**F**) Isolated pattern separation effects of the given manipulation for theta (blue) or gamma (green) modulated inputs as a function of input similarity. (**G**) Isolated effect of the given manipulation on

Figure 6—figure supplement 3 continued on next page

Figure 6—figure supplement 3 continued

mean ΔR_{out} (left) and the coefficient of variance (ΔCoV) of pattern separation between individual comparisons (right). (**H, I**) Time-resolved analyses of isolated effects of spatial tuning (left) and MF facilitation (right) for theta (top row) and slow gamma (bottom row) modulated inputs. In each subpanel, the bottom left and middle insets show ΔR_{out} as a function of input similarity of the first and last time windows respectively. The bottom right insets show the evolution of the mean ΔR_{out} over time.

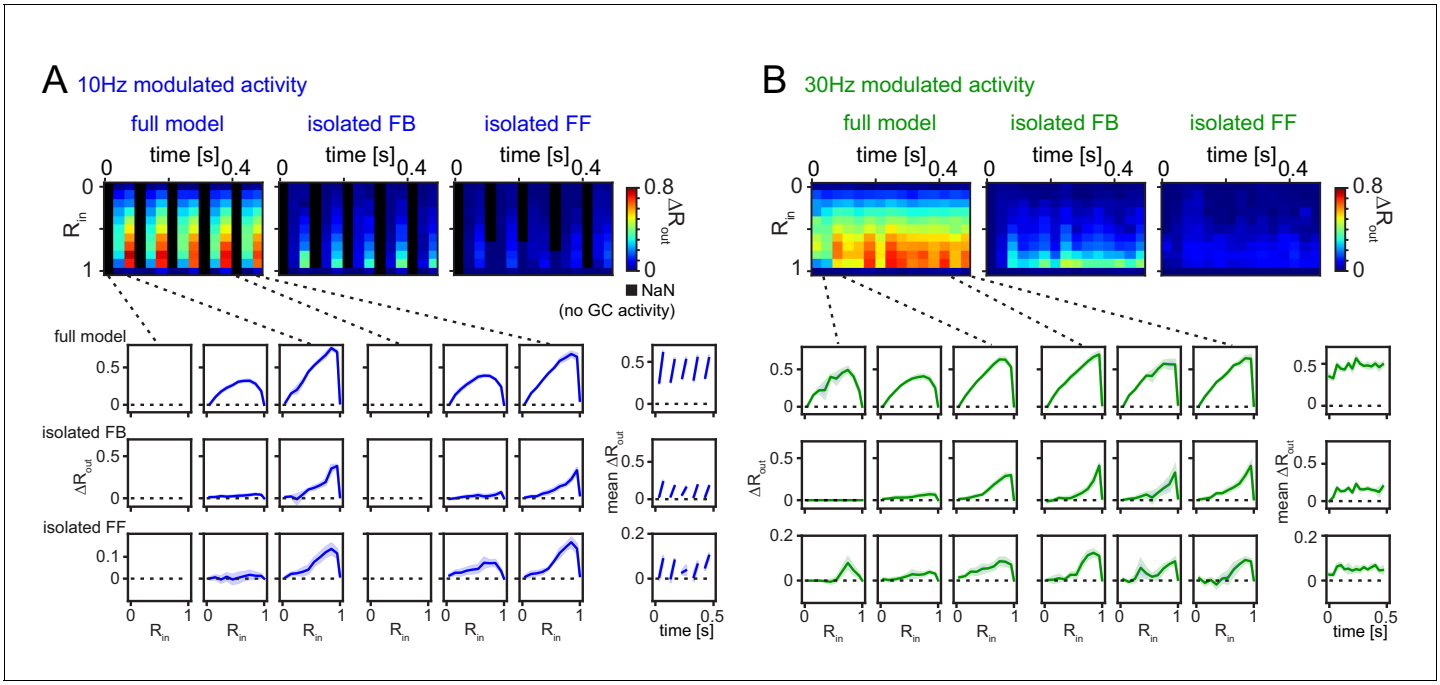

Figure 6—figure supplement 4. Robustness for shorter analysis time-window. (**A**) 33 ms time-resolved pattern separation effects of the full model, isolated feedback (FB) or feedforward (FF) inhibition for theta modulated input (10 Hz). All analyses were performed as above but with rate vector correlations computed for 33 ms time windows (instead of 100 ms or 600 ms, as in ***Figure 6***). The bottom insets show ΔR_{out} as a function of input similarity for the first and last three time windows. The bottom right insets show the evolution of the mean ΔR_{out} over time. (**B**) Same as (**A**) but for slow gamma (30 Hz) modulated inputs. Data represent mean ± SEM of n = 7 random network seeds.

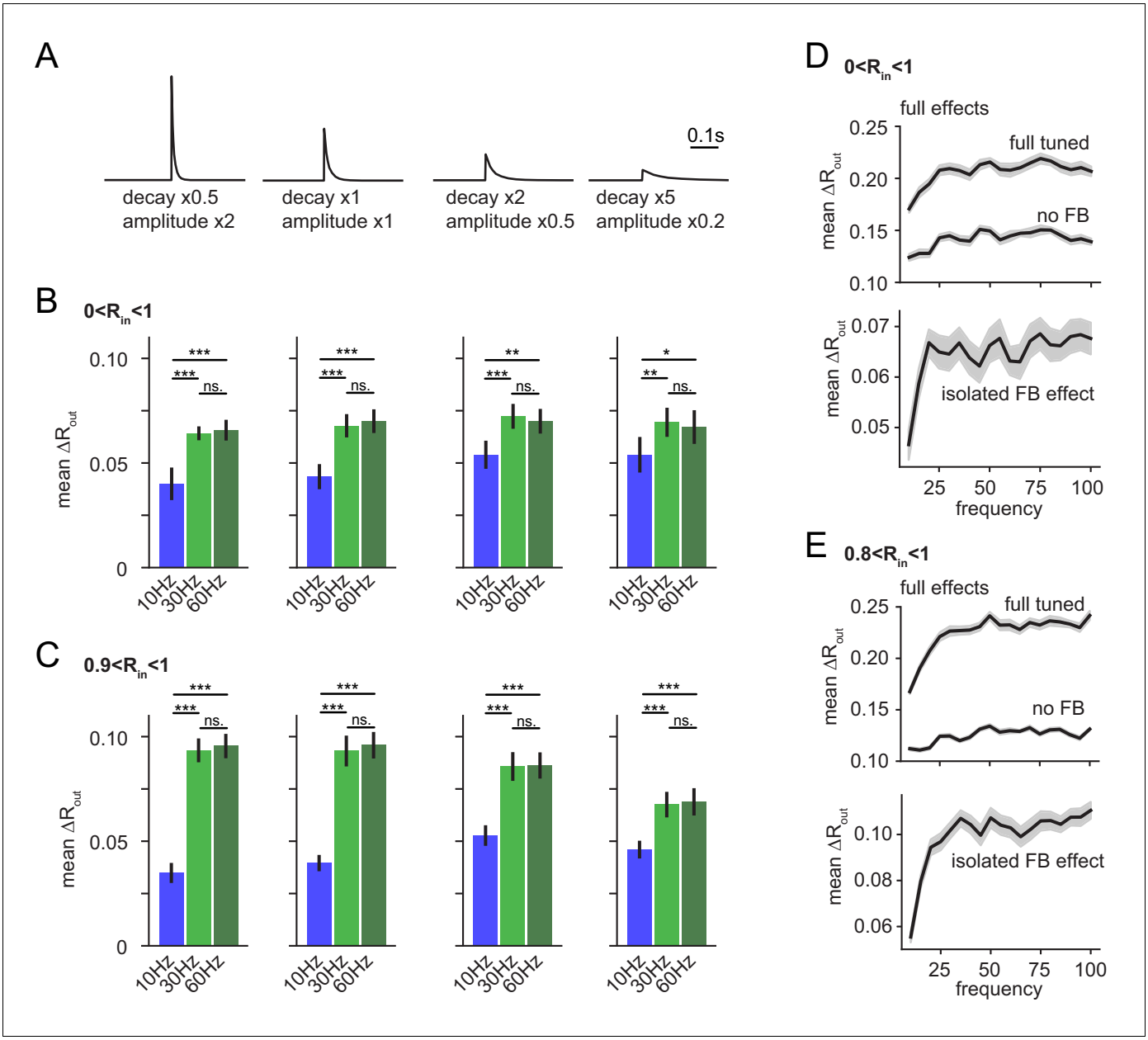

Figure 6—figure supplement 5. Robustness over various IPSC decay time-constants and over the full gamma range. (**A–C**) To test if the frequency dependence of feedback inhibitory pattern separation remained robust for different IPSC decay time constants we probed a range of altered time constants (our experimentally matched time constant x0.5, x1, x2 and x5) while maintaining total inhibitory conductance in the network constant by complementary adjustment of IPSC amplitude. As we expected a potential interaction between IPSC decay and modulation frequency, we probed model runs for each factor with 10 Hz, 30 Hz and 60 Hz modulation. The isolated feedback inhibitory effects were computed and impacts of decay and frequency were examined with 4 × 3 ANOVAs followed by Tukey posttests for differences between frequencies. Asterisks indicate significance in posttests given significant overall effects (*p<0.05,**p<0.01,***p<0.001). (**A**) Illustration of modified IPSC time-courses. (**B**) Mean pattern separation effect of isolated feedback inhibition over the full input similarity range ($0 < R_{in} < 1$). (**C**) Same as (**B**) but only for highly similar input patterns. Analyses in A-C were performed on seven new network seeds with simulation and analysis otherwise identical to ***Figure 6***. (**D–E**) To probe the robustness of frequency-dependent feedback inhibitory pattern separation over an even larger range of frequency modulation, we next simulated the effects over a range from 10 to 100 Hz in 5 Hz steps. To provide computational tractability, we performed only eight runs per frequency (instead of 24 runs as in all other simulations) leading to fewer pattern comparisons, and somewhat noisier readouts. For the majority of frequencies, no input comparisons with $R > 0.9$ occurred so we defined ($0.8 < R_{in} < 1$) as highly similar input patterns, potentially leading to a slight underestimation of our effects.

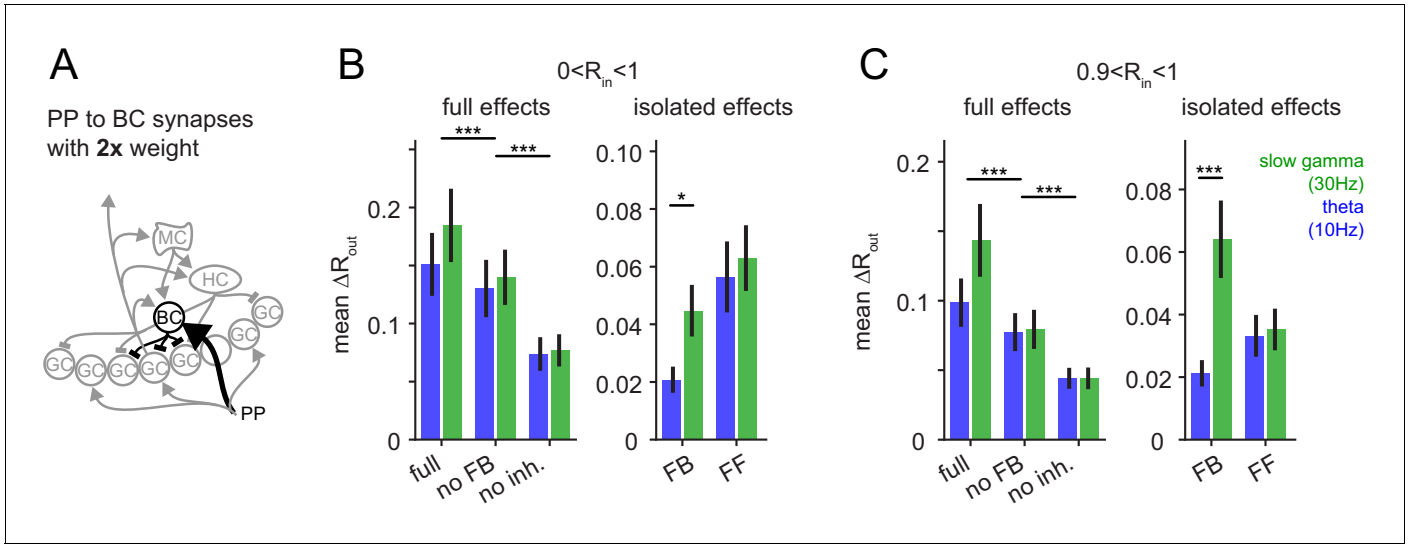

Figure 6—figure supplement 6. Robustness for increased feedforward inhibition. To test if the frequency-dependent enhancement of feedback inhibitory pattern separation of highly similar inputs was sensitive to the changes in the relative strengths of feedforward and feedback inhibition, we increased the perforant path (PP) to basket cell (BC) synapse weight 2x. (**A**) Illustration of the network alteration. (**B**) The resulting full pattern separation effects (left) and isolated feedback (FB) and feedforward (FF) effects (right) as mean over all input similarities. (**C**) Same as (**B**) but only for highly similar input patters. Full effects were tested with 2 × 3 ANOVAs followed by Sidak's postests for differences between conditions. Isolated effects were tested with 2 × 2 ANOVAs followed by Tukey posttests for differences between frequencies. Asterisks indicate significance in posttests given significant overall effects (*p<0.05,**p<0.01,***p<0.001).

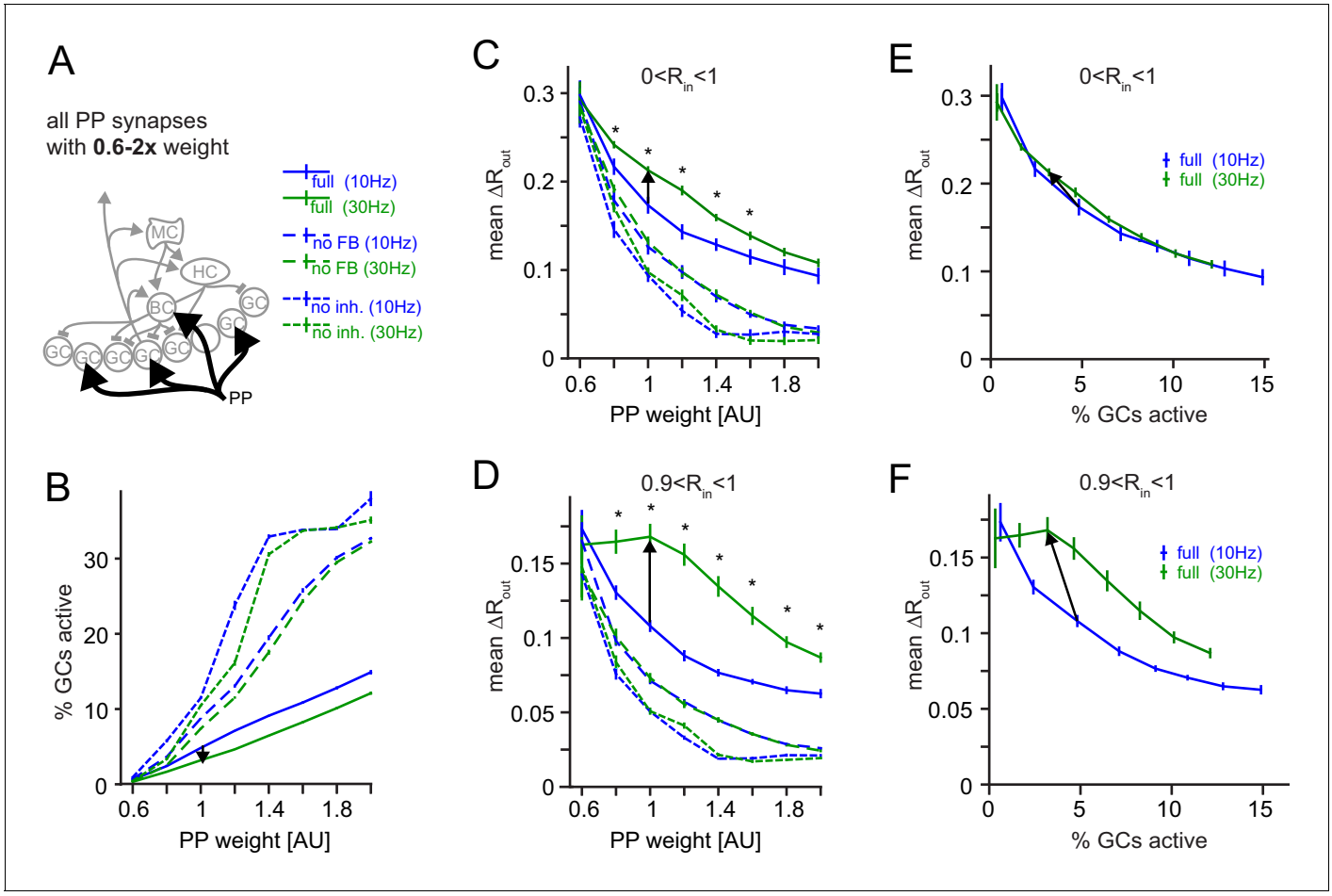

Figure 6—figure supplement 7. Robustness for increased perforant path (PP) drive. The weight of the PP input synapses was varied between 0.6x to 2x their original weight. (**A**) Illustration of the network alteration. (**B**) Active GC fractions for the full network (full), the no feedback inhibition network (no FB) and the no inhibition network (no inh.), each for 10 and 30 Hz modulated PP input. The black arrow indicates the frequency effect for the default PP-weight (1x). (**C**) Full pattern separation effects over all input similarities ($0 < R_{in} < 1$). Asterisks indicate $p<0.05$ (uncorrected t-tests). (**D**) Full pattern separation effects for highly similar input patterns ($0 < R_{in} < 1$). Asterisks indicate $p<0.05$ (uncorrected t-tests). (**E**) Data for the full network from (**B**) and (**C**) plotted to show pattern separation as a function of GC sparsity. The arrow represents the default PP input strength. (**F**) Same as E, but only for highly similar input patterns.

6.3 Summary

We incorporated the quantitative properties of feedback inhibition in the dentate gyrus into a computational model and found that its role in pattern separation depends on the frequency modulation of the input patterns. Thus far, pattern separation has been investigated mostly as a computation that depends mostly on the static elements of a circuit, such as threshold and overall connectivity. Our model proposes that network dynamics could influence the extent of pattern separation. This finding might have implications in brain areas other than the dentate gyrus since neuronal activity in most areas is temporally structure by oscillation activity.

7 References

Allen, K., & Monyer, H. (2015). Interneuron control of hippocampal oscillations. *Current Opinion in Neurobiology*, *31*, 81–87. https://doi.org/10.1016/j.conb.2014.08.016

Amaral, D. G., Scharfman, H. E., & Lavenex, P. (2007). The dentate gyrus: Fundamental neuroanatomical organization (dentate gyrus for dummies). In *Progress in Brain Research* (Vol. 163, pp. 3–22). Elsevier. https://doi.org/10.1016/S0079-6123(07)63001-5

Anderson, C. M., Zhang, B., Miller, M., Butko, E., Wu, X., Laver, T., Kernag, C., Kim, J., Luo, Y., Lamparski, H., Park, E., Su, N., & Ma, X.-J. (2016). Fully Automated RNAscope In Situ Hybridization Assays for Formalin-Fixed Paraffin-Embedded Cells and Tissues. *Journal of Cellular Biochemistry*, *117*(10), 2201–2208. https://doi.org/10.1002/jcb.25606

Bacon, T. J., Pickering, A. E., & Mellor, J. R. (2020). Noradrenaline Release from Locus Coeruleus Terminals in the Hippocampus Enhances Excitation-Spike Coupling in CA1 Pyramidal Neurons Via β-Adrenoceptors. *Cerebral Cortex*, *30*(12), 6135–6151. https://doi.org/10.1093/cercor/bhaa159

Benarroch, E. E. (2018). Locus coeruleus. *Cell and Tissue Research*, *373*(1), 221–232. https://doi.org/10.1007/s00441-017-2649-1

Berg, S., Kutra, D., Kroeger, T., Straehle, C. N., Kausler, B. X., Haubold, C., Schiegg, M., Ales, J., Beier, T., Rudy, M., Eren, K., Cervantes, J. I., Xu, B., Beuttenmueller, F., Wolny, A., Zhang, C., Koethe, U., Hamprecht, F. A., & Kreshuk, A. (2019). ilastik: Interactive machine learning for (bio)image analysis. *Nature Methods*, *16*(12), 1226–1232. https://doi.org/10.1038/s41592-019-0582-9

Braganza, O., & Beck, H. (2018). The Circuit Motif as a Conceptual Tool for Multilevel Neuroscience. *Trends in Neurosciences*, *41*(3), 128–136. https://doi.org/10.1016/j.tins.2018.01.002

Buhl, E. H., Szilágyi, T., Halasy, K., & Somogyi, P. (1996). Physiological properties of anatomically identified basket and bistratified cells in the CA1 area of the rat hippocampus in vitro. *Hippocampus*, *6*, 294–305.

Cadwell, C. R., Palasantza, A., Jiang, X., Berens, P., Deng, Q., Yilmaz, M., Reimer, J., Shen, S., Bethge, M., Tolias, K. F., Sandberg, R., & Tolias, A. S. (2016). Electrophysiological, transcriptomic and morphologic profiling of single neurons using Patch-seq. *Nature Biotechnology*, *34*(2), 199–203. https://doi.org/10.1038/nbt.3445

Cadwell, C. R., Sandberg, R., Jiang, X., & Tolias, A. S. (2017). Q&A: Using Patch-seq to profile single cells. *BMC Biology*, *15*(1), 58. https://doi.org/10.1186/s12915-017-0396-0

Cadwell, C. R., Scala, F., Li, S., Livrizzi, G., Shen, S., Sandberg, R., Jiang, X., & Tolias, A. S. (2017). Multimodal profiling of single-cell morphology, electrophysiology, and gene expression using Patch-seq. *Nature Protocols*, *12*(12), 2531–2553. https://doi.org/10.1038/nprot.2017.120

Cauli, B., Audinat, E., Lambolez, B., Angulo, M. C., Ropert, N., Tsuzuki, K., Hestrin, S., & Rossier, J. (1997). Molecular and Physiological Diversity of Cortical Nonpyramidal Cells. *The Journal of Neuroscience*, *17*(10), 3894–3906. https://doi.org/10.1523/JNEUROSCI.17-10-03894.1997

Cayco-Gajic, N. A., Clopath, C., & Silver, R. A. (2017). Sparse synaptic connectivity is required for decorrelation and pattern separation in feedforward networks. *Nature Communications*, *8*(1), 1116. https://doi.org/10.1038/s41467-017-01109-y

Cayco-Gajic, N. A., & Silver, R. A. (2019). Re-evaluating Circuit Mechanisms Underlying Pattern Separation. *Neuron*, *101*(4), 584–602. https://doi.org/10.1016/j.neuron.2019.01.044

Chavlis, S., Petrantonakis, P. C., & Poirazi, P. (2017). Dendrites of Dentate Gyrus Granule Cells Contribute to Pattern Separation by Controlling Sparsity. *Hippocampus*, *27*(1), 89–110. https://doi.org/10.1002/hipo.22675

Chavlis, S., & Poirazi, P. (2017). Pattern separation in the Hippocampus through the eyes of computational modeling. *Synapse*, *71*(6), e21972. https://doi.org/10.1002/syn.21972

de Almeida, L., Idiart, M., & Lisman, J. E. (2009). A Second Function of Gamma Frequency Oscillations: An E%-Max Winner-Take-All Mechanism Selects Which Cells Fire. *Journal of Neuroscience*, *29*(23), 7497–7503. https://doi.org/10.1523/JNEUROSCI.6044-08.2009

Espinoza, C., Guzman, S. J., Zhang, X., & Jonas, P. (2018). Parvalbumin+ interneurons obey unique connectivity rules and establish a powerful lateral-inhibition microcircuit in dentate gyrus. *Nature Communications*, *9*(1), 4605. https://doi.org/10.1038/s41467-018-06899-3

Fasano, C., Rocchetti, J., Pietrajtis, K., Zander, J.-F., Manseau, F., Sakae, D. Y., Marcus-Sells, M., Ramet, L., Morel, L. J., Carrel, D., Dumas, S., Bolte, S., Bernard, V., Vigneault, E., Goutagny, R., Ahnert-Hilger, G., Giros, B., Daumas, S., Williams, S., & El Mestikawy, S. (2017). Regulation of the Hippocampal Network by VGLUT3-Positive CCK-GABAergic Basket Cells. *Frontiers in Cellular Neuroscience*, *11*, 140. https://doi.org/10.3389/fncel.2017.00140

Ferrante, M., Migliore, M., & Ascoli, G. A. (2009). Feed-forward inhibition as a buffer of the neuronal input-output relation. *Proceedings of the National Academy of Sciences*, *106*(42), 18004–18009. https://doi.org/10.1073/pnas.0904784106

Freund, T. F., & Buzsáki, G. (1996). Interneurons of the hippocampus. *Hippocampus*, *6*, 347–470.

Freund, T. F., & Katona, I. (2007). Perisomatic Inhibition. *Neuron*, *56*(1), 33–42. https://doi.org/10.1016/j.neuron.2007.09.012

Friedrich, R. W., & Laurent, G. (2001). Dynamic Optimization of Odor Representations by Slow Temporal Patterning of Mitral Cell Activity. *Science*, *291*(5505), 889–894. https://doi.org/10.1126/science.291.5505.889

Garcia, S., Guarino, D., Jaillet, F., Jennings, T., Pröpper, R., Rautenberg, P. L., Rodgers, C. C., Sobolev, A., Wachtler, T., Yger, P., & Davison, A. P. (2014). Neo: An object model for handling electrophysiology data in multiple formats. *Frontiers in Neuroinformatics*, *8*. https://doi.org/10.3389/fninf.2014.00010

Gibson, W. G., Robinson, J., & Bennett, M. R. (1991). Probabilistic Secretion of Quanta in the Central Nervous System: Granule Cell Synaptic Control of Pattern Separation and Activity Regulation. *Philosophical Transactions: Biological Sciences*, *332*(1264), 199–220.

Gouwens, N. W., Sorensen, S. A., Baftizadeh, F., Budzillo, A., Lee, B. R., Jarsky, T., Alfiler, L., Arkhipov, A., Baker, K., Barkan, E., Berry, K., Bertagnolli, D., Bickley, K., Bomben, J., Braun, T., Brouner, K., Casper, T., Crichton, K., Daigle, T. L., … Zeng, H. (2020). *Toward an integrated classification of neuronal cell types: Morphoelectric and transcriptomic characterization of individual GABAergic cortical neurons* [Preprint]. https://doi.org/10.1101/2020.02.03.932244

Grimes, W. N., Seal, R. P., Oesch, N., Edwards, R. H., & Diamond, J. S. (2011). Genetic targeting and physiological features of VGLUT3+ amacrine cells. *Visual Neuroscience*, *28*(5), 381–392. https://doi.org/10.1017/S0952523811000290

Gschwend, O., Abraham, N. M., Lagier, S., Begnaud, F., Rodriguez, I., & Carleton, A. (2015). Neuronal pattern separation in the olfactory bulb improves odor discrimination learning. *Nature Neuroscience*, *18*(10), 1474–1482. https://doi.org/10.1038/nn.4089

Halasy, K., Buhl, E. H., Lörinczi, Z., Tamás, G., & Somogyi, P. (1996). Synaptic target selectivity and input of GABAergic basket and bistratified interneurons in the CA1 area of the rat hippocampus. *Hippocampus*, *6*, 306–329.

He, M., Tucciarone, J., Lee, S., Nigro, M. J., Kim, Y., Levine, J. M., Kelly, S. M., Krugikov, I., Wu, P., Chen, Y., Gong, L., Hou, Y., Osten, P., Rudy, B., & Huang, Z. J. (2016).

Strategies and Tools for Combinatorial Targeting of GABAergic Neurons in Mouse Cerebral Cortex. *Neuron*, *91*(6), 1228–1243. https://doi.org/10.1016/j.neuron.2016.08.021

Herzog, E., Gilchrist, J., Gras, C., Muzerelle, A., Ravassard, P., Giros, B., Gaspar, P., & El Mestikawy, S. (2004). Localization of VGLUT3, the vesicular glutamate transporter type 3, in the rat brain. *Neuroscience*, *123*(4), 983–1002. https://doi.org/10.1016/j.neuroscience.2003.10.039

Hosp, J. A., Strüber, M., Yanagawa, Y., Obata, K., Vida, I., Jonas, P., & Bartos, M. (2014). Morpho-physiological criteria divide dentate gyrus interneurons into classes: Interneuron Diversity in Mouse Dentate Gyrus. *Hippocampus*, *24*(2), 189–203. https://doi.org/10.1002/hipo.22214

Hu, H., Gan, J., & Jonas, P. (2014). Fast-spiking, parvalbumin+ GABAergic interneurons: From cellular design to microcircuit function. *Science*, *345*(6196), 529–542. https://doi.org/10.1126/science.1255263

Hunter, J. D. (2007). Matplotlib: A 2D Graphics Environment. *Computing in Science & Engineering*, *9*(3), 90–95. https://doi.org/10.1109/MCSE.2007.55

Ilicic, T., Kim, J. K., Kolodziejczyk, A. A., Bagger, F. O., McCarthy, D. J., Marioni, J. C., & Teichmann, S. A. (2016). Classification of low quality cells from single-cell RNA-seq data. *Genome Biology*, *17*(29). https://doi.org/10.1186/s13059-016-0888-1

Kalisky, T., Oriel, S., Bar-Lev, T. H., Ben-Haim, N., Trink, A., Wineberg, Y., Kanter, I., Gilad, S., & Pyne, S. (2018). A brief review of single-cell transcriptomic technologies. *Briefings in Functional Genomics*, *17*(1), 64–76. https://doi.org/10.1093/bfgp/elx019

Katona, I., Acsády, L., & Freund, T. F. (1999). Postsynaptic targets of somatostatin-immunoreactive interneurons in the rat hippocampus. *Neuroscience*, *88*(1), 37–55. https://doi.org/10.1016/S0306-4522(98)00302-9

Kaufman, S. (1995). Tyrosine Hydroxylase. In F. F. Nord & A. Meister (Eds.), *Advances in Enzymology—And Related Areas of Molecular Biology* (pp. 103–220). John Wiley & Sons, Inc. https://doi.org/10.1002/9780470123164.ch3

Kawaguchi, Y., & Kondo, S. (2002). Parvalbumin, somatostatin and cholecystokinin as chemical markers for specific GABAergic interneuron types in the rat frontal cortex. *Journal of Neurocytology*, *31*(3/5), 277–287. https://doi.org/10.1023/A:1024126110356

Kim, H., Kim, M., Im, S.-K., & Fang, S. (2018). Mouse Cre-LoxP system: General principles to determine tissue-specific roles of target genes. *Laboratory Animal Research*, *34*(4), 13.

Klausberger, T. (2009). GABAergic interneurons targeting dendrites of pyramidal cells in the CA1 area of the hippocampus. *European Journal of Neuroscience*, *30*(6), 947–957. https://doi.org/10.1111/j.1460-9568.2009.06913.x

Kosaka, T., Hama, K., & Nagatsu, I. (1987). Tyrosine hydroxylase-immunoreactive intrinsic neurons in the rat cerebral cortex. *Experimental Brain Research*, *68*(2). https://doi.org/10.1007/BF00248804

Lee, B. R., Budzillo, A., Hadley, K., Miller, J. A., Jarsky, T., Baker, K., Hill, D., Kim, L., Mann, R., Ng, L., Oldre, A., Rajanbabu, R., Trinh, J., Braun, T., Dalley, R., Gouwens, N. W., Kalmbach, B. E., Kim, T. K., Smith, K., … Berg, J. (2020). *Scaled, high fidelity electrophysiological, morphological, and transcriptomic cell characterization* [Preprint]. Neuroscience. https://doi.org/10.1101/2020.11.04.369082

Leutgeb, J. K., Leutgeb, S., Moser, M.-B., & Moser, E. I. (2007). Pattern Separation in the Dentate Gyrus and CA3 of the Hippocampus. *Science*, *315*(5814), 961–966. https://doi.org/10.1126/science.1135801

Lovett-Barron, M., Turi, G. F., Kaifosh, P., Lee, P. H., Bolze, F., Sun, X.-H., Nicoud, J.-F., Zemelman, B. V., Sternson, S. M., & Losonczy, A. (2012). Regulation of neuronal input transformations by tunable dendritic inhibition. *Nature Neuroscience*, *15*(3), 423–430. https://doi.org/10.1038/nn.3024

Lun, A. T. L., McCarthy, D. J., & Marioni, J. C. (2016). A step-by-step workflow for low-level analysis of single-cell RNA-seq data with Bioconductor [version 2; referees: 3 approved, 2 approved with reservations]. *F1000Research*, *5*(2122).

Maccaferri, G., & Lacaille, J.-C. (2003). Interneuron Diversity series: Hippocampal interneuron classifications – making things as simple as possible, not simpler. *Trends in Neurosciences*, *26*(10), 564–571. https://doi.org/10.1016/j.tins.2003.08.002

Madisen, L., Garner, A. R., Shimaoka, D., Chuong, A. S., Li, L., Gu, H., Mills, M., Cheng, A., Tasic, B., Nguyen, T. N., Sunkin, S. M., Benucci, A., Nagy, A., Miyawaki, A., Empson, R. M., Knöpfel, T., Boyden, E. S., Reid, R. C., Carandini, M., & Zeng, H. (2015). Transgenic mice for intersectional targeting of neural sensors and effectors with high specificity and performance. *Neuron*, *85*(5), 942–958. https://doi.org/doi:10.1016/j.neuron.2015.02.022

Marr, D. (1969). A THEORY OF CEREBELLAR CORTEX. *J. Physiology*, *202*, 437–470.

Marr, D. (1971). Simple Memory: A Theory for Archicortex. *Philosophical Transactions of the Royal Society of London. Series B, Biological Sciences*, *262*(841), 23–81.

McKinney, W. (2010). *Data Structures for Statistical Computing in Python*. 56–61. https://doi.org/10.25080/Majora-92bf1922-00a

McNamara, C. G., & Dupret, D. (2017). Two sources of dopamine for the hippocampus. *Trends in Neurosciences*, *40*(7), 383–384. https://doi.org/10.1016/j.tins.2017.05.005

McNamara, C. G., Tejero-Cantero, Á., Trouche, S., Campo-Urriza, N., & Dupret, D. (2014). Dopaminergic neurons promote hippocampal reactivation and spatial memory persistence. *Nature Neuroscience*, *17*(12), 1658–1660. https://doi.org/10.1038/nn.3843

Monyer, H., & Markram, H. (2004). Interneuron Diversity series: Molecular and genetic tools to study GABAergic interneuron diversity and function. *Trends in Neurosciences*, *27*(2), 90–97. https://doi.org/10.1016/j.tins.2003.12.008

Müller, C., & Remy, S. (2014). Dendritic inhibition mediated by O-LM and bistratified interneurons in the hippocampus. *Frontiers in Synaptic Neuroscience*, *6*. https://doi.org/10.3389/fnsyn.2014.00023

Müller-Komorowska, D., Opitz, T., Elzoheiry, S., Schweizer, M., Ambrad Giovannetti, E., & Beck, H. (2020). Nonspecific Expression in Limited Excitatory Cell Populations in Interneuron-Targeting Cre-driver Lines Can Have Large Functional Effects. *Frontiers in Neural Circuits*, *14*, 16. https://doi.org/10.3389/fncir.2020.00016

Muñoz-Manchado, A. B., Bengtsson Gonzales, C., Zeisel, A., Munguba, H., Bekkouche, B., Skene, N. G., Lönnerberg, P., Ryge, J., Harris, K. D., Linnarsson, S., & Hjerling-Leffler, J. (2018). Diversity of Interneurons in the Dorsal Striatum Revealed by Single-Cell RNA Sequencing and PatchSeq. *Cell Reports*, *24*(8), 2179-2190.e7. https://doi.org/10.1016/j.celrep.2018.07.053

Olsen, S. R., Bhandawat, V., & Wilson, R. I. (2010). Divisive Normalization in Olfactory Population Codes. *Neuron*, *66*(2), 287–299. https://doi.org/10.1016/j.neuron.2010.04.009

Pawelzik, H., Hughes, D. I., & Thomson, A. M. (2002). Physiological and morphological diversity of immunocytochemically defined parvalbumin- and cholecystokinin-positive interneurones in CA1 of the adult rat hippocampus. *The Journal of Comparative Neurology*, *443*(4), 346–367. https://doi.org/10.1002/cne.10118

Pedregosa, F., Varoquaux, G., Gramfort, A., Michel, V., Thirion, B., Grisel, O., Blondel, M., Prettenhofer, P., Weiss, R., Dubourg, V., Vanderplas, J., Passos, A., & Cournapeau, D. (2011). Scikit-learn: Machine Learning in Python. *Journal of Machine Learning Research*, *12*, 2825–2830.

Pelkey, K. A., Calvigioni, D., Fang, C., Vargish, G., Ekins, T., Auville, K., Wester, J. C., Lai, M., Mackenzie-Gray Scott, C., Yuan, X., Hunt, S., Abebe, D., Xu, Q., Dimidschstein, J., Fishell, G., Chittajallu, R., & McBain, C. J. (2020). Paradoxical network excitation by glutamate release from VGluT3+ GABAergic interneurons. *ELife*, *9*. https://doi.org/10.7554/eLife.51996

Pelkey, K. A., Chittajallu, R., Craig, M. T., Tricoire, L., Wester, J. C., & McBain, C. J. (2017). Hippocampal GABAergic Inhibitory Interneurons. *Physiological Reviews*, *97*(4), 1619–1747. https://doi.org/10.1152/physrev.00007.2017

Pouille, F., & Scanziani, M. (2001). Enforcement of Temporal Fidelity in Pyramidal Cells by Somatic Feed-Forward Inhibition. *Science*, *293*(5532), 1159–1163. https://doi.org/10.1126/science.1060342

R Core Team. (2020). *R: A language and environment for statistical computing.* [R]. R Foundation for Statistical Computing, Vienna,. https://www.R-project.org/

Rolls, E. T. (1989). Functions of Neuronal Networks in the Hippocampus and Neocortex in Memory. In *Neural Models of Plasticity* (pp. 240–265). Elsevier. https://doi.org/10.1016/B978-0-12-148955-7.50017-5

Root, D. H., Mejias-Aponte, C. A., Zhang, S., Wang, H.-L., Hoffman, A. F., Lupica, C. R., & Morales, M. (2014). Single rodent mesohabenular axons release glutamate and GABA. *Nature Neuroscience*, *17*(11), 1543–1551. https://doi.org/10.1038/nn.3823

Savanthrapadian, S., Meyer, T., Elgueta, C., Booker, S. A., Vida, I., & Bartos, M. (2014). Synaptic Properties of SOM- and CCK-Expressing Cells in Dentate Gyrus Interneuron Networks. *Journal of Neuroscience*, *34*(24), 8197–8209. https://doi.org/10.1523/JNEUROSCI.5433-13.2014

Savitt, J. M. (2005). Bcl-x Is Required for Proper Development of the Mouse Substantia Nigra. *Journal of Neuroscience*, *25*(29), 6721–6728. https://doi.org/10.1523/JNEUROSCI.0760-05.2005

Scharfman, H. E. (2007). The CA3 "backprojection" to the dentate gyrus. In *Progress in Brain Research* (Vol. 163, pp. 627–637). Elsevier. https://doi.org/10.1016/S0079-6123(07)63034-9

Scharfman, H. E. (2016). The enigmatic mossy cell of the dentate gyrus. *Nature Reviews Neuroscience*, *17*(9), 562–575. https://doi.org/10.1038/nrn.2016.87

Schindelin, J., Arganda-Carreras, I., Frise, E., Kaynig, V., Longair, M., Pietzsch, T., Preibisch, S., Rueden, C., Saalfeld, S., Schmid, B., Tinevez, J.-Y., White, D. J., Hartenstein,

V., Eliceiri, K., Tomancak, P., & Cardona, A. (2012). Fiji: An open-source platform for biological-image analysis. *Nature Methods*, *9*(7), 676–682. https://doi.org/10.1038/nmeth.2019

Schnütgen, F., Doerflinger, N., Calléja, C., Wendling, O., Chambon, P., & Ghyselinck, N. B. (2003). A directional strategy for monitoring Cre-mediated recombination at the cellular level in the mouse. *Nature Biotechnology*, *21*(5), 562–565. https://doi.org/10.1038/nbt811

Seabold, S., & Perktold, J. (2010). Statsmodels: Econometric and Statistical Modeling with Python. *Python in Science Conference*, 92–96. https://doi.org/10.25080/Majora-92bf1922-011

Soltesz, I., & Losonczy, A. (2018). CA1 pyramidal cell diversity enabling parallel information processing in the hippocampus. *Nature Neuroscience*, *21*(4), 484–493. https://doi.org/10.1038/s41593-018-0118-0

Somogyi, J., Baude, A., Omori, Y., Shimizu, H., Mestikawy, S. E., Fukaya, M., Shigemoto, R., Watanabe, M., & Somogyi, P. (2004). GABAergic basket cells expressing cholecystokinin contain vesicular glutamate transporter type 3 (VGLUT3) in their synaptic terminals in hippocampus and isocortex of the rat. *European Journal of Neuroscience*, *19*(3), 552–569. https://doi.org/10.1111/j.0953-816X.2003.03091.x

Sun, X., Bernstein, M. J., Meng, M., Rao, S., Sørensen, A. T., Yao, L., Zhang, X., Anikeeva, P. O., & Lin, Y. (2020). Functionally Distinct Neuronal Ensembles within the Memory Engram. *Cell*, *181*(2), 410-423.e17. https://doi.org/10.1016/j.cell.2020.02.055

Takeuchi, T., Duszkiewicz, A. J., Sonneborn, A., Spooner, P. A., Yamasaki, M., Watanabe, M., Smith, C. C., Fernández, G., Deisseroth, K., Greene, R. W., & Morris, R. G. M. (2016). Locus coeruleus and dopaminergic consolidation of everyday memory. *Nature*, *537*(7620), 357–362. https://doi.org/10.1038/nature19325

The Petilla Interneuron Nomenclature Group (PING). (2008). Petilla terminology: Nomenclature of features of GABAergic interneurons of the cerebral cortex. *Nature Reviews Neuroscience*, *9*(7), 557–568. https://doi.org/10.1038/nrn2402

Urban-Ciecko, J., & Barth, A. L. (2016). Somatostatin-expressing neurons in cortical networks. *Nature Reviews Neuroscience*, *17*(7), 401–409. https://doi.org/10.1038/nrn.2016.53

van der Maaten, L., & Hinton, G. (2008). Visualizing Data using t-SNE. *Journal of Machine Learning Research*, *9*, 2579–2605.

van der Walt, S., Colbert, S. C., & Varoquaux, G. (2011). The NumPy Array: A Structure for Efficient Numerical Computation. *Computing in Science & Engineering*, *13*(2), 22–30. https://doi.org/10.1109/MCSE.2011.37

Virtanen, P., Gommers, R., Oliphant, T. E., Haberland, M., Reddy, T., Cournapeau, D., Burovski, E., Peterson, P., Weckesser, W., Bright, J., van der Walt, S. J., Brett, M., Wilson, J., Millman, K. J., Mayorov, N., Nelson, A. R. J., Jones, E., Kern, R., Larson, E., … Contributors, S. 1 0. (2020). SciPy 1.0—Fundamental Algorithms for Scientific Computing in Python. *Nature Methods*, *17*(3), 261–272. https://doi.org/10.1038/s41592-019-0686-2

Wolf, F. A., Angerer, P., & Theis, F. J. (2018). SCANPY: Large-scale single-cell gene expression data analysis. *Genome Biology*, *19*(1), 15. https://doi.org/10.1186/s13059-017-1382-0

Xin, J., Mark, A., Afrasiabi, C., Tsueng, G., Juchler, M., Gopal, N., Stupp, G. S., Putman, T. E., Ainscough, B. J., Griffith, O. L., Torkamani, A., Whetzel, P. L., Mungall, C. J., Mooney, S. D., Su, A. I., & Wu, C. (2016). High-performance web services for querying gene and variant annotation. *Genome Biology*, *17*(1), 91. https://doi.org/10.1186/s13059-016-0953-9

Yao, Z., van Velthoven, C. T. J., Nguyen, T. N., Goldy, J., Sedeno-Cortes, A. E., Baftizadeh, F., Bertagnolli, D., Casper, T., Chiang, M., Crichton, K., Ding, S.-L., Fong, O., Garren, E., Glandon, A., Gouwens, N. W., Gray, J., Graybuck, L. T., Hawrylycz, M. J., Hirschstein, D., … Zeng, H. (2021). A taxonomy of transcriptomic cell types across the isocortex and hippocampal formation. *Cell*. https://doi.org/10.1016/j.cell.2021.04.021

Yassa, M. A., & Stark, C. E. L. (2011). Pattern separation in the hippocampus. *Trends in Neurosciences*, *34*(10), 515–525. https://doi.org/10.1016/j.tins.2011.06.006

Yim, M. Y., Hanuschkin, A., & Wolfart, J. (2015). Intrinsic rescaling of granule cells restores pattern separation ability of a dentate gyrus network model during epileptic hyperexcitability: INTRINSIC RESCALING AND NEURONAL NETWORK PATTERN SEPARATION. *Hippocampus*, *25*(3), 297–308. https://doi.org/10.1002/hipo.22373

8 Acknowledgements

I want to thank Prof. Dr. Heinz Beck for his support throughout our projects. Heinz has given me enormous amounts of trust and freedom. Working with him has been a privilege and I am grateful.

I also want to thank Prof. Dr. Michael Pankratz who has supported me as second thesis supervisor and member of my thesis advisory committee. His feedback and ideas were highly appreciated. In this vein I also want to thank Prof. Dr. Christian Henneberger and Prof. Dr. Susanne Schoch for their support and feedback during our thesis advisory committee meetings. I also thank Dr. Laura Ewell for her support during these meetings and beyond.

I especially want to thank Prof. Dr. Florian Mormann who has supported me since my master studies, and I appreciate his continued support during my PhD.

Pedro Royero has established patch seq in our lab and I want to thank him for passing the technique and many of its details onto me. Thank you to Dr. Kristian Händler and Heidi Theiss who were my main contacts at the PRECISE core facility (DZNE, Bonn), where they did a great job with the single cell sequencing of the patch seq samples.

I want to thank Prof. Dr. Sandra Blaess and Dr. Erick Martinez Chavez for the great collaboration with the RNAscope experiments.

Special thanks to Dr. Oliver Braganza for bringing me into his project.

Thanks to André Haubrich who has given me extremely helpful feedback on this thesis.

Thanks to Dr. Thoralf Opitz and Dr. Tony Kelly for teaching me patch clamp early during my PhD and master thesis.

Thank you to everyone else in the lab for the great time.

I also want to thank the International Max Planck Research School for Brain and Behavior, especially our coordinator Ezgi Bulca.

I want to thank my parents for their unconditional support. Ohne eure Unterstützung hätte ich es nicht geschafft.

Most importantly of course I am indebted to my wife Joanna. I love you.